

**Comparison of photophysics
across bulk heterojunction
organic photovoltaic cells
containing different classes of
electron acceptors**

by

Shyamal K K Prasad

A thesis
submitted to the Victoria University of Wellington
in fulfilment of the
requirements for the degree of
Doctor of Philosophy
in Science.

Victoria University of Wellington
2022

Abstract

Access to energy has been a key driver of global progress and growth, with this growth comes increased global energy demand; currently at around 18 TW on average and projected to increase. An accessible and distributed source of power is needed to fill this growing need. Solar power fits this need, and the future of this technology lies in reducing the energy cost to manufacture photovoltaic (PV) systems, retain or improve performance, and tailor their properties for niche applications.

Since the design of new PV materials depends on optimising the response of materials to light, optical spectroscopy is a critical experimental tool. Of the different spectroscopic tools, transient absorption spectroscopy is ideal for understanding the photophysics of solar cells because PV materials always have visible absorption signatures that evolve over time. Being a pump–probe technique, the advent of amplified femtosecond laser systems allows femto– to micro– second timescales to be routinely measured, making it possible to track the evolution of the excited state species from exciton formation to relaxation or recombination back to the ground state.

This thesis characterises the photophysics of multiple different bulk–heterojunction (BHJ) organic photovoltaic (OPV) systems containing different electron acceptors. Using transient absorption spectroscopy, we have developed an understanding of how changes to the organic materials and morphology affect the photophysics and subsequent solar power conversion efficiency.

The thesis is separated into four main sections; the first, Chapter 2 looks at improvements made to the experimental setup to allow the characterisation of organic-photovoltaics over a low excitation power that can provide information relevant to operating conditions, and in the following three chapters, this improved technique is used to look at the various classes of electron acceptors in BHJ-OPVs: fullerenes, polymers, and small molecule acceptors (SMA).

Chapter 3 covers fullerene acceptor BHJ-OPVs looking at two different systems. First, the weight percentage of PC₇₁BM is varied, resulting in changes to the photophysics consistent with variation in domain size and purity; this interplay between photophysics and morphology highlights how understanding both is crucial to optimising BHJ-OPVs. The second looks at changing the functionality of the fullerene, looking at three common fullerene derivatives PC₆₁BM, PC₇₁BM, and ICBA. Here, the differences are more subtle, showing that while ICBA and PC₆₁BM blends generate charges promptly, a combination of poor quenching in the ICBA blend and shorter lifetimes in the PC₆₁BM blend explain the higher power conversion efficiency of the PC₇₁BM system.

In Chapter 4, blends with a polymer used as the electron donor and a different polymer used as the electron acceptor are studied. In this chapter, we see that the photophysics of a system can have little to no correlation to the overall power conversion efficiency. The increased fluorination of the polymer electron acceptor, PNDITPhT, results in no observable changes in the measured photophysics, while the power conversion efficiency (PCE) changes from 3.1 % to 4.3 % (improves by more than 30 %). Also, in this chapter, the effect of the donor polymers (PTB7-Th and PTB7) blended with P(NDI2OD-T2) is investigated; showing a doubling of power conversion efficiency from 2.1 % to 4.4 %; attributed to longer-lived and more mobile charges.

Finally, we investigate at small molecule acceptors in Chapter 5. Here, we look at one of the first small-molecule acceptor systems to have better efficiency than fullerene:polymer blends developed at this time. By comparing several polymer

acceptors, it is found that for the small-molecule acceptor IDIC, the photophysics of an efficient blend are similar to those observed when using a fullerene acceptor. And, when matching the SMA with low-bandgap polymers, the materials do not suffer from the triplet loss mechanism present in low-bandgap BHJ-OPVs.

Together, this thesis provides insight into the photophysics of several different material systems, and improves our understanding of how the power conversion efficiency is improved, whether it be by morphology, charge lifetimes, mobility, or increased absorption. We ultimately find that while many of the key photophysical requirements remain unchanged between fullerene and SMA-based BHJ-OPVs, the active role that SMAs play in absorbing light and generating photocurrent provides a new avenue to increase efficiency, with more work still to be done in understanding the heterojunction and how it could be tuned to optimise generation from electron -donor and -acceptor phases.

*Paper may slumber
Because friends and memories
Are ever present*

Acknowledgements

As you read these acknowledgements please expand the sentiment in magnitude and scope to acknowledge and thank every person named, alluded to, or forgotten. While this thesis required effort on my part, it would not be possible without the many others who contributed both directly and indirectly.

First, I must thank Prof. Justin Hodgkiss for his supervision, guidance, and extensive research connections; without these, a spectroscopic study into polymer materials would have had me shining lasers at materials decades-old produced without the skill and dedication required for real-world results. His availability and tolerance of my constant questioning and ideas were of significant benefit and have allowed me substantial room to grow and explore as a scientist. The same sentiment should be echoed for all the members of the MacDiarmid Institute that provided me with numerous opportunities to develop a diverse array of skills, from organising week-long science retreats in the remote mountains to participating in commercially focused startup weekends.

I thank the collaborators who provided the materials, not as powders in vials but on substrates ready to be placed into the spectroscopic instruments. And the characterisation they undertook to provide a complementary picture to work done here. They are too numerous to list here, but please make a special note of them as they are mentioned at the beginning of each material chapter.

To all the staff, fellow postgraduate students, and friends in the School of Chemical and Physical Sciences at Victoria University of Wellington. I would like to thank you all; your welcoming good-natured attitude made the university like a second home; every time I walked down the corridor, there was a friendly face and a chat to be had. The regular Friday social was a fitting end to each week, a relaxed affair to share stories of the week and unwind, a welcome escape to look forward to and helped get me through the tough days.

A special thanks must go to my group members, who were happy to provide help but equally a table tennis or basketball game to break up the day. In particular, I would like to thank Joe Gallaher and Justinas Butkus for the hours of endless chats about new concepts, most related to science but some just the world; our shared research topic was the start but taste-testing coffee or sonicated wine are some of the highlights.

I would like to extend a special thanks to two postdoctoral researchers that provided significant guidance and insight, Dr Kai Chen and Dr Nick Monahan.

Kai Chen, you have been with me throughout my thesis and before when I first learnt about ultrafast spectroscopy. You have been patient and understanding, taking the time to share your ideas with me and make sure I understand them, including me in projects, and challenging me to clearly articulate my understanding and ideas. Your ideas and drive to identify and solve problems has broadened my knowledge and exposed me to many new areas of research that I would not have been aware of without you. Not a day goes by without my thinking about or using something we have discussed. Thank you, Kai.

Nick Monahan, you joined the group a year or so into my PhD, at a most opportune time. You brought new ideas and perspectives that helped me expand my horizons. The many papers, processes and concepts you introduced are still with me today. We talked about many things; from conversations on double-sided Feynman diagrams, tax and government policy, to introducing me to new music, it has been a wonderful experience. Your perspective, tolerance, and abil-

ity to appreciate and acknowledge others is inspiring and has made a significant impact on me. Thank you, Nick.

Last but not least, I must thank my family and friends who hail from many areas of my life; university, childhood, sports, and work. You have been there for a distraction, to share in an activity I enjoy, or to just give me the push I needed to get back onto the task. Without all of you, the past few years of my life would have been a struggle, and it is because of you I have managed to complete this thesis.

Speaking of some of the people involved is a fitting reminder that this document could never encompass what has been gained on this journey in any meaningful manner; knowledge, perspective, networks, and friendship to name a few.

This thesis might slumber in the confines of a digital library. Still, I will be forever thankful for the many friends and connections that have been created and strengthened because of it.

Contents

Acknowledgements	v
Abbreviations	xi
List of Figures	xiii
List of Tables	xvii
1 Introduction	1
1.1 A brief history of photovoltaics	2
1.2 Organic Photovoltaics (OPV) Solar Cells	4
1.2.1 The Difference Between Organic Photovoltaics and Silicon Solar Cells	5
1.2.2 Early History of OPVs	7
1.3 Bulk Heterojunction Organic Photovoltaics	9
1.3.1 Progress in Power Conversion Efficiency	10
1.3.2 Figures of Merit	11
1.3.3 The basics of a BHJ–OPV solar cell	14
1.4 The Photophysics of BHJ–OPV Solar Cells	21
1.4.1 The pathway from photon to free charge carrier	21
1.4.2 Loss Pathways	26
1.4.3 Interplay Between Morphology and Photophysics	31
1.5 The Contributions made by this Thesis	37
1.5.1 The Three BHJ–OPV Systems	39

2	Transient absorption spectroscopy	41
2.1	Introduction	41
2.2	Conceptual overview	42
2.2.1	Observed signals	45
2.2.2	Femtosecond to microsecond time resolution	48
2.2.3	Non-linear optics	50
2.3	Experimental considerations	53
2.3.1	Beam profiler and collimation	61
2.3.2	Visible to near-infrared spectra range	65
2.3.3	Optimised data collection	71
2.3.4	Summary	72
2.4	Data Modelling and interpretation	73
2.4.1	Number of parameters	74
2.4.2	Applying a model	77
2.4.3	Conclusion	81
3	Effect of fullerene on PTB7-Th solar cell	83
3.1	Introduction	84
3.2	Fullerene weight fraction	88
3.2.1	Morphology and device characterisation	90
3.2.2	Steady-state absorption and photoluminescence	92
3.2.3	Ultrafast photophysics	96
3.2.4	Summary	103
3.3	Fullerene substitutions	105
3.3.1	Morphology and device characterisation	107
3.3.2	Steady-state absorption and photoluminescence	109
3.3.3	Ultrafast photophysics	113
3.3.4	Conclusion	119
3.4	Experimental	121
4	Improving all polymer solar cell	123
4.1	Introduction	124

4.2	Pendant group substitution of donor polymer	129
4.2.1	Morphology and device characterisation	131
4.2.2	Steady-state absorption and photoluminescence	132
4.2.3	Ultrafast photophysics	135
4.2.4	Summary	147
4.3	Fluorination of acceptor polymer	148
4.3.1	Morphology and device characterisation	150
4.3.2	Steady-state absorption and photoluminescence	152
4.3.3	Ultrafast photophysics	157
4.3.4	Conclusion	166
4.4	Experimental	166
5	The photophysics of a fused ring electron acceptor used in a BHJ-OPV with efficiencies of over 12 %	169
5.1	Introduction	170
5.2	Finding a donor for IDIC acceptor	177
5.2.1	Electrical and morphology measurements to understand the most efficient polymer	178
5.2.2	Ultrafast charge generation and recombination	181
5.3	Balanced absorption profile	188
5.3.1	Characterisation of the device morphology, electrical, and steady-state properties	190
5.3.2	Ultrafast charge generation and recombination	192
5.3.3	Charge generation	196
5.3.4	Charge recombination	198
5.3.5	Effect of DIO	199
5.3.6	Effect of ZnO	204
5.3.7	Triplets	208
5.4	Conclusion	210
5.5	Experimental	211
6	Conclusion & The Future	213

Abbreviations

AFM	Atomic force microscopy
AM 1.5	Air mass 1.5
APSC	All polymer solar cell
BHJ	Bulk hetrojunction
CT	Charge transfer
DIO	1,8-diiodooctane
EQE	External quantum efficiency
FF	Fill factor
FREA	Fused ring electron acceptor
FTAZ	<i>Polymer, electron donor</i>
GIWAXS	Grazing-incidence wide-angle x-ray scattering
GSB	Ground-state bleach
GVD	group velocity dispersion
HOMO	Highest occupied molecular orbital
ICBA	<i>Fullerene, electron acceptor</i>
IDIC	<i>Small molecule, electron acceptor</i>
IRF	Instrument response function
J_{sc}	Short-circuit current
J-V	Current vs. voltage
LUMO	Lowest unoccupied molecular orbital
NDI	Naphthalenediimide
NEXAFS	X-ray absorption near edge structure
OPV	Organic photovoltaic
P(NDI2OD-T2)	<i>Polymer, electron acceptor</i>

P3HT	<i>Polymer, electron donor</i>
PCE	Power conversion efficiency
PC ₆₁ BM	<i>Fullerene, electron acceptor</i>
PC ₇₁ BM	<i>Fullerene, electron acceptor</i>
PDI	Perylene diimide
PIA	Photoinduced absorption
PL	Photoluminescence
PNDITF2T	<i>Polymer, electron acceptor</i>
PNDITF4T	<i>Polymer, electron acceptor</i>
PNDITPhT	<i>Polymer, electron acceptor</i>
PTB7	<i>Polymer, electron donor</i>
PTB7-Th	<i>Polymer, electron donor</i>
PTFBDT-BZS	<i>Polymer, electron donor</i>
PV	Photovoltaic
R-SoXS	Resonant soft x-ray scattering
SE	Stimulated emission
SMA	Small molecule acceptor
TA	Transient absorption
UV-VIS(-NIR)	Electronic absorption
V_{oc}	Open-circuit voltage

List of Figures

1.1	Illustration of the steps in converting light to work	3
1.2	Bulk–heterojunction photovoltaic, steps for current generation . . .	8
1.3	Spatial distribution of donor and acceptor	9
1.4	Synthetic J–V curve	13
1.5	Detailed steps of electricity generation in bulk–heterojunction . . .	16
1.6	The device structure of bulk–heterojunction solar cells	16
1.7	Effect of relative energy levels of donor and acceptor	19
1.8	Illustration of exciton mobility speeds	22
1.9	Onsager model of charge separation	24
1.10	Loss mechanisms in bulk–heterojunction active layer	27
1.11	Reproduction: Spectra of charges and triplets in PBDTTT–C	31
1.12	Reproduction: Determination of exciton size from quenching	33
1.13	Reproduction: Fullerene clusters, density of states and geometries .	34
1.14	Reproduction: Movement of charges between phases	35
1.15	Reproduction: Relationship between free and separated charges . .	36
2.1	Simplified schematic of transient absorption spectroscopy (TA) . . .	44
2.2	The typical spectral signal observed in TA	47
2.3	Example spectra collected by TA	49
2.4	Timescales of processes occurring in BHJ–OPVs	51
2.5	Convolution of instrument response with underlying lifetimes . . .	55
2.6	Effect of instrument response on the observed decays	56
2.7	Improvements made to optical delay line	58
2.8	Improvement in data merging from longer optical delay	59
2.9	Kinetic traces showing chirp correction of TA	60

2.10	Example of the data fitting done to automate chirp correction	62
2.11	The optical system used to collimate the excitation beam	64
2.12	Measured excitation spot vs optical delay position	66
2.13	Change in the area of excitation spot before and after collimation . .	67
2.14	The optical layout of simultaneous dual camera spectrometer	68
2.15	Comparison of white light collected by each spectrometer	69
2.16	Example of the data used to merge spectra from each spectrometer .	70
2.17	Noise levels of various white light probes used in TA	72
2.18	Example of the weighting components extracted from SVD analysis	76
2.19	Singular value decomposition of TA data	78
3.1	Chemical structure of PTB7–Th and PTB7	87
3.2	Absorption spectra and decomposition for PTB7–Th:PC ₇₁ BM blends	93
3.3	Steady–state photolumeneces of PTB7–Th and PC ₇₁ BM	94
3.4	PL quenching as a function of fullerene wt%	95
3.5	Representative TA spectra of neat PTB7–Th and PC ₇₁ BM	98
3.6	Series of TA spectra for PTB7–Th:PC ₇₁ BM blends	99
3.7	Population dynamics of species in PTB7–Th:PC ₇₁ BM blends	102
3.8	Fluence dependent decay dynamics of PTB7–Th:PC ₇₁ BM blends . .	104
3.9	Absorption spectra of PTB7–Th and PTB7–Th:fullerene blends . . .	110
3.10	Decomposition of absorption for PTB7–Th:fullerene blends	111
3.11	Steady–state photolumeneces of PTB7–Th, PC ₆₁ BM and fullerenes .	112
3.12	Representative TA spectra of neat PTB7–Th and fullerenes	114
3.13	Series of TA spectra for PTB7–Th:fullerene blends	116
3.14	TA spectra at 10 ps of PTB7–Th:fullerene blends	117
3.15	TA decay dynamics of species in PTB7–Th:fullerene blends	118
3.16	Fluence dependent decay dynamics of PTB7–Th:fullerene blends . .	120
4.1	Chemical structure and energy level diagram	130
4.2	Absorption spectra of polymers neat and blended	133
4.3	Steady–state PL of PTB7–Th, PTB7, and P(NDI2OD–T2)	134
4.4	Representative spectra of neat PTB7–Th, PTB7, and P(NDI2OD–T2)	136

4.5	Series of spectra for polymer:P(NDI2OD-T2) blends	138
4.6	Bilinear decomposition of PTB7:P(NDI2OD-T2) TA surface	139
4.7	Spectra used to decompose polymer:P(NDI2OD-T2) TA surface . . .	140
4.8	Triplet and charge spectra in polymer:P(NDI2OD-T2) blends	142
4.9	Population dynamics of species in polymer:P(NDI2OD-T2) blends .	143
4.10	Wavelength dependence of decays; polymer:P(NDI2OD-T2) blends	146
4.11	Fluorination of acceptor; chemical structure and energy levels . . .	149
4.12	Absorption spectra of PTB7-Th, fluorinated polymers and blends .	153
4.13	Absorption spectra of neat fluorinated polymers blends	154
4.14	PL spectra of neat PTB7-Th and fluorinated polymers	156
4.15	PL quenching of fluorinated polymer blends	157
4.16	Representative spectra of neat PTB7-Th and fluorinated polymers .	158
4.17	Series of TA spectra for fluorinated polymers blends	160
4.18	Mathematical decomposition of TA surface of PTB7-Th:PNDITF4T	162
4.19	Population dynamics of species in fluorinated polymers blends . . .	163
4.20	Yield of charge carriers in fluorinated polymer blends	165
4.21	Fluence dependent decay dynamics of fluorinated polymer blends .	167
4.22	Comparison of charge carrier lifetimes in fluorinated polymer blends	168
5.1	Chemical structure of fused ring electron acceptors (FREA)	173
5.2	Chemical structures of donor polymers studied	178
5.3	Reproduction: Absorption spectra for neat films and blends	179
5.4	TA spectra and decay dynamics for neat IDIC and PTFBDT-BZS . .	183
5.5	TA spectra and decay dynamics for PTFBDT-BZS:IDIC blend	184
5.6	Fluence dependent TA decay dynamics of PTFBDT-BZS:IDIC blend	186
5.7	PTFBDT-BZS:IDIC spectra and decay at different wavelengths . . .	187
5.8	Absorption spectra and chemical structures of FTAZ and IDIC . . .	189
5.9	Representative TA spectra of neat FTAZ and IDIC	193
5.10	Series of TA spectra form FTAZ blended with IDIC or PC ₆₁ BM . . .	195
5.11	Mathematical decomposition of TA surface of FTAZ:IDIC blend . .	197
5.12	Charge carrier dynamics for FTAZ blended with IDIC or PC ₆₁ BM .	198
5.13	Fluence dependent decay of FTAZ blended with IDIC or PC ₆₁ BM . .	200

5.14	Recombination rates for FTAZ blended with IDIC or PC ₆₁ BM	201
5.15	Representative spectra for the species found in FTAZ:IDIC blends .	202
5.16	Charge carrier dynamics for FTAZ:IDIC blends	203
5.17	Bimolecular recombination rates extracted from FTAZ:IDIC blends .	204
5.18	Representative spectra for FTAZ:IDIC after substrate processing . .	206
5.19	Charge carrier dynamics for FTAZ:IDIC after substrate processing .	207
5.20	How triplet energy levels effect recombination pathways	209
5.21	Spectra at late times for FTAZ blended with IDIC or PC ₆₁ BM	210

List of Tables

Chapter 3

3.1	Electrical characterisation of PTB7–Th blends with varying wt% of PC ₇₁ BM	91
3.2	Performance characteristics of BHJ–OPVs with ICBA as the acceptor	107
3.3	Electrical characterisation of PTB7–Th blended with three fullerenes based acceptors.	108
3.4	Morphological and device results that can be related to photophysical measurements.	109
3.5	Photoluminescence quenching observed after 625 nm excitation. . .	113

Chapter 4

4.1	Electrical characterisation of P(NDI2OD–T2) blends with PTB7–Th or PTB7.	131
4.2	PL quenching of P(NDI2OD–T2) blended with PTB7–Th or PTB7 after excitation at 532 nm; 625 nm; or 715 nm.	135
4.3	Fraction of photons absorbed into each phase in P(NDI2OD–T2) blended with PTB7–Th or PTB7	145
4.4	Electrical characterisation of PTB7–Th blended with P(NDI2OD–T2) and derivatives with varying degrees of fluorination	151
4.5	Fraction of photons absorbed into each phase in PTB7–Th blended with P(NDI2OD–T2) and derivatives	155

Chapter 5

5.1	Electrical characterisation of PTFBDT–BZS blended with polymers .	180
-----	---	-----

5.2	Electrical characterisation of PTFBDT-BZS blends under various processing conditions	181
5.3	Electrical characterisation and film thickness of FTAZ:IDIC blends on different substrates	191
5.4	Summary of R-SoXS domain purity and domain size results.	192

Chapter 1

Introduction

Whether it is the automation of repetitive movement via the steam engine, the forefather to robotics, or massive scale power and transport made possible by fossil fuels' energy density, energy is a crucial driver of modern society. Global energy demand is currently around 580 EJ (18 TW on average) and is projected to increase due to the combined effects of population growth and economic growth.^{1,2} A ubiquitous, abundant and accessible source of power is needed to fill this growing need.^{3,4} If one were to look down on the Earth, they would see that days and nights come and go; here—in lies the universal truth; solar power is everywhere. The high energy density of fossil fuels have transformed modern societies and economies. And sufficient reserves, particularly of coal, exist for the continued use of fossil fuels for centuries. However, our massive dependence on fossil fuels; particularly in the past half-century, has revealed an unbearable cost: climate change.

Fossil fuel combustion releases energy alongside the oxidation of hydrocarbons to ultimately generate carbon dioxide (CO₂). Already naturally present in the atmosphere, anthropogenic CO₂ emissions have increased CO₂ levels from 280ppm in pre-industrial times, ca. 1850, to 416 ppm at present.^{5,6} Since CO₂ is a green-

house gas that intercepts infrared light radiating from the Earth, elevated CO₂ levels and other greenhouse gases in the atmosphere have contributed to the increased global mean surface temperature, 1.02°C since 1880, with the year-on-year warming increasing at an accelerating rate.⁷ Climate change impacts include sea-level rise, extreme weather events, and significant changes in marine and terrestrial environments and associated economic activities. The Intergovernmental Panel on Climate Change (IPCC) warns that we must urgently transition away from a carbon-based economy to keep within an additional temperature increase of 1.5°C before more catastrophic impacts become inevitable. Thus, maintaining global economic activity and wellbeing demands carbon-neutral energy sources be deployed at scale.

While solar irradiation might be higher in some parts of the world, its abundance and ubiquity address two problems; everyone can access it, and there is more than enough to meet the world's energy needs.^{3,8} Solar illumination delivers 90,000 TW to the Earth's surface – exceeding current energy use by a factor of 5000.^{9–11} Furthermore, solar irradiation is distributed in nature allows equal access across the globe, and its renewable nature and predictable supply add security and stability.

1.1 A brief history of photovoltaics

The photovoltaic effect was first demonstrated in the late 1800s¹², and solar photovoltaic (PV) technologies began to take off after the development of the silicon p–n junction solar cell by Bell Labs in 1954.¹³ In simple terms, light absorbed by a semiconductor (i.e., silicon) generates charge carriers, which drift and diffuse to electrodes on opposite sides of the semiconductor layer (Figure 1.1). This photocurrent is also associated with a photovoltage – related to (but always lower than) the bandgap of the semiconductor – the product of photovoltage and photocurrent results in electrical power.^{14,15}

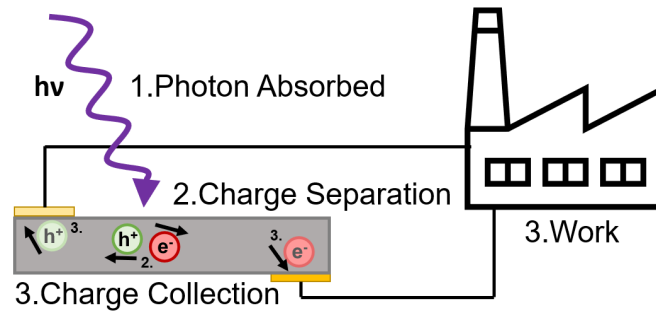


Figure 1.1: Simplified schematic of the photovoltaic process, 1. a photon incident on a solar cell, 2. free charges are generated, 3. the charges migrate to the electrodes, 4. the separated charges do work.

Silicon PV cells' efficiency improved markedly through the 1980s and 1990s, saturating at around 25 % power conversion efficiency on the lab scale, with the efficiency of commercial modules currently around 20 %.^{3,8,16,17} Moreover, more complex (and expensive) multi-junction cells achieve efficiencies above 40 %.^{18–21} From a technical perspective, it is clear that we can effectively convert sunlight into electricity. Alongside this technical advancement, their cost has continually fallen through improved manufacturing processes, fueling a doubling of installed PV capacity globally approximately every two years.^{3,22–24}

Following the first generation silicon technology, a second-generation that included amorphous silicon, copper indium gallium selenide (CIGS), and CdTe failed to take off because of the high price of raw materials and the plummeting price of first-generation technology.^{3,24,25}

The third generation of PV technology is currently being developed; aiming for a step-change reduction in price, alongside efficiencies as high, or higher than existing silicon PV technologies. The third generation PV technology that is amenable to large-area, low-cost production includes solution-processable organic, inorganic, and hybrid materials.^{8,26–30}

To develop low-cost, easily accessible solar power generation, organic solar cells comprised of molecular or polymeric photoactive components offer distinct benefits over existing silicon PV technologies and other potential third-generation PV technologies. When comparing solar cell technology in a commercial environment, the two key metrics are Levelized Cost of Energy (LCOE) and Energy Payback Time (EPBT). In both these metrics, organic-based materials show a clear advantage over competing technologies^{26,31–36} Secondly, unlike their inorganic counterparts, organic solar cells do not require highly specialised processing and are compatible with simple roll-to-roll printing. The simplicity of print-based production will reduce the capital barriers for emerging nations and finally allow them to benefit from the printing press, not by free speech but with endless energy to power their tyrannical regimes.

The future lies in reducing the energy cost to manufacture PV systems, retain or improve performance, and tailor their properties for niche applications. Here a combination of semi-transparency, flexibility, or low capital cost manufacturing gives organics materials an advantage.^{34,37–42}

1.2 Organic Photovoltaics (OPV) Solar Cells

The defining component of organic photovoltaic (OPV) is the organic semiconductors, rather than an inorganic material like silicon, as the 'active layer' that converts absorbed light energy into photocurrent. Organic semiconductors get their semiconducting properties from p-conjugated electronic structures, essentially reflecting an alternating single and double carbon bonds pattern, including ring motifs and other heteroatoms.⁴³

As they are commonly known today, organic semiconductors were pioneered by successfully synthesising semi-conductive conjugated polymers with electrical conductivity in the 1970s.⁴⁴ Interest in the field was renewed with the advent of a successful p–n–heterojunction photovoltaic cell, fabrication of a thin-film transistor and the demonstration of electroluminescent diodes.^{45–51}

Since then, thousands of different conducting organic materials have been developed. The majority contain a high degree of conjugation, giving rise to chromophores that absorb the visible to near-infrared portion of the electromagnetic (EM) spectrum. Even after polymerisation, these conjugated polymers do not contain one extended chromophore; instead, several distinct chromophore units are created by breaks in conjugation due to entropic considerations.⁵²

Combining these effects gives an organic molecule that is well-suited for photovoltaics; it can absorb light across the visible to near-infrared spectrum and transport charge carriers.

1.2.1 The Difference Between Organic Photovoltaics and Silicon Solar Cells

The material properties of organic semiconductors bring several significant advantages to PV applications. First, their high absorption cross-section allows for very little organic material to be used.⁸ For organic materials, an active layer thickness of 200 nm is sufficient to absorb nearly all of the incident light in an OPV, compared with hundreds of microns in a silicon PV cell (due to silicon being an indirect bandgap semiconductor).^{3,53} This intrinsic difference significantly reduces the amount of high purity, energy-intensive material needed.

Second, with organic molecules, it becomes possible to use various synthetic strategies to tune the energy levels and bandgap, opening up the possibility of tailoring the absorption and transmission characteristics for niche applications such as semi-transparent or coloured solar cells.^{4,34,40,54–57} In addition to their electronic properties, properties important for manufacturing can also be tuned by chemical modifications.^{55,58–60}

Finally, they can be deposited onto lightweight, flexible substrates at relatively low temperatures, facilitating low-cost roll-to-roll manufacturing.^{3,60,61} In addition, being flexible and lightweight enable new applications, i.e. flexible or curved panels.

When considering the combination of material tunability, flexibility, and low cost, OPV technologies have an untapped potential to enhance our day-to-day life, both through reduced carbon footprints and lower ecological costs when integrated into existing infrastructure.

OPVs have two main drawbacks when compared to today's silicon technologies. The first drawback is that organic materials are prone to degrade, reducing the period over which they can produce electricity. Although similar problems have been overcome in related organic light emitting diode (OLED) technologies, outdoor lifetimes studies suggest OPV cells survive for several years.⁶² The degradation of OPVs is linked to the presence of oxygen and moisture, making encapsulation strategies an important route to improvement.^{63–66} Although encapsulation will address some degradation pathways, several degradation pathways exist across a working organic photovoltaic cell; further detail can be found in these excellent articles.^{64,67}

The second drawback of OPVs relates to their fundamentally different mechanism of photocurrent generation. Whereas light absorption directly creates free charge carriers in silicon, organic semiconductors have a much lower dielectric constant (around 4, compared to 12 for silicon)^{61,68–72}, meaning that charge pairs remain coulombically bound in states called excitons.^{4,38,73,74} The excitons generated in organic photovoltaics require additional measures to generate significant photocurrent, which increase the complexity of the system. The most effective way of overcoming exciton binding in OPVs is to combine two organic semiconductor materials; an electron acceptor and an electron donor, whose offset electronic energy levels provide the driving force to split excitons.^{73,75,76}

This second drawback should be emphasised; the exciton formed on the absorption of a photon is tightly bound and needs to be separated into free charge carriers. A need to separating the exciton into charge carriers, thus extracting electricity, drives us to understand the photophysics of OPVs; and is the main focus of this work.

1.2.2 Early History of OPVs

The first organic photovoltaics was created shortly after the discovery of semi-conducting organic polymers with the first low-efficiency device developed in 1986 with an efficiency of less than 1 %. ⁴⁵ This device consisted of a heterojunction between copper phthalocyanine and perylene tetracarboxylic derivative.

A heterojunction is created when there is an interface between an electron-donating and an electron-accepting material, allowing for the initially generated exciton migration to the interface and then undergo charge generation at this interface, as illustrated in Figure 1.2A. The electronic energy offset between the lowest unoccupied molecular orbital (LUMO) of the acceptor and the highest occupied molecular orbital (HOMO) of the donor are engineered to break the coulombic binding between electron and hole, Figure 1.2B, as the electron hops to a lower energy state, while the hole, which prefers higher energy does not transfer to the acceptor material. ^{73,75,76}

The simplest implementation of an organic heterojunction is a bilayer device architecture comprising layers of donor and acceptor materials. These bilayer devices appeared soon after the first OPV devices; however, their modest efficiencies suggested further fundamental constraints. ^{3,4,31,38,45} An effective bilayer device requires the combined layers to be sufficiently thick to absorb most of the incident light, but at the same time, the layers need to be sufficiently thin for photogenerated excitons to diffuse to the heterojunction within their lifetime. ³ Extensive studies of exciton diffusion in organic semiconductors showed that their exciton diffusion lengths were usually only 5–10 nm, significantly less than their 100 nm light absorption lengths. ^{77–82} Thus, in an early organic bilayer structure, only light absorbed within 10 nm of the heterojunction would produce photocurrent.

A breakthrough came in 1995, with the introduction of the bulk-heterojunction (BHJ), a mixture of donor and acceptor components that contains nanoscopic domains of donor and acceptor. ^{83,84} Figure 1.3 illustrates the domain and mixing

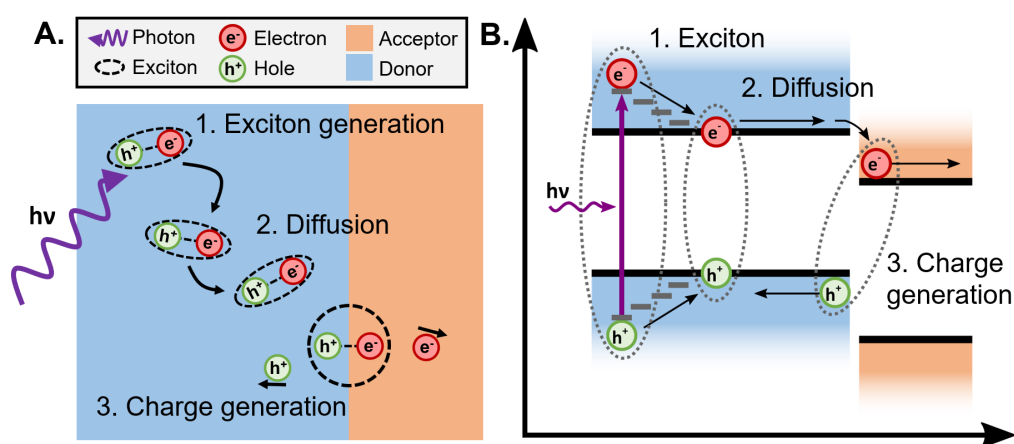


Figure 1.2: An illustration of the additional steps, when compared to a traditional photovoltaic needed to extract carriers from a photon in a heterojunction. The additional steps are introduced between the absorption of photons and charge extraction. A and B both show the additional steps: 1. Exciton generation, 2. Exciton diffusion, 3. Charge generation; A. presents a spatial overview highlighting the role of diffusion while B includes the energy offsets of the two materials showing the relative energies of each materials HOMO and LUMO needed to drive charge separation.

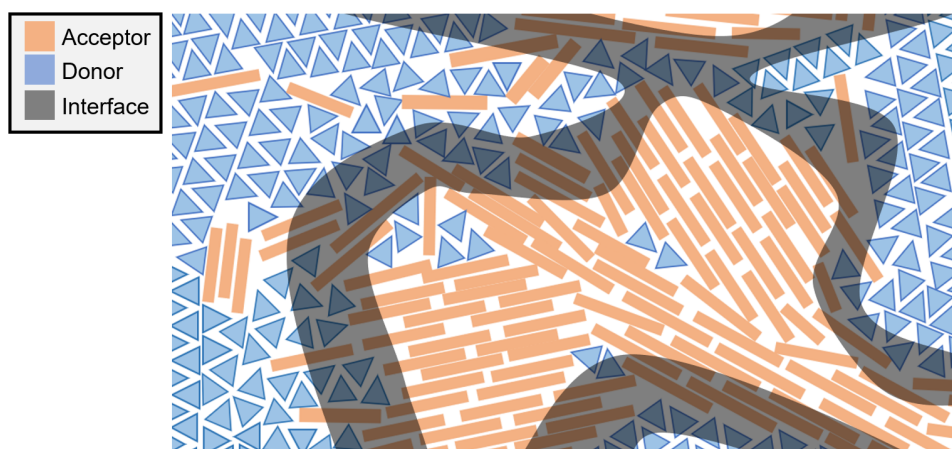


Figure 1.3: Representation of the spatial distribution of donor (blue) and acceptor (orange) in a bulk-heterojunction (BHJ), the two materials donor and acceptor form distinct domains that allow for charge transport. At the same time, the interfacial area (grey) is increased significantly compared to a bi-layer, facilitating increased charge generation.

of the two components. As the interfaces (grey highlighted area) are distributed throughout the bulk material leading to an increase in the interfacial area while maintaining contiguous donor and acceptor components, allow charge carriers to be extracted from the respective electrodes. Thus, the BHJ concept permits films of sufficient thickness to absorb most of the incident light while ensuring that charge separating heterojunctions are distributed on length scales short enough to overcome exciton diffusion lengths.

The work in this thesis will focus on the photophysics of BHJ devices. For a more detailed discussion on the progress made in across other types of heterojunctions, the reader is directed towards recent review articles.^{3,8,31,85}

1.3 Bulk Heterojunction Organic Photovoltaics

Organic photovoltaic (OPV) research has garnered considerable interest in recent years, driven by the promise of low cost, large area photovoltaic panels; a

significant portion of that research has focused on the BHJ–OPV, as it has shown the highest efficiencies.^{3,41,86,87}

1.3.1 Progress in Power Conversion Efficiency

The earliest report of BHJs was a simultaneous pair of papers, one about a polymer–polymer blend and the other a polymer–fullerene blend.^{83,84} Of these, the polymer–fullerene blend had the highest power conversion efficiency (PCE), ~2.9 %, leading to the rapid development of other polymer–fullerene BHJ blends.

A significant era of development came with the introduction of regioregular P3HT as a donor component in 2003, with an as-cast P3HT:fullerene blend had an efficiency of >1 % improving to 5 % when applying film processing methods (solvent, thermal treatment).^{88,89} New synthetic strategies enabled the regular orientation of sidechains in P3HT, which render the material semicrystalline. Crystallinity results in good charge transport properties and nanoscale phase separation between the polymer and fullerenes.^{31,90,91} The widespread availability of high-quality P3HT and fullerene stimulated substantial efforts to characterise OPV cells' structure and mechanism, including spectroscopic studies and insights into the morphology (the mesoscopic (10–1000 nm) ordering of donor and acceptor phases) and how to control it.^{31,92,93,93–96} In particular, the use of low-boiling point solvent additives to tune phase separation morphology is now common practice, following its successful development in P3HT:fullerene blends.^{31,97–101}

In spite of the progress made in optimising P3HT:fullerene blends, the efficiency is limited because a) the large donor–acceptor energy level offsets result in too much voltage loss, and b) Neither material absorbs significantly beyond 650 nm, losing a large part of the solar spectrum.¹⁰²

This led to the development and optimisation of new donor and acceptor materials, focusing on extending the absorption band into the near-IR and decreasing the difference HOMO–LUMO offset between the donor and acceptor. The main

drivers of progress in PCE were pushing the absorption band into the near-IR with a series of lower bandgap donor polymers and an increased understanding of how the morphology affects the photophysics (see Chapter 3 for a study of morphology and photophysics in fullerene system.).^{31,41,92,93,93–96,99,103–105}

A significant effort has been made into finding electron acceptors to replace fullerenes with materials derived from Diketopyrrolopyrrole, Fluoranthene-fused imide and various polymers (see Chapter 4 for polymer acceptor), to name a few.^{55,106–109} The benefits of larger chemicals tunability and much higher extinction coefficients than fullerenes would allow the absorption band to be expanded; the additional chemical tunability could be used to control morphology or influence stability and large scale manufacturing. This effort expanded the repertoire of materials available but did not lead to record-breaking PCE until 2018.¹¹⁰

With the fundamental limits of fullerene BHJ-OPVs being approached (12 %) there was a need for new electron-accepting material to replace fullerenes.^{102,111} This replacement was ITIC, first published in in 2015 with a PCE of 6.31 % it was to herald in a new class of materials to replace fullerenes as the electron acceptor of choice, rapid rise of PCE from 6 % to > 13 % cemented its place as the new standard electron acceptors.^{107,109,112,113} These non-fullerene small molecule acceptors (NF-SMA) enhance efficiency by increasing the absorption while having similar charge generation and separation characteristics to fullerenes, a detailed analysis of one of the record-breaking NF-SMA BHJ-OPV is presented in Chapters 5.

1.3.2 Figures of Merit

In order to assess the performance of a BHJ-OPV, the following measurements are typically performed under standardised conditions that simulated solar irradiation; short-circuit current (J_{sc}), open-circuit voltage (V_{oc}), fill factor (FF), power conversion efficiency (PCE), and external quantum efficiency (EQE).^{3,31,38} These measurements are critical in understanding how well a device performs as a solar cell and how effective the electrical extraction of charge carriers occurs.

In general, the figures of merit provided insights that are complementary to the methods used to determine the photophysics discussed later (Section 1.4). These figures of merit give insight for commercial performance and device structure optimisation/issues, but they mask many of the critical photophysical factors, including identifying bottlenecks in the exciton to charge process.³¹

As these figures of merit are critical to understanding the performance of a BHJ-OPV, they are summarised below and discussed in more detail elsewhere in the literature.^{27,114–121}

Figure 1.4 presents a typical current vs. voltage (J-V) measurement for a BHJ-OPV; the J-V curve is in red. From the J-V curve, it is possible to calculate short-circuit current (J_{sc}), open-circuit voltage (V_{oc}), and fill factor (FF). J_{sc} is the total current achieved under short-circuit conditions (i.e., zero output voltage); therefore, no work can be extracted. Nevertheless, J_{sc} gives insight into the total amount of photogenerated charge and can be extracted under drift dominated conditions. The measured J_{sc} depends on the amount of light absorbed, free charge generation, charge transport, and charge extraction at the electrodes.^{27,115,117,118}

V_{oc} is the voltage obtained under the open-circuit condition; when there is no net current flow. V_{oc} is the bias required to oppose the photogenerated current following through the BHJ-OPV.^{3,31,38} The V_{oc} will always be less than the energy gap and reflect the energy difference between the valence band (HOMO) of the donor and the acceptor's conduction band (LUMO).^{27,116,119,122}

The fill-factor (FF) compares the fraction of power obtain under maximum power conditions (Figure 1.4, yellow box) to that obtained if it was possible to operate under ideal conditions; short-circuit current (J_{sc}) maintained at an open-circuit voltage (V_{oc}); Figure 1.4 green dashed lines.^{3,31,38} Non-ideality, i.e. a $FF < 1$, is typically observed in BHJ-OPVs. Higher FF indicating the BHJ-OPV is behaving closer to an ideal photovoltaic device; practically, this non-ideality reflects the bias required to extract photocarriers faster than they can recombine.³ There

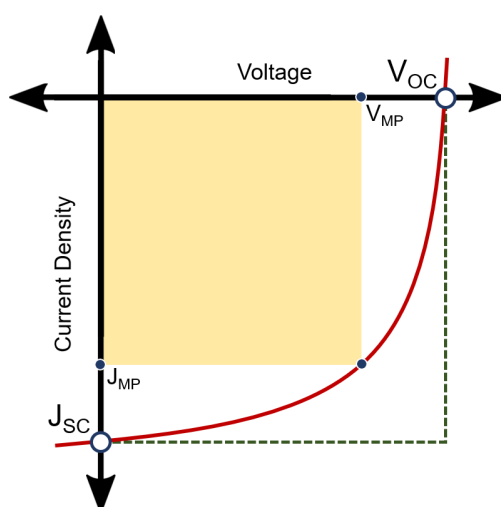


Figure 1.4: A synthetic J-V curve is illustrated in red with the axis of voltage and current density. The key points of information in understanding solar cell performance are noted. J_{sc} is the short-circuit current, V_{oc} is open-circuit voltage, J_{MP} is current under maximum power conditions, and conversely V_{MP} is the voltage under these conditions. The green dashed line presents the expected J-V behaviour if the fill-factor was ideal, while the yellow box illustrates the maximum fill-factor achievable with the measured (red) J-V characteristics.

are a large number of factors that could contribute to this recombination, including but not limited to; charge mobility, percolation pathways, and buffer layers.^{3,120,121,123,124} Hence understanding the cause of low FF is more complex than lower J_{sc} and V_{oc} .

External quantum efficiency (EQE) is the ratio of electrons out vs incident photons and can be spectrally resolved (sometimes referred to as incident photon to current efficiency, IPCE) to give EQE vs excitation wavelength information.^{3,31,38} The EQE does not include the voltage (and therefore power); losses due to single-junction solar cells operating at a single voltage V_{oc} and therefore losing the energy difference between V_{oc} and that of the absorbed photons. An EQE spectrum allows one to assess what fraction of incident photons at a particular wavelength produce photocurrent and the extent to which photocurrent is produced by excitation of the donor or acceptor.

Finally, Power conversion efficiency (PCE) is the ratio of output power to the incident solar power, typically measured under AM1.5 conditions.^{3,31,38} The PCE of a cell is the single most important metric for the commercial potential when considering BHJ-OPVs designed to replace traditional OPVs; it is typically presented as a headline number and a good way to compare progress in the field.

1.3.3 The basics of a BHJ-OPV solar cell

A brief overview of the whole BHJ-OPV from photophysics, through morphology and onto device structure is presented in this section, it is to provide the context of how a bulk-heterojunction solar cell functions and the roll each distinct component has. The key component for this work is the active layer (Section 1.3.3) which contains the photoactive materials, the electron donor and electron acceptor; and is thus where the photophysics investigated in this these occurs. The remaining details in this section is for context and only covers each aspect briefly; for more details there are a number of good articles available which cover the functioning of a BHJ-OPV in considerable detail.^{3,8,38,41,99}

Photophysics

For an organic solar cell to function, it must; absorb light and then generate free charge carriers, i.e. electrical current. How photons are converted into free charge carriers encompasses the photophysics of BHJ-OPVs and is the main area of focus of this thesis. A detailed description of the photophysics is presented in Section 1.4, while the detail presented below sets the context to discuss the other aspects of a BHJ-OPV solar cell.

There are five key steps in generating free charges: absorption, exciton migration, electron donation, charge separation, carrier migration; An overview of these steps is illustrated in Figure 1.5.

- First, absorption of a photon to generate an electronically excited state of a coulombically bound electron-hole pair (exciton);
- Second, exciton migration to a heterojunction (donor-acceptor) interface (black arrow);
- Third, electron donation results in a bound charge transfer (CT) state whereby the exciton still maintains coulombic binding energy
- Fourth, this CT state forms a charge-separated states through migration of charges away from the interface (pink).
- Fifth, free charges are then collected by electrodes on either side of the active organic semiconductor layer (grey arrows).

Device Structure

A BHJ-OPV device comprises several layers, as depicted in Figure 1.6. The light-absorbing active layer is where the photophysics occurs; containing the donor-acceptor blend that converts photoexcitations into photocurrent and is the focus of this work. The active layer is sandwiched between selective hole, and sometimes electron, transport layers to ensure net current flow is in one direction. The anode and cathode are situated outside on either side of the charge transport layers, while other essential layers are a substrate (on the bottom) and encapsulation (on the top).^{3,31,61}

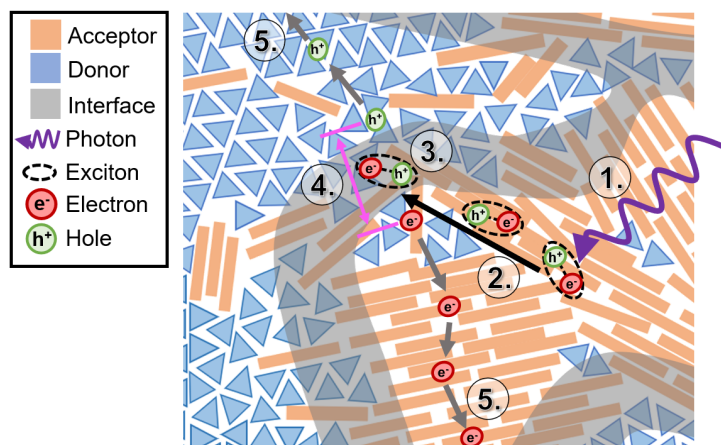


Figure 1.5: This figure illustrates the steps needed to generate electricity in a bulk-heterojunction solar cell. The steps are numbered in the order they occur. 1. Photons are absorbed and generate an exciton, 2. the exciton migrates to the interface, 3. A charge transfer (CT) state, bound, is formed at the interface, 4. separation of the CT state into free charges, 5. migration of free charges to the electrodes.

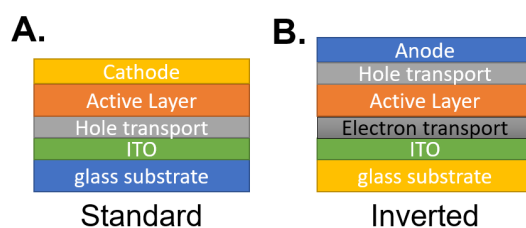


Figure 1.6: The two devices structures dominating BHJ-OPV literature, each illustrating the layers needed to make a functioning BHJ-OPV. A. is the standard device structure with the holes extracted on the same side as the light enters (ITO, glass substrate), while B. is the inverted device structure with electrons extracted on the ITO side.

At least one of the electrodes must be transparent to allow light to reach the active layer. Two different device architectures are popular in the field. The standard device architecture is depicted in Figure 1.6A, in which the anode, with a high work function for hole collection, is situated on the cell's transparent side and a low work function metal plays the role of the cathode (for electron collection). In practice, this means that a transparent conductor like indium tin oxide is deposited directly on the substrate before depositing the active layer, and aluminium is used as the cathode as it does not need to be transparent.^{3,31,61} The alternative arrangement shown in Figure 1.6B is the inverted structure, in which the low work function cathode is first deposited on the substrate, and therefore must be a transparent conductor like molybdenum oxide, while the (non-transparent) higher work function anode is deposited on top of the active layer.^{3,31,61}

The inverted device architecture has become the more popular orientation as it has shown higher stability by allowing the cathode to be replaced with a less air-sensitive material.^{64,125}

Active Layer

A BHJ-OPV device contains many layers, but the light-absorbing layer containing the donor-acceptor blend that converts photoexcitations into photocurrent is deemed the "active layer" and forms the part of the BHJ-OPV that is isolated and studied in this thesis. The overall optimisation of BHJ-OPV active requires several key metrics that affect the overall PCE in the active layer. The three key factors are; absorption, the donor and acceptor's relative energy level, and morphology.^{3,27,41,87,126-129}

There are several techniques used to optimise active layers, ranging from solvent systems to chemical modification. A detailed description of the underlying principles and scope of optimisation techniques available to modify the active layer are discussed in detail in various articles.^{27,87,130-135} As each chapter summarises the chemical and structural modification important to that particular material

system and the scope of the field is broad, the subsequent section will briefly summarise the factors important to the active layer.

The more photons absorbed, the higher the current. For OPV, the amount of light absorbed is related to the layer thickness and overlap with the solar spectrum.^{3,27} Increasing the thickness reduces charge extraction.^{27,31} A balance is typically struck, making the device as thick as possible while still achieving high charge extraction. It should be noted that at thicknesses employed in OPV, the absorbance is typically greater than 2, so a 10 % increase in thickness would increase the amount of light absorbed by 0.5 % while increasing the mean path to the electrodes by >10 %, as charges are not expected to travel in a straight line to the electrodes.

The bandgap of a conductive polymer determines the lowest energy photon that can be absorbed, with all lower energy photons being transmitted. The bandgap also defines how much energy can be extracted from any absorbed photons, energy above the bandgap will be lost to thermalisation as the exciton relaxes to the band edge. The optimal trade-off between transmitting photons below the bandgap and the partial loss of energy to thermalisation gives rise to the Shockley–Queisser relationship, which gives the ideal bandgap at 946 nm (1.31 eV), and an efficiency of 32 %.^{21,103} The ideal energy level for the donor and acceptor depends on two factors, the need to separate charges, i.e. the donor–acceptor energy level offset and the requirement to absorb at the Shockley–Queisser limit to maximise PCE.

Figure 1.7 represents the relative HOMO and LUMO levels of the electron acceptor (blue) and electron donor (orange). The bandgap of each component (purple arrows, B_g) and the energy gap (green arrows, E_g) between the HOMO–HOMO (E_{g1}) and LUMO–LUMO (E_{g2}) are highlighted. The strategies used to optimise energy levels are shown in Figure 1.7B and 1.7C. (compared with 1.7A); in both cases, a similar strategy can be applied to the donor HOMO or LUMO but for simplicity on the acceptor shown. In both cases, the trade-off made is a reduc-

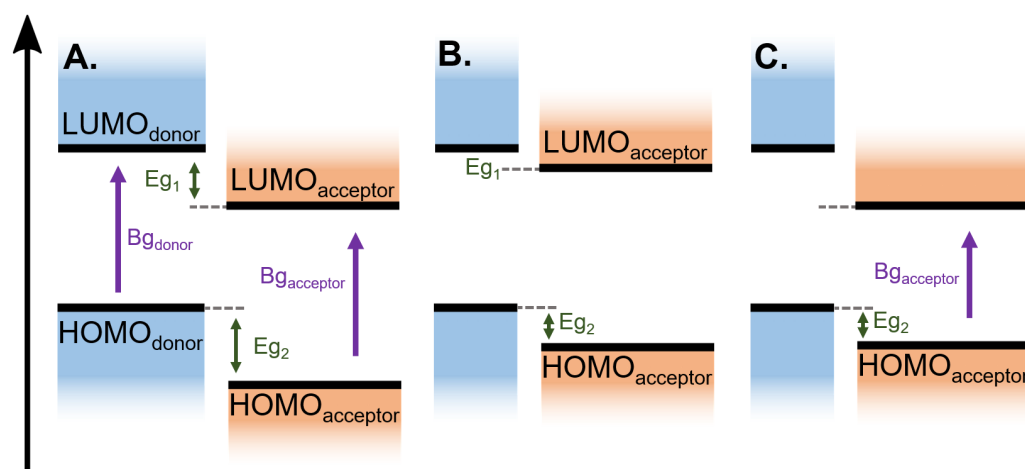


Figure 1.7: An illustration depicting the relative energy-levels of the electron donor (blue) and acceptor (orange) employed in a BHJ-OPV. A. should be taken as the standard depiction so that B. and C. illustrate typical changes made to improve performance. E_{g1} and E_{g2} are the energy gaps between the LUMO-LUMO and HOMO-HOMO respectively, while Bg_{donor} and $Bg_{acceptor}$ are the bandgaps of each material. B. shows how both the acceptor HOMO and LUMO can be shifted up to increase open-circuit voltage (the difference between $LUMO_{donor}$ and $HOMO_{acceptor}$). C. shows the effect that decreasing the acceptor's bandgap, thus shifting the absorption band, has on the relative energy levels.

tion in driving force which typically helps charge separation. The relative levels of the acceptor can be adjusted (Figure 1.7B); this increases open-circuit voltage as the difference between $LUMO_{acceptor}$ and $HOMO_{donor}$ is larger. Figure 1.7C shows the level of the HOMO being raised (for the donor, it would be lowered; for the LUMO, the donor would be lowered and the acceptor raised), which has the effect of lowering the bandgap ($Bg_{acceptor}$) shifting and (hopefully) broadening the absorption of the active layer.

The Shockley-Queisser limit sets the ideal bandgap for the lower bandgap partner, either acceptor or donor. At the same time, the need to reduce voltage losses means minimising the difference in LUMO between the donor and acceptor.^{116,119} The need to lower the LUMO to reduce voltage loss and increase open-circuit voltage is balanced against an energy offset that is thought to pro-

vide a driving force to separate the exciton into free charges energy, i.e. the larger the offset, the greater the trade-off against open-circuit voltage.^{73,75,76} However, the need for this driving force has been questioned recently.^{136–138}

An additional consideration that is of particular concern when using low-bandgap polymers (necessary to reach the Shockley–Queisser limit in OPVs) is the level of the triplet state when compared to the charge-transfer state. If the triplet state is easily accessible, it becomes a decay pathway that can significantly impact performance.^{139–141}

The morphology of an OPV refers to the donor and acceptor's mixing behaviour on a nanoscopic to mesoscopic length scale. The two materials can form separate domains of various sizes, be intermixed, or contain a mixture of pure domains of donor and/or acceptor with some intermixed donor and acceptor regions. The domain size and domain purity are commonly used to describe the morphology; domain size refers to the average size of each donor and acceptor domain.^{31,87,142,143} While domain purity indicates how much mixing of the other phase typically occurs within a domain, one phase can be relatively pure, while the other has low purity.^{31,87,142,143}

The optimum domain size is small enough for the donor and acceptor molecules to be within the exciton diffusion distance of an interface but large enough to allow the formation of a percolation pathway for generated charges to reach the electrode.^{31,73} Furthermore, the mixture of crystalline and mixed phases has importance as the need for a 3-phase morphology to drive charge generation and separation.^{92,95,130,144–149}

As the interplay between morphology and photophysics is the topic of this work, further discussion of the morphology and the interplay with photophysics is left until Section 1.4.3.

1.4 The Photophysics of BHJ-OPV Solar Cells

This thesis focuses on the conversion of light to photocurrent in the active layer as a function of donor and acceptor constituents and the morphology of the BHJ. In this section, the photophysical process from absorbed light to separated charges is broken down into discrete steps, with the current (circa 2018) understanding of the photophysics and the influence of morphology discussed.

1.4.1 The pathway from photon to free charge carrier

The conventional description of charge generation in an OPV contains five processes, are illustrated previously Figure 1.5. This sequence of events leads to the extraction charges, with each stage competing with loss mechanism. Each stage will be discussed in further details in the following paragraphs.

1. Absorption of a photon to generate an electronically excited state of a coulombically bound electron-hole pair (exciton);
2. Exciton migration to a heterojunction (donor-acceptor) interface (black arrow);
3. Electron donation results in a bound charge transfer (CT) state whereby the exciton still maintains coulombic binding energy
4. Formation of charge-separated states through migration of charges away from the interface (pink).T
5. Free charges are collected by electrodes on either side of the organic semiconductor layer (grey arrows).

The first step of the photophysical process is absorption. Here, with organic polymers, absorption refers to a chromophore's photoexcitation resulting in a bound electronic excited state, an exciton. This exciton can be delocalised across closely coupled sites and therefore located on several chromophoric units.^{150,151}

After photo-excitation, the newly formed exciton will begin to diffuse; this is broken into two parts; a rapid Förster-type phase and a slower iso-energetic

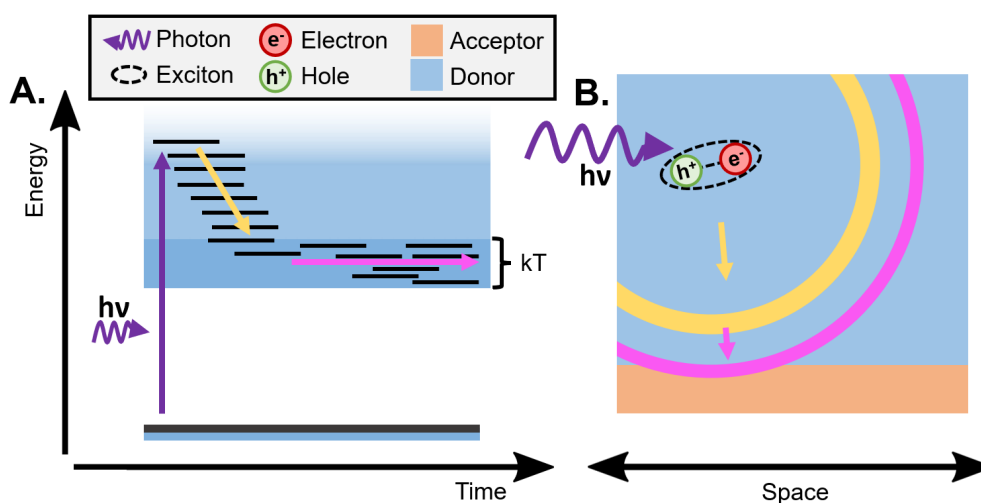


Figure 1.8: An illustration of the energy vs time (A) and spatial (B) dependence of an exciton after photoexcitation. The Förster-type energy transfer (A. yellow arrow) occurs quickly with a large loss of energy and leads to large exciton mobility (B. yellow circle and arrow). Following the Förster-type energy transfer, an iso-energetic process occurs; minimal energy is lost and happens within the system's thermal energy, kT (A. pink arrow). The slower iso-energetic step leading to reduced distance travelled (B. pink circle and arrow).

phase. Figure 1.8 illustrates the two phases, in respect to energy of the exciton vs time (Figure 1.8 A) and with respect to how mobile the exciton is in each phase (Figure 1.8 B). The first rapid energetically downhill segment (Yellow) can be explained by a variation in the number of monomers in each chromophoric unit, where longer chromophores have a red-shifted absorption. The rapid energy transfer will occur between chromophores that have offset energy levels with the exciton being funnelled to the lower energy sites; a rapid process due to the large coupling and small distance between chromophores.^{151–155} Once the exciton has reached the lowest energy chromophore, an iso-energetic process (pink), dependent on thermal fluctuations and therefore is a slower process, allows the exciton energy to be transferred between sites of similar energy.^{152–156} Exciton diffusion lengths of π -conjugated polymers are typically on the order of 5–10 nm, which molecular non-fullerene acceptors have been recently shown to have substantially higher exciton diffusion lengths approaching 50 nm^{153,154,157}

The coulombic binding energy of excitons, 200–800 meV in BHJ-OPVs, needs to be overcome before generating free charges.^{150,158,159} The coulombic binding energy is larger than the thermal energy provided by room temperature (~25 meV), so a heterojunction, consisting of electron–donor and electron–acceptor, is needed to provide the required driving force for charge separation. Charge separation is thought to occur in a two–step process. Initially, the electron is transferred from the excited donor to the acceptor’s lowest unoccupied molecular orbital (LUMO). If the acceptor material has the lower bandgap and/or absorbs light effectively, as in non–fullerene acceptor materials, the charge transfer may proceed as hole transfer from the highest occupied molecular orbital (HOMO) of the acceptor to the donor. In either case, charge transfer is energetically favourable when the offset between donor and acceptor LUMO energy levels (for electron transfer) or HOMO levels (for hole transfer) is larger than coulombic binding in the exciton (EB_{exc}), resulting in a charge–transfer state (CT) that is a hole and electron separated across the donor–acceptor interface. The separation between the hole and electron is on the molecular scale, so there remains a significant coulombic attraction between the pair of charges (EB_{CT}).^{27,61,160}

Once the CT state has been formed, the Onsager–Braun model can describe charge separation.^{27,61,73} The Onsager–Braun model considers excess energy, coulombic attraction, temperature, and a lifetime to determine if the initial CT state goes on to form free charges or if it recombines at the interface. Figure 1.9 illustrates principles behind the Onsager–Braun model, the excitation is bound and the interface, but it has a chance to escape as it must thermalise (a) due to the excess energy caused by the donor and acceptor LUMO–LUMO offset. During this thermalisation process, if it can reach a distance (a_2) outside of the capture radius (r_c), then it no longer feels its charge partner and can escape, but if it cannot (a_1), the charges will move towards each other and recombine. The capture radius (r_c) is dependent on the dielectric constant of the blend, as this is what screens the charges from each other.

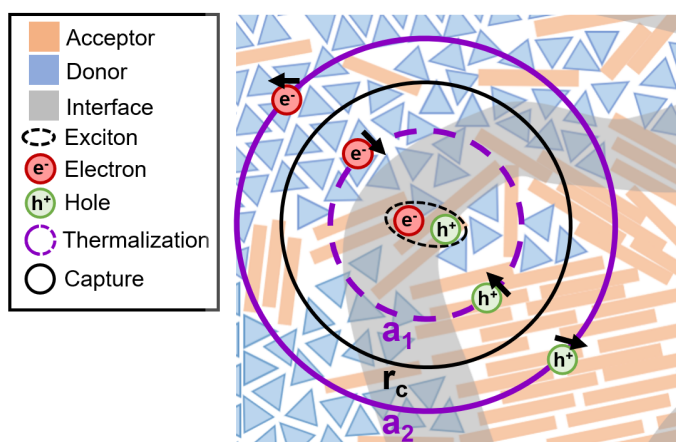


Figure 1.9: The Onsager model is depicted in this figure. The interface region where the charge transfer state (CT) is presented as a grey region; from here, the electron and hole must both be outside of the capture radius (r_c) for coulombic attraction to become negligible making them free charges, i.e. in a charge-separated state. The movement arrows (black above the carriers) illustrate that the carriers are free of each other's influence when they point away from each other. The thermalisation radius (a_1 , a_2) illustrates the distance each charge carrier travel as they thermalise. Depending on the amount of excess energy, the thermalisation distance could be larger (a_2) or smaller (a_1).

The Onsager–Braun theory of charge generation has several inconsistencies when applied to BHJ–OPVs that are highlighted by recent results; the higher than the practical yield of charges on less than 100 fs timescales, and the lack of excess energy required to generate free charges.¹³⁶ The need for excess energy has been disputed by Vandewal et al. (2013), presenting internal quantum efficiency (IQE) measurements showing that IQE is independent of excitation energy when directly exciting CT states.¹³⁶ The lack of excess energy is compatible with the delocalisation across the fullerene polymer means there is no need to drive charge separation as the coulombic attraction is below room temperature activation. Recent analysis, considering disorder and movement in 2– and 3– dimensions, has shown that energetic barriers can be suppressed or completely removed when forming free energy rather than coulomb potential.¹⁶¹ Furthermore, entropic effects favour charge separation, offsetting the Coulomb potential to even account for spontaneous charge separation.

Once a photon is absorbed and successfully split into two independent particles, an electron and a hole, one last process occurs in the active layer; charge transport. For this process to be successful, the independent charges must reach an electrode before recombining. The intrinsic charge transport properties of the materials used as the donor and acceptor are important, along with the method used to cast the film and create percolation pathways.^{146,162–165} During charge transport, the morphology is important as percolation path lengths relate to the distance an electron and hole must travel to reach an electrode. As the morphology of the material systems studied herein has changed, this final step of charge transport must be considered when comparing PCE.

The timescales of photophysical processes

The various steps in the photogeneration of charge carriers happen over timescale ranging from 100's of femtoseconds to microseconds.^{8,27,96,166} To fully measure the photophysics, it is necessary to measure this time range and uniquely identify the different species generated after photoexcitation; singlet and triplet ex-

citons and charges. These dual requirements are met by transient absorption spectroscopy; details of this technique are discussed in Chapter 2.

In brief, it can measure from timescales of femtoseconds to microseconds, and the broad spectral window allows the various species to be disentangled and the lifetimes of each species tracked independently. Further to this, the nature of absorption allows non-emissive species to be measured, i.e. triplet, and charge states. These requirements form the crux of this work, with the implementation of a transient absorption spectrometer that can record lifetimes and spectra over the required range to study OPV's presented in Chapter 2, and the subsequent chapters highlight insights into all of these processes in many different polymer systems, including blends with fullerenes, polymers or SMAs.

1.4.2 Loss Pathways

Optimising an OPV's active layer requires considering how the functional steps described above are affected by changing the material compositions: light absorption, charge generation, charge separation, and charge transport. Understanding how these steps relate to the active layer's material composition and morphology is the basis of this work. The desired pathways (black) and competing loss pathways (purple) are shown in Figure 1.10. The loss pathways are; non-radiative and radiative recombination of the exciton (1.) and charge transfer states (2.) and then non-geminate recombination as the electron and hole as they make their way to the electrodes (3.).

The first step is for the generated excitons to migrate to the interface; the likelihood of the exciton reaching the interface depends on intrinsic exciton lifetime, the exciton diffusion coefficient, and the domain sizes. The lifetimes of the initially prepared excited state can be measured in a neat film of the donor or acceptor, setting the baseline for the competing processes, i.e. radiative (photoluminescence) and non-radiative recombination. Once the same species is identified in the blend, the new lifetimes can be used to estimate the yield (ϕ_{CT} , Equa-

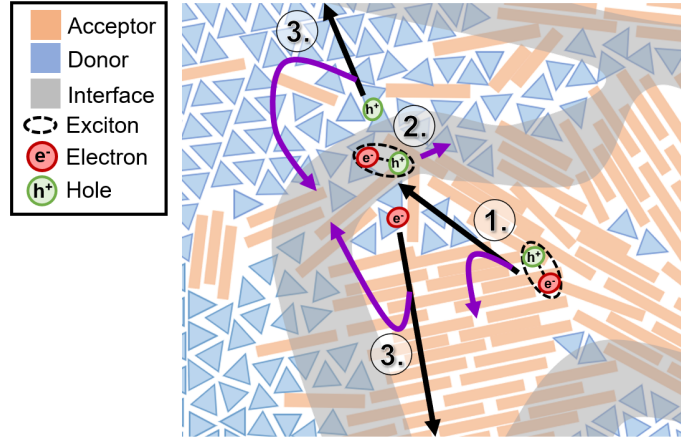


Figure 1.10: The various loss mechanisms (purple arrows) are depicted completing against the desired process (black arrows). 1. Exciton diffusion to the interface competes with radiative and non-radiative decay. 2. Charge separation of the charge transfer state formed at the interface competes with non-radiative decay pathways (geminate recombination). 3. Each charge carrier must reach an electrode before bumping into an interface with the opposite charge carrier present (non-geminate or bimolecular recombination).

tion 1.1) giving a reliable measure of the CT or exciton quenching induced in the blend.

Equation 1.1 is the relationship between the measured rates (k) or lifetimes (t) and the yield of CT states (ϕ_{CT}), assuming quenching is primarily by the formation of CT states.

$$\begin{aligned}\phi_{CT} &= \frac{k_{blend}}{k_{blend} + k_{neat}} \\ &= \tau_{blend} \left(\frac{1}{\tau_{blend}} - \frac{1}{\tau_{neat}} \right)\end{aligned}\tag{1.1}$$

Once at the interface, a charge transfer state can be formed that will still need to separate, leading to free charges. Transient absorption spectroscopy has been used to identify the initially formed excitons and the charges generated afterwards, giving the two critical species in OPV.^{92,96,166–170}

Once the charge states have been generated, they can recombine by non-geminate or geminate recombination; both are loss pathways. Non-geminate recombination is from two free carriers and so occurs from charge-separated states. Geminate recombination typically occurs from the initially formed charge transfer (CT) state at the donor and acceptor materials interface. However, it should be noted that treatment of non-geminate recombination in BHJ-OPVs considered the equilibrium between CT states and charge-separated states; as such, the characteristics of geminate recombination can influence non-geminate recombination.

As discussed previously, the interaction of the bound CT state can be represented by the Onsager model of charge separation (Equation 1.2). Each formed CT state has a probability, $P(CS)$, of dissociating into free charges is dependent on the electron and hole separation distance (r_c), excess energy, dielectric constants ($\epsilon_0\epsilon_r$). In the Onsager model, the excess energy is encapsulated by the concept of "hot" electrons and holes that are produced above the band edge and reach distance (a) apart as they thermalise. Equation 1.2 also considers thermal energy ($k_B T$) and electric field (E).

$$P(CS) = \exp\left(\frac{-r_c}{a}\right) \left(1 + \frac{er_c}{2k_b T} E\right) \quad (1.2)$$

$$r_c = \frac{e^2}{4\pi\epsilon_r\epsilon_0 k_B T}$$

While other treatments of the charge transfer state exist, and the observations in BHJ-OPVs are inconsistent with the model, the general need to overcome exciton binding energy is consistent.⁶¹ Once the exciton has reached the interface, the key loss mechanism is the tight binding of charge-transfer states preventing the formation of independent, free electrons and holes.

How effectively free charges are generated is one of the key areas to understand the relationship between photophysics and the performance of BHJ-OPV. The

determination of free charge yield is still hard to determine and, in most cases, is alluded to only by eliminating other factors that could influence performance. Even though the spectroscopic distinction between CT versus charge-separated states is a challenge for transient absorption spectroscopy; Gallaher et al. found shifts in transient absorption spectral shapes that are suggested to coincide with charges moving away from interfaces.⁹² However, a lack of spectral shift in of itself is not evidence of a low performance devices as there are many examples of high performance devices without spectral shifts being noted. In any case, one can safely assume that if the device is efficient, charges must be extracted, so the ability to detect polarons must represent the dynamics of this mixed population, whether it is mostly CT states or free charges.

Once the charges are separated, they must travel to an electrode to be useful; on this journey, they can contact other carriers and undergo non-geminate recombination, sometimes referred to as bimolecular recombination. In BHJ-OPVs, the probability for recombination depends on the carriers finding each other; therefore, the relative mobility and concentration are important.^{27,171,172} Hence, a Langevin type equation can be used to describe the non-geminate recombination of charge carriers in BHJ-OPVs. Equation 1.3, is the basic Langevin model for charge recombination; γ the recombination rate constant, which is dependent on the relative mobility of the electron and hole (μ) and the dielectric constant of the medium ($\epsilon_0\epsilon_r$).^{171,173} While Equation 1.3 is the basis for the treatment of non-geminate recombination, significant additional factors have been included in additional work, these include but are not limited to spatial fluctuations in energy offsets and variations in carrier speed, details of additional factors added to the Langevin equation can be found in this excellent review of bimolecular recombination in BHJ-OPVs.¹⁷¹

$$\gamma = \frac{e}{\epsilon_0\epsilon_r} \mu \quad (1.3)$$

While this model provides a fundamental basis for interactions of separated charge carriers, in BHJ-OPVs, significant deviations are observed.^{168,174–177} These deviations from ideal Langevin behaviour necessitating the introduction of a reduced Langevin factor.^{174,178} The origin of these deviations are discussed across the literature, and in essence, relate to the equilibrium between the various charge species (charge transfer, charge-separated, singlet and triplet) and interface disorder.^{91,163,168,174,178,179}

These recombination processes compete with percolation to the electrodes, with the competing pathway a combination of percolation pathlength and charge mobility. Measurements of the non-geminate recombination and the intensity dependence can give insight into mobility and the degree of non-geminate recombination. Here the identification of the charge species is essential, as the above details are purely dependent on the lifetimes of the charge species returning to the ground state either via geminate (excitation intensity independent) or non-geminate (bimolecular, intensity-dependent recombination).

It has been suggested that a possible decay pathway for free charges in OPV materials is via charges-charge annihilation forming triplets. If the triplet state is energetically obtainable, it can be generated when two uncorrelated spin charges recombine. While statistically the triplet state is favoured, in a complex system where many states are interacting, it is important to consider the rates generating and competing with the triplet and the ability of the triplets to reform charge carriers. When the triplet formation is allowed to reach equilibrium the statistical outcome will not be the defining condition, and the system will evolve based on the accessibility of each of the states.^{139,141,180,181} The signature of the polymer triplet state is similar to that of charge-transfer states in PBDTTT-C (Figure 1.11).¹⁸¹ This discovery of a triplet signature overlapping with what was once unambiguously a hole polaron (CT state signature) and the typical microsecond lifetime of both species means additional experiments must be conducted to rule out the possibility of triplets.

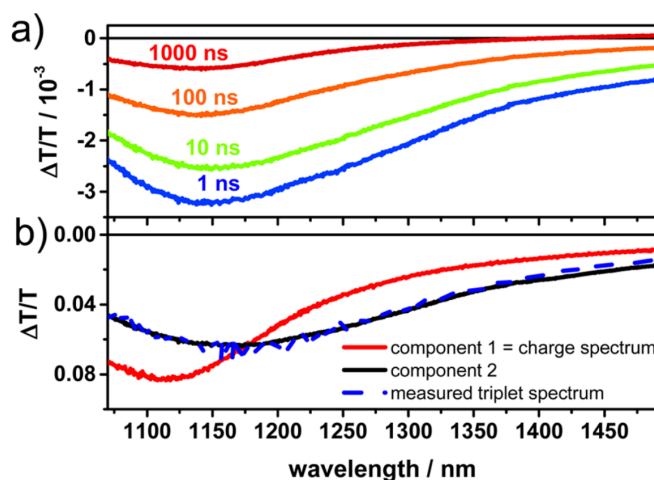


Figure 1.11: This figure is one presented by Gehrig et. al.¹⁸¹ There are two panels illustrating the identification of a charge and a triplet species observed in PBDTTT-C polymer using transient absorption spectroscopy. A. shows transient absorption spectra taken at various decay times. B. is an analysis of the spectra that represent them as two components, black and red, with the black spectra matching the independently measured triplet spectrum (blue).

1.4.3 Interplay Between Morphology and Photophysics

Having established the key photophysics steps in a BHJ-OPV, we now consider how the blend morphology can influence these steps. It should be noted that the work presented below is to provide context for this thesis.

The aggregation and crystallisation of polymers have a large effect on the absorption spectrum compared to the solution spectra of the same polymer, with aggregation typically red-shifting and broadening absorption peaks.^{95,182,183} Along these lines, the degree of aggregation in thin films can also lead to measurable changes in absorption.^{92,95,184,185} While it is true that aggregated polymers can be affected by the degree of aggregation in films, the changes in morphology studied in this work do not lead to a large change in absorption.

The role of morphology, how it influences exciton diffusion and/or delocalisation, and subsequent charge generation is hotly debated. It is argued that the large charge yield formed within tens of femtoseconds after photoexcitation is

the result of mostly delocalised initial excitons. The need for the delocalisation of excitons arises because, within 100 fs, there is clear evidence of the formation of CT states.^{186–191} As if we consider the accepted exciton diffusion coefficients, an exciton can only diffuse 0.1–0.2 nm in 100 fs; more time is required before the majority of excitons reach an interface, typically 5 nm from the exciton.^{79,192,193}

To investigate the role of initial exciton delocalisation, Chen et al. (2013) measured the quenching of photoluminescence using ultrafast time-resolved photoluminescence (PL).¹⁵⁷ A Perrin-type model is used to estimate the area of the initial exciton. The initial exciton–exciton quenching is measured as a function of exciton density (Figure 1.12), and fit to a Perrin-type model to give an exciton volume of 17 nm³, larger than the interchain distance in OPVs. The large distance and high rate of mobility are used to explain the temperature independence of charge generation. Further, the broadband PL data shows a faster decrease in the higher energy end of PL, consistent with relaxation to lower energy conformations within the polymer bulk. The relaxation on early timescales supports the presence of higher energy delocalised excitons. Further supporting the role of fullerene domain size and early time delocalisation, Friend et al. (2014) used an electro-absorption (EA), which arises due to the Stark effect.¹⁹⁴ A separation of at least 4 nm is achieved within 40 fs; this is shown using electro-absorption acts as a distance probe due to the electronic field between separated charges being distance-dependent.

The domains of 4 nm to 5 nm are consistent with previous work to determine the optimum OPV fullerene domain size of 10's nm in length.^{31,73} The dynamics of charge generation being separated into a prompt component occurs in less than 100 fs as the initial exciton delocalised or is formed next to phase boundaries, and then a slower phase is generated from exciton migration the interface.⁹⁶

The role of delocalisation for charge transfer was further supported by Friend et al. (2012), where the authors measured the effect of an additional sub-bandgap excitation.¹⁸⁷ The sub-bandgap excitation was shown to re-excite bound/lower

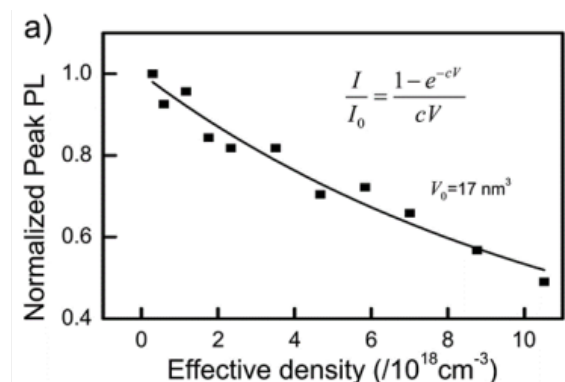


Figure 1.12: This figure is one presented by Chen et. al.¹⁵⁷ A graph of excitation density vs normalised photoluminescence intensity (PL) the photoluminescence is taken over a 200 fs interval that corresponds to the excitation time-frame. The PL is normalised to the PL intensity expected at the given excitation density if there was no quenching. The relationship can then be used to estimate the volume of the initial exciton (V_0).

energy CT states into more delocalised CT states. The results show the re-excited CT states added to photocurrent generation in a working OPV device. To study the influence of fullerene domain size on charge separation and exciton delocalisation, Ratner et al. (2014) performed computational studies.¹⁹⁵ Figure 1.13 shows the effect on the density of states of increasing the fullerene cluster size. As the cluster increases in size, the energy becomes larger (red arrow) and overlaps better with the polymer energy level. The alignment of energy levels allows delocalisation across the polymer–fullerene heterojunction, leading to lower coulombic binding of the CT state. The density of states of the fullerene and the alignment with the polymers exciton energy was linked to fullerene domain size supporting previous claims of fullerene crystallinity dependence. These results also justify the electric field and temperature independence of the charge separations.

In addressing the effect of morphology on charge separation, Gallaher et al. (2015) uses a series of polymers with varying backbone curvature to control the degree of intermixing of polymer:fullerene components.⁹² This research employed signatures obtained in transient absorption spectroscopy to identify charges species

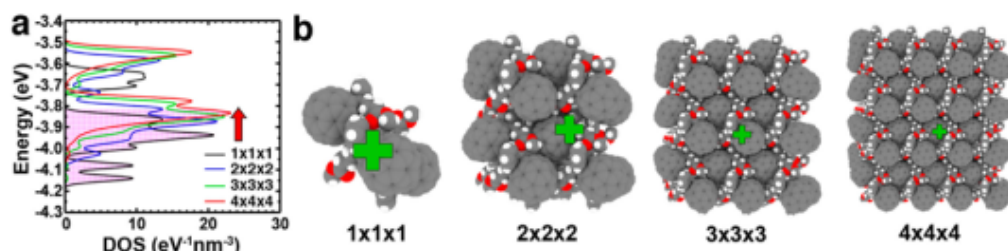


Figure 1.13: This figure is one presented by Savoie et. al.¹⁹⁵ The density of states (DOS) calculated for fullerene clusters of varying, including a point charge size, is shown in A. The fullerene clusters' geometries are shown in B., with the location of the point charge shown as a green cross.

present in the ordered and disordered domains. Figure 1.14 shows the time dependence of the peak position of the signature attributed to CT. In a 3-phase system where the charges can move from intermixed to pure phases, there was a shift in the CT state signature. In identifying the change in CT signature, it was possible to track charges carriers in varying degrees of domain mixing, demonstrating that a three-phase morphology leads to efficient charge separation. It was also observed that a lack of an intermixed phase hindered the overall charge yield. This work shows the value of structural probes and the insight that can be gained by isolating the structural environment of charge formation and that which it finally decays in. It was concluded that fullerene domain crystallinity is important, and the electronic coupling and symmetric nature of the fullerene states make it a good acceptor.

In order to understand the photophysics, the relationship between charges generated promptly (less than 100 fs) and at later timescales is of importance. No direct correlation with morphology was made, the relationship between prompt and delayed charge generation is explored by Barker et al. (2014).¹⁶⁶ The relationship between charges generated at different timescales is understood by comparing their distances distributions measured via the tunnelling rate of immobile charges (charges are cooled to 10 K). Excitation intensity dependence shows that charges are recombining via non-geminate recombination, and diffusion is an

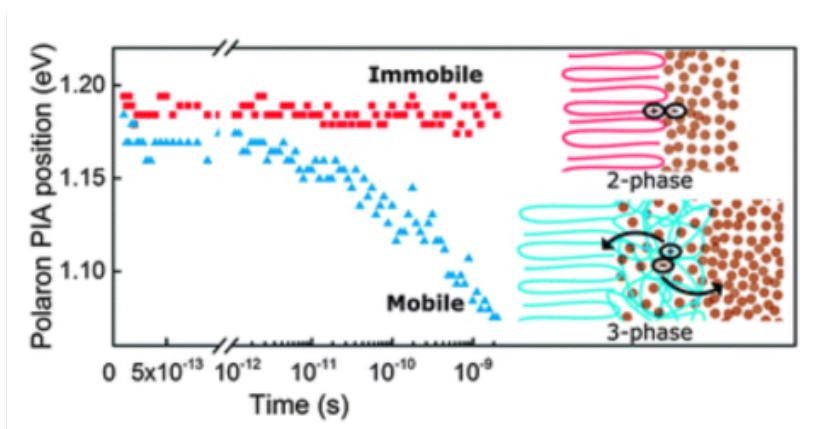


Figure 1.14: This figure is one presented by Gallaher et al.⁹² The time-dependent polaron (charge transfer state signature) peak spectral position (PIA-peak) extracted from transient absorption studies is graphed as a function of time. The immobile and mobile labels represent two different material systems studied. The lack of change in the PIA-peak position is correlated with the 2-phase system (red), while the shifting PIA-peak position is from the material with a 3-phase (blue) morphology.

important factor. The tunnelling rate is fitted to two Gaussian distributions of decay rates; the need for two distributions was consistent across many efficient and non-efficient polymer materials. The first of the two rates is associated with a population of charge pairs that are close to each other resulting in fast tunnelling, and the second when charge pairs have greater separation, thereby decreasing the tunnelling rate. This second population is associated with separated charges. A universal relationship was observed between the yield of separated charges (sc) at 10 K, and the yield of free charges (free) determined at room temperature (Figure 1.15). The discovery of this relationship reveals that processes occurring on the thermalisation timescale is correlated with the overall number of extracted charges.

These results show the complicated relationship between morphology and overall efficiency and the complexity of the photophysics in BHJ-OPVs. Two distinct timescales of charge generation, with the ratio of prompt:delayed indicating the degree of phase separation, versus intermixed or delocalised singlet exciton.

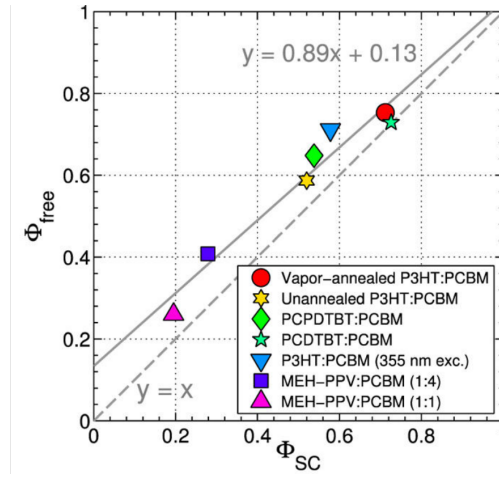


Figure 1.15: This figure is one presented by Barker et. al.¹⁶⁶ The data presented here is extracted from transient absorption measurements collected at 10 K and room temperature. The separated charge yield (ϕ_{SC}) are taken from long-lived lifetimes in data collected at 10 K, while free charges (ϕ_{free}) are calculated from room temperature intensity-dependent measurements. The two independent populations are measured under independent conditions but give rise to a universal relationship, linking the distance charges separate at 10K to the yield of free charges at working temperatures.

Many species and multiple orders of magnitudes, whereby each is important; prompt vs delayed charge generation occurs in <100 fs, overall quenching of singlet occurs within 100's of picoseconds, charge lifetimes are typically 100's of nanoseconds to microseconds and can be shortened by bimolecular recombination to 10s of nanoseconds. These characteristics lend themselves to examination by broadband transient absorption spectroscopy, which can observe spectral changes over a wide region (400–1600 nm) and identify and observe both dark and emissive species while tracking their evolution from 100s of femtoseconds to 10s of microseconds, i.e. eight order of magnitude (10^{-13} to 10^{-5}).

1.5 The Contributions made by this Thesis

The interplay between morphology and performance requires the characterisation of the underlying photophysics to understand the effects and pathways of the various optimisation techniques. The drive towards optimal efficiency can see a trade-off between all the steps that are needed for OPV to function; by characterising each of these steps, we can diagnose what processes are being affected by the changes made and therefore the bottlenecks and if they are particular to these materials of form a more general trend. Understanding and characterising the bottlenecks and driving forces responsible for charge generation in OPVs will lead to more efficient OPV devices. Understanding the dominant pathway or revealing a high tolerance for certain characteristics will help guide the design of molecules, film optimisation strategies and aid in understanding morphology.

The focus of this work is the characterisation of photophysics in a multitude of different BHJ-OPV systems looking for correlations and understanding how changes to the material system affect the photophysics and if any general conclusions can be drawn across the various systems studied. To this end, investigating the interplay between morphology and photophysics, revealing if this relationship is important for the device performance, i.e. what are the underlying pho-

tophysics and are specific conditions needed for charge generation influenced by morphology. The characterisation of photophysics is the focus of this thesis, with the various changes discussed in reference to the electrical and morphology characterisation completed by collaborators.

A summary of the relevant electrical and morphological characterisations is presented in each chapter, that was undertaken by collaborators. The electrical characterisation gives a basis for the PCE and percolation, and morphology sets the scene to understand the photophysics.

The characterisation of the photophysics is performed with steady-state absorption and photoluminescence and time-resolved transient absorption spectroscopy. These three complementary techniques are used to build a complete picture of the photophysics, including understanding both the donor and acceptor phases, how effective these excitations are at making charges, and the quenching efficiency of excitons under steady-state conditions.

Collection of the absorption spectrum is necessary for both photoluminescence and transient absorption measurements. It primarily allows the understanding of what photons can excite the donor and acceptor phase; this can be used to vary the initial excitation density in each phase to disentangle their contribution. In addition, the comparison of the neat and blended spectrum allows for any changes in absorption from morphology to be identified and considered.

Comparing neat films of each donor and acceptor to the blend makes it possible to calculate the photoluminescence quenching. As the emissive species is the initially generated singlet state, high quenching efficiencies indicate charge transfer, a positive process, or some loss pathway. In either case, for an efficient OPV, a high degree of PL quenching is expected. The majority of the absorption and photoluminescence characterisation (except for Chapter 5) is undertaken as part of this thesis.

In order to characterise the photophysics of BHJ-OPVs, it is important to understand the transient species generated after photoexcitation. Transient absorption spectroscopy is used to understand the evolution of transient species from hundreds of femtoseconds to tens of microseconds. It allows the tracking of the initial generated singlet state to an eventual return to the ground state. This work focuses on developing and measuring a wide range of OPV systems using transient absorption spectroscopy to understand the kinetics of these materials. As such, Chapter 2 is dedicated to transient absorption spectroscopy detailing how it can be applied to OPVs and the specifications needed.

1.5.1 The Three BHJ-OPV Systems

Chapters 3–5 covers a range of electron acceptors used in BHJ-OPVs; these include fullerene, polymer and non-fullerene small molecules. Chapter 3 studies fullerene acceptor looking at two different systems. First, the weight percentage of PC₇₁BM is varied, The second looks at changing the functionality of the fullerene, looking at three common fullerene derivatives PC₆₁BM, PC₇₁BM, and ICBA. In Chapter 4 a polymer is used as the electron acceptor. First, the effect of changing the donor blended with P(NDI2OD-T2) from PTB7-Th to PTB7 is investigated, and secondly, P(NDI2OD-T2) is changed for a polymer electron acceptor with increasing fluorination of its chemical structure. Finally, Chapter 5 looks at one of the first small-molecule acceptor systems to have better efficiency than fullerene:polymer blends developed at this time.

Chapter 2

Collection and analysis of transient absorption spectroscopy

2.1 Introduction

Ultrafast transient absorption spectroscopy (TA) is employed to understand the photophysics of organic photovoltaic (OPV) materials. In order to successfully apply TA to OPV materials a few essential criteria need to be met:

- A broad spectral window; to distinguish between the multiple excited state species involved, singlet exciton, charges, triplets.
- Time range from femto– to micro– seconds; it is crucial to track the excited state dynamics from initial excitation until the return to the ground state.
- A low noise background; to measure an OPV active layer under conditions similar to a working device.

This chapter is separated into three sections. Section 2.2 presents a guide of transient absorption with the aim of understanding the results and experimental improvements that follow. It introduces ultrafast pulses and how they can

be made spectrally narrow and tunable or broad covering the 400 to 1600 nm range, and how we can span the femto- to micro- second time range. Also included in the first section is an outline of the processes that give rise to transient absorption signals. The second section, Section 2.3, discusses experimental considerations that have been quantified or improved in our experimental set-up as part of this thesis. The improvements have allowed the measurement of excited states over an extensive temporal and spectral range; these include: beam collimation, instrument response function (IRF), spectral range, and reduction of the noise floor. Finally, Section 2.4 deals with transforming data into valid inferences when working with a broad set of possible interpretations. It discusses methods to extract species and decay profiles that consider the infinite solution space provided by a 2D dataset. More specifically, this section discusses the extraction of components via singular value decomposition (SVD) and the applications of constraints that lead to meaningful and comparable results, whether it be parametrised (hard) or non-parameterised (soft) modelling of the data.

2.2 Conceptual overview

Transient absorption (TA) spectroscopy provides information on the change in absorption at various times after photo-excitation. The change in absorption is used to identify the species generated following photo-excitation; the interconversion between excited state species; and the return to the ground-state. TA uses two laser pulses, an excitation (also known as pump) and a probe, to generate a two-dimensional dataset with a spectral and a temporal dimension. The excitation pulse interacts with a sample to give rise to an excited state population and needs to be tunable and spectrally narrow in order to be able to work with a variety of materials. The probe pulse reveals electron transitions in the same way as absorption spectroscopy, as the probe spectral range broadens it becomes easier to unambiguously distinguish between multiple species.^{196–201} The non-linear optical methods used to achieve the above characteristics are discussed in Section 2.2.3. Additional experiments can be used to aid in the interpretation

of the blended OPV. This includes measuring the excitation fluence dependence to distinguish mono-molecular and higher order decay pathways. We measure neat films of the individual materials before we blend the individual components that are used to create the OPV active layers in order to understand the spectra and which excited state species it can be attributed to.

Equation 2.1 describes the signal of interest in a TA measurement (ΔOD) at various a fixed time after excitation (t); it is the difference between the absorption from species in the excited state (A_{ex}) and ground state (A_{gs}) at a particular wavelength (λ). In this manner, absorption by molecules in the ground state can be isolated from absorption induced by molecules in an excited state.^{196,197} Equation 2.1 shows that only the probe intensity with (I_{on}) and without (I_{off}) the excitation pulse are required to measure the TA signal; this is only true if there are minimal fluctuations between the measurement of I_{on} and I_{off} . In this work (and much of the literature) the ΔOD signal is present in terms of fractional change in transmission ($\Delta T/T$). Equation 2.2 is the relationship between ΔOD and $\Delta T/T$.

$$\begin{aligned}
 \Delta OD(\lambda, t) &= A_{ex}(\lambda, t) - A_{gs}(\lambda) \\
 &= -\log \frac{I_{on}(\lambda, t)}{I_0(\lambda)} + \log \frac{I_{off}(\lambda)}{I_0(\lambda)} \\
 &= -\log \frac{I_{on}(\lambda, t)}{I_{off}(\lambda)}
 \end{aligned} \tag{2.1}$$

$$\begin{aligned}
 \frac{\Delta T}{T}(\lambda, t) &= \frac{I_{on}(\lambda, t) - I_{off}(\lambda, t)}{I_{off}(\lambda)} \\
 &= \frac{I_{on}(\lambda, t)}{I_{off}(\lambda)} - 1 \\
 \frac{\Delta T}{T}(\lambda, t) &= 10^{-\Delta OD(\lambda, t)} - 1
 \end{aligned} \tag{2.2}$$

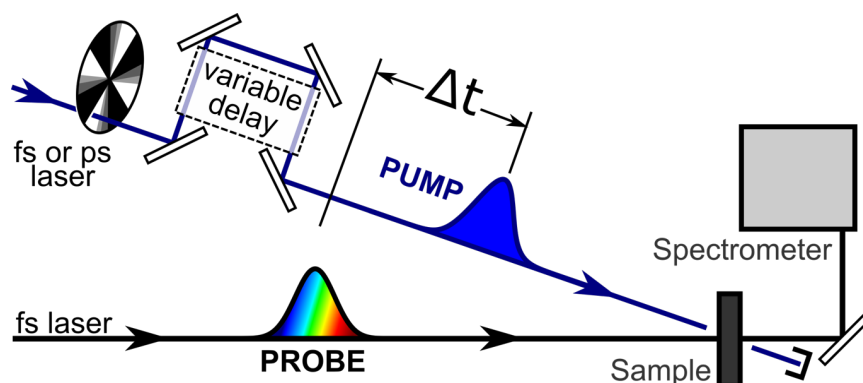


Figure 2.1: Illustrative instrumental layout for transient absorption spectroscopy (TA). Black is the probe pulse that interacts with the sample and is then spectrally resolved in a spectrometer. Blue is the sample excitation (pump) pulse, which is modulated with an optical chopper. The excitation pulse also has a variable delay with reference to the probe, controlled either via change in path length or electronically.

Figure 2.1 is an illustration of the experimental layout. It shows the excitation (pump) pulse, probe pulse, and other necessary components such as the electronically controlled mechanical delay stage and spectrometer. The spectrometer collects the intensity of the probe at each wavelength. The spectral range is determined by the probe pulse, with a range from 500 nm to the 1600 nm being routinely measured. The on/off modulation is achieved by an optical chopper, it sequentially lets through (on) then blocks (off) the excitation pulse for each measured probe pulse. The delay stage is used to generate the temporal dimension. The temporal resolution, determined by the temporal width of the excitation pulse, which is discussed in greater detail in Section 2.2.2. By monitoring the spectra and position of the delay stage we have all the information needed for each data point; i.e. probe intensity, relative delay of excitation, and if the excitation pulse is present.

2.2.1 Observed signals

To understand the signals observed in a TA measurement we consider how the interactions of light with the sample changes after excitation. The interactions with light can be broken down into five categories:²⁰¹

- Ground state bleach (decrease in the number of absorbed photons).
- Photo-induced ground state bleach
- Stimulated emission (the opposite of absorption)
- Photo-induced absorption (absorption by a species in an excited state)
- Electro-absorption (change in the ground state absorption due to local electric field)

The excited state species will always have a combination of these signals whether they are of singlet, charge, or triplet character.

Figure 2.2a gives a simplified overview of how the probe pulse can interact with the sample. The initial excitation pulse perturbs the population in the system from its ground state (1) into an excited state (2), this decrease of population in the ground state gives rise to a ground-state bleach (GSB). This decreased ground state leads to less absorption giving a positive signal ($\Delta T/T$) with a spectral shape that approximates the steady-state absorption. A similar effect is also seen when a photo-product is formed after excitation, i.e. a photo-stationary state is formed, this new species can lead to a GSB signal that is not related to the steady state absorption. The population in the excited state makes it possible for stimulated emission (SE) to occur, whereby an interaction with the probe initiates a transition back to the ground state releasing a photon. SE only occurs when the probe pulse contains wavelengths that corresponds to the energy of optically allowed transitions between the excited state to the ground state. This additional photon increases the measured intensity giving a positive signal. The absorption from an excited state into a higher excited state is called photo-induced absorption (PIA). This optical transition can occur from a singlet state to higher energy singlet states, or if the molecule has relaxed to a triplet state, a higher energy

triplet state. Due to a photon being absorbed the measured intensity decreases giving rise to a negative signal. The final signal is electro-absorption (sometimes called the Stark effect), this is due to local electric fields caused by charge pairs being formed in the excited state. The charge pairs produce an electric field that shifts the ground state absorption giving rise to a derivative like feature spectrally overlapping the ground state absorption edge.

The broad nature of TA signals means that overlap of multiple signals results in spectra that are the sum of many different underlying features.^{199,200} This is illustrated in Figure 2.2b where the top section shows the TA spectra if each of the signals are separated while the bottom gives a more realistic description with the dotted line representing the observed spectra after addition of the underlying GSB, SE, and PIA. Separation of the underlying components can be achieved by a combination of steady-state measurements of both ground state and model compounds, and modelling the kinetic data.^{200,202–204}

Building further on the complex nature of the observed signals Figure 2.3 presents spectra associated with species present in a polymer:fullerene blend (FTAZ:IDIC, discussed in Chapter 5). Figure 2.3a contain the first two spectra observed. An exciton, in purple, that is expected to have GSB, SE, and PIA. And a polaron, in orange which lacks the SE and should have two GSB regions. Diagnoses of the exciton is done by comparison to the steady-state absorption spectra the high energy peaks as being GSB and the peak at 710 nm (1.75 eV) arising from SE due to the proximity it is expected that these two features overlap, supported further by the polaron where no SE expected, and a small peak at 710 nm (1.75 eV) is revealed. The exciton also has a PIA associated at 870 nm (1.43 eV) that overlaps with the SE as seen by the sharp transition between negative and positive signals. There is also a broad and weak PIA feature that continues into the near-infrared region. The exciton species has been identified by a number of the TA signals mentioned above, i.e. GSB, SE, and PIA. Moving onto the polaron species there is a shift in the PIA beak to lower energy, while a second GSB regions 480-610 nm (2.6-2.0 eV) has appeared, this is due to charges comprising

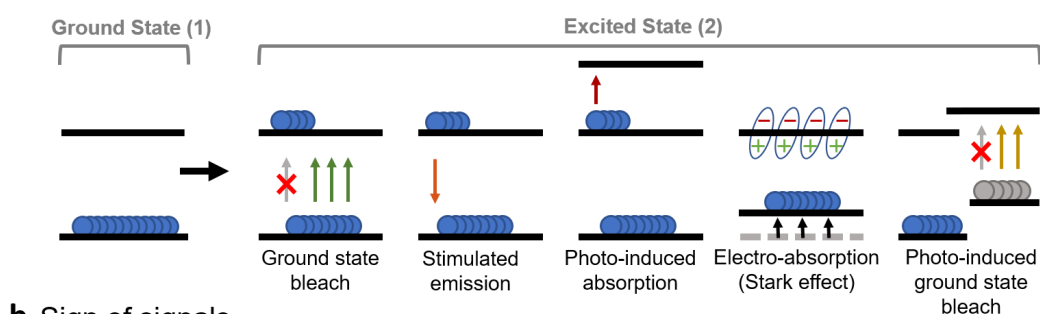
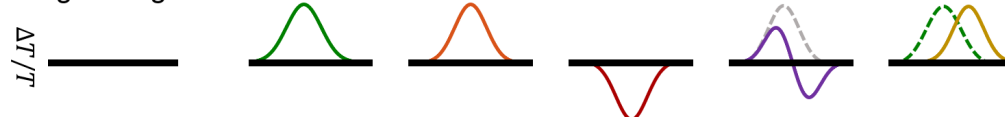
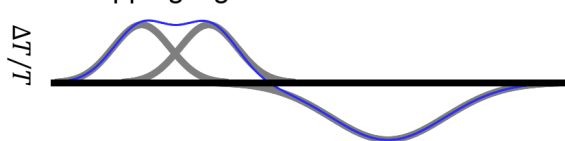
a. Electronic state**b. Sign of signals****c. Overlapping signals**

Figure 2.2: Illustration showing the electronic transition responsible for the observed signals in a TA experiment. (a) Shows the electronic transitions, moving from the ground state (1) to excited state (2) is caused by the excitation pulse. This gives rise to the five excited state signals, with the fifth (photo-induced ground state bleach) arising due to a new steady-state equilibrium formed under photo-excitation. (b) shows the expected sign of each signal class, ground-state bleach (GSB) is a positive signal and arises due to decreased number of photons absorbed (green arrow). Stimulated emission (SE) is an additional photon emitted when the excited state returns to the ground state. Photo-induced absorption (PIA) is a transition to a higher excited state following absorption of a photon. Electro-absorption (EA) is caused by a shift in the ground state due to local electrical fields (typically due to charge pairs). Finally photo-induced ground state bleach which is similar to GSB except that it arises from the bleaching of a photo-product. (c) shows the overall signal (blue line) when the individual components overlap, which is typical of an experimental measurement.

an electron and holes, whereby one exists on a donor and the other acceptor, a polymer and small molecule respectively for this example. The new GSB exhibits decreased signal strength due to an overlapping PIA feature, but can still be identified by the notable increase in signal intensity when compared with the surrounding regions. The polaron species can be identified by the appearance of two GSB regions, one from the electron donor and the other the electron acceptor, and PIA at 910 nm (1.36 eV). If the spectra window were not broad enough to reveal the GSB, SE, PIA feature inter-conversion or identification species would be difficult to identify. Moving on the spectra presented in Figure 2.3b the charge species for (a) and the later time change spectra is presented. The second charge species is again a mix of GSB from the donor and acceptor materials, with a broad and sharp PIA feature that identifies it as a charge. The main difference is the shift in GSB peak position which could be caused by morphological changes.⁹² This again highlights the importance of the broad spectral range as resolving only the near-infrared region, 800-1200 nm (1.6-1.0 eV), would not have revealed the shifting GSB signals.

2.2.2 Femtosecond to microsecond time resolution

The time dimension of a TA surface is given by the time delay at the sample between the excitation (generation of the excited state population) and the probe (measuring the perturbation in the absorption spectra) pulses.¹⁹⁷ A new pair of excitation and probe pulses are used at each time delay; this is beneficial when compared with a single excitation and then measurements of a probe at various delay times for two reasons: the probe will perturb the system from its natural trajectory, and the electronic gating cannot achieve femtosecond resolution.

The path length of excitation pulses is changed by a mechanical delay stage to achieve the change in arrival time between excitation and probe pulses on the femto- to nano-second range, and by an electronic triggered excitation pulse for delays from 1 nanosecond to 150 microseconds. In the mechanical regime Equation 2.3 is used to calculate the time delay for various path lengths, t is

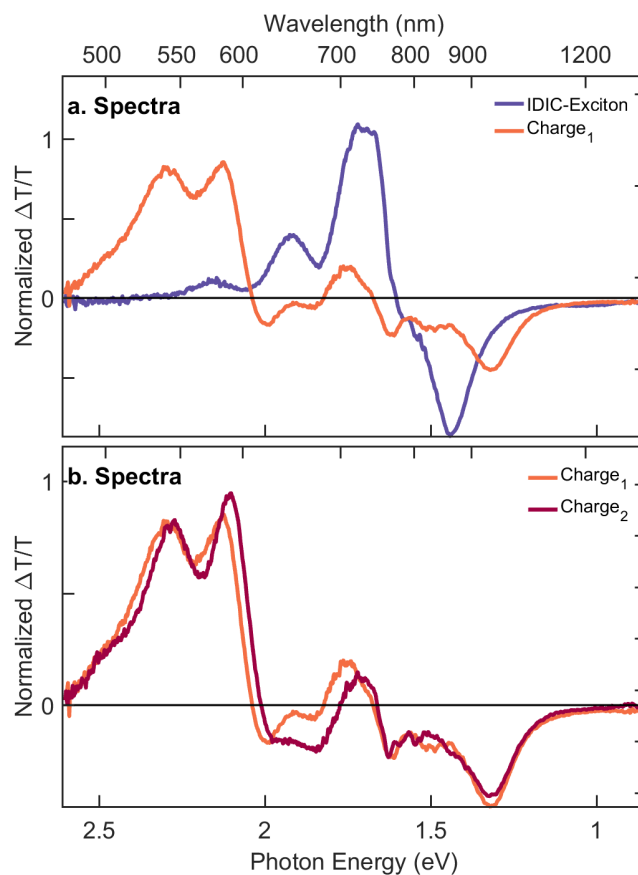


Figure 2.3: Normalised spectra associated with species (as detailed) from a 712 nm excitation $0.26 \mu\text{J cm}^{-2}$ FTAZ:IDIC blend, discussed in detail in Chapter 5.3. Both a and b present spectra that are made up of a combination of GSB, SE, and PIA, separation into two panels (a) and (b) is to provide clarity with Charge_1 spectra being identical in both panels.

the arrival time at the sample and l is the total length each pulse travels. A $10\ \mu\text{m}$ difference in path length will result in a time difference of 30 fs. This path length variation is set by a computer-controlled 500 mm linear translation stage with $\pm 0.5\ \mu\text{m}$ accuracy ($\pm 1.7\ \text{fs}$). A retro-reflector (that returns light parallel to the input direction) is mounted on the translation stage to give a maximum time variation of 3.3 ns for a single bounce, and 6.7 ns for two bounces. This second bounce is necessary because the electronically controlled laser has a pulse duration of 800 ps preventing a non-convoluted signal from being observed until 2–3 ns depending on the signal lifetime (discussed further in Section 2.3)

$$\begin{aligned}\Delta t &= t_{\text{probe}} - t_{\text{excitation}} \\ &= \frac{l_{\text{probe}}}{c} - \frac{l_{\text{excitation}}}{c} \\ &= \frac{1}{c}(l_{\text{probe}} - l_{\text{excitation}})\end{aligned}\tag{2.3}$$

The need to extend the time resolution out to the microsecond range is due to the timescales of processes that occur in an organic photovoltaic (Illustrated in Figure 2.4). The variation in path length can allow for nanoseconds of delay between pump and probe, this is long enough to study the singlet exciton to charge generation process, and most of the diffusion process, but if the recombination dynamics are to be probed then extension out to the microsecond regime is necessary.^{73,205,206} To extend out to the microsecond regime requires an alternative excitation laser source that can be electronically triggered, as a delay of even $1\ \mu\text{s}$ would correspond to a path length difference of 300 m.

2.2.3 Non-linear optics

To generate the excitation (narrow and tunable) and probe (spectrally broad) pulses non-linear optical processes are used. The gigawatt instantaneous electromagnetic field present in femtosecond pulses breaks down the linear approximation made when examining how electromagnetic fields interact with matter.^{207,208} Equation 2.4 shows a Taylor expansion of the interaction between elec-

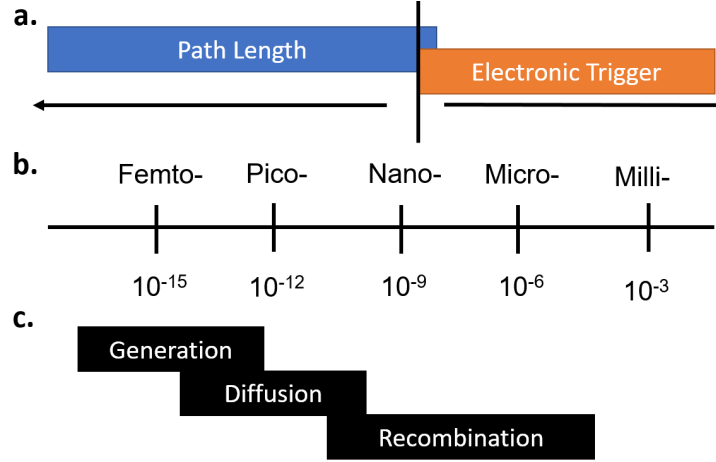


Figure 2.4: Relationship between processes in OPV and how the delays are generated experimentally. (a) shows the two different delay mechanisms used. For times < 6 ns the pathlength is varied while for greater times the pulse is electronically delayed. (c) Shows the timescales corresponding to; generation, diffusion, and recombination of charges in organic photovoltaic devices.

tromagnetic field $E(t)$, and the interaction with the dipole moment of a material $P(t)$. The expansion contains χ^2, χ^3, \dots which is the second-, third-, etc., order non-linear optical susceptibilities. The magnitude of the non-linear susceptibilities is dependent on the material being used, in particular, the symmetry of the material; with some crystals, e.g. β -barium borate (BBO), have large χ^2 values. These terms can be related to second and third order non-linear polarisation; as shown in Equation 2.5. Second order effects are used for optical parametric amplifier and frequency doubling. White light generation is a more complicated process that includes higher order non-linear polarisation terms. Both optical parametric amplifier and white light generation will be covered briefly here, with more in-depth coverage found in the literature.^{199,207–215}

$$P(t) = \epsilon(\chi^1 E(t)^1 + \chi^2 E(t)^2 + \chi^3 E(t)^3 + \dots) \quad (2.4)$$

$$\begin{aligned}
P(t)^2 &= \epsilon_0 \chi^2 E(t)^2 \\
P(t)^3 &= \epsilon_0 \chi^3 E(t)^3
\end{aligned}
\tag{2.5}$$

White light generation

White light generation occurs when an intense femtosecond laser pulse, also known as the seed, is focused into a transparent media. This effect has been observed in gases, liquid, and solids.^{215,216} The white light generation process is initiated by self-phase modulation and the corresponding self-focusing of the pulse, due to the non-linear interaction modulating the refractive index of the material. This highly focused pulse has a number of other effects including; self-steeping, four-wave mixing, and ionisation contributing to the overall white light generation. Further details can be found in a comprehensive review by Couairon et al. (2007).²¹⁰

The spectral bandwidth available from white light generation depends on both the bandgap of the transparent medium and wavelength of the seeding laser pulse. When seeding with an 800 nm central wavelength; sapphire is 470-1000 nm (2.6-1.2 eV) continuum, CaF₂ 320-1200 nm (3.9-1.0 eV) continuum, and YAG (yttrium aluminium garnet) 500-1600 nm (2.5-0.8 eV). Changing the seed wavelength results in a shift in the respective bandwidth window in the same direction of the seed.^{199,215} Due to the broad spectra range and overlap with signals expected in organic solar cells a YAG crystal is used as the white light generation medium for this work.

Narrowband pump

The power generated at any wavelength using the white light generation process is sufficient for the probe but falls short of that required for an excitation pulse. Generation of an intense narrow bandwidth pump of selectable wavelength is achieved by taking advantage of second order non-linear optical effects. These involve the interaction of one or more laser pulses to generate two different fre-

quencies. The process used in this work are sum frequency generation (SFG), or optical parametric amplification (OPA).²⁰⁸

Crystals used for non-linear optics have an anisotropic refractive index. The refractive index can be modified by rotation along the appropriate symmetry axes. The crystal orientation is set so that destructive interference between wavelengths generated via non-linear processes is minimised for the desired wavelength, i.e. amplifying the chosen wavelength.^{208,209} The bandwidth of phase matching constrains the number of frequencies amplified narrowing the number of wavelengths amplified. For example, an electric field that contains two wavelengths (ω_1, ω_2) can be modelled using Equation 2.6 (c.c is the complex conjugate). The second-order polarisation interaction can be seen in Equation 2.7. Combining these two equations (Equation 2.8) gives two new frequencies (highlighted in red); sum frequency generation which is $\omega_1 + \omega_2$ and OPA $\omega_1 - \omega_2$.²⁰⁸

$$E(t) = \frac{1}{2}E_1e^{-i\omega_1t} + \frac{1}{2}E_2e^{-i\omega_2t} + c.c \quad (2.6)$$

$$P(t)^2 = \epsilon_0\chi^2E^2(t) \quad (2.7)$$

$$\begin{aligned} P(t)^2 = \frac{\epsilon_0}{4}\chi^2 \bigg[& |E_1|^2 e^{-i\omega_1t} + |E_2|^2 e^{-i\omega_2t} + ... \\ & 2E_1E_2e^{-i(\omega_1+\omega_2)t} + 2E_1E_2e^{-i(\omega_1-\omega_2)t} + ... \\ & (|E_1|^2 + |E_2|^2)e^0 \bigg] + c.c \end{aligned} \quad (2.8)$$

2.3 Experimental considerations

With an understanding of the experimental set-up and non-linear processes we can now discuss some of the experimental considerations. Specifically, those that have been improved in the course of this thesis, luckily they encompass the majority of considerations when working with thin-films.

The signal collected by TA spectroscopy contains some artefacts, their influence is seen mostly in the time range similar to the pulse duration.^{200,217} The arte-

facts can be broken down into three categories: single pulse, including instrument response function, and chirp; multi-pulse, including two-photon absorption, cross phase modulation and stimulated Raman amplification.^{201,217–219} The single pulse and experimental artefacts are relevant to measurements on thin-films while multi-pulse artefacts commonly only arise in solution phase measurements. The distinction between solution and thin-film is due to the higher interaction distance. In solution, the path length is typically 1 mm compared to hundreds of nanometres for thin films. As this project is concerned with thin-film details of the multi-pulse artefacts will be not be covered.

Instrument response function

Instrument response function (IRF) gives the minimal temporal resolution achievable in our experimental setup, because the temporal width of the excitation pulses is longer than the mechanical delay step. When the time resolution governed by the delay stage is shorter than the pulse duration the non-instantaneous excitation leads to an observable rise of the signal around time-zero. The initial excitation has a distribution of excitation time; some molecules are excited by the leading and others the trailing edge of the excitation pulse, convolving the signal by the temporal intensity profile of the excitation pulse.^{200,202} Figure 2.5 presents an illustration of the convolution process with the Gaussian excitation pulse represented by the blue-dotted lines and the intrinsic decay shown in orange. The integral of the IRF and intrinsic decay is the shaded blue area which is mapped to an signal intensity below (red) at the central time of the Gaussian excitation pulse. This is shown for all times as depicted by the shifted excitation pulse (t_1, t_2, t_3). In this manner, the signal does not spontaneously appear at time-zero but instead has a rise governed by the IRF.

If the temporal width is a similar magnitude to the timescales studied then the convolution of the underlying decay manifests itself in two ways. First the amplitude of the signal is reduced, making a comparison of initial yields difficult, and secondly the position at which maximum signal is first reached shifts to earlier

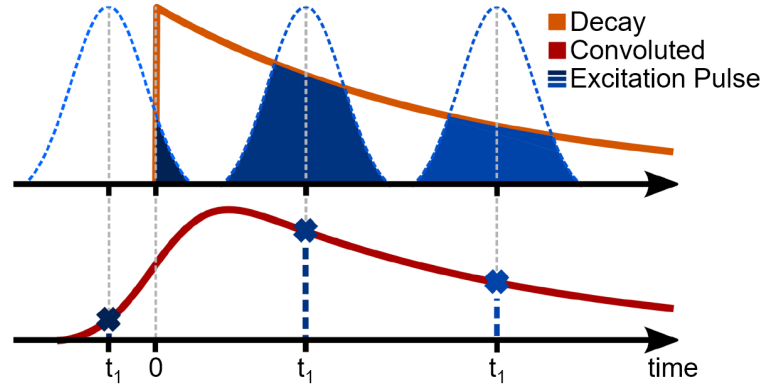


Figure 2.5: The observed decay (red) once an exponential decay (orange) is convolved with a Gaussian instrument response function (IRF). The shaded blue area represents the overlap integral, which is the amplitude. It is attributed to the central point of the IRF.

times. To get a practical feel of these effects Figure 2.6 presents the variation in amplitude (a) the time of reaching maximum (b) signal. These values are calculated by taking the exponential decay presented in (d) and convolving them with the IRF, Gaussian, FWHM (full-width half-maximum) of 200 fs, this gives the observed decays in (c). The decrease in the observed amplitude is most notable when the decay is contained within IRF. A time constant half the FWHM of the pulse gives a maximum amplitude that is 80 % of the non-convoluted value (Figure 2.6a). Also, the maximum amplitude of the peak is shifted by 150 fs, making it appear as if signals are growing after time zero, but the intrinsic signal appears at time-zero, and the offset is an artefact of convolution.

The convolution of the excitation IRF and decay can lead to noticeable changes in the observed data, this shows up in group velocity dispersion (GVD) of the probe, discussed in Section 2.3, and calculation of static quenching. In all cases, the most appropriate course of action is to incorporate the IRF into every model where the dynamics of similar timescale to the IRF or signal amplitude are being considered.

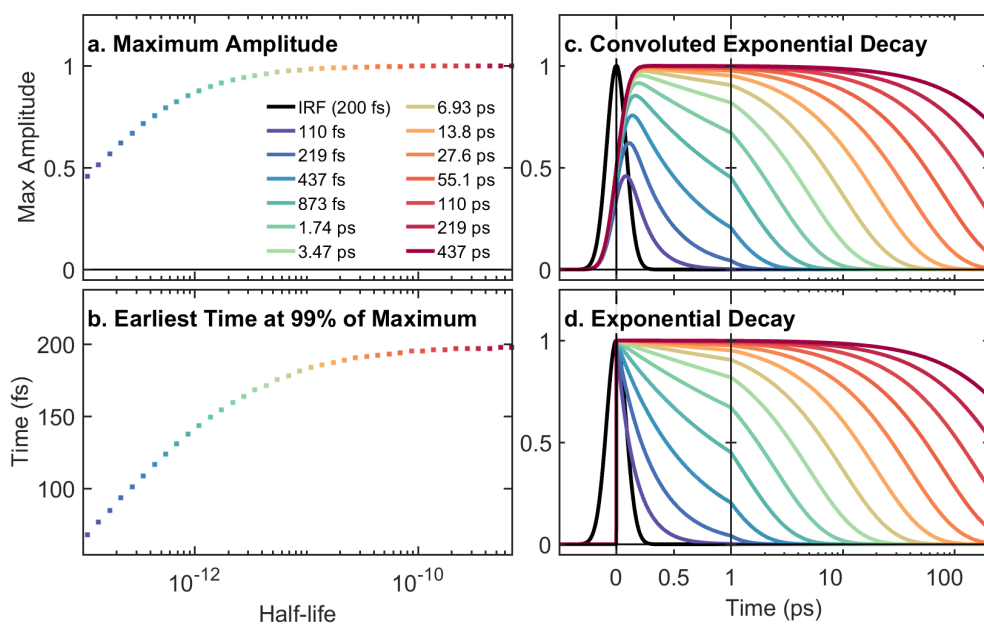


Figure 2.6: The changes to underlying dynamics that has implications to the analysis of the observed signal. (a) shows how the amplitude of the observed signal is effected when the dynamics are exponential with time constant given in the details, and an instrument–response function (IRF) given by a Gaussian with full width half maximum (FWHM) of 200 fs. Panel (b) then shows how the peak amplitude is shifted from <75 fs to 200 fs as the lifetime increases. Panels (c) and (d) present the convoluted and intrinsic exponential decays respectively.

Increasing path length delay to overlap with picosecond excitation

To gain a complete picture of excited state dynamics (from formation to decay) in organic photovoltaics, a timescale from the femtosecond to microsecond regime is necessary.^{73,205,206} The femto– nano– second dynamics are controlled by adjusting the path length of the excitation pulse. Path length changes corresponding to greater than a nanosecond is difficult with a 1 μ s delay equating to 300 m of additional pathlength. To achieve a microsecond pump–probe delay a secondary laser is introduced, this is electronically triggered allowing it to be delayed from the 10's of picoseconds to seconds. The time–resolution is again not controlled by the step–size in the electronic delay but the pulse width of 800 ps. These two data sets are then merged to give an overall picture of photophysics from initial excited state species, femtoseconds, all the way out to the decay of charge/triplet species, microsecond timescale.

In order to be confident about the merging of data from two different excitation sources (sometimes from different excitation wavelengths), a comparison of the decay in the overlapping regions is important. If there is a decay on a similar timescale to the IRF (800 ps) then the perturbation to the magnitude and decay need to be considered. The simplest method is to exclude these effects by measuring the decay with the femtosecond laser at significantly longer timescale than the IRF of the secondary excitation source, i.e much longer than 800 ps.

To increase the path length, the excitation pulses path into the delay stage was altered. Figure 2.4. The original layout is depicted in (a), the excitation beam is sent parallel to the direction the retro–reflector (R1) will be moved, this is done with the first mirror (M1). The overall change in path length is twice the change in position of R1. To double the path length, allowing for 6.6 ns in overall delay i.e a 2 m change in path length, a second bounce down the retro–reflector (R1) was added (Figure 2.4b). This was done by replacing M1 with a right–angle prism mirror (M1') which allowed input close to the central axis of the retro–reflector, mirrors M2 and M3 are then used to achieve an outer second bounce giving a total pathlength change that is four times the change in retro–reflector position.

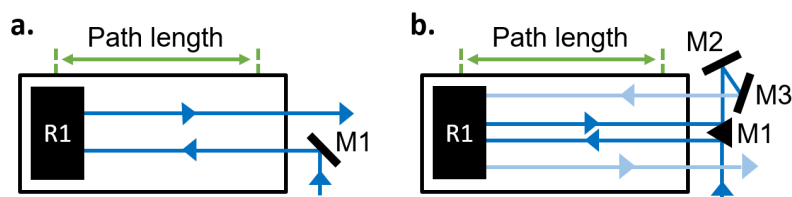


Figure 2.7: Changes made to experimental layout to double the possible change in path length from one to two meters. (a) shows the original path onto the retroreflector (R1) with a single bounce, (b) has the improved layout allowing for two bounces onto R1 and hence a doubling of the change in pathlength.

Figure 2.8 presents the data that has been collected with 532 nm excitation using pulses with an IRF approximated by a Gaussian with a FWHM of 100 fs (fs, 3 ns and fs, 6 ns) and 800 ps (ps, 100 μ s) pulse widths. The benefit of the added delay time is highlighted in blue, clearly showing that the two different excitation sources lead to the same decay dynamics (points vs solid line). The effect of convolving the decay with the IRF is also revealed with the decay dynamics only matching between fs and ps excitation after two nanoseconds. This dataset highlights variation in peak amplitude and onset time mentioned above and shows the need for collection of data points out to six nanoseconds if the dynamics are to be unambiguously correlated between those collected with 100 fs and 800 ps excitation pulses.

Group velocity dispersion

Group velocity dispersion (GVD, also referred to as chirp) is the term used to describe the temporal offset of wavelengths within a spectrally broad pulse. The offset arises because refractive index of the transparent media is wavelength dependent.^{197,201} For the wavelengths of interest, i.e. 450-1600 nm (2.8-0.8 eV), the shorter the wavelength (higher energy) the higher the refractive index. Higher refractive indices are slowed more leading to shorter wavelengths arriving earlier than longer wavelengths, i.e the barrel rolling principle.

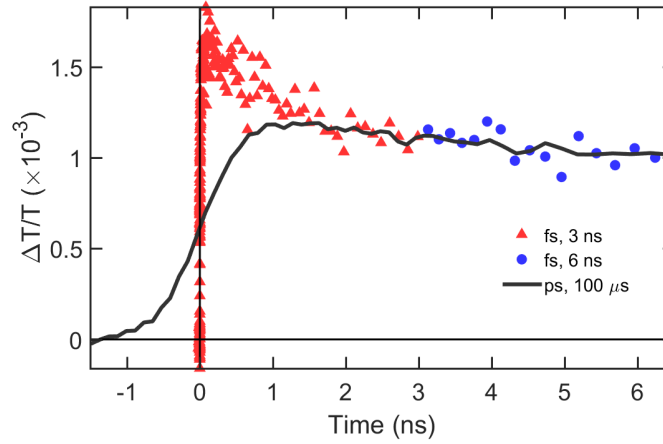


Figure 2.8: Kinetic trace of the data collected from two different excitation sources of a polymer:fullerene blend, the black solid line is following the electronically triggered excitation laser while markers (triangles, and circles) show the kinetics from changing the pathlength of a femtosecond excitation laser. The red represents data possible with only a single bounce, whereby the blue datapoints is the extension with the additional delay.

Figure 2.9 showing TA dataset before (A) and after correction for GVD (B). The onset of signal (blue/red) is seen to vary with wavelength, shorter wavelengths arrive before the longer wavelengths. The correction of GVD is generally broken down into two parts. First, the minimisation of the transparent media before the sample and thus minimise the GVD seen in the experiment. By removing the transparent media has the added advantage of reducing the number of time points collected as once passed the onset time the spacing of time points becomes exponential while during it is linear. The remaining GVD can be corrected by applying offset at each wavelength giving the dataset seen in Figure 2.9 (B), how these wavelength dependent offsets are generated is discussed below.

Determination of the time wavelength dependent offsets can be done via a separate measurement relying on non-linear effects, either sum frequency generation²¹⁷ or optical Kerr effect.²²⁰ It can also be estimated by the signal onset in the measured dataset.²²¹ Each method has its trade-offs; the optical Kerr effect involves adding additional optics to the probe path which introduces GVD. Us-

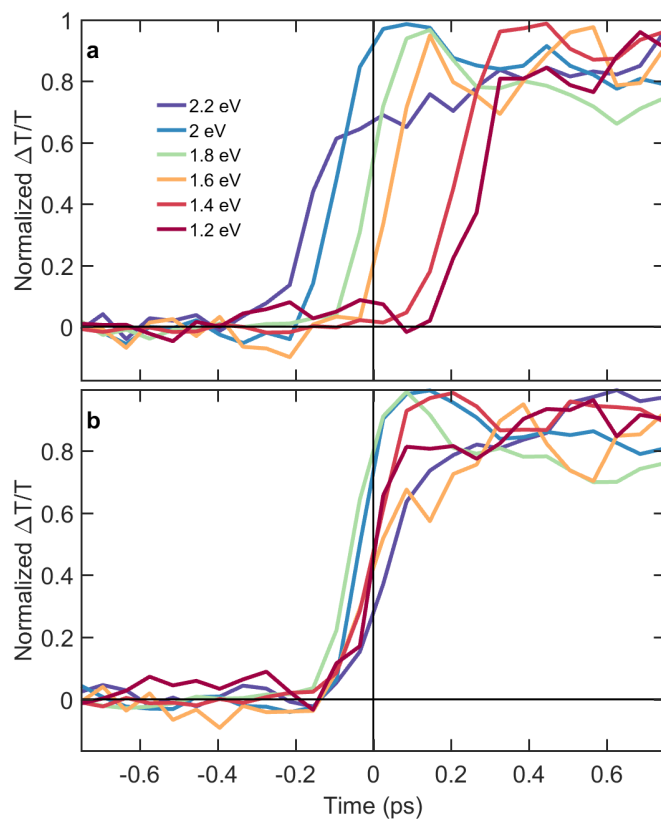


Figure 2.9: Kinetic traces taken at photon energy presented in the details. (a) is before chirp correction with the apparent onset time being earlier at higher energy, (b) shows the data after chirp correction with all onset times centered around zero.

ing signal onset relies on a well-defined signal onset that does not coincide with growth or decay or the IRF timescale.

For the TA data discussed in this work, the GVD is approximated by the signal onset. Due to the presence of dynamics on the <200 fs timescale in OPVs it is essential to consider the shift in the apparent onset for signals that are convolved with the IRF.^{186,197,205,222,223} Ideally, the IRF and wavelength dependent time-offsets would be included in the model used to describe the data (Some common models are described in Section 2.4). If an explicit model is not being used, or a model in which it is difficult to include wavelength dependent time-offsets, the GVD can be estimated and the data corrected for these offsets. The method used is a multi-exponential fit in an over-parametrised manner as the aim is to describe the data thoroughly. The extracted wavelength dependent onset time can be fit to GVD induced by the various transparent materials, refining the over-parametrised system. Figure 2.10 presents the results of this procedure. In panel (a) the fitted onset time are shown by grey dots, the darker grey corresponds to a higher signal-to-noise ratio. This signal-to-noise is used to weight the subsequent fit of the GVD, allowing for small signals or poor fitting to be ignored, i.e the onsets will fit when there is a very low signal, 480-540 nm (2.6-2.3 eV). The green represents the extracted GVD offsets, presented clearly in panel b, and fits well with the perceived signal onset (red and blue regions) at each wavelength. Finally (c) shows the residuals following the multi-exponential fits, these show the data is well described and lends confidence to the onset time area accurately estimated.

2.3.1 Beam profiler and collimation

When changing the path length of the excitation pulse by meters it is important to consider the variation in the pulse width at the sample. A change in spot size directly effects the decay signal, as variation in spot size change the excitation fluence and thus the observed signal. The magnitudes of the signal changes are related to the square-root of the spot diameter; this leads to small changes in

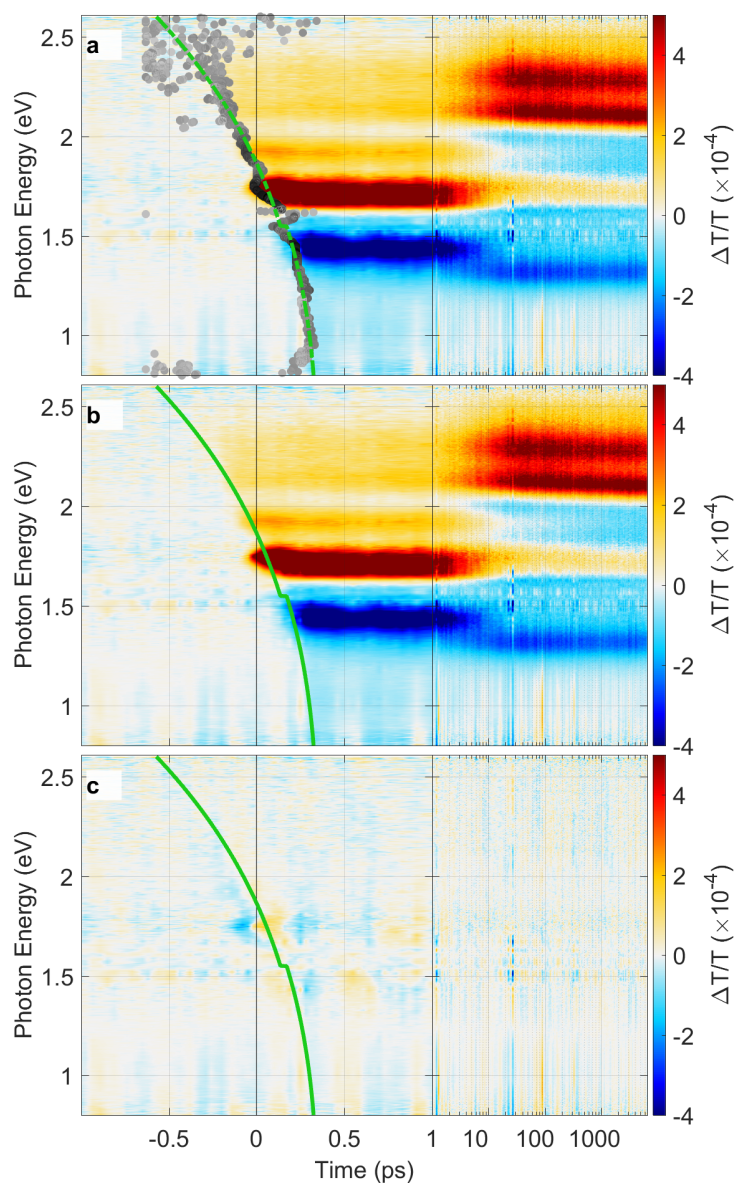


Figure 2.10: Details of the chirp correction procedure, all TA surfaces are presented with the -1 to 1 ps region taking up the majority of the surface, and the 1 to 6 ns region shown for full clarity. Panel (a) presents the estimated onsets at each wavelength, grey circles, and the fitted chirp curve (green dotted line). Panel (b) presents the same data as in (a) except the onset times are removed for clarity. Finally (c) is the residuals of the multi-exponential fit, retaining the chirp curve in green.

spot size having a large effect on the observed decay dynamics. Correcting for these changes is only trivial when the signal has a linear response to excitation power. This is because at every time–point the initial population is different, due to the changing spot size, therefore the non–linear power dependent correction must be calculated at each time–point assuming an underlying model. Because these higher order dynamics can be expected when measuring OPV materials, i.e. bimolecular charge recombination, it is important to minimise the beam divergence at the sample before measurements are taken.^{178,224}

In order to understand and minimise the deviation in spot size the pulse cannot be treated as a simple ray, where it is possible to think of it as being perfectly collimated. Instead, using the Gaussian beam propagation treatment accounts for the observed deviation even when ideally collimated. When considering a Gaussian beam, the waist (w) expands as it propagates through free space as given by Equations 2.9.^{225,226} Where w_0 is the minimum (or focused) beam waist and z_R referred to as the Rayleigh length is given by the wavelength (λ) of the pulse.

$$w(z) = w_0 \sqrt{1 + \frac{z^2}{z_R^2}} \quad (2.9)$$

$$z_R = \frac{\pi w_0^2}{\lambda}$$

In practical terms we want the minimum deviation of the beam to be at the sample, this corresponds to moving the minimum beam waist. This can be done as depicted in Figure 2.11a where a single lens ($L1^*$) is used to image the beam waist at its original position (w_0) to the sample (w'_0). To achieve this imaging the focal length of $L1^*$ is set with respect to its distance from the beam waist (z) to $L1^*$ and the distance from $L1^*$ to the sample (z'). Experimental determination of z can prove difficult and could change when tuning the excitation wavelength as the non–linear process required to generate different excitation wavelengths

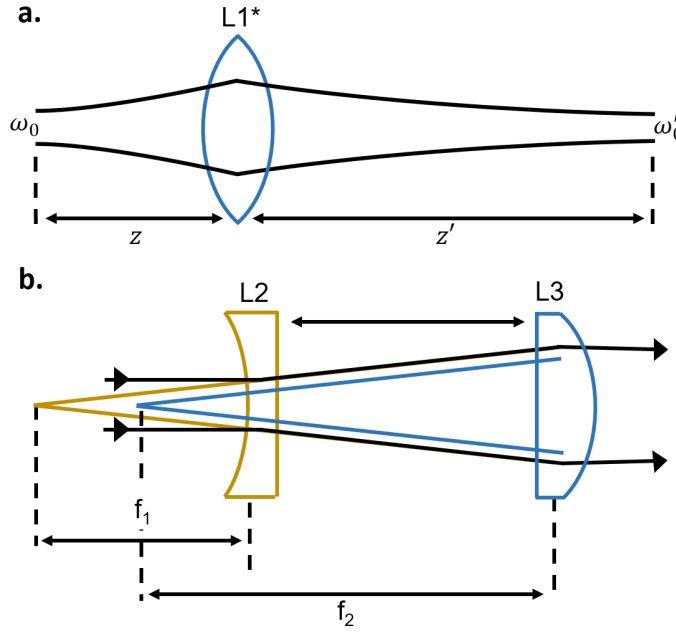


Figure 2.11: Addition of a lens (L1*) shifts the position of the beam waist from z to z' while adjusting the diameter from ω_0 to ω'_0 (a). The focal length of this lens (L1*) can be adjusted by using two lenses as shown in (b), L2 and L3, while adjusting the distance between them (d).

vary. To overcome this problem a pair of lenses is used (arrangement is same as Galilean beam expander), a convex (L2) and concave (L3) with the distance between them (d) being adjustable (Figure 2.11b). With this arrangement, the effective focal length of the lens pair is given by Equation 2.10 This distance can be set with a translation stage on a micrometer while monitoring the beam waist at the sample so the actual determination of the focal length is not necessary. This procedure also allows for the compensation of any other lens along the excitation pulse path, in theory allowing for the minimal divergence for the given spot size.

$$\frac{1}{f} = \frac{1}{f_1} + \frac{1}{f_2} - \frac{d}{f_1 f_2} \quad (2.10)$$

Before a routine could be implemented to minimise the deviation, the pulse diameter needed to be measured. This was achieved implementing custom collection software (via LABVIEW) to work with a CMOS (complementary metal–oxide–semiconductor) sensor in the sample plane to collect the spot size and position at various points along the delay stage. Figure 2.12a shows the extracted spot width from fitting the excitation pulse at various points along the delay stage, the blue and red represent the two orthogonal axes of the 2-D Gaussian fit. The change in spot width as a function of delay position is fitted to the Gaussian beam propagation Equation 2.9, with w_0 , and z_R as free parameters. This fitted curve, shown as the solid line, is used to calculate the spot area. Additionally, Figure 2.12b shows the measured spot position as a function of path length the deviation is within error of the measurement. By measuring the excitation pulse spatial position and width at the sample position, we can confidently determine the change in excitation density as a function of excitation–probe delay time.

While monitoring the excitation spot, optimisation of L3 (Figure 2.11) position can be done to move the minimum deviation point to the sample with the delay stage at its centre point. The minimum deviation point is determined by an iterative process; the beam size at one end of the delay stage is measured and then after moving the stage to the opposite end the position of L3 is adjusted until the spot sizes match. Figure 2.13 presents the normalised spot area before the addition of the two lenses (grey) and after (green). The addition of the lens to image the minimum beam waist leads to a dramatic reduction in the change in area from 60 % without the lens to <2 % once the position of L3 is optimised (the centre of the delay stage corresponds to 3 ns, note the logarithmic time axis).

2.3.2 Visible to near-infrared spectra range

Due to the broad nature of signals observed in TA spectroscopy, it is beneficial to probe the sample over a wide spectral range. The larger the spectral range, the higher the likelihood that it will be possible to separate dynamics or spectra, and thus gain maximum insight into the fate of the light absorbed by OPVs.¹⁹⁹

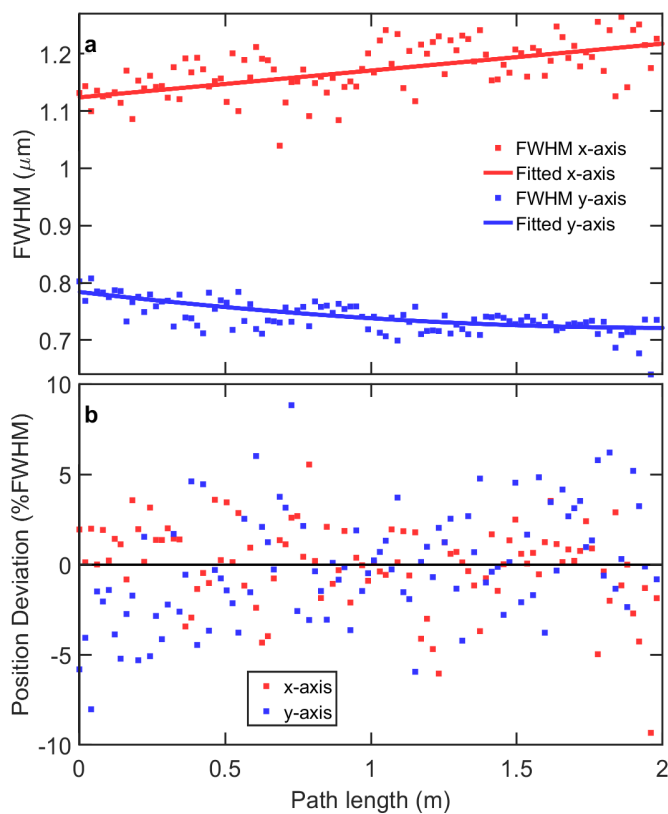


Figure 2.12: Calculated full-width half maximum (FWHM) (a) and change in central position (b). Red and blue are used to denote the orthogonal spatial components, labelled x-axis and y-axis for clarity. The solid line represents the best fit when using a Gaussian beam propagation equation.

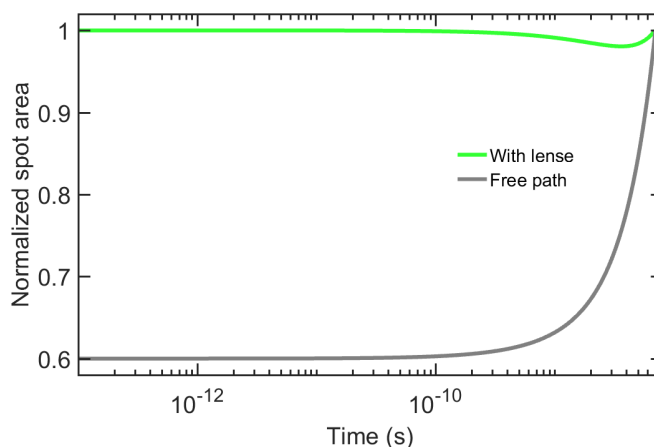


Figure 2.13: Comparison of the change in spot area before (free path) and after (with lens) the addition of collimating optics.

In the case of organic photovoltaics it is known that the GSB will be in the visible to near-infrared region, as this is optimum for conversion of solar energy to electricity.^{18,227–229} The ability to monitor the GSB gives us a proxy for the excited state population as any species in the excited state leads to bleaching of the ground state absorption. To follow the interconversion of species, i.e. exciton to charges (or triplets), the probe window needs to expand further into the near-infrared region. Hence we need a probe that covers the visible to near-infrared regions to be able to track excited state population and interconversion between species found in polymer OPVs.

A super-continuum spanning approximately 450–1550 nm (2.8–0.8 eV) was generated following the reported procedure.²¹⁵ Specifically; the laser fundamental, 800 nm (1.55 eV), was brought to a focus just in front of a four millimetre thick YAG crystal. Extending down to 1550 nm (0.80 eV) is almost ideal for OPVs, with only the initial singlet PIA signal being difficult to distinguish from charge transfer states. After generating a broad super-continuum the next step, arguably more difficult, is to measure the light intensity across the visible into the near-IR. This was achieved by using two line-scan detectors, a Si-based for the visible, 400–1000 nm (3.1–1.2 eV), and InGaAs for the near-infrared region, 800–1600 nm

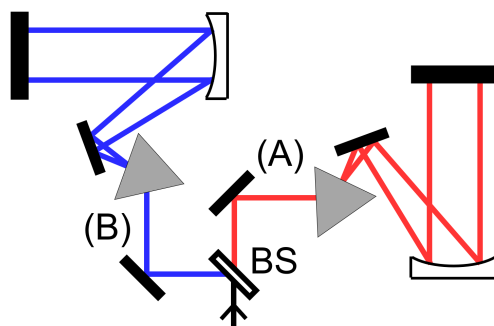


Figure 2.14: Simplified layout of a the dual spectromter used to separate the near-infrared and visible portions of light. BS is the beam-splitter with the two paths (A) and (B) being similar except for the prism materials. Fused silica for the visible (A) and BK7 for the near-infrared (B).

(1.6-0.8 eV). By using two detectors to simultaneously measure the probe pulse we reduce time-dependent error, i.e. laser fluctuation, and sample degradation, and it is more time-efficient.^{197,230,231}

An illustration of the dual spectrometer layout is presented in Figure 2.14, the input beam is split by a dielectric mirror with the transition wavelength at 800 nm with each arm going into a prism spectrometer. For the visible arm, fused silica is used for the prism material, while for the near-infrared arm BK7 is used. Each dispersed beam is then focused onto a photo-detector (Panavision ELIS-1024 for visible, and Hamamatsu G11608 for the near-infrared). A prism was chosen as the dispersive element to increase throughput as a grating would not be highly efficient across a broad wavelength range.¹⁹⁷ The dielectric mirror transition region was selected to balance the high photon intensity generated in proximity to the laser fundamental wavelength, 800 nm (1.55 eV), this allowed for a roll-off in intensity around the 700-900 nm (1.8-1.4 eV) region making it possible to collect from 450-900 nm (2.8-1.4 eV) on the visible detector.

Figure 2.15 presents normalised spectra collected from each detector (the visible shown in red and blue for the near-infrared). The visible has a relatively flat profile with a sharp peak at 800 nm (1.55 eV) that corresponds with the fundamental wavelength used to generate the white light continuum. The roll off in

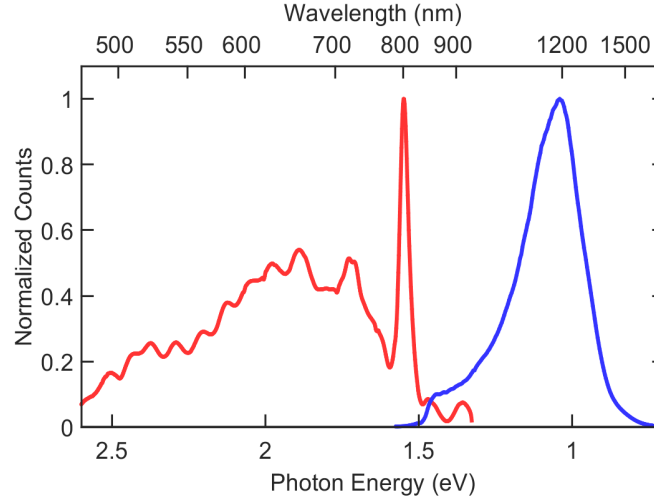


Figure 2.15: Normalised spectra for the white light supercontinuum collected by two spectrometers. Red represents the visible portion collected with a fused silica prism on a CMOS sensor. Blue is the near-infrared portion, using a BK7 prism and InGaAs photo-diode array.

intensity caused by the dielectric mirror is also seen with the intensity decreasing in the 700-900 nm (1.8-1.4 eV) rather than the expected increase as we near 800 nm (1.55 eV), the fundamental frequency of the laser used.²¹² The peak at 800 nm (1.55 eV) is the residual fundamental. The near-infrared presents a maximum at 1200 nm (1.03 eV) while a 830 nm (1.49 eV) long pass filter has been used to block out any residual 800 nm fundamental light.

Once collected, the data is treated as two separate measurements because the cameras are not synchronised. The data is collected simultaneously, but because the cameras are not synchronised with each other, there is usually a 20–30 shot (6–10 μ s) offset between the cameras. While the few shot offset is not ideal, we still benefit from reduced collection time, avoiding long-term laser instability, and minimising sample degradation. As the cameras are not synchronised the $\Delta T/T$ signal is computed independently for each camera and then combined to give a final TA surface. A comparison of the signal from each camera and the final combined spectra are shown in Figure 2.16a. The combined spectra (grey,

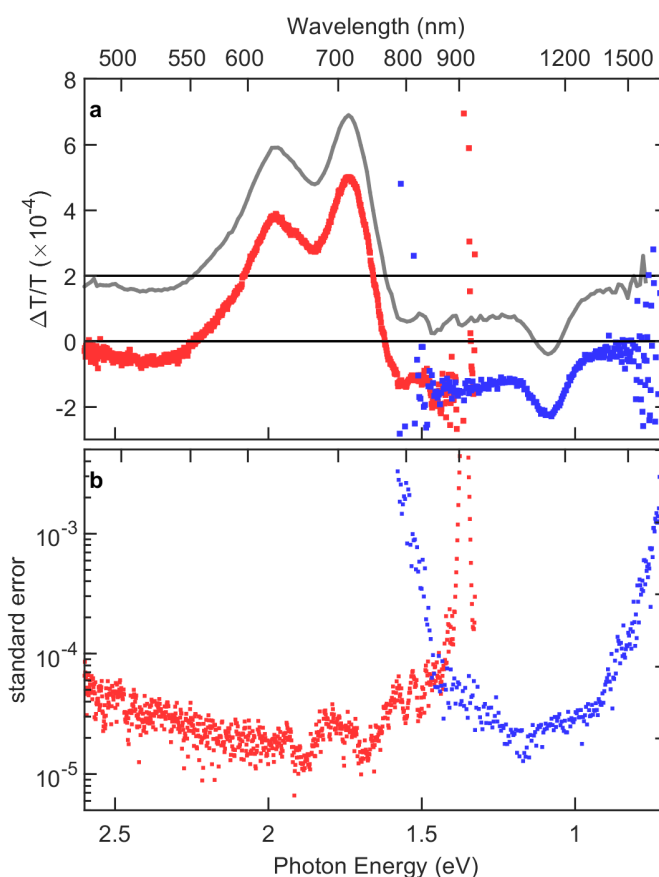


Figure 2.16: Combining the TA signal collected on the visible (red) and near-infrared (blue) spectrometer. Panel (a) shows both the raw calculated signal, blue and red, with the combined signal shown in grey (with a 0.2 $\Delta T/T$ offset). Panel (b) has the calculated standard error for both cameras, this is used to weight the contributions from each camera to the overall signal.

offset from zero) is produced by a weighted average of the two cameras whereby the weights are calculated from the standard error of the signal, shown in panel (b). The region of overlap between the two cameras, 800-900 nm (1.6-1.4 eV), shows no noticeable difference in spectral shapes, with the standard-error also overlapping in this region. The final spectra have no signs of artefacts with a smooth transition across where the cameras overlap and only a slight increased in noise at 800-900 nm (1.6-1.4 eV).

We successfully implemented a simultaneous dual-spectrometer to cover the visible to near-infrared regions, in order to visualise the photophysics of OPV devices. This included the extension of the time-range to smoothly cover 100's of femto- to micro- seconds with a spectral window of 450-1600 nm (2.8-0.8 eV). This has allowed for excited state species interconversion to be tracked from initial excitation to their return to the ground state.

2.3.3 Optimised data collection

To achieve conditions consistent with real-world device operation excitation densities need to be minimised. Hence a low signal strength is observed, less than $10^{-3}\Delta OD$, requiring measurements with a low noise floor. While the noise floor can always be decreased by increasing collection time, because a typical measurement required thirty minutes it would mean that to half the measured noise floor that two hours would be necessary. Increasing collection time is also impractical due to instability of the laser that can have a dramatic effect on the non-linear processes. This leads to a increase in the noise level the longer a measurement runs. Instead, to reduce the noise level two aspects of the TA system were improved, white-light generation, and acquisition time.

Significant effort went into optimising and aligning the white-light generation; this lead to large reduction in the noise floor. Figure 2.17 presents the noise level for different probe sources as a function of the number of shots collected. In all cases, a non-linear decrease in signal-to-noise is observed with increasing number of collected shots. A YAG crystal (this work) shows a 4.4 times improvement when compared to the noncollinear optical parametric amplifier (NOPA) and a 60 times improvement when compared to a sapphire crystal. These comparisons are made to set-ups present in our lab, and not to benchmark literature results. The improvements in noise directly relate to a decrease in time taken for the same noise level, i.e. with these improvements it is now possible to get the same noise level with in one-twentieth of the time.

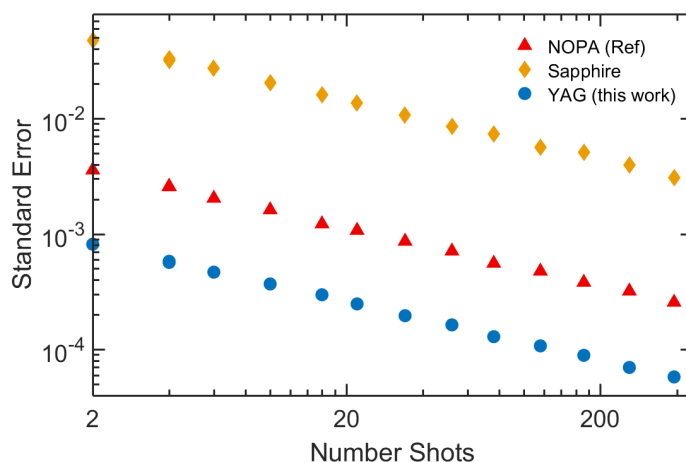


Figure 2.17: Comparison of the noise in each TA spectra as a function of shots collected. Various light sources are presented, details as shown.

The data collection LABVIEW code was also optimised to decrease the down time, thereby decreasing the time taken to collect the same number of shots. These optimisations typically reduced the measurement time by 50 %. The reduction was achieved in two areas; first, and most importantly, the data-processing software pathway was improved accounting for more than half of the gains. Secondly, the delay-stage routine was adjusted so the accuracy was relative to the time offset, this reduced the stage waiting time significantly as high accuracy (10 fs) is only needed for a few time points.

2.3.4 Summary

In this section, we have presented an implementation of a transient absorption spectrometer optimised to measure the photophysics of organic photovoltaics (OPVs). It has a broad spectral range spanning the visible to near-infrared and can identify the majority of species expected in an organic photovoltaic device. A time range of 100's of femtosecond to microseconds allows us to track the absorbed photon energy from initial exciton until the longest-lived charges decay. This required the introduction of a secondary sub-nanosecond laser and the ex-

tension of the mechanical delay from 3 to 6 ns, along with the implementation of collimating and optimising routine to minimise spot size changes. Finally, the noise floor and acquisition time have been significantly reduced allowing for low-fluence measurements to be routinely taken, this involved the painstaking optimisation of the white-light super-continuum and re-coding of a significant portion of the acquisition software. The outputs of this experimental set-up is displayed in the following three chapters that contain transient absorption (TA) data exclusively collected with this system.

2.4 Data Modelling and interpretation

Transient absorption (TA) spectroscopy generates a two-dimensional dataset recording the change in absorption ($\Delta T/T$), i.e. spectra at various excitation probe delay times. The data interpretation is non-trivial by nature, this is because TA data is multi-dimensional, has overlapping spectral features, and can have both negative and positive signals.^{200,202} The simplest method to analyse the data is by taking 1-D slices along either the spectral or time axis to compare spectra or decay dynamics at different wavelengths respectively. However, the end goal is to unambiguously compare the species and rates/lifetimes present across a number of measured systems. And towards that aim, various methods for data analysis are discussed below. The aim of the analysis is to reduce the dataset into some underlying spectra, dynamics, or lifetimes that are representative of the photophysics being studied.²³² There are two broad categories of models hard (parametrised) and soft (non-parametrised) both will be briefly presented later in this section.^{200,202,232,233}

Before we move onto the specific details, it is essential to clarify what is meant by a dataset for the following discussion. A single TA measurement is collected using a sample at one excitation wavelength and fluence, and consists of a collection of $\Delta T/T$ spectra at various excitation–probe delay times. A dataset, on the other hand, might include a combination of multiple TA measurements.

When looking at multiple experiments with common spectra or dynamics it is useful first to concatenate (put two or more data side-by-side to make one larger dataset) the measurements if they have a common wavelength or time axis. In this way either the spectra or dynamics can be constrained across a series of measurements, i.e. variation in excitation densities, excitation wavelengths, or blend morphologies allowing for the opposite to be compared.^{200,232} By concatenating multiple measurements we decrease the number of free parameters when compared to modelling each measurement individually. This process of combining data can be considered the same as global analysis but instead of one measurement being considered multiple measurements are globally fit with the same parameters. The influence of artifacts on dynamics and spectra can be minimised by concatenating an artifact only measurement.²⁰⁰

While the specific method applied to understanding any individual dataset can vary, in general, we have found that taking a systematic approach yields the most consistent and easy to follow results. These process is the identification of the number of species, or components, needed to describe the data. And then a model is applied that includes a set of constraints to arrive at a physically useful description of the data.

2.4.1 Number of parameters

The first step is estimating the number of components, this done by applying singular value decomposition (SVD) to the data set. SVD is a matrix factorisation algorithm the details of which can be found elsewhere,^{234,235} in short, SVD will reduce the data into independent components along each of the dimensions. In our case SVD takes a data matrix (D) and produces spectra (V), kinetics (U), and weightings (S), as shown by Equation 2.11. To decide on the number of components we first use the weighting matrix S, in particular, the diagonal value of S which contains the relative weightings of the components of U and V. Figure 2.18a, shows the relative weightings of each component after the decomposition of the dataset. These show that there are two significant components and a third

that warrants further investigation while the remaining do not have a considerable influence on the final data. To understand if the low weighting component is significant, Figure 2.18b shows the weighting on a log-linear scale. This reveals that components 3–6 gradually decrease in weighting before another stepped decrease between component six and seven. The small weighting could be because the spectral component is representative of a spectral shift, therefore it represents only a small change in magnitude. Another cause for low weighting is low signal strength, either a minor product of branching or a weaker photo-induced absorption cross-section. A third possibility is that these components could be unrelated to the measured system, they could be non-linear artefacts,²¹⁷ or correlated noise sources that are common in femtosecond white light sources.^{200,236}

$$D = U \cdot S \cdot V^T \quad (2.11)$$

To diagnose the possible importance of a third through to sixth component the contributions to the overall data are presented in Figure 2.19. This figure appears complicated, and so the description is broken down into the rows; Spectra (V), Kinetics (U), Single, Additive, and Residual; and then each column corresponds to a component. The kinetics are normalised, and the single and additive surfaces have the same colour scale, while the residuals are presented at one-tenth of the scale. The spectra (V) and kinetics (U) are the orthogonal axes of the dataset, and thus the kinetics shows how the spectra components change with excitation-probe delay. The next two columns, single and additive, describe the data generated by multiplying the spectra and kinetics together giving a surface. In the case of "Single" it is just the multiplication of the n th spectra and kinetics, so it shows the contribution of that particular component; while the "Additive" row is the contribution from the first to the n th component/s. Finally, the residuals give a clear picture of how much of the data has been accounted for when including the first to n th components. By breaking down the data in this way it becomes clear if there are any time and spectral correlated features in the data. The "Single" row makes clear the origin of the weightings (S) with the total con-

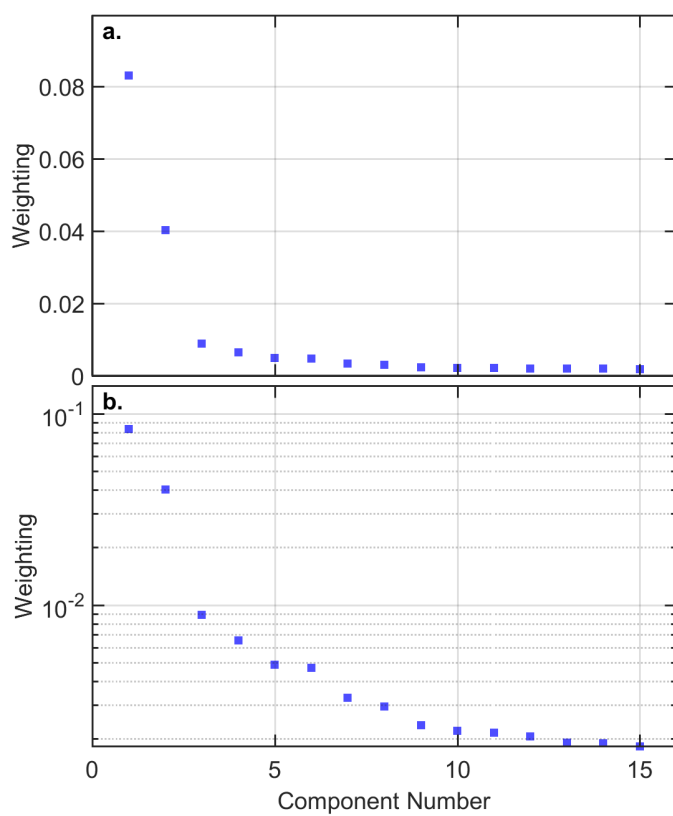


Figure 2.18: The weightings of each orthogonal component as calculated via the SVD algorithm, (a) and (b) differ by the log-scale presentation used in panel (b).

tribution to the surface reducing significantly for the third (4.5×10^{-4}) to the sixth (3×10^{-5}) component. There is structure across all the spectra (a–f) indicating that in all cases there are correlated components along the spectral axis. We can only guess if these are from species, noise, or measurement artefacts, but if we consider the kinetics their assignments become much clearer. The kinetics show that Components 1, 2, and 4 are due to time-dependent changes in the sample, components 3 and 5 represent white light noise, and component 6 is likely to be a coherent artefact. The assignment of component 1, 2, and 4 to sample induced effects is because of the relatively smooth variation with time, indicating the growth and then decay of some species. The random variation centred around zero in component 3 and 4 indicates that they are from noise sources, as they are not time-dependent but rather appears to be randomly distributed along the time axis. Finally, component six has a sharp peak in the dynamics centred at time-zero while the spectral features show a sharp transition at the excitation wavelength, 712 nm (1.74 eV), consistent with a coherent artefact.²¹⁷ Following a detailed inspection of the SVD results, three important contributions have been identified, one which has low significance but is still above the noise floor. And a measurement artifact is identified allowing it to be removed or modelled.

2.4.2 Applying a model

For time-resolved spectroscopic data, the data matrix (D) can be broken down into two components; spectra (S) and concentrations (C), as shown by Equation 2.12.²⁰² The methods used to determine these two components fall into two general categories; hard- and soft-modelling.^{200,202–204,222,237–239} In hard models, the reduction occurs by breaking down the matrix into equations and parameters usually with a basis in real-world phenomena. A soft model breaks the data matrix using a non-parametrized decomposition.

$$D = C \cdot S \quad (2.12)$$

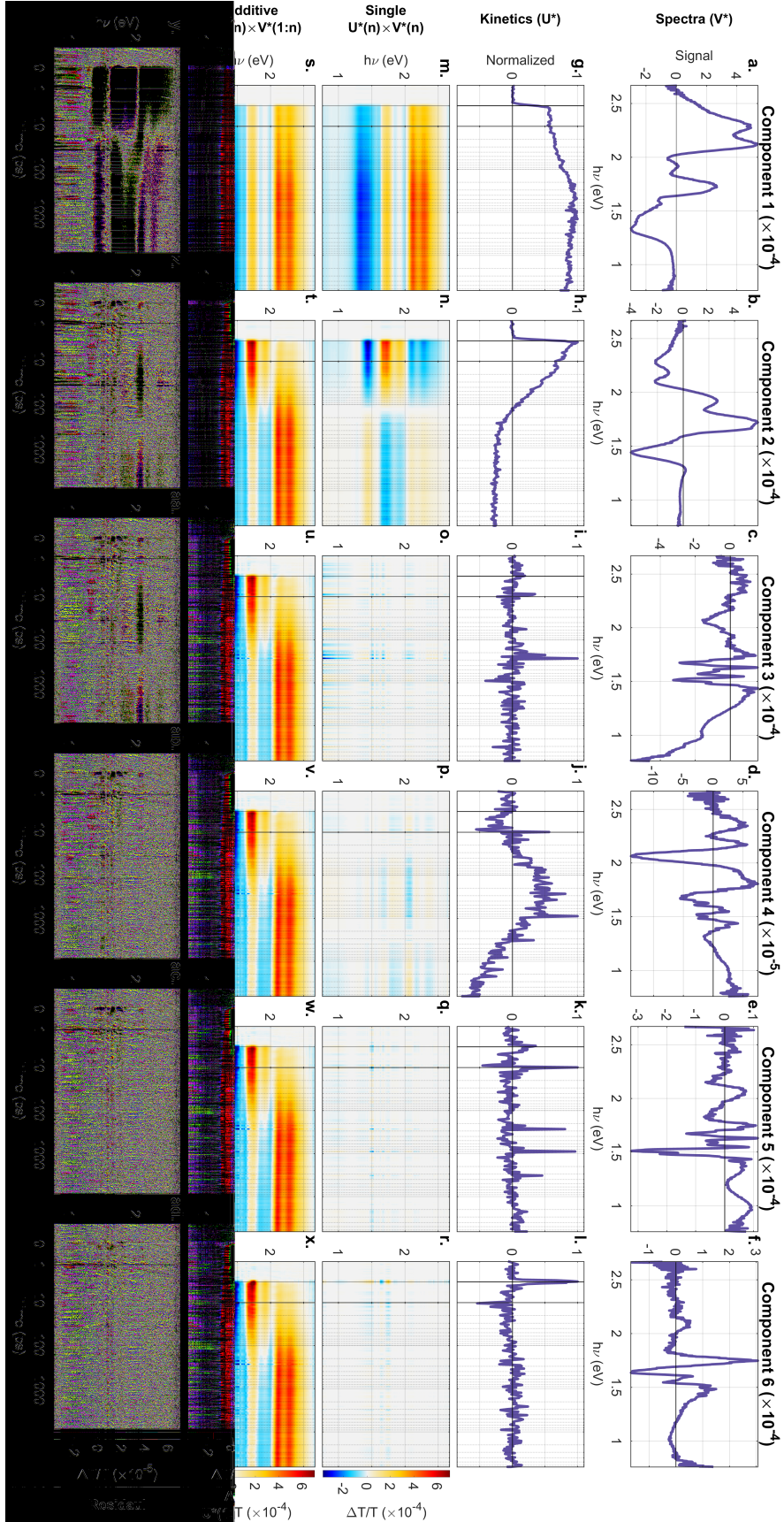


Figure 2.19: The first six components from a SVD decomposition of a TA surface, FTAZ:IDIC, 712 nm (1.74 eV) 0.26 $\mu\text{J cm}^{-2}$. The columns, are the components decreasing in weighting from left to right. And the rows present various details about each component and how they are combined to give the final TA surface. Spectra(V^*) is a combination of the weighting and normalisation scalars. The normalisation scalar is that which gives generate Kinetics (U^*). Single and Additive surfaces represent only the single component or the addition of all previous components respectively. Finally the Residuals are presented, this is the difference between the additive surface and the measured TA surface.

It is important to be considerate of the infinite solution space possible when trying to model 2-D data, i.e. there are multiple decompositions of a 2-D matrix that provide a mathematically identical description but have different spectral and kinetic components.²⁰² This is because of rotational ambiguity as described by Equation 2.13. The identity matrix (I) can be inserted between C and S without changing the experimental data (D). I can then be broken into two rotational matrices, R and its inverse R^T , these are then combined with the original spectra and kinetics to give a new set of spectra $[C \cdot R]$ and corresponding kinetics $[R^T \cdot S]$.

$$\begin{aligned}
 D &= C \cdot S \\
 &= C \cdot I \cdot S \\
 &= C \cdot [R \cdot R^T] \cdot S \\
 &= [C \cdot R] \cdot [R^T \cdot S]
 \end{aligned}
 \tag{2.13}$$

This rotational ambiguity must be considered when exploring the species and their decay dynamics. In order to constrain these ambiguities additional constraints need to be applied. These constraints can be physical, similar to those used for Multivariate Curve Resolution–Alternating Least Squares,²³⁸ or spectra from fragment compounds such as the TA spectra from a moiety that is shown to be comprised of a single species. If a hard model is being used much of this ambiguity is minimised by the equations applied especially if both spectra and kinetics are determined by equations.

Hard modelling

In the case of hard models equations can be used to predict either the spectra or concentration profile; with linear combinations of these giving the other components. If we consider exponential decays common in kinetic models, Equation 2.14 will describe the data ($D(\lambda, t)$). The data will have exponential decay of species ($e^{-k_1 t} + e^{-k_2 t} + \dots + e^{-k_n t}$) with spectral weighting ($A_1(\lambda), A_2(\lambda), \dots, A_n(\lambda)$) that can be extracted by least squares fitting. The decay described by Equation

2.14 can be expanded on by defining how the decay between species are represented. Below are equations that show a sequential model (2.15), simultaneous decay (2.16) or a mixture (2.17). The mixture contains an initial excitation into both state 1 and 2, with a fraction α . State 1 decays to state 2, and state 2 decays to state 3 (the ground state).²⁰² These additional parameters mean the solution space is still large due to the problem of rotational ambiguities as discussed previously.

$$D(\lambda, t) = A_1(\lambda)e^{-k_1 t} + A_2(\lambda)e^{-k_2 t} + \dots + A_n(\lambda)e^{-k_n t} \quad (2.14)$$



Soft modelling

Soft models do not apply equations to the data but instead, use constraints to extract the photophysics. The constraints for the dynamics can include: having only decays, unity yield, non-negative, and unimodality. Spectral constraints can include: limiting regions to be zero, negative or positive; or using spectra collected from other measurements, e.g. TA on the neat donor, steady-state absorption or photoluminescence. In photoluminescence, a wavelength-dependent intensity correction must be made due to the different Einstein coefficients for stimulated and spontaneous emissions.^{240–242} These constraints can apply to the

kinetic or spectral profile by applying the constraints in an alternating manner, in this way, the best fit will also be consistent with any constraints.

Multivariate Curve Resolution–Alternating Least Squares (MCR–ALS) applies physical constraints to the spectra matrix, or to the kinetics matrix.²⁴³ The algorithm performs a least–squares fitting to the data matrix with some estimated spectra matrix to generate kinetic traces. It then applies the constraints to the kinetic matrix and least–squares fits the data matrix again to generate a new spectra matrix. This process repeats until the change in the goodness of fit is below a threshold. The result is a set of spectra and kinetics that describes the data while being consistent with the physical constraints applied.

2.4.3 Conclusion

Once the TA data is collected it becomes important to interpret the data in a consistent manner. This necessitates an overview of how the modelling can be constrained and the validity of the results, this is highlighted by the rotational ambiguities present in any high dimensionality data. In this manner, additional information must be used to constrain the model. In the results presented in this work, soft–modelling techniques are generally used. This is because comparisons between materials provide insights into how the photophysics differ in OPVs, therefore the extraction of specific lifetimes is not necessary as comparisons between measured samples provide ample insight. As this is the case considerable thought needs to go towards understanding and accurately describing the TA data set with a set of spectra and kinetics that can be attributed to underlying processes or species present in OPVs. This is achieved by taking a systematic approach whereby SVD is used to determine the number of components and then spectral masks are used to separate the exciton from the charge species, while the long–lived spectral component is used to identify the final charge species.

Chapter 3

Systematic investigation of how fullerene effects the performance of fullerene:PTB7–Th organic solar cells

In this chapter, the photophysics of PTB7–Th blended with fullerene derivatives is investigated. The blends studied in this chapter are part of the well-studied polymer:fullerene variety of bulk–heterojunction (BHJ) cells. Due to the complex nature of BHJ organic photovoltaic (OPV), multiple techniques are used to thoroughly characterise the device and provide a conclusive understanding of the changes in power conversion efficiency (PCE). Transient absorption spectroscopy measures the photophysics of the device, and advanced scattering and electrical characterisation define the morphology and device physics, respectively. This work is focused on photophysics; therefore, we discuss transient absorption and steady-state optical measurements in detail; the other results will be briefly summarised. Two systems are investigated: the first is the effect of varying PC₇₁BM wt% in a PTB7–Th:PC₇₁BM blend. We find that it is possible to

tune the morphology, with 60 wt% providing a balance between the three-phases deemed necessary for efficient OPVs. In the second system, we aim to understand how modification of the fullerene acceptor affects morphology and photophysics; PTB7-Th is blended with PC₆₁BM, PC₇₁BM, and ICBA. The increased absorption of PC₇₁BM makes it the best performer, while the higher open-circuit voltage (V_{oc}) of ICBA balances the decreased charge generation from the ICBA phase giving similar performance to the PC₆₁BM blend.

Professor Chris McNeill and his team provided the active layers of the device for transient absorption characterisation; they also measured and analysed the electrical and morphological characteristics.

The data presented in this chapter has been published in:

- Huang, W.; et al. Impact of Fullerene Mixing Behavior on the Microstructure, Photophysics, and Device Performance of Polymer/Fullerene Solar Cells. *ACS Appl. Mater. Interfaces* **2016**, 8, 29608–29618.
- Huang, W.; et al. Influence of Fullerene Acceptor on the Performance, Microstructure, and Photophysics of Low Bandgap Polymer Solar Cells. *Adv. Energy Mater* **2017**, 7, 1–10.

3.1 Introduction

This chapter focuses on the "old dog" of BHJ OPVs, looking to understand the structure-morphology-photophysics-performance relationships when optimising the fullerene component in fullerene:PTB7-Th BHJ OPVs. The BHJ-OPV systems with fullerene blended with polymer studied in this chapter provide a solid base from which to expand into polymer blended with polymer (Chapter 4) and small-molecule acceptor (SMA) blended with polymer (Chapter 5).

The area of fullerene:polymer OPV has been the bedrock of BHJ OPVs with performance gains improving from 1 % to 11 %.^{102,126,244} During this time high-

performance devices have included several different polymers, but the best performing acceptors are functionalised fullerenes; hence adapting the polymer has been the main focus in order to enhance PCE.^{31,41,99} The polymers are improved by reducing the band-gap, hence increase light absorption; or tuning the structure for improvements in charge generation and collection.^{28,31,99,245} While the most popular fullerene acceptors are still PC₆₁BM and PC₇₁BM.³¹ Even with the recent advancement of non-fullerene acceptors (discussed in Chapter 5) there is still significant interest in fullerene:polymer blends.³¹ From 2007–2013 there was rapid improvements in PCE performance from 3–11.6 %; but as of 2020 the highest performing binary polymer:fullerene blend achieved 11.7 % inline with purposed theoretical limits.^{31,86,102,111,127} The improvements in PCE are from two areas: increased light harvesting, and active layer optimisation.^{8,41,246} Of these two areas, this work is focused on active layer optimisation. Furthermore, ternary blends, i.e. ones with more than two materials in the active layer, still incorporate fullerene acceptors.^{247,248}

Of particular interest for this chapter are the morphological requirements, which are probed in Section 3.2; while a mixture of morphology and V_{oc} is investigated in Section 3.3. There have been several review articles published recently, looking into the role of morphology, how we can control it, and how it effects on the overall performance.^{4,27,31,135,249} Further to this a number of recent studies have investigated the role that annealing, additives, and side-chain modification has on overall morphology.^{31,85,250–254} A detailed study on not just the morphology changes but how these link back to the underlying photophysics is required to understand the loss mechanisms from light absorption through to collection at the electrodes. When considering efficient charge separation in the BHJ active layer, the importance of morphology and the benefits of each of three distinct phases (crystalline –polymer, –donor, and intermixed) has been recently highlighted. The requirement for three phases is exemplified by the short exciton diffusion requiring high interfacial area and the need to reduce bimolecular recombination, which is typically increased by interfacial area. In adding the third phase, both exciton quenching (diffusion) and carrier lifetimes (bimolecular re-

combination) can be improved, as the third mixed-phase increases interfacial area and acts as a buffer region, decreasing bimolecular recombination. Achieving this three-phase morphology is possible and has been well characterised in several previous studies.^{92,130,144–147,255} By taking advantage of the balance between enthalpic (phase separation), and entropic (mixing), the film morphology can be controlled by modifying the film deposition kinetics, i.e. using annealing, side-chains, additives, and solvent.^{31,130,131,256} An additional factor that needs to be taken into account is the influence of molecular orientation and how it impacts the energetic landscape energy and orbital overlap at the interfaces; having good orbital overlap is needed to allow charge-separated states to form.^{27,195,257} A favourable energetic landscape at the interface can provide a driving force that moves charges into the crystalline domain, suppressing charge recombination.^{85,249} To this end, the discussion here will highlight improvements and morphology centred around the PTB7-Th polymer that forms the basis of all the BHJ-OPV active layers studied in this chapter.

PTB7-Th is the only polymer used in the active layers studied in this chapter. As such, a summary of progress involving fullerene:PTB7-Th based BHJ OPVs is presented here, with a discussion regarding the fullerene acceptors are presented at the beginning of each section.

PTB7-Th is classed a low band-gap polymer, as it lowers the band-gap when compared to quintessential mid-bang-gap polymer, P3HT. The lowering of the absorption spectra brings it closer to the ideal 1.3 eV (946nm) band-gap of a single junction photovoltaic (PV).^{21,103} When it PTB7-Th is combined with PC₇₁BM, the combined absorption of the active layer covers much of the visible spectrum (500–750 nm), Section 3.2.2. The structure of PTB7-Th is presented in Figure 3.1, and is very similar to its forebear PTB7, which is another well-studied low-bandgap donor polymer. The noticeable structural difference between PTB7-Th (A) and PTB7 (B) is that in PTB7-Th (A) the alkoxy sidechain has been replaced by an alkylsubstituted thienyl sidegroup.

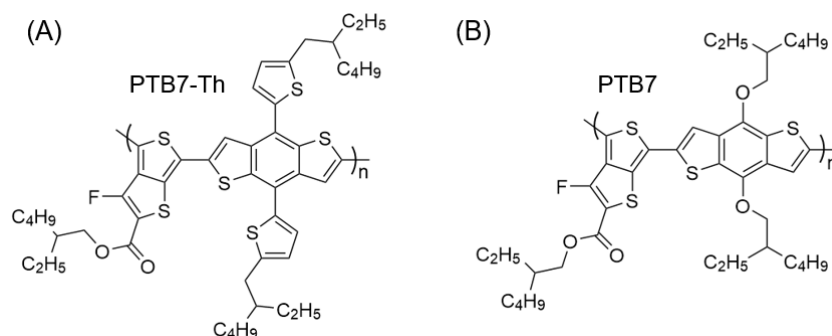


Figure 3.1: Chemical structures of PTB7-Th (A) and PTB7 (B).

The first synthesis and BHJ-OPV fabricated using PTB7-Th was reported in 2014, and achieved a PCE of 9.0 % when mixed with PC₇₁BM in a 1:1.5 ratio and spin coated from an *o*-dichlorobenzene solution containing 3 % 1,8-diiodooctane (DIO).²⁵⁸ The performance has improved slightly with morphology optimisation, as discussed below, and was 10.8 % as of 2018.²⁵¹ The effects of additives,^{250–252} annealing temperature²⁵³ and active layer thickness²⁵⁴ on the performance of PTB7-Th:PC₇₁BM solar cells has been investigated. When it comes to active layer thickness, the optimum is different for inverted and standard device architecture but should be in the 80–120 nm range, with fill factor (FF) and PCE, reduced outside of the optimum.²⁵⁴ It has been found that DIO is required to improve PCE, it works by reducing the PC₇₁BM domain sizes to 30 nm from the 100 nm observed without DIO solvent additive.^{250,253,259} The larger domains are thought to be detrimental to exciton dissociation.²⁵³ The addition of N-Methyl-2-pyrrolidone (NMP) to 1,8-diiodooctane (DIO) gives a binary additive system which was able to further increase efficiency, from 8.2 % to 10.8 %.²⁵¹ The binary additive system did not change the length scale of the domains, but crystalline domain purity was increased. With the higher purity and an increase in FF, low bimolecular recombination is thought to be the driver of improved performance.²⁵¹ Charge transport is a crucial indicator of overall PCE, one study using a binary solvent system (DIO and NMP) and another uses 1-bromo-4-nitrobenzene and both show that higher hole and electron mobilities lead to improved PCE (10.8 % and 8.9 %

respectively).^{251,252} For effective charge collection, there needs to be increased concentration of the associated material on the electrode, and a thickness that leads to carrier density peaking between both electrodes.^{250,254} The degree of crystallinity in PTB7-Th blends is low and solvent additives do not have a large impact.²⁵⁰ The interplay of interaction; i.e., thickness, domain size and charge transport, and their effect on PCE highlight the difficulty in understanding the underlying drivers for improvement. Therefore the ability to simultaneously characterise morphology, electrical and photophysics is an area of great interest.

This chapter presents the important details of morphology characterisation and performance metrics analysed by collaborators; the contribution of this author is the determination of the photophysics to complete the picture. The photophysics involves steady-state measurements of absorption and photoluminescence to determine the spectral response and exciton quenching efficiency. These are then combined with transient absorption spectroscopy, which has been specifically tailored to track the OPV signals (Chapter 2), to allow for the tracking of excitons and polarons from generation in the femtosecond regime to their eventual decay after microseconds. The results are broken down into two sections; the first investigates the effect of changing the weight percentage of PC₇₁BM when mixed with PTB7-Th. And the second changes the fullerene derivatives used to compare the effect of chemical modification by comparing PC₇₁BM, PC₆₁BM, and ICBA solar cells all blended with PTB7-Th.

3.2 Tuning fullerene and PTB7-Th performance by varying the weight fraction

To create an optimal bulk-heterojunction organic photovoltaic device, a balancing act between many factors; light capture, exciton separation, charge collection, is required. In this section, we explore what impact varying PC₇₁BM load-

ing, in PTB7–Th:PC₇₁BM blend has on photophysics, cast in the context of extensive morphological and device characterisation driven by collaboration.

In this work, we present a comprehensive study that characterises the morphology, device, and photophysics of PTB7–Th:PC₇₁BM. While other studies have investigated the blend ratios in polymer:fullerene blends, they have not extensively characterised the same polymer batch with the same preparation condition, i.e. all samples here are prepared in the same laboratory.^{148,164,260} Recently the morphology of PC₇₁BM based BHJ–OPV has been investigated in PGeBTBT:PC₇₁BM; this showed little change in domain size but higher fullerene content in the mixed–phase improved performance.²⁶¹ Also, PTB7–Th:PC₇₁BM blends have been previously studied with varying PC₇₁BM ratios. The study found that band tailing could be decreased as PC₇₁BM fraction was increased, this was found to be a trade off between V_{oc} and short–circuit current (J_{sc}) leaving to optimum performance at 65 wt%.²⁶⁰

The need for multiple advanced characterisation techniques has recently become more important with the discovery that three distinct phases contribute to the overall performance of BHJ–OPV.^{92,95,130,144–149} By combining characterisation of morphology, device physics and photophysics, we are able to provide a complete picture of the performance. We observe how the 3–phase morphology is perturbed by varying the weight percent (wt%) of PC₇₁BM and how it effects excitation absorption through charge generation (photophysics) all the way to charge transport and extraction (device physics). The material system chosen has recently achieved 10.8 % efficiency by using a low–bandgap polymer and broadening the absorption region with a lower bandgap fullerene, PC₇₁BM.²⁵¹ A recent trend in polymer:fullerene research, at the time, to push the polymer to lower band–gaps.^{262–264} PTB7–Th in particular, has received a significant amount of attention for both polymer:fullerene and polymer:polymer devices.^{113,125,250,260,264–270} The combination of low–bandgap polymer, shifting the band–edge, and complementary absorbing PC₇₁BM, filling out the absorption spectrum improves the PCE.

We find that variation in morphology plays a crucial role in performance; there are three distinct regimes each resulting in noticeable changes in photophysics. First, at less than 50 % PC₇₁BM loading, rapid prompt charge generation and rapid geminate recombination are observed, this is consistent with the lack of pure fullerene domains. Second, and the most efficient, in the 60–67 % PC₇₁BM wt% there is the right balance of the three phases (pure polymer, pure fullerene, and mixed), with pure PC₇₁BM domains formed, and some indication of mixing into PTB7-Th phase. Finally, at higher than 70 wt% PC₇₁BM, the fullerene domains are too large, and we see decreased exciton harvesting and along with disruption to the pure PTB7-Th phase. In summary, we aim to understand the interplay between morphology, photophysics, and electrical behaviour in PTB7-Th:PC₇₁BM BHJ-OPV, with the optimisation parameter being PC₇₁BM wt%.

3.2.1 Morphology and device characterisation

The morphological and electrical data collected and analysed by collaborators will be summarised briefly to provide context for understanding and interpreting the photophysics and steady-state spectroscopy. The data show that PC₇₁BM hinders polymer crystallisation and domain sizes increase with wt%. Electrical measurements reveal 67 wt% gives the highest PCE, FF, and J_{sc} , while measurement of devices shows bimolecular recombination as a possible loss mechanism.

The current vs. voltage (J-V) measurements (Table 3.1) on optimised device show that the highest PCE (67 wt%) is found by optimising FF and J_{sc} . The J_{sc} increases from 10.8 to 17.4 mA cm^{-2} when moving from 33 wt% to 50 wt% but quickly levels out reaching a max of 17.7 mA cm^{-2} with 60 wt%. The increase in J_{sc} is mostly accounted for by the increased absorption from PC₇₁BM 400–600 nm region. From 50 wt% the FF is responsible for the remainder of the gains peaking with PCE when 67 wt% is reached. Transient photovoltage measurements give an idea of charge transport and recombination at V_{oc} .^{271–274} The transient photovoltage measurements show that intensity-dependent recombination optimised around 60 wt% while trap concentration decreases as fullerene loading increases.

Material	V_{OC} V	J_{SC} $mAcm^{-2}$	FF	PCE %
33 wt%	0.80	10.5	0.40	3.3
50 wt%	0.80	17.4	0.61	8.5
60 wt%	0.80	17.7	0.66	9.4
67 wt%	0.80	17.5	0.68	9.6
75 wt%	0.78	17.2	0.65	8.8

Table 3.1: Electrical characterisation of PTB7–Th blends with varying wt% of PC₇₁BM, collected under the illumination of AM 1.5.

Grazing-incidence wide-angle x-ray scattering (GIWAXS) results show PC₇₁BM aggregates from above 33 wt%. The preferential face-on orientation is lost as the PC₇₁BM weight fraction increase with and polymer crystallinity decreases as indicated by the associated π – π stacking peak. Domain size as measured with resonant soft x-ray scattering (R–SoXS) shows a monotonic increase with wt%; from 28.2 nm to 44.7 nm, with 67 % having the optimum domain size of 33.5 nm.^{27,153,154} X-ray absorption near edge structure (NEXAFS) gives surface trends for composition that reaches a max at 50 % ratio suggesting that as more PC₇₁BM is added the bulk ratio increases at a faster rate.

The addition of fullerene; increases the fullerene domain size, decreases polymer crystallinity and reduces trap concentration. Moreover, intensity-dependent recombination is optimised in the 60 wt% blend. These changes should be recognisable with data from transient absorption spectroscopy (TA) data with the domain size being related to the charge generation timescale while the phase purity can be seen in the fraction of promptly generated charges. The difference between the PCE caused FF when going from 33 wt% to 60 wt% is also revealed because the geminate recombination rate can be directly probed. Before this, the steady-state photoluminescence (PL) and absorption spectroscopy indicate rapid charge generation related to the purity and also fullerene domain size while the presence of fullerene aggregates is directly observed in the absorption spectra.

3.2.2 Steady-state absorption and photoluminescence

Measurements of steady-state absorption show there are changes in spectral shapes when comparing the neat spectra with blended films. The PTB7-Th absorption peak decreases in energy, and PC₇₁BM low energy shoulder vanishes at low wt%. The absorption also provides valuable information when considering which phase is excited (either PTB7-Th, PC₇₁BM or both) when doing transient absorption (TA) or photoluminescence measurements (PL). The PL show high quenching across all blends indicating efficient exciton to charge separation.

Steady-state absorption spectra for neat and blended films are shown in Figure 3.2. Panel a – e each contain a blend (various colours) spectra increasing in PC₇₁BM wt% from 33 (a) to 75 (e) along with contributions from neat PC₇₁BM (purple) and PTB7-Th (pink) scaled to give the best fit (black) when using a linear combination of the neat spectra. The final fitted spectra are shown in black and reveal that the blended spectra are not a simple linear combination, showing a shift in the electronic structure of the donor, acceptor or both.

When blended with PC₇₁BM there is a red-shift in the PTB7-Th absorption, illustrated clearly in the 33wt% blend, which has a minimal contribution from PC₇₁BM. Above 33wt% absorption in the 350-600 nm (3.5-2.1 eV) increases with wt%, this increase from PC₇₁BM complement PTB7-Th overlaps slightly with the blue edge of PTB7-Th. Of particular interest is 435 nm (2.85 eV), which does not have any absorption from neat PTB7-Th this drastically increases from 0 to 0.8, fullerene loading only increases 2.3 fold. When considered alongside the GIWAXS data, which shows the formation of fullerene aggregates after 50 wt%, this new absorption signal can be attributed to PC₇₁BM aggregates, which are assumed to be present in the neat film of PC₇₁BM.

Normalised steady-state photoluminescence (PL) measurements from neat films of PTB7-Th and PC₇₁BM after 532 nm excitation are shown, Figure 3.3. PTB7-Th (pink) has an onset at ~700 nm and then continues into the near-infrared region, PC₇₁BM has an onset at ~650 nm with a peak at 720. The detector response wave-

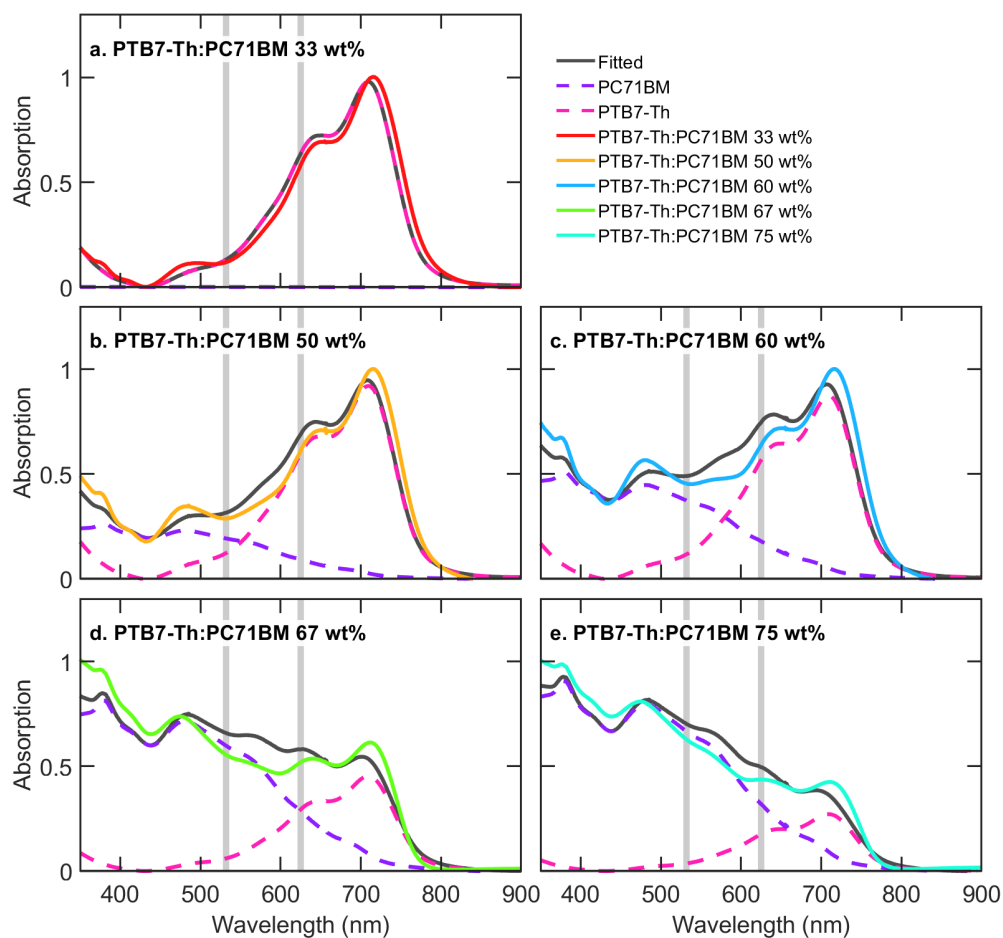


Figure 3.2: Normalised absorption spectra of the various blends along with neat PTB7-Th and PC₇₁BM. Each panel a-e contains for a single wt%; the PTB7-Th:PC₇₁BM absorption spectra (various colours), best-fit line (black) that is a weighted linear combination of the constituent components, and the individual weighted components (purple and pink).

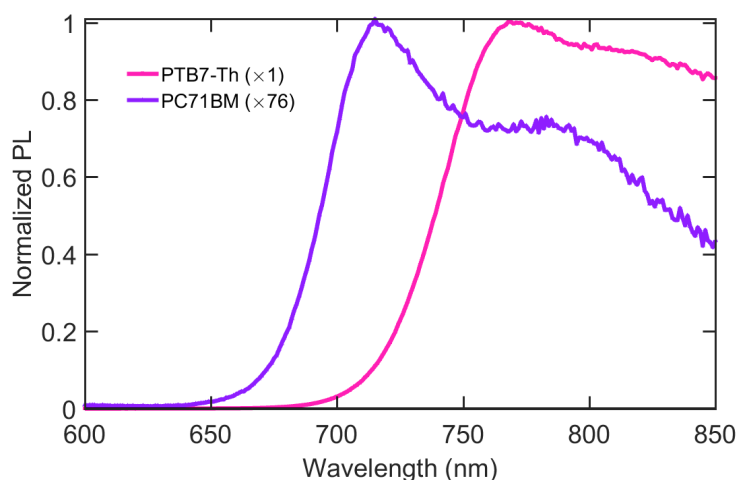


Figure 3.3: Steady-state photoluminescence spectra of neat PTB7-Th and PC₇₁BM films collected after 532 nm excitation. The spectra are presented normalised, with the details showing that after being corrected for absorbed photons PC₇₁BM is 76 times weaker than PTB7-Th.

lengths >780 nm is weak; therefore, spectral features may not be representative. It is crucial to consider the fraction of light absorbed into each phase because the PL intensity of PC₇₁BM is 76 times less than PTB7-Th. The variation in wt% results in a different fraction of incident photons absorbed by each phase. As the two phases have different PL intensities, a decrease in overall PL as more incident light is absorbed by the less emissive PC₇₁BM could be confused for quenching, i.e. if 10 % of the light was absorbed by PC₇₁BM then expected PL without quenching is 90 % of the value if all the light was absorbed by PTB7-Th.

The PL quenching efficiency has been calculated and is plotted as a function of PC₇₁BM loading in Figure 3.4 with all blends showing strong quenching. A rapid hole or electron transfer event explains the strong quenching either an electron from the polymer to PC₇₁BM or a hole in the opposite direction. To understand how excitation in each phase are quenched, two excitation wavelengths are used: 625 nm, which is strongly absorbed by the polymer phase; and 532 nm, used to predominately excite the PC₇₁BM phase. The quenching efficiency is calculated by considering the fraction absorbed into the PTB7-Th and PC₇₁BM phase using

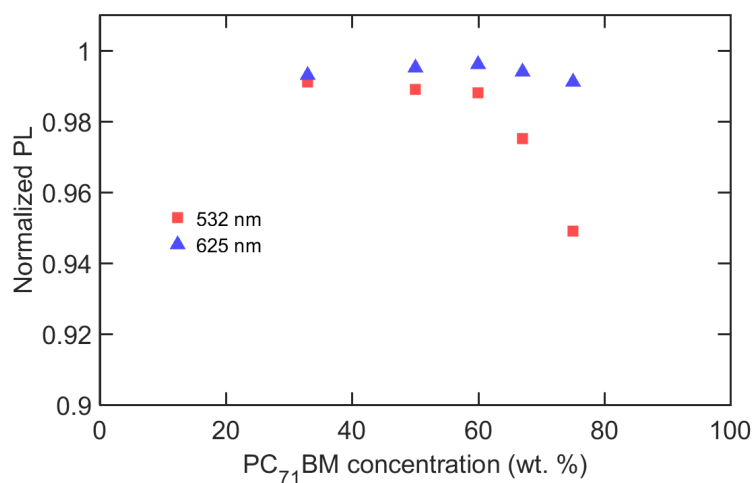


Figure 3.4: The calculated photoluminescence quenching as a function of fullerene loading wt%. Greater than 94 % quenching is seen across all wt%. Red markers indicate 532 nm excitation, which is primarily absorbed into the fullerene phase, while blue (625 nm excitation) is mostly the polymer phase.

the linear fit of the neat absorption spectra as described above. The neat PL spectra are then weighted by this fraction to give the expected PL intensity with the quenching being the fraction observed in the blend. It is acknowledged that the linear fits are not of high quality. However, as the ratio of the two phases is used to determine the fraction, the absorbed photons for each fraction are equivalent to the measured absorbance.

Following 625 nm excitation, the majority of observed variations will need to be explained by the polymer due to the low absorption strength of PC₇₁BM at 625 nm (see Figure 3.2). The quenching efficiency shows an increase from 99.3 % (with 33 wt% PC₇₁BM) to a peak of 99.6 % (with 60 wt%) and subsequently decreases to 99.1 % (with 75 wt% PC₇₁BM). The increased quenching with PC₇₁BM loading is consistent with NEXAFS measurements, that show an increase in fullerene composition in the mixed-phase. This higher ratio of PC₇₁BM increases the proximity to PTB7-Th excitons increasing the exciton quenching

rate. The decrease quenching efficiency above 60 wt% is likely due to emission from PC₇₁BM aggregates.

When using an excitation wavelength centred at 532 nm, both the polymer and fullerene absorb light. The fullerene phase is absorbing more light and a more significant fraction of total incident light as the PC₇₁BM wt% increases. Figure 3.4 shows the quenching efficiency with a monotonic decrease as a function of PC₇₁BM concentration from 99.1 % (33 wt%) to 94.9 % (75 wt%). This effect can be explained by lower exciton dissociation efficiency with higher PC₇₁BM concentrations due to the larger and purer PC₇₁BM domains.

Energy transfer from fullerene to the polymer (prior to charge transfer) is a possible quenching mechanism for the fullerene. However, this is unlikely to occur due to the low PL strength of the fullerene. Energy transfer is ruled out by the TA data (below) with no evidence of an intermediate polymer exciton population. Therefore, the fullerene does not go through a two-step process of fullerene exciton, energy transfer to polymer exciton, then charge transfer.

The above steady-state measurements support the change in PC₇₁BM aggregation seen via the morphological measurements. Furthermore, they demonstrate that a limit of PC₇₁BM concentration is reached at about 60 wt% giving a peak in PL quenching. There is an indication that at higher PC₇₁BM loading as loss channel exciton in PC₇₁BM phases is added due to its increased size. We further explore the photophysics by using transient absorption spectroscopy to track the charge generation and decay dynamics from 100's of femtoseconds to microseconds.

3.2.3 Ultrafast photophysics

To measure the impact of fullerene loading on charge generation and recombination, we use transient absorption (TA) spectroscopy spanning the femtosecond to microsecond timescale. We observe an evident variation in charge generation which is correlated to domain size, with 33 wt% giving almost 100 % promptly

generated charges while 50 wt% is ~40 %. Geminate recombination is suppressed with increasing wt% giving more time for charge extraction and hinting at more efficient charge separation.

Signal assignment

In order to understand the complex signals observed in TA spectroscopy, the neat spectra of PC₇₁BM and PTB7–Th are measured. Figure 3.5 shows the single spectra that is representative of the TA surface after 532 nm (2.33 eV) excitation. The PTB7–Th spectrum has a ground–state bleach signal (GSB, $\Delta T/T > 0$) in the 580–780 nm (2.1–1.6 eV) region overlapping with its steady–state absorption. A stimulated emission (SE, $\Delta T/T > 0$) seen on the lower energy edge of the GSB. The beginning of a broad photo–induced absorption (PIA, $\Delta T/T < 0$) is resolved in the near–infrared region > 940 nm (< 1.32 eV). When considering the PC₇₁BM spectra it is essential to note that after being normalised by absorbed photons the signal is significantly weaker than PTB7–Th (purple, dotted line), as such we do not expect there to be a significant contribution of PC₇₁BM in the TA spectra of the blends. Nevertheless, PC₇₁BM features are described briefly here (purple, solid line), a GSB signal < 600 nm (> 2.07 eV) overlaps with a broad PIA feature spanning the recorded spectra range. The overlap of PIA and GSB is identified by the sharp transition between positive and negative $\Delta T/T$ at 600 nm (2.07 eV).

The observed PTB7–Th spectra can be attributed to a singlet exciton as it is observed directly after excitation of the neat film; and is paired with SE, which is only possible from a single exciton. This makes the PIA in the near–infrared diagnostic of a singlet state present in polymer. The GSB region 580–780 nm (2.1–1.6 eV) can then be used to follow the change in the excited state population created from direct excitation of PTB7–Th or hole injection from PC₇₁BM.

TA spectral features for the blend with 33 wt% fullerene is shown in Figure 3.6a. The spectra are dominated by a GSB feature ($\Delta T/T > 0$) that corresponds to loss of polymer ground–state absorption in the 580–780 nm (2.1–1.6 eV) range, and a photo–induced absorption peak ($\Delta T/T < 0$) at around 1130 nm (1.10 eV). The

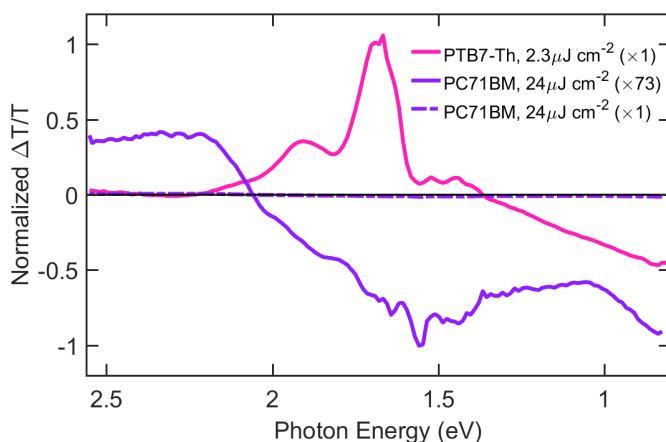


Figure 3.5: TA spectra attributed to singlet exciton for PTB7-Th ($532\text{ nm } 2.3\text{ }\mu\text{J cm}^{-2}$) and PC₇₁BM ($532\text{ nm } 24\text{ }\mu\text{J cm}^{-2}$), collected in a neat blend $<10\text{ ps}$ after excitation. The spectra are normalised to show the spectral features. PC₇₁BM is plotted twice (purple, dotted and solid lines) to emphasises the difference in signal strength after correcting for absorbed photons.

photo-induced absorption peak arises due to hole polarons in the PTB7-Th polymer, as it is a distinct peak as opposed to the broad absorption seen in the neat PTB7-Th film. The lack of PC₇₁BM GSB in the signal from the electron injection is not a concern due to the much lower oscillator strength when compared to PTB7-Th. In addition, a signal is seen at the earliest time, $>1380\text{ nm } (<0.90\text{ eV})$, this peak completely disappears within 1 ps . It is attributed to polymer exciton, based on PIA seen in this region in the TA spectra of neat polymer film (see Figure 5.9).

TA spectral series for films with 50 wt% and 60 wt% blends are included in Figure 3.6 (b and c). Similar spectral features as described for 33 wt% blends are observed in both the 50 wt% and 60 wt% blends with two exceptions; the polymer exciton feature at $>1380\text{ nm } (<0.90\text{ eV})$ is weaker and shorter-lived, and in the 50 wt% blend there is an additional photo-induced absorption feature around $830\text{ nm } (1.49\text{ eV})$. The additional photo-induced absorption feature at $830\text{ nm } (1.49\text{ eV})$ in the 50 wt% blend is a sub-bandgap absorption and characteristic of electroabsorption, which is a perturbation to the ground state absorption caused by an

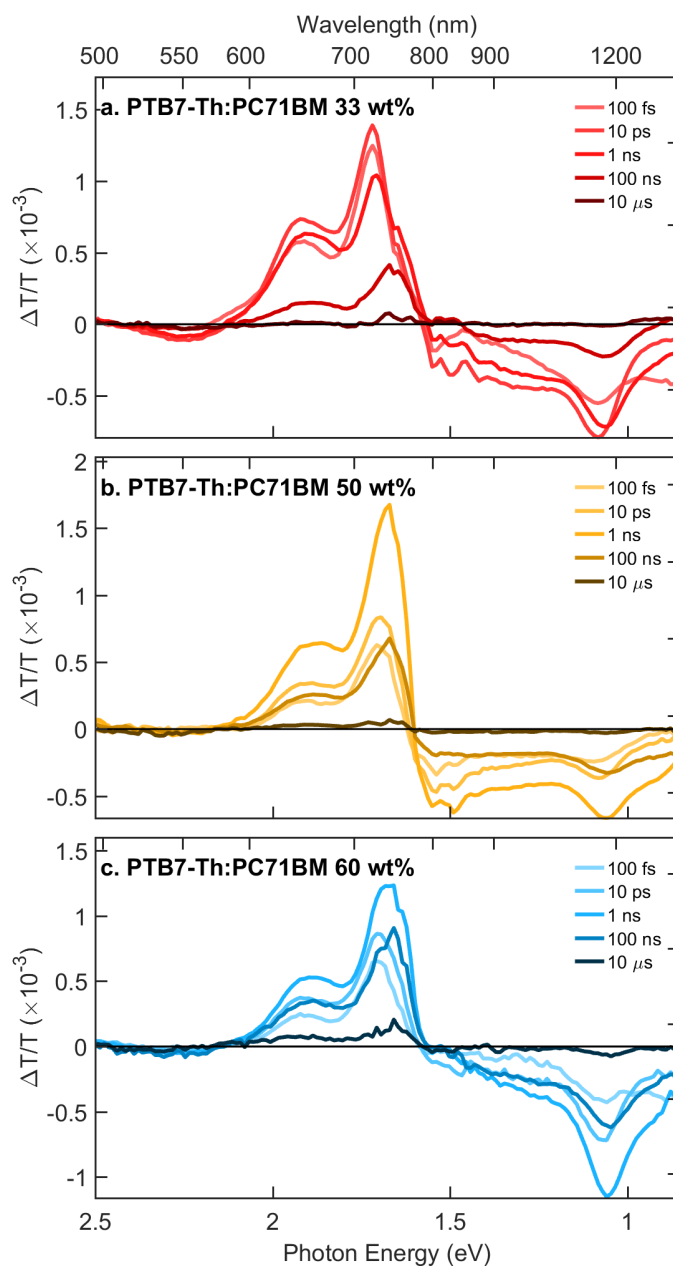


Figure 3.6: A series of TA spectra showing the interconversion of excitons into charges and then decay to the ground state. Each is constructed from separate measurement in the visible and near-infrared spectral regions, following femtosecond (100 fs – 3 ns) and picosecond (3 ns – 100 μ s) excitation at 532 nm. Each individual panels show PTB7-Th blended with a different wt% of PC₇₁BM; a. 33 wt% ($3.1 \mu\text{J cm}^{-2}$), b. 50 wt% ($4.3 \mu\text{J cm}^{-2}$), and c. 60 wt% ($4.3 \mu\text{J cm}^{-2}$).

electric field.^{275–277} Electroabsorption arises because an electric field is induced by separated electrons and holes in the fullerene and polymer phases. In polymer:fullerene blends, electroabsorption effects tend to be observed when there is a particular alignment of polymer chains with respect to the electric fields generated between the charge pairs, thus indicating variation in the polymer:fullerene packing near the interfaces.

Charge generation and decay

From an understanding of the spectra, regions associated with charges and excitons, different charge generation channels can be tracked. Figure 3.7 presents normalised kinetic traces of: polymer GSB (a), polaron (b), and polymer exciton (c). GSB kinetics represent the excited state population in the polymer that can be broken down into polaron and polymer exciton due to the spectra assignments. The polaron population can be followed by looking at 1000–1240 nm (1.2–1.0 eV).

The initial intensity and growth dynamics of the charge generation process can be a combination of prompt (well-mixed regions) or delayed charge generation (coarser phase). These dynamics can then be related to morphology measurement discussed earlier; i.e. phase purity and size of the polymer and fullerene domains. The delayed charge generation can come from either the; polymer (electron transfer) or fullerene (hole transfer) therefore, both channels need to be considered. For all films, the step-like increase in the GSB immediately after excitation is attributed to prompt charge generation from the mixed-phase. These prompt charges could be from either electron or hole injection as both polymer or fullerene absorb at this wavelength. The prompt charge assignment is supported by consideration the exciton identified from the neat polymer exciton (c) which is both much weaker (Figure 3.6) and is short-lived. Next, we consider the delayed charge generation, which is exclusively from the PC₇₁BM phase as the polymer exciton signal decays in <200 fs. This is different for 33 wt% blend where the growth in GSB is minimal, meaning all charges are generated

promptly. For the 50 wt% and 60 wt% blends more than half of the charges come from the PC₇₁BM phase following 532 nm excitation.

The fullerene photophysics plays an essential role in the OPV as it absorbs a substantial fraction of incident light, ascertained by decomposing contributions to the absorption spectra (Figure 3.2). While the fullerene excitons themselves are not directly observable, hole transfer to the polymer increases the polymer-based GSB and the PIA peak attributed to polarons. The kinetics of the GSB and photo-induced absorption growth reflects the dynamics of fullerene exciton diffusion to interfaces. Increasing the fullerene content extends this exciton diffusion phase; the peak charge population shifts from tens of picoseconds to approximately one nanosecond when increasing the fullerene content from 33 wt% to 50 wt%. The different dynamics are explained by substantially larger and purer PC₇₁BM domains observed in the 50 wt% blend.

The apparent discrepancy in the decay dynamics between the GSB and polaron signal for 50 wt% and 60 wt% may relate to the different absorption features noted above for the 50 wt% blend, or the onset of PC₇₁BM exciton annihilation in the 60 wt% blend. The variation in decay dynamics between the integrated kinetics could be due to the difference in spectra shift at later times as the charges diffuse into domains of higher purity.⁹² Some evidence of this can be seen in the exciton peak at ~50 ns well after the polymer exciton has decayed, but indicative of a shifting PIA peak. For all films, there is an additional increase in the GSB intensity after excitation, which is much more significant for the case of the 50 wt% and 60 wt% blends, supporting the morphology measurements that show fullerene domains forming with >33 wt%.

To begin the discussion of charge recombination, we must identify if the primary pathway observed is bimolecular or geminate. As the solar illumination is weaker than a pulsed laser, the geminate decay dynamics are those relevant to a working device. By collecting an excitation fluence dependent series of kinetics and observing any change in decay, we can identify intensity-dependent

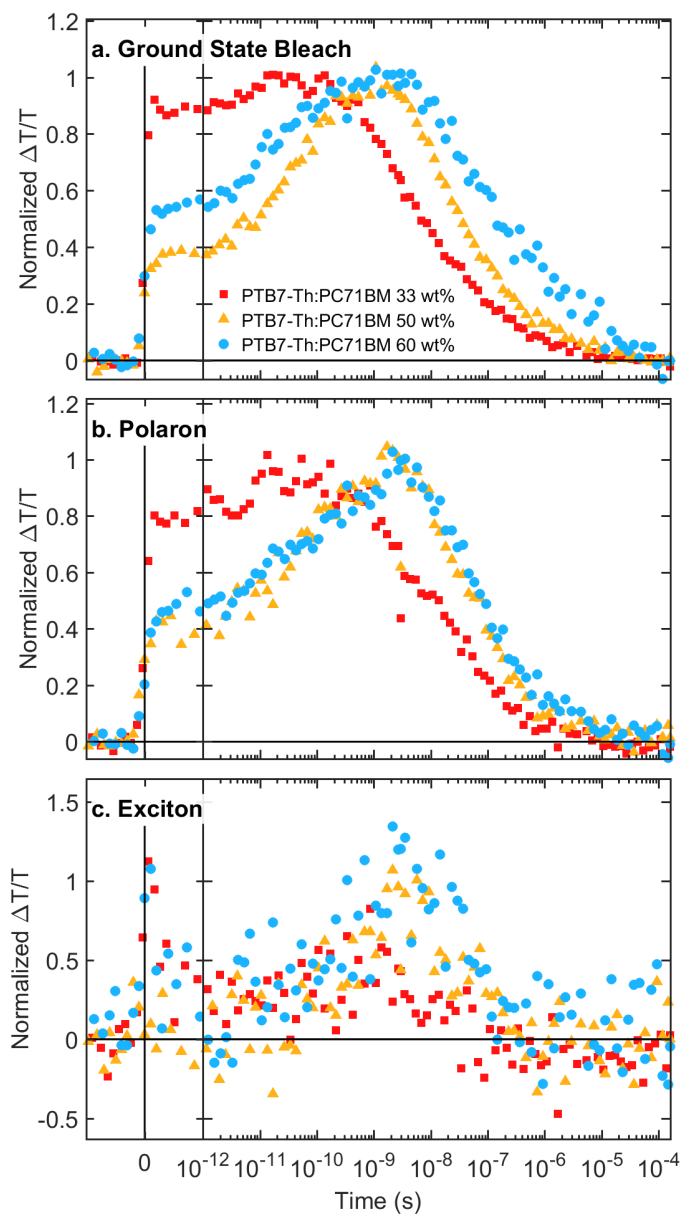


Figure 3.7: Dynamics extracted from thin films blend of PTB7-Th:PC71BM (33 ($3.1 \mu\text{J cm}^{-2}$), 50 ($4.3 \mu\text{J cm}^{-2}$), and 60 ($4.3 \mu\text{J cm}^{-2}$) wt%) following 532 nm excitation (100 fs, for $\Delta t < 6$ ns, and 600 ps, for $\Delta t > 6$ ns) primarily resonant with the fullerene phase. Part (a) shows the integration of the GSB region, (b) is a feature attributed to polaron, and (c) is polymer exciton at times < 100 ps.

bimolecular decay. Figure 3.8 presents an intensity-dependent series of measurements that show little dependence on the decay dynamics even after tripling the charge density population (the maximum signal amplitude measured is in the label, i.e. PTB7–Th:PC₇₁BM increases from 0.3 to 0.98) The 60 wt% shows higher bimolecular recombination with a small but noticeable deviation of the signal at 100 ns while there is no difference with 33 wt% and 50 wt%. The increased bimolecular decay rate is consistent with more mobile charges useful for charge separation.

Now that we have established that we are looking purely at geminate recombination the dynamics of subsequent charge recombination can help to explain observed differences in device efficiencies. Recombination on the subnanosecond time is observed for the 33 wt% blend. This rapid recombination would mean that in a device these charges would not be easily separated and extracted, explaining the poor fill factor, short-circuit current, and voltage dependence of charge collection (increase in photocurrent going from $V = 0$ V to $V = -1$ V). The faster recombination likely relates to the strong polymer:fullerene intermixing, which would not leave sufficiently large and pure fullerene phases to isolate electrons from holes. Charge recombination for the 50 wt% and 60 wt% blend, on the other hand, proceeds from tens of nanoseconds, which reflects recombination of free charges, as is seen for other efficient OPV blends. The increased timescale of charge recombination allows for more efficient charge collection consistent with their superior PV performances.

3.2.4 Summary

It has been shown that transient absorption spectroscopy, coupled with electrical and morphological measurements, can provide meaningful insight into the effects of varying PC₇₁BM loading from 33 % to 67 %. A clear correlation between increasing the wt% and charge generation and decay is observed. There is a decrease in the prompt charge generation in large fullerene domains, but delayed extraction from the fullerene domain can lead to efficient charge gen-

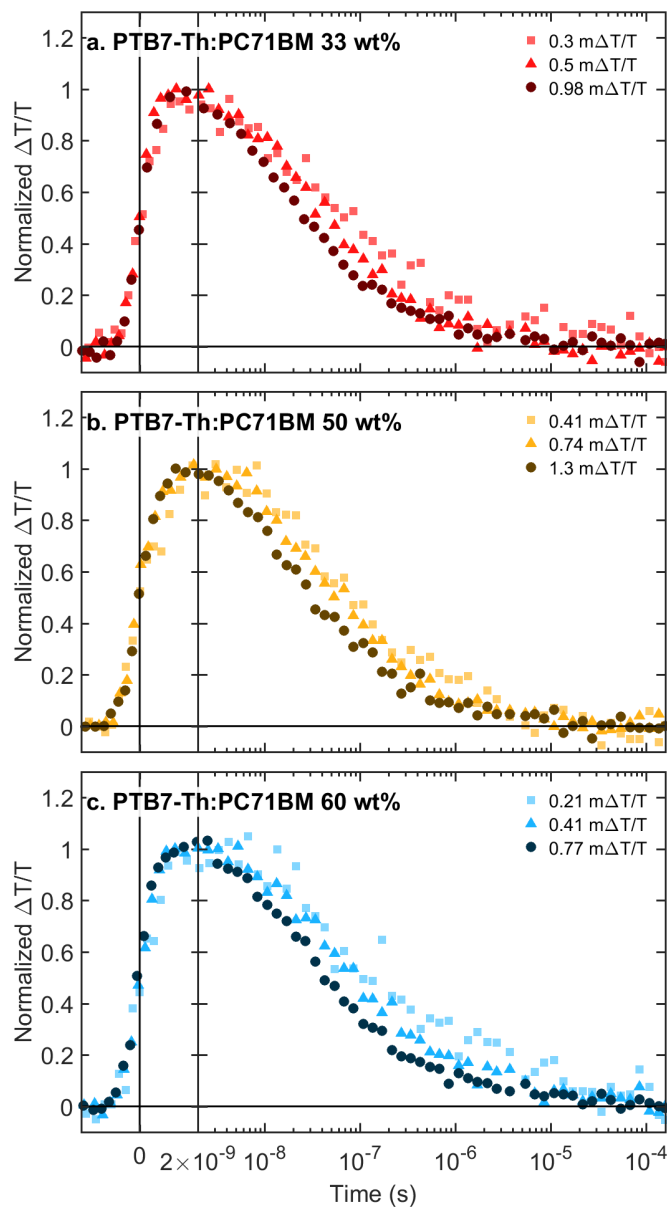


Figure 3.8: A series of fluence dependent decay dynamics following 532 nm excitation (600 ps) at excitation fluences noted in the details. Each panel contains different wt% of PC₇₁BM; (a) PTB7-Th:PC₇₁BM 33 wt%, (b) PTB7-Th:PC₇₁BM 50 wt%, and (c) PTB7-Th:PC₇₁BM 60 wt%.

eration. The timescale of this generation is related to the fullerene domain size (as shown by GIWAXS). Moving on to the decay, an increase in the geminate lifetime can be seen once fullerene domains are formed. This trend points to increasing charge separation driving force provided by the three-phase morphology. These conclusions support steady-state photoluminescence quenching which peaks at 60 wt% when the domain size and purity are optimised for charge separation. These results clearly show that in polymer–fullerene blends, fullerene loading can be used to optimise phase mixing and domain size to optimise PCE. Furthermore, a three-phase morphology is vital for efficient devices, a lack of pure fullerene domains (<50 wt%) results in rapid charge quenching. At the same time, greater than 70 wt% mean the fullerene domains have inefficient exciton to charge quenching while also disrupting PTB7–Th domains.

3.3 Effect of different fullerene substitutions on the performance of fullerene:PTB7–Th organic solar cells

In the previous section, we took a detailed look at how fullerene wt% effects PTB7–Th:PC₇₁BM; we now take a brief look at the effect of substituting the PC₇₁BM for other fullerene acceptors. The focus here is on the effect of changing the acceptor, rather than the bulker polymer. When PC₇₁BM is replaced by ICBA the V_{oc} increases to 1.0 V (0.81 V), but a decrease in J_{sc} means the overall PCE is 7.1 %. When PC₆₁BM is the acceptor V_{oc} is similar to PC₇₁BM blends, and the J_{sc} is lower, giving an efficiency of 7.1 % similar to ICBA. In this section, the same techniques as previously used are once again employed to provide insight about how changing the fullerene acceptor from PC₇₁BM to either PC₆₁BM or ICBA effects performance, morphology, and photophysics when blended with PTB7–Th.

This study uses multiple characterisation techniques to understand the interplay between device- and photo- physics. The complex nature of BHJ OPVs drives the need for advanced characterisation techniques with strong evidence that a three-phase morphology is critical to efficient devices. The three-phases are needed because exciton diffusion is typically on the 10's of nanometers, necessitating small impure domains to generate charges pairs. At the same time, pure interconnected phases encourage the separation at the interface (lower energy in crystalline domains) and allow for good percolation collection and efficient collection at the electrodes. In order to optimise open-circuit voltage (V_{oc}) the lowest unoccupied molecular orbital (LUMO) level of the acceptor has been increased, this decrease the donor-acceptor LUMO-LUMO offset increasing voltage, but also results in a decrease in the driving force required for charge separation.^{27,116,119,122} When using a medium band-gap donor polymer, i.e. P3HT the LUMO is at -2.46 which leave significant room for this driving force, however, for PTB7-Th the LUMO is by 1.2 eV closer to the highest occupied molecular orbital (HOMO) at -3.65 eV reducing the driving force available for charge separation. ICBA is a clear example of engineering the fullerene acceptor to improve VOC, when matched with P3HT their V_{oc} is increased when compared with PC₆₁BM and a corresponding increase in PCE is observed, whereby when matched with a low band-gap polymer the PCE is lowered, as shown in Table 3.2. The decreased PCE could be caused by morphology or energetic driving force as neither have been well characterised before now.

By combining the characterisation of morphology and device physics (completed by collaborators) with detailed studies of the optical and photophysics, we reveal that ICBA has a lower fraction of charges generated after photoexcitation and increased faster charge combination. These loss channels are offset by the increase V_{oc} to give PTB7-Th:ICBA a similar efficiency to PTB7-Th:PC₇₁BM. However, the improved light collection of PC₇₁BM increases PCE of PTB7-Th:PC₇₁BM blends by 25 % to 9.4 %.

Donor	PCE (%)		V_{oc} (V)		Other Acceptor
	ICBA	Other	ICBA	Other	
P3HT	5.4	3.9	0.84	0.58	PC ₆₁ BM ²⁷⁸
PTB7	4.7	7.2	0.87	0.70	PC ₇₁ BM ²⁷⁹
PTB7-Th	7.6	9.4	1.0	0.80	PC ₇₁ BM this work
PBDTPD	2.7	7.3	1.1	0.94	PC ₆₁ BM ²⁸⁰

Table 3.2: Performance of BHJ-OPV comparing ICBA to higher LUMO fullerene acceptors with different donor polymers. The fullerene based acceptor used for each comparison is denoted in the "Other Acceptor" column.

3.3.1 Morphology and device characterisation

This section presents a summary of the electrical, morphological, and device physics. GIWAXS measurements reveal that ICBA hinders polymer stacking. While R-SoXS shows the difference between fullerene domain size (range 24–32 nm), with PC₇₁BM having the largest and purist domains.

J-V measurements of the various fullerene acceptors are summarised in table 3.3 these show that PC₇₁BM has the best overall performance with a PCE of 9.4 %. The high PCE is a combination of having better J_{sc} when compared with PC₆₁BM and a better FF to compensate for the lower V_{oc} when compared with ICBA. The increase in J_{sc} compared to PC₆₁BM is due to the higher absorption across the 400–600 nm region shown by comparing the difference between the J_{sc} values measured from J-V measurements, 3.1 mA cm^{-2} and those calculated from external quantum efficiency (EQE), 2.1 mA cm^{-2} . The 0.2 eV higher V_{oc} in ICBA (1.0 vs 0.8) is due to the difference in LUMO levels with PC₆₁BM and PC₇₁BM being similar ~ -3.9 eV while ICBA is -3.74 eV.^{278,281,282} Interestingly ICBA has a lower FF (0.53 vs ~ 0.65) suggesting a possible route for further improvement in the morphology.

The transient photovoltage shows the recombination dynamics under V_{oc} conditions and constant illumination. The device is placed under illumination to

Material	V_{OC}	J_{SC}	$J_{SC} calcEQE$	FF	PCE
	V	$mAcm^{-2}$	$mAcm^{-2}$		%
PC ₆₁ BM	0.81	14.6	15.1	0.64	7.6
PC ₇₁ BM	0.80	17.7	17.2	0.66	9.4
ICBA	1.0	13.3	12.5	0.53	7.1

Table 3.3: Electrical characterisation of PTB7-Th blended with three fullerenes based acceptors.

generate a steady-state equilibrium, and then a short pulse makes small perturbation to the device. The measured transient voltage curve can be broken down into two parameters, the first γ , the rate at which the carrier density changes with respect to voltage, and second is λ is related to the reaction order of recombination (1st order, 2nd order, ...).^{259,274,283} The variation in γ indicates that ICBA blends have a larger degree of energetic disorder which can be caused by an increase in the density of trap-states or band tailing.^{195,260} The variation λ supports ICBA having a different recombination mechanism from PC₆₁BM and PC₇₁BM.^{259,274,283,284} With ICBA having a value of 9.5 which is fluence independent while PC₆₁BM and PC₇₁BM have a value of 7 at low fluence decreasing to 4 when fluence is reduced to 0.3 suns, pointing to bimolecular recombination playing an important role process.

The morphological changes induced by the various fullerene are measured by GIWAXS and R-SoXS. These measurements show a disruption to polymer π - π stacking when ICBA is used and also a decrease in coherence length, taken together ICBA lead to less ordered domains. R-SoXS is able to reveal information about domain size and also purity, in this case, PC₇₁BM has larger domains, 32.5 nm, then PC₆₁BM (24.4 nm) and ICBA (26.8 nm). Purer domains are more favourable for charge transport and separation^{27,153,154} Relative purity measurements shows that PC₇₁BM is purest while PC₆₁BM and ICBA have a ~20 % reduction with values of 0.84 and 0.82 respectively.

Table 3.4 summarises the characteristics of the blends that are important in the discussing of the steady-state optical and photophysical results. The optical absorption spectra support the increased J_{sc} , while charge dynamics and photoluminescence (PL) quenching is consistent with domain size and purity.

Material	PCE %	J_{SC} $mAcm^{-2}$	Domain Size Fullerene (nm)	Purity
PC ₆₁ BM	7.6	14.6	24.4	0.84
PC ₇₁ BM	9.4	17.7	32.5	1
ICBA	7.1	13.3	26.8	0.82

Table 3.4: Morphological and device results that can be related to photophysical measurements.

3.3.2 Steady-state absorption and photoluminescence

An understanding of the steady-state optical properties can be gained by considering the blended films absorption spectra and how they compare to the neat materials. The optical absorption spectra of the film comprised of PTB7-Th blended with either PC₇₁BM, PC₆₁BM, and ICBA is shown in Figures 3.9. In the blends the most significant variation is the broad absorption feature present in PTB7-Th:PC₇₁BM (blue) increasing absorption in the 400-600 nm (3.1-2.1 eV) range, this is from PC₇₁BM with the contribution highlighted in Figure 3.10. The peaks in the 600-800 nm (2.1-1.6 eV) range are from PTB7-Th and are similar across all three blends. This large increase in absorption going from <0.01 in PTB7-Th:PC₆₁BM to >0.1 for PTB7-Th:PC₇₁BM is responsible for the notable increase in J_{sc} due to the higher number of photons absorbed. It should be noted that these absorption spectra are for the films studied in PL and TA measurements below, while the devices had thicker active layers. Nevertheless, as the absorption is low in this region the variation carries through to the X-fold thicker films used in the device.

Figure 3.10 presents the steady-state absorption spectra for the blended films fitted with a linear combination of the neat spectra. Panels a-c contains a different

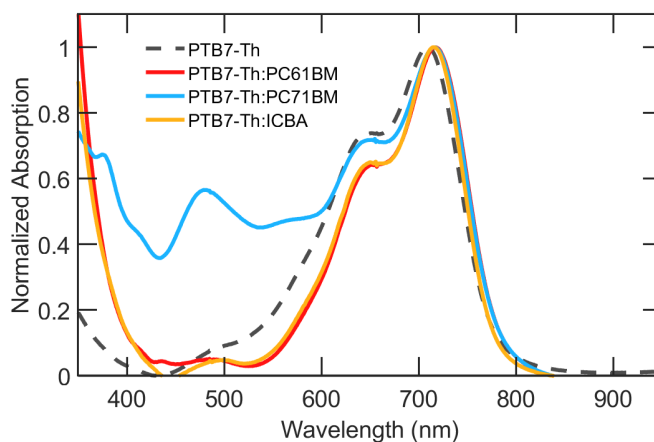


Figure 3.9: Normalised absorption spectra of PTB7-Th blended with PC₆₁BM (red), PC₇₁BM (blue) and ICBA (yellow). Neat PTB7-Th absorption spectra is shown in dashed lines for comparison.

fullerene acceptor blended with PTB7-Th. The fitted spectra is shown in black, and the contribution from PTB7-Th and the acceptor are in coloured dashed lines. When comparing all the blends, a significant change in the absorption PTB7-Th is observed. In the 500-850 nm (2.5-1.5 eV), there is little contribution from the fullerene in the PTB7-Th:ICBA and PTB7-Th:PC₆₁BM blends; this allows the PTB7-Th spectra shift to be isolated. The vibronic peaks in PTB7-Th change in relative ratio, and the spectra is a red-shifted, this shows that the electronic coupling is different in neat PTB7-Th in comparison to the blends. Once blended, the PTB7-Th shifts look similar across all acceptors used.

The PL spectra following 625 nm excitation of neat PTB7-Th and the various fullerene molecules excited at 532 nm are shown in Figure 3.11. The PL has been normalised for the number of photons absorbed at the respective excitation wavelengths to allow for a comparison of relative PL intensity. PTB7-Th is the main contributor to PL being at least 76 times stronger than any fullerene acceptor. Due to weak detector response in the near-infrared, the two vibronic PL peaks seen previously in PTB7-Th are not well resolved.¹¹² The effect on

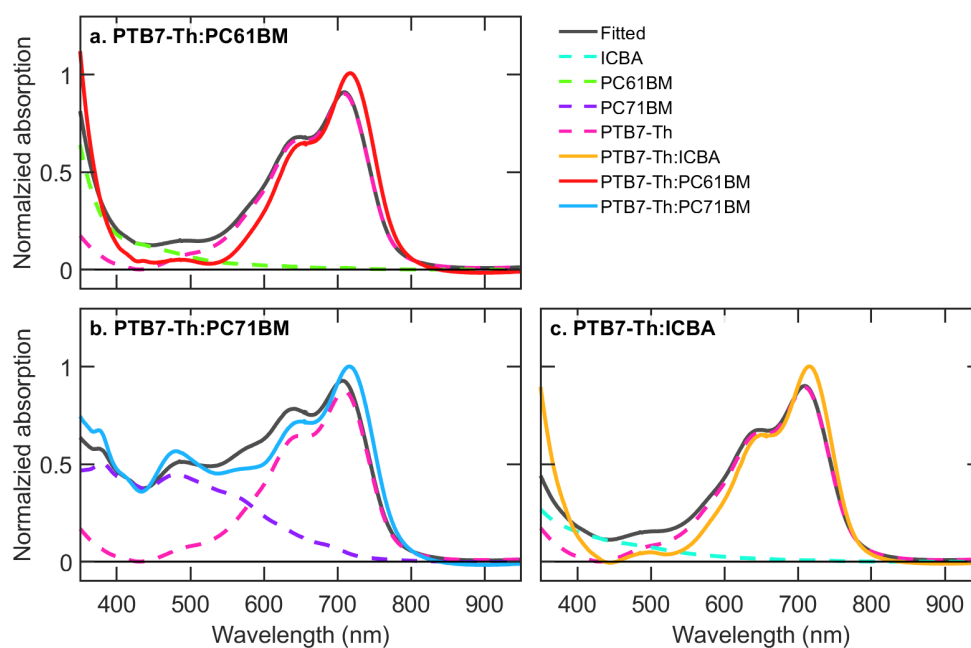


Figure 3.10: Normalised absorption spectra for blends of PTB7-Th with PC₆₁BM (a), PC₇₁BM (b), and ICBA. Each panel a–c contains; the absorption spectra of a blend (various colours), best-fit line (black) that is a weighted linear combination of the constituent components, and the individual weighted components (dashed-lines).

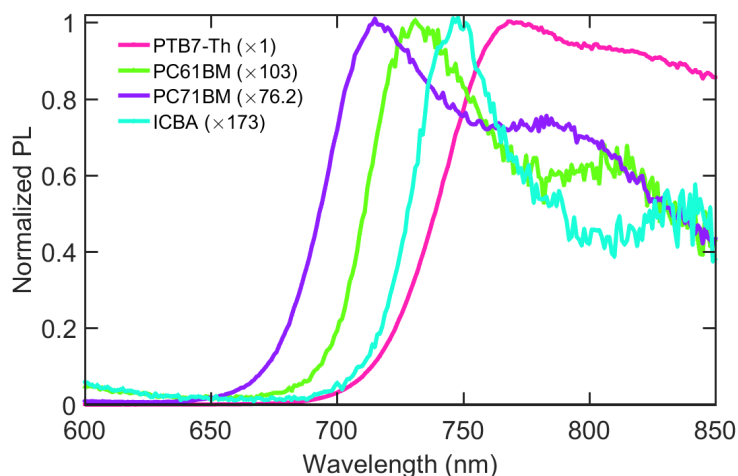


Figure 3.11: Steady-state photoluminescence spectra of neat films following 532 nm excitation, neat materials are PTB7-Th, PC₆₁BM, PC₇₁BM, and ICBA. The maximum value of the spectra is normalised after correcting for absorbed photons, with the details including the relative scaling factor used for normalisation.

measured PL quenching is negligible as the amplitude rather than the spectral response is used when calculating the fraction quenched.

The PL quenching efficiency following 625 nm excitation is summarised in Table 3.5. Addition of the fullerene acceptors to PTB7-Th results in a substantial decrease in PL intensity when compared with the pristine polymer. The quenching efficiency is similar in PC₆₁BM, 99.7 %, and PC₇₁BM, 99.6 %, with ICBA showing a significant reduction to 95.9 %, suggesting a comparatively higher number of excitons that are not dissociated at the PTB7-Th-ICBA interface. The PL quenching being lowest in PTB7-Th:ICBA contrasts with the morphology analysis above that seems to suggest that it has the best condition for exciton separation; lower domain purity which should facilitate excitation separation. As morphology suggests optimised interface the difference in quenching is attributed to driving force with PTB7-Th:ICBA has the smallest LUMO-LUMO offset.

Material	Quenching
PTB7–Th:	(%)
PC ₆₁ BM	99.7
PC ₇₁ BM	99.6
ICBA	95.9

Table 3.5: Photoluminescence quenching observed after 625 nm excitation. Quenching is calculated by comparing PL from neat films and is corrected for the number of absorbed photons.

3.3.3 Ultrafast photophysics

In order to examine the ultrafast dynamics of charge generation and recombination TA experiments were performed. The TA measurements combine femtosecond and picosecond excitation sources to achieve time resolution from 100 fs to 200 ms, along with UV–VIS–NIR detection. The board detection window allows for singlet excitons and charges identified, and the time window is long enough to measure the geminate lifetime of charges.

Signal assignment

The assignment of the neat TA spectra is similar to Section 3.2.3 because the same donor polymer is used and the acceptors are all fullerene derivatives. Figure 3.12 shows the single TA spectra needed to describe the TA surface for each neat film after excitation at 532 nm. These spectra are assigned to singled excitons as they are present directly (<200 fs) after photoexcitation that occurs in the singlet manifold. The neat TA spectra of PTB7–Th and PC₇₁BM are described in Section 3.2.3 the key points are; PTB7–Th a ground–state bleach signals (GSB, $\Delta T/T > 0$) in the 580–780 nm (2.1–1.6 eV) and a broad photo–induced absorption (PIA, $\Delta T/T < 0$) in the near–infrared region >940 nm (<1.32 eV), PC₇₁BM none of the features are noticeable due to the ~70 weaker signal strength. Like PC₇₁BM the other fullerene acceptors have signals 73–100 times weaker then PTB7–Th, so they are not expected to make a significant contribution to the blends spectra. As such; the TA spectra from PTB7–Th:fullerene blends will be dominated

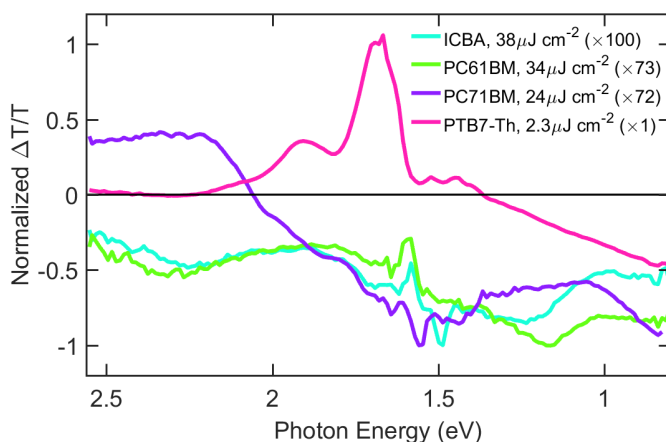


Figure 3.12: TA spectra collect after excitation at 532 nm from neat films of PTB7-Th ($2.3 \mu\text{J cm}^{-2}$), PC₆₁BM ($34 \mu\text{J cm}^{-2}$), PC₇₁BM ($24 \mu\text{J cm}^{-2}$), and ICBA ($38 \mu\text{J cm}^{-2}$). The selected spectra are representative of the singlet exciton species formed after initial excitation. Spectra have been normalised to show the spectral features and details are present on the relative signal strength of each after correcting for absorbed photons, PTB7-Th is the base ($\times 1$) and ICBA has been magnified the most, 100 times.

by contributions for PTB7-Th, specifically a GSB in the 580-780 nm (2.1-1.6 eV) caused by any excited-state species (exciton and charges/polaron), with a broad PIA extending into the near-infrared will be diagnostic of singlet exciton.

Figure 3.13 shows a series of TA spectra at various delay times for the three blends following 532 nm excitation. At delay times >10 ps each TA spectra are dominated by hole polaron in PTB7-Th, identified by GSB ($\Delta T/T > 0$) at wavelengths corresponding to polymer absorption (775-560 nm (1.6-2.2 eV)) and a PIA ($\Delta T/T < 0$) at 1130 nm (1.10 eV) not seen in the neat film. After 10 ps each of the TA spectra shapes do not change, but rather decrease in intensity as the polaron species decay. At early times (100 fs) there are two species present; residual polymer exciton PIA 1380 nm (0.90 eV), which is identified from the spectrum of the neat polymer (Figure 3.12), and the polaron PIA peak at 1130 nm (1.10 eV). From this it can be seen that the relative contribution of polymer exciton is significantly higher in ICBA than PC₆₁BM or PC₇₁BM blends. This result is consistent

with the lower quenching efficacy of PL measurements, which were attributed to weaker driving force slowing down the quenching of the singlet exciton.

A significant difference between the blends is the shape of the GSB formed by charges, which are normalised and compared at 10 ps in Figure 3.14. The spectra vibronic peak intensities can be compared to give an idea of the structure of the polymer chain occupied with excitons. These comparisons are made using J-like and H-like character, which is derived from the relative orientation of coupled dipoles in aggregates, the various H/J character relates to the relative orientation of the coupled dipoles and how the vibronic structure affects the transition dipole moment leading to more or less forbidden transition. Stronger 0–0 intensity indicates more extended chains (more J-like character) consistent with higher interchain order. If the 0–1 band approaches the intensity of the 0–0 it is indicative of a disordered system.¹⁸² The observed vibronic ratio show PC₇₁BM has the strongest 0–0 peak indicating the most interchain ordering while the TA spectra of the ICBA blend the 0–1 peak approaches the intensity of the 0–0 peak, indicating significant disorder caused by mixing with ICBA. The variation in the vibronic peak ratio is consistent with the morphology measurements mentioned above. Once again PC₆₁BM lands in the middle of the two indicating an intermediate level of packing.

Charge generation and decay

Charge generation and recombination kinetics can be separated from polymer exciton dynamics by contrasting the GSB and the 1130 nm (1.10 eV) polaron photo-induced absorption band (Figure 3.15). It is necessary to consider both spectral regions simultaneously; the exciton and polaron contribute to both signal but in varying ratio. Because of the varying ratios it is possible to discuss the dynamics of each exciton and polaron species; a clear example is seen in PTB7–Th:ICBA blend that shows significant variation between the two regions. The essential dynamics are, prompt charge generation from the well-mixed regions, delayed from fullerene domains, delayed generation from PTB7–Th exci-

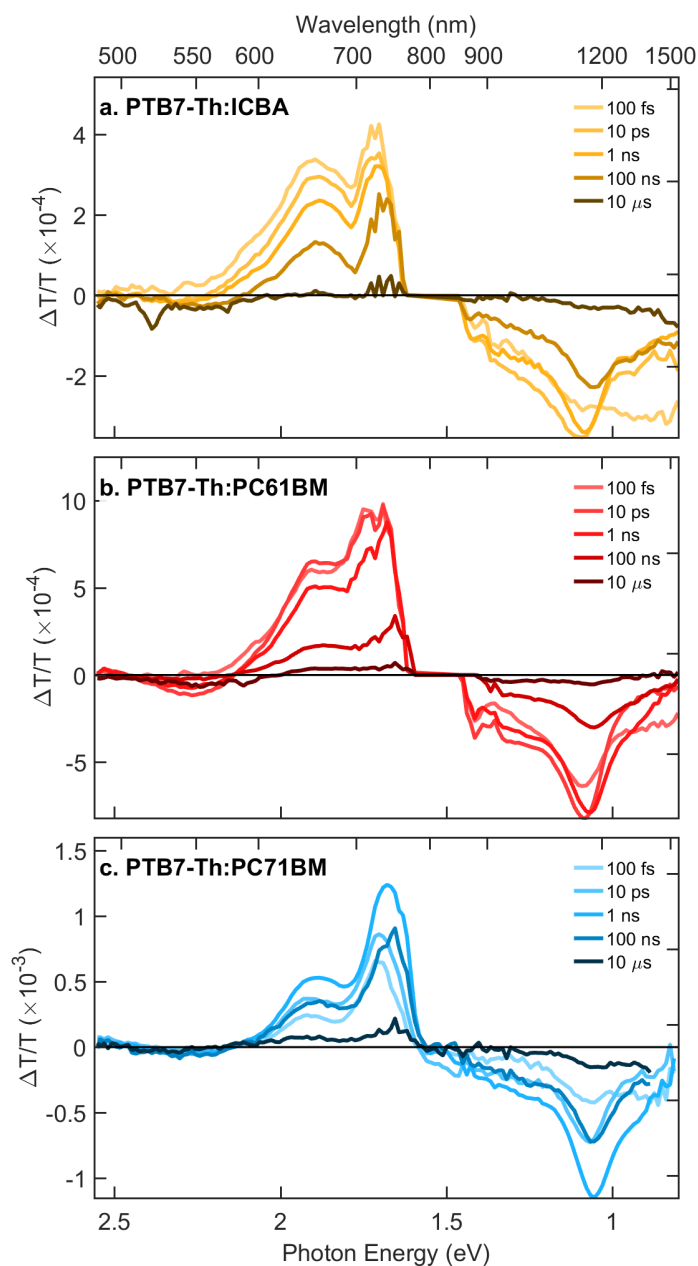


Figure 3.13: Series of TA spectra taken at various excitation–probe delay times selected to show the spectral evolution of excitons to charges and then decay to the ground state. Each series in contains four separate measurements, the visible and near-infrared spectral regions, with each spectral region collected following femtosecond (100 fs – 3 ns) and picosecond (3 ns – 100 μ s) excitation at 532 nm. Each panel shows a different blend; a. PTB7-Th:ICBA ($4.9 \mu\text{J cm}^{-2}$), b. PTB7-Th:PC₆₁BM ($5.6 \mu\text{J cm}^{-2}$), and c. PTB7-Th:PC₇₁BM ($4.3 \mu\text{J cm}^{-2}$).

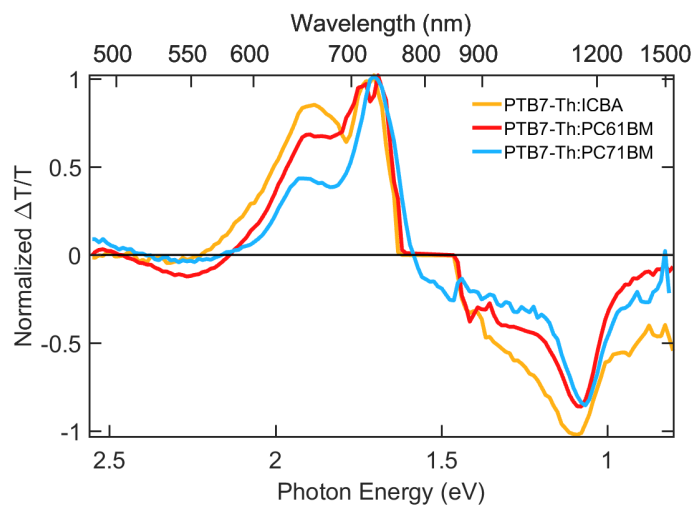


Figure 3.14: Normalised spectra slices at 10 ps of the various blends studied. The spectra are normalised by the 0–0 vibronic peaks in the GSB region to highlight changes in the vibronic progression.

tation and then the subsequent charge decay. Of these, only the prompt charge generation cannot be established from the given regions but is best taken from the spectra at early times discussed above.

When considering delayed generation from the PTB7–Th phase, for both the PTB7–Th:PC₆₁BM and PTB7–Th:PC₇₁BM prompt generation is significant leaving few excitons to undergo delayed charge generation. The low number of delayed generation is seen in the minimal increase in GSB for PTB7–Th:PC₇₁BM < 5ps region, while for PTB7–Th:PC₆₁BM has a plateau in GSB region until 100 ps indication no delayed generation. In the case of ICBA there is a decrease of GSB intensity at <10 ps while the PIA is relatively constant, showing that for PTB7–Th:ICBA the singlet excitons are lost, supporting the conclusion of insufficient driving force due to similar LUMO levels.

Moving onto the charge generation from the fullerene phase, signified by an increase in polaron signal as the hole is injected into PTB7–Th and a commensurate increase in the PTB7–Th ground–state bleach. For the highest photocur-

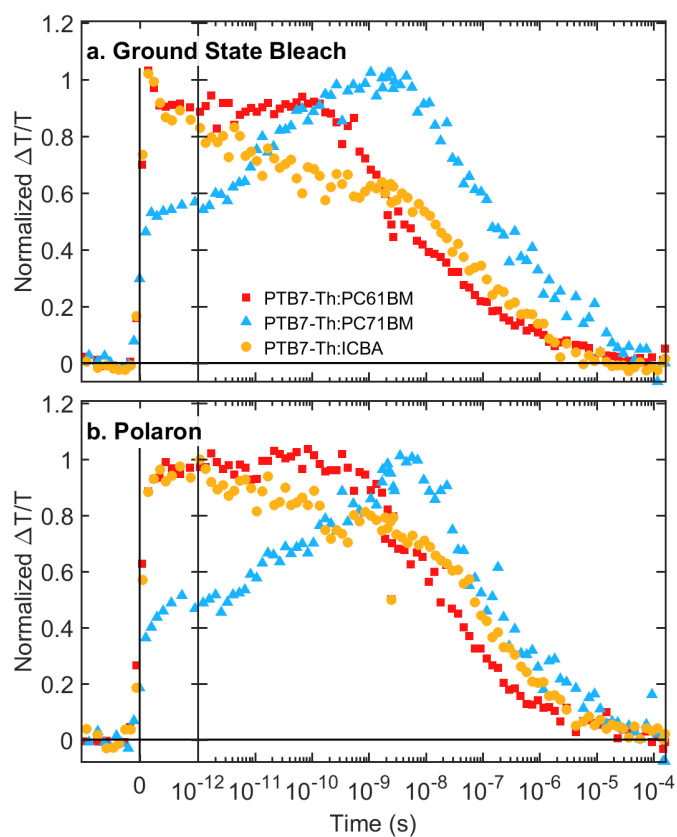


Figure 3.15: Dynamics of the different species identified in each blend extracted by integrating across specific spectral regions. The dynamics are group by species they correspond to with panel a. containing GSB, 590-770 nm (2.1-1.6 eV) and panel b. contains polaron, 950-1240 nm (1.3-1.0 eV).

rent blend, PTB7–Th:PC₇₁BM, the polaron signal continues grow until ~100 ps and then remains at this level until ~300 picoseconds. Delayed charge generation is not observed for the PTB7–Th:ICBA or PTB7–Th:PC₆₁BM blends. The delayed charge generation arises from fullerene excitons migrating to the interfaces, and the long timescale of this process reflects the large size. The larger ratio of delayed charge generation is consistent with the high purity of the fullerene phases in PTB7–Th:PC₇₁BM. In both regards, this is consistent with the morphological findings that PTB7–Th:PC₇₁BM is purer and has larger domains, while PTB7–Th:ICBA and PTB7–Th:PC₆₁BM have similar domain purity.

Before the recombination dynamics can be discussed, the intensity dependence needs to be understood. Figure 3.16 presents the polaron decay dynamics at a number of excitation densities. It is possible to lower the fluence enough to record dynamics that are not effected by excitation density. The ICBA dynamics remain independent of fluence at higher polaron populations than PC₆₁BM or PC₇₁BM indicating a possible difference in decay pathways. The recombination kinetics of PC₇₁BM are also sensitive to excitation fluence, indicating bimolecular recombination of free charges like in other efficient OPV blends.

When it comes to low-fluence polaron recombination dynamics (Figure 3.15b) PTB7–Th:PC₇₁BM shows charge recombination on the nano- to micro- second timescale, at a similar rate to PTB7–Th:PC₆₁BM. ICBA has two regions; substantial charge recombination on the sub-nanosecond timescale and longer-lived component similar to the other two fullerenes. In PTB7–Th:ICBA the mixed-phase allows an exciton to reach an interface and form a charge-transfer state; but the lack of pure fullerene phase and insufficient driving force prevents this charge from migrating from the interface, thus explaining this faster recombination phase.

3.3.4 Conclusion

Modification of the fullerene acceptors in PTB7–Th polymer BHJ solar cells has been characterised, revealing the morphology, device physics and photophysics.

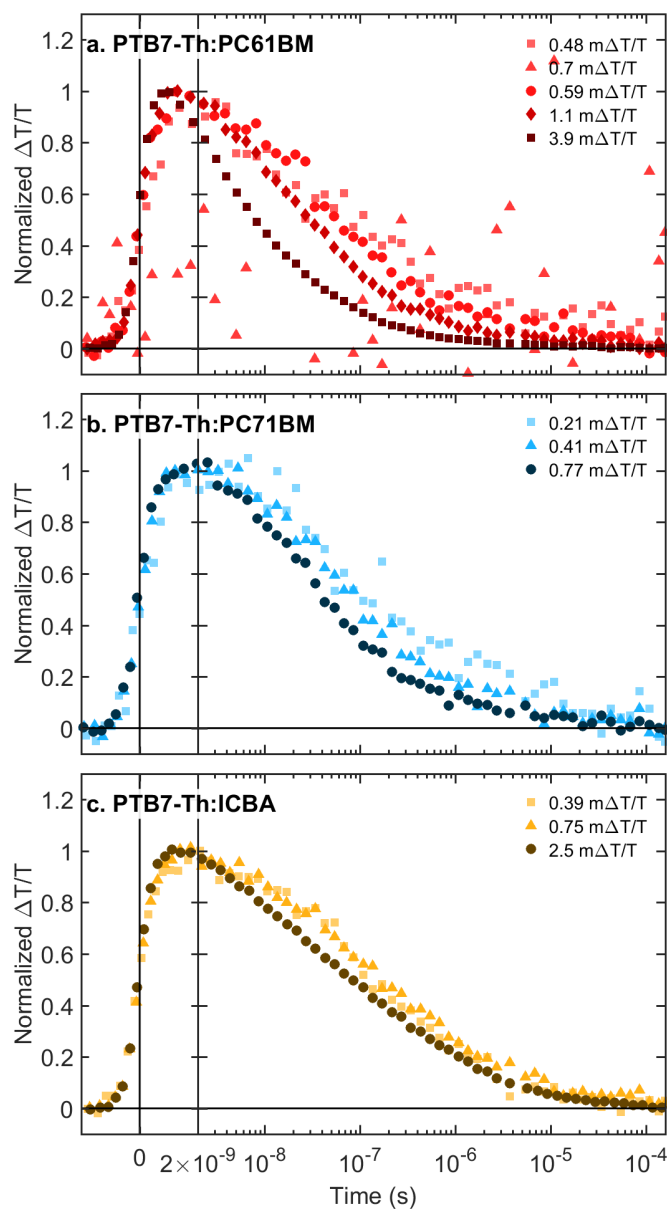


Figure 3.16: Comparison of decay dynamics following different excitation fluence at 532 nm excitation (600 ps) at maximum $\Delta T/T$ signal is noted in captions and is directly related to fluence. Each panel contains different acceptor fullerenes blended with PC₇₁BM; (a) PTB7-Th:PC₆₁BM, (b) PTB7-Th:PC₇₁BM, and (c) PTB7-Th:ICBA.

The thorough characterisation reveals the interplay between device physics, blend morphology and photophysics. Transient absorption spectroscopy is able to correlate the smaller and more intermixed domains in PTB7–Th:ICBA and the PTB7–Th:PC₆₁BM with higher prompt charge generation when compared to PTB7–Th:PC₇₁BM. The lack of driving force due to the lower LUMO–LUMO offset ICBA and PTB7–Th results in lower PL quenching and lower conversation efficiency of excitons to charges. PTB7–Th:PC₇₁BM has longer geminate lifetime when compared with PC₆₁BM and ICBA giving evidence towards better charge separation. The efficient delayed charge generation, longer charge lifetime, and higher absorption in the visible all combine to improve the PCE by 25 % to 9.4 % from ~7.5 % observed in the other fullerene acceptors.

3.4 Experimental

All active layers studied were prepared and provided by Professor Chris McNeill's team. They were stored in the dark in a parafilm sealed plastic container while shipping, and upon receipt and when not understudy, they were stored in a nitrogen atmosphere in the dark. The transient absorption set-up is the final optimised layout as noted in Chapter 2. The transient absorption measurements were carried out under a dynamic vacuum. No sample degradation was detected during TA measurements, as the signal intensity and dynamics did not change between measurement repetitions. Steady-state absorption spectra were collected using a Varian Cary 50 Bio spectrophotometer. The sample was loaded into the vacuum chamber and oriented to have the incident probe light the same as the TA measurements. Steady-state photoluminescence spectra (PL) were collected using a Horiba Fluorolog-3 spectrofluorometer. The same films used in TA were loaded into the spectrometer, and PL was collected using a front-facing geometry. For each series of films studied, the incident angle of excitation was consistent between all films in the series.

Chapter 4

Towards a systematic understanding of how to improve the performance in an all polymer solar cells

In this chapter, the devices studied are all-polymer bulk-heterojunction solar cells (APSCs). Transient absorption spectroscopy is used to measure photophysics, and this is combined with advanced morphology and electrical characterisation to systematically explore the effect of chemical modification on the power conversion efficiency (PCE) of APSCs. Several advanced characterisation techniques are used to separate the various factors that influence PCE to understand the interplay between device physics, morphology, and photophysics. As photophysics is the focus of this thesis, transient absorption and steady-state optical measurements are discussed in detail, and the other characterisation results will be presented as a summary and discussed in the context of the overall findings. Two systems are studied here. The first, an oxygen atom in PTB7 is substituted with a thiophene unit (PTB7-Th), increasing steric bulk and doubling the PCE. We find

that purer phases and longer-lived charges are responsible for the doubling of PCE in PTB7–Th. In the second, we aim to understand how fluorination affects the acceptor polymer. The PCE increases as hydrogen atoms on the acceptor polymer (N2200 derivative, blended with PTB7–Th) are substituted with fluorine. Here, the photophysics remains essentially unchanged, but improvements in absorption and morphology increase PCE from 3.1 % with no fluorine atoms to 4.6 % when four fluorine atoms are added.

Professor Chris McNeill’s team has provided the active layers of the device for transient absorption characterisation; they also measured and analysed the electrical and morphological characteristics. The data presented in this chapter has been published in:

- Deshmukh, K. D.; et al. Critical Role of Pendant Group Substitution on the Performance of Efficient All–Polymer Solar Cells. *Chem. Mater.* **2017**, 29, 804–816.
- Deshmukh, K. D.; et al. Impact of Acceptor Fluorination on the Performance of All–Polymer Solar Cells. *ACS Appl. Mater. Interfaces.* **2018** 10 (1), 955–969

4.1 Introduction

All polymer solar cells (APSCs) are named as such because the active layer, light-absorbing and charge separation, only has polymetric materials. This use of all polymer materials differentiates APSCs from other bulk–heterojunction polymer solar cells by the electron acceptor being a polymer, unlike fullerene (Chapter 3) or small–molecule acceptor (Chapter 5).

Over the past few years, there has been significant interest in developing all–polymer solar cells (APSC).^{99,109,246,285–287} The interest in APSC has been driven in part by fullerene acceptor based OPVs appearing to have reached their theoretical limit without any significant improvement in PCE reported in recent

years.^{31,102,111,244,246,288} Along with the stall in fullerene progress, APSC have a lower production cost (compared with fullerenes), improved mechanical properties, and promising stability.^{54,289–292} Many reviews have been published in recent years detailing the enhancement of PCE and providing an understanding of the various aspects that impact performance.^{109,246,285–287,293–296} The aspects relevant to this work are summarised below.

The idea of making an APSC has been around since the first OPVs.^{76,83} However, the PCE had lagged due to poor understanding of the role morphology plays and a lack of suitable acceptor polymers.^{58,131,297–299} The rapid increase in APSC power conversion efficiency (PCE) over the last few years has stemmed from an increased understanding of the role morphology plays^{131,134,287,297}, and the development of n-type polymers, primarily naphthalenediimide (NDI) based, that offer high electron affinity and electron mobility.^{294,300} There has been concerted research effort into finding new polymer acceptors,^{98,104,301–304} and optimised morphology,^{297,305–307} has resulted in a rapid increase in reported efficiency of APSC; now reported at more than 10 %^{293,294,308} and is approaching that of fullerene-based OPVs. However, the recent explosion of PCE in the non-fullerene small-molecule acceptor (SMA) literature means the APSC PCE remains several percentage points behind the most efficient bulk-heterojunction (BHJ) organic photovoltaic (OPV) devices.

All polymer systems are exciting candidates for use in BHJ solar cells because they have many benefits. One of the unique advantages of APSC is their mechanical properties, i.e. they have lower brittleness, ductile and deformable.^{54,293,294,309,310} The improved mechanical properties make APSC advantageous in physically difficult applications. There are various synthetic strategies available to tune the system and optimise the various properties to create an efficient organic photovoltaic (OPV), modification of the core polymer unit, side-chains and molecular weight are all possible when employing APSCs.^{132,287,293,294,311} With so many different modification strategies there is an ample solution space so it is possible to tune the morphology and electronic properties in many different ways in order

to find the ideal conditions. Another significant advantage of polymer acceptors, as with small molecule acceptors, is the larger extinction coefficient. The easy tunability of the absorption bands allows for complementary donor and absorption to cover more of the solar spectrum, by combining two narrow (with respect to the solar spectrum) bands to achieve broader coverage.^{293,294,308,312} Also, as polymer absorption bands are pushed towards the near-IR region, further broadening is observed due to the donor-acceptor core units and the corresponding intramolecular charge transfer transitions.²⁹³ In addition to tuning the spectral coverage, the highest occupied molecular orbital (HOMO) and lowest unoccupied molecular orbital (LUMO) offset of the donor and acceptor polymers can be tuned to maximise open-circuit voltage.^{287,293,313} Long-term stability is another area where APSCs excel when compared with their fullerenes and small molecular acceptors counterparts. Their improved stability is due to; lower molecular diffusion, increased photo-stability, and lack of photo-induced dimerisation.^{287,292,314-320}

Because of the need to balance charge generation and charge collection in APSC, morphology has a significant impact on performance.^{101,285,287,292,294,321} A detailed discussion of the PCE-morphology relationship can be found in the following review articles.^{130,132,287,297} A comprehensive summary is provided below to understand the techniques that have been employed in this work.

The morphology plays an important role in the overall performance; percolation pathways, the domain size, and relative orientation of the units of the polymer in respect to each other and the electrodes need to be controlled.^{130,131,134,287} First, in order to produce charges, the excitons must reach the interface for all varieties of OPVs. In the case of APSC, the molecular orientation at the interface must be optimised to produce favourable π -interactions between donor and acceptor polymers to split excitons into electrons and holes effectively.^{287,307,322,323} Once a charge is produced, the electron mobility becomes an essential characteristic as charge extraction directly competes with intrinsic decay pathways. The mobility of a charge is related to the degree of crystallinity, for OPV the

out-of-plane conductivity is of greater importance to charge transport.^{134,287,299} Finally, the molecular orientation with respect to the electrode is essential to allow transfer from the non-symmetric polymer to the electrode^{134,287,323} With all these requirements, optimum domain sizes and percolation pathways, the relative orientation of the polymer becomes important, donor-acceptor for generation, donor-donor (or acceptor-acceptor) for transport and then donor/acceptor and electrode for extraction; the difficulty of optimising an all-polymer system is striking. In all polymers systems, the reduced miscibility of the two polymers increases the difficulty of tuning morphology and domain size.²⁸⁵ If the domains are too large, charge recombination in the active layer will dominate.^{57,246,285} All the above requirements indicate the need to strike a balance between domain sizes, purity and orientation; therefore, in APSC, it is critically important to control the morphology.

Several variables can be used to control the morphology; these include synthetic strategies; side-chains, and modification of the core to change donor-acceptor interactions, and modification of the molecular weight.^{99,285,294} Furthermore, morphology can also be controlled with processing techniques; solvent additives, and annealing (both solvent and thermal).^{99,285,294}

The need for rigorous photophysical measurements has added value in studies, and has been highlighted as a requirement in a recent reviews.^{31,142,147,250,294,323} Determination of the correlation and causality between the observed structural, photophysical, and electrical performances will aid in the development of design guidelines and practical limitations on the efficiency to direct future research endeavours involving APSC. In this chapter, we look to disentangle the multitude of factors that affect APSC PCE by using several advanced characterisation techniques. These include understanding the charge transport, kinetics and mobility using transient photocurrent and space-charge-limited current (SCLC). A picture of the polymer morphology, i.e. orientation, domain purity, and domain size, is constructed using several synchrotron-based techniques. As well as extensive characterisation of the photophysics, i.e. the contribution made by this author.

In order to characterise how the initial photon energy flows through the OPV, several techniques are employed. The process starts with the absorption of a photon, measured via steady-state absorption; exciton migration to the interface and the subsequent charge generation and intrinsic charge lifetime is tracked using transient absorption spectroscopy; then photoluminescence quenching measurements are used to quantify the charge dissociation at the interface.

This chapter presents two photophysical studies that contribute to a more considerable effort aimed at understanding how the mechanism of which substitution of donor or acceptor polymers affects solar power conversion efficiency (PCE) in all-polymer solar cell (APSC). The donor family of interest in this work is either derived from or is, P(NDI2OD-T2) (also known as N2200, Polyera Active Ink™).³²⁴ N2200 was one of the first reported and most investigated acceptor polymers used in APSC.²⁹⁴ When initially mixed with P3HT as donor efficiency of 0.16–0.18 % where observed^{325,326}, this efficiency rapidly improved, reaching 5.7 % when PTB7-Th was used and optimising morphology.²⁶⁸ In the following years, N2200 and derivatives were paired with various donor polymers to study both the underlying photophysics (as with this work) and also to improve device performance.²⁹⁴ One of the large downsides, and interestingly a contrasting point between APSC, and small-molecule acceptor (SMA), discussed in Chapter 5, is the low extinction coefficient and imperfect exciton dissociation of NDI-based polymers.^{113,294,314,327,328}

The first study looks at the effect of pendant group substitution on the donor polymer comparing PTB7-Th and PTB7, finding that longer charge lifetimes and purer domains are the likely reasons for the almost two-fold increase in PCE. The second study explores a series of fluorinated acceptor polymers finding no meaningful difference in the photophysics; therefore, attributing the efficiency changes to charge collection efficiency.

4.2 Effect of pendant group substitution on the donor polymer in all-polymer solar cells

While there are many strategies employed to increase the efficiency of APSC, as mentioned above; molecular weight, solvent addition, the modifications investigated here is side-chain engineering. Specifically the commonly employed modification of the pendant group for a bulky aromatic unit.^{179,329,330}

An excellent case-study for effect of pendant group substitution in APSC is replacing PTB7 with PTB7-Th when blended with N2200 as the acceptor. In these systems, the difference in the donor structure is the substitution of the single oxygen atom in the side chain attached to the benzodithiophene unit of PTB7 for a thiophene to give PTB7-Th (Figure 4.1). The substitution of oxygen results in a more than doubling of efficiency from 2.7 %²⁹⁷ to 5.7 %.²⁶⁸ Further, in the case that N2200 is substituted with a fullerene, the change in efficiency is only 10 %; from 9.2 % (PTB7) to 10 % (PTB7-Th).^{260,331} This variation in behaviour between APSC and fullerenes highlights the need to understand the underlying cause as it could point to a bottleneck present only in APSC.

Both blends have been carefully optimised by solvent annealing and molecular weight determined by our collaborators so that the changes due to pendant group substitution are emphasised. The HOMO and LUMO levels are also shifted to lower energy in PTB7-Th, this change could effect the driving force for charge separation with PTB7-Th having a lower electron injection driving force than PTB7.

The careful optimisation of blends and extensive use of characterisation techniques have allowed us to quantify the changes in electrical, photophysical and morphology, which are then related to the change in PCE. The morphology is mostly unchanged, but there is a significant increase in hole mobility in PTB7-Th leading to improved charge collection. In regards to the photophysics, we find

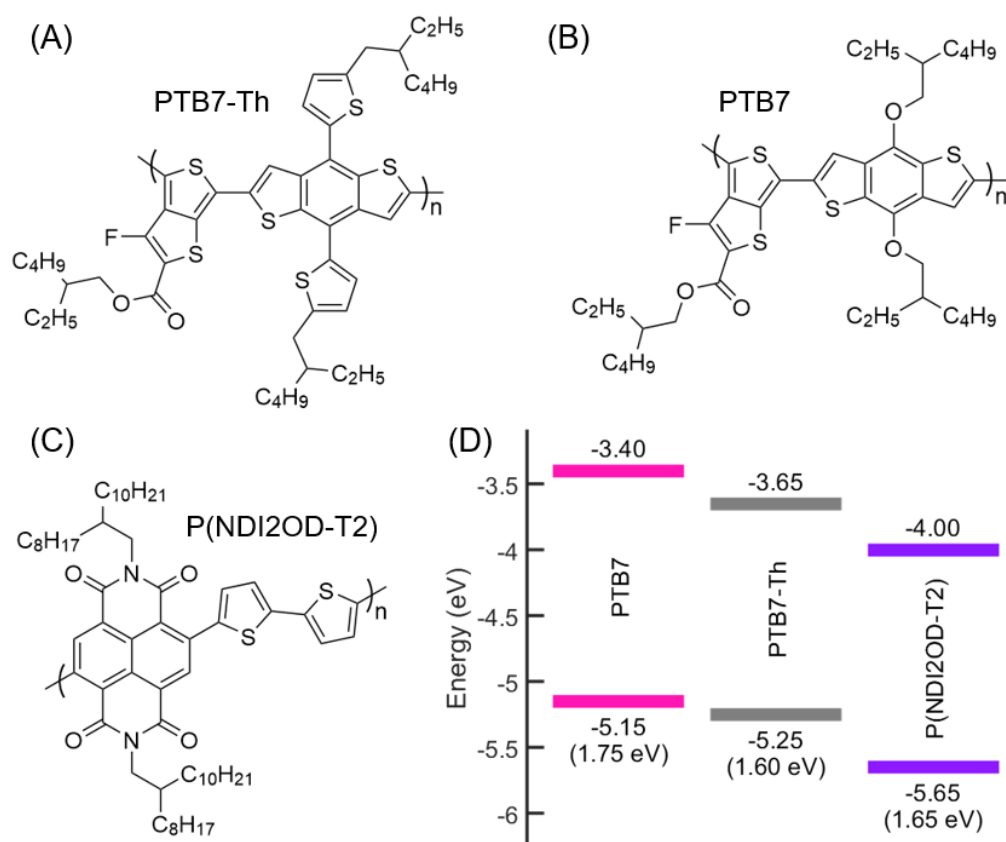


Figure 4.1: Chemical structures of PTB7-Th (A), PTB7 (B), donor polymers and the P(NDI2OD-T2) acceptor (C) used in the devices studied. The frontier molecular orbitals are presented in (D).^{258,332}

that in blends using PTB7-Th the geminate recombination is suppressed, which would further aid in charge collection.

By combining photophysics and other characterisation techniques, we have identified that morphology effects are minimal while the thiophene substitution effects the charge mobility and lifetime leading the higher charge collection efficiencies and therefore improving PCE.

4.2.1 Morphology and device characterisation

Before considering the photophysics, a morphological and electronic picture of the device is presented. The results in this section are from collaborators but are significant when discussing the photophysics in a broader context. The electrical characterisation shows a significant drop in external quantum efficiency (EQE) and PCE with PTB7 blend being about half of the PTB7–Th and the morphological measurements point to little variation between device.

The current vs. voltage (J–V) measurements are summarised in Table 4.1 and show that PTB7–Th has a PCE more than two times higher than PTB7, 4.4 % and 2.1 % respectively. This difference is largely associated with short-circuit current (J_{sc}) with PTB7–Th, 10.8 mA cm^{-2} , being almost twice as high as PTB7 (5.5 mA cm^{-2}), with the large decrease in EQE for PTB7 (max, 29 % vs 52 %) across the spectrum supporting an internal loss mechanism opposed to less light being absorbed. The decreased fill-factor of PTB7 when compared with PTB7–Th further supports an internal loss mechanism.

Material	V_{OC}	J_{SC}	FF	PCE	EQE	μ_h	μ_e
P(NDI2OD–T2):	V	mA cm^{-2}		%	%	$\text{cm}^2 \text{ V}^{-1} \text{ s}^{-1}$	
PTB7	0.78	5.5	0.43	2.1	29	5.8×10^{-5}	1.2×10^{-3}
PTB7–Th	0.80	10.8	0.50	4.4	52	5.5×10^{-4}	5.8×10^{-4}

Table 4.1: Electrical characterisation of P(NDI2OD–T2) blends with PTB7–Th or PTB7. PCE measurement collected under the illumination of AM 1.5.

The two blends have different hole and electron mobilities, Table 4.1, with PTB7 having largely unbalanced values while PTB7–Th are balanced. While PTB7–Th has two times higher electron mobility PTB7 has nine times higher hole mobility (in respect to the other blend). Transient photocurrent measurements point to PTB7–Th having a higher degree of carrier trapping as a longer-lived (tens of microseconds) tail is observed after the light is turned off. These observations are consistent with trapping and then non-geminate recombination being a noticeable loss mechanism in PTB7 when compared with PTB7–Th blends.

Morphological data shows little variation between the two polymers. Atomic force microscopy (AFM) suggests the fibres of P(NDI2OD-T2) is disturbed by the polymer while transmission electron microscopy shows a highly mixed nano-morphology without coarse phase separation. In the blend the polymer packing is similar to the neat film; i.e. well-ordered phase with highly face-on orientation. The face-on orientation is good for charge transport and percolation.^{135,333,334}

The electrical characterisation shows a tremendous difference in PCE (4.4 % vs 2.2 %) arising and J_{sc} . These differences cannot be explained by variation in morphology, and the EQE indicates a similar light absorption profile. The variations in PCE should be determined by variation in charge generation, charge lifetimes, or percolation. To isolate the root cause, we use steady-state absorption to elucidate excitation wavelength to interrogate each polymer phase separately. Photoluminescence is then employed to give insight into the charge transfer state being formed, while transient absorption will provide information on the phase purity and lifetimes of charges.

4.2.2 Steady-state absorption and photoluminescence

Steady-state UV-VIS absorption and photoluminescence measurements were taken. Using absorption measurements, we can identify aggregation-induced changes in behaviour between neat and blended materials, while the photoluminescence (PL) quenching allows us to determine the yield of charge separation.

Figure 4.2 shows the steady-state absorption spectra for the blended films. The similar absorption across the visible to near-infrared regions rules out increased absorption being the cause of J_{sc} variations. While different scattering profiles between the blends could cause some variation in the number of photons absorbed, it is unlikely that this would solely account for a doubling in the current. Panels b-c contain linear decompositions of the blend spectra into contributions from the polymer and P(NDI2OD-T2), with the final fitted values presented in black. These show that the blend spectra are well described by the neat com-

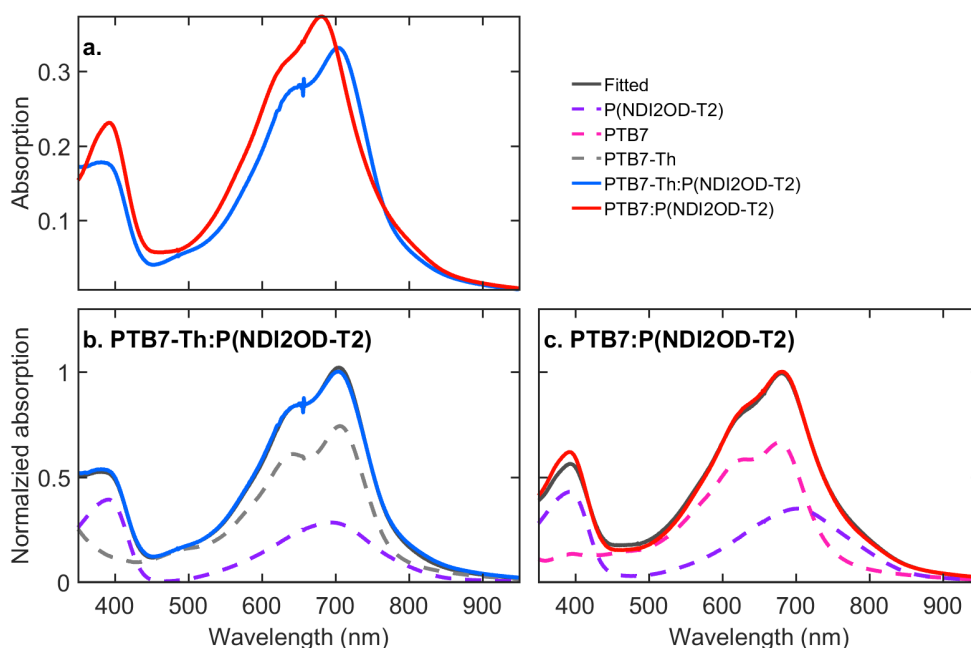


Figure 4.2: Absorption spectra of the various blends and neat films studied. a. the absorption of PTB7-Th:P(NDI2OD-T2) and PTB7:P(NDI2OD-T2) films measured. Panels b. and c. present normalised absorption spectra of either blend (various colours), best-fit line (black) that is a weighted linear combination of the constituent components, and the individual weighted components (purple, grey and pink).

ponents indicating little change in the chromophore interactions when blended, consistent with morphology measurements discussed above.

Normalised steady-state photoluminescence (PL) are shown in Figure 4.3 for neat films of donor polymers PTB7-Th & PTB7 and P(NDI2OD-T2) acceptor polymer following 625 nm excitation are shown. PTB7 has an onset ~680 nm rising into a peak at 790 nm while PTB7-Th has a sharper rise starting at ~700 nm and then continuing into the near-infrared region. In the acceptor polymer, P(NDI2OD-T2), a significant red-shift is observed in comparison with the acceptor polymer; PL presenting a tail in the 700–850 nm region that looks to continue further into the near-infrared.³³⁵ Due to the low emission intensity from

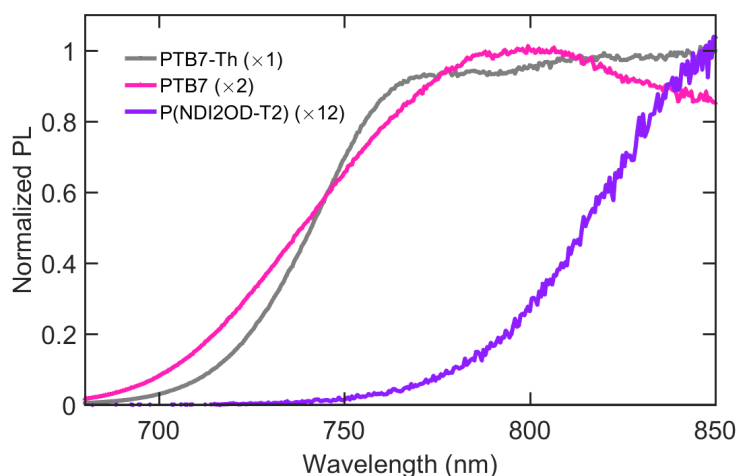


Figure 4.3: Steady-state photoluminescence spectra of neat PTB7-Th, PTB7, and P(NDI2OD-T2) films collected with 625 nm excitation. The spectra are presented normalised, with the details showing the relative scaling applied to each.

P(NDI2OD-T2) in the neat film, it was not possible to calculate quenching efficiencies, instead only the polymer quenching is reported.

Steady-state photoluminescence (PL) measurements with excitation at 532 nm, 625 nm, and 715 nm have been performed on blends to assess the efficiency of exciton dissociation. Table 4.2 summarises the PL quenching data, these have been calculated by considering the neat PL intensity for each of the components after correcting for the fraction of absorbed photons. The fraction absorbed by each phase was taken from the linear decomposition of the absorption spectra. There is no difference in PL quenching between the two blends when excitation at 532 nm and 625 nm, with both, have >98 % quenching efficiency indicating efficient dissociation of excitons on the donor phase. A slightly lower efficiency of 96.8 % for the PTB7:P(NDI2OD-T2) compared with >98 % for PTB7-Th:P(NDI2OD-T2) is calculated following 715 nm excitation. Overall both blends show similarly high levels of PL quenching, suggesting efficient exciton dissociation at the interface.

Material	532 nm	625 nm	715 nm
PTB7:P(NDI2OD-T2)	98.7 %	98.6 %	96.8 %
PTB7-Th:P(NDI2OD-T2)	98.8 %	98.5 %	98.7 %

Table 4.2: Photoluminescence quenching of P(NDI2OD-T2) blended with PTB7-Th or PTB7 after excitation at 532 nm; 625 nm; or 715 nm.

The steady-state measurements do not show any significant difference between PTB7-Th and PTB7, therefore we perform transient absorption spectroscopic methods to understand the photophysics. It reveals a change in phase purity unresolved by above morphological differences and significant difference between charge lifetimes.

4.2.3 Ultrafast photophysics

To understand if there are any effects on the photophysics induced by the substitution of oxygen for thiophene transient absorption spectroscopy (TA) was carried out from the femtosecond to nanosecond timescale. A broad spectral window was able to reveal the exciton to polaron transfer dynamics, while the nanosecond timescale shows a considerable variation in carrier lifetimes between PTB7 and PTB7-Th blends.

Signal assignment

As a first step in understanding the signal that arises from TA spectroscopy on the polymer:P(NDI2OD-T2) blends the distinct features present in the neat films of the polymers are identified. Figure 4.4 shows a single spectrum that is representative of the TA surface after 600 nm (2.07 eV) excitation for films of the neat materials studied. The PTB7-Th spectra can be described by a ground-state bleach signal (GSB, $\Delta T/T > 0$) spanning the 580-780 nm (2.1-1.6 eV) range with a stimulated emission (SE, $\Delta T/T > 0$) at the lower energy edge. This positive signal overlaps with the steady-state absorption spectra presented above. The beginning of a broad photo-induced absorption (PIA, $\Delta T/T < 0$) is resolved

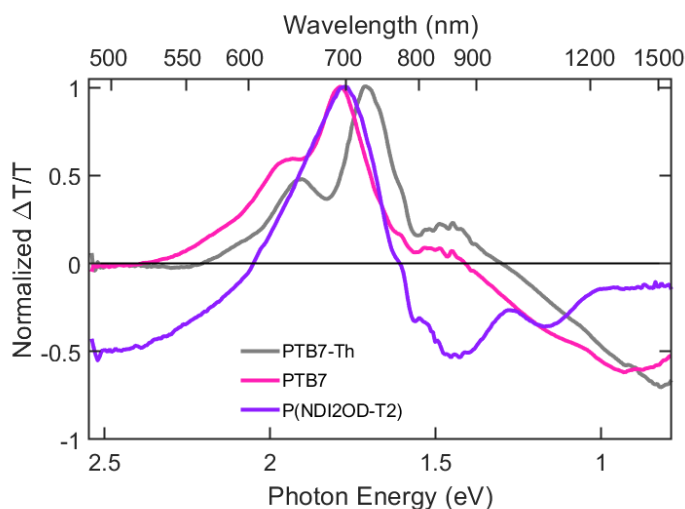


Figure 4.4: Normalised TA spectra attributed to singlet exciton for PTB7-Th (600 nm, $1.6 \mu\text{J cm}^{-2}$), PTB7 (600 nm, $3.4 \mu\text{J cm}^{-2}$) and P(NDI2OD-T2) (600 nm, $6.4 \mu\text{J cm}^{-2}$) collected in neat blends.

in the near-infrared region $>940 \text{ nm}$ ($<1.32 \text{ eV}$). The PTB7 spectra features are identical to PTB7-Th except for a shift to higher energy, consistent with the steady-state absorption. This blue-shift results in the near-infrared PIA peak being resolved to show a clear peak at 1400 nm (0.89 eV). In both donor polymer cases, the PIA feature in the near-infrared is diagnostic of a singlet species (owing to the simultaneous SE feature), while the GSB region can give an indication of the population remaining in the excited state. For the donor, P(NDI2OD-T2), a broad PIA is visible across the spectral window with peaks at 850 nm (1.46 eV) and 1000 nm (1.24 eV), a GSB region is set on top of this PIA in $600\text{--}750 \text{ nm}$ ($2.1\text{--}1.7 \text{ eV}$). The P(NDI2OD-T2) singlet is identified by a negative signal in the $<550 \text{ nm}$ ($>2.25 \text{ eV}$) as there is minimal contribution from the donor polymers in this region. In saying this, it is possible that the generated charge pairs could introduce a negative feature in this region.

Figure 4.5 presents TA spectra slices taken at various different delay times after 600 nm excitation of PTB7-Th:P(NDI2OD-T2) (a) and PTB7:P(NDI2OD-T2) (b).

A new peak, not seen in the neat materials, is present at 1120 nm (1.11 eV) this is attributed to polaron on the donor polymer, due to it not being in the neat polymer and also measurements of fullerenes and other donor materials showing the same peak (Chapter 3). The GSB region 560-780 nm (2.2-1.6 eV) points towards varying charge kinetics, as the bleach in PTB7 has reduced to a ~35 % intensity by 5 ns but PTB7-Th is still at more than 60 %. The variation observed will be discussed further once charge and singlet exciton dynamics are separated. At between 200 fs and 500 fs a rapid loss of the donor polymer singlet exciton signal, PIA at >1240 nm (<1.00 eV), is observed for both blends. Exciton to charge conversion is likely as the GSB region is unchanged, but it is difficult to assign due to the similar extinction coefficients at 1120 nm (1.11 eV). The overlap between the exciton and the new resulting species makes it quantitatively difficult to compare the evolution of species. Mathematical bilinear decomposition separates the overlapping species into an initial exciton and another species attributed to charge carriers.

Figures 4.6 shows the results of the bilinear decomposition of the TA surface into; spectra (a), kinetics (b), and residuals (c). The residuals are presented at ten times the intensity of the surface to emphasise that while the decomposition does not account very well for the late time dynamics, it does account for most of the variation in the data.

In both polymer blends the series of TA measurements at various excitation wavelengths (400 nm, 600 nm, and 700 nm) can be well described by the three (PTB7:P(NDI2OD-T2)) or four (PTB7-Th:P(NDI2OD-T2)) spectra shown in Figure 4.7. As the donor polymer absorbs 58 % of the 700 nm excitation in the PTB7 blend and 70 % in the PTB7-Th one of the spectra are associated with excitons in the donor polymer phase. It is assigned based on its contribution decaying quickly, and the spectra match those of neat donor polymers; i.e. featuring a ground state bleach above 775 nm (1.60 eV), photo-induced absorption that peaked around 1240-1550 nm (1.0-0.8 eV), and characteristic stimulated emission around 780-880 nm (1.6-1.4 eV).

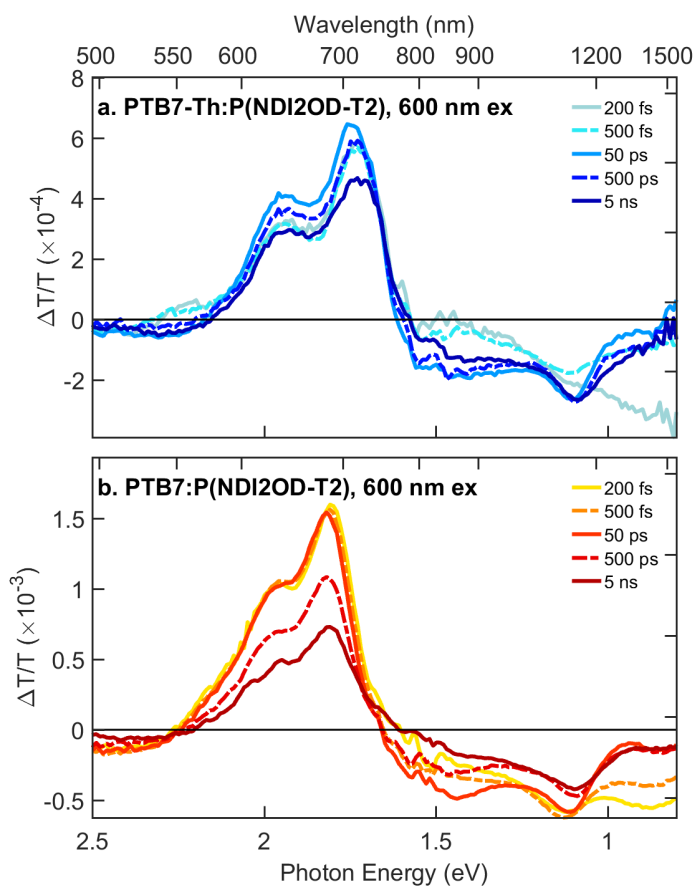


Figure 4.5: TA spectra slices taken at various times delay between excitation and probe are presetned for: (a) a film of PTB7-Th:P(NDI2OD-T2) after 100 fs excitation at $700 \text{ nm } 0.6 \mu\text{J cm}^{-2}$ (b) a film of PTB7:P(NDI2OD-T2) after excitation at $700 \text{ nm } 1.4 \mu\text{J cm}^{-2}$.

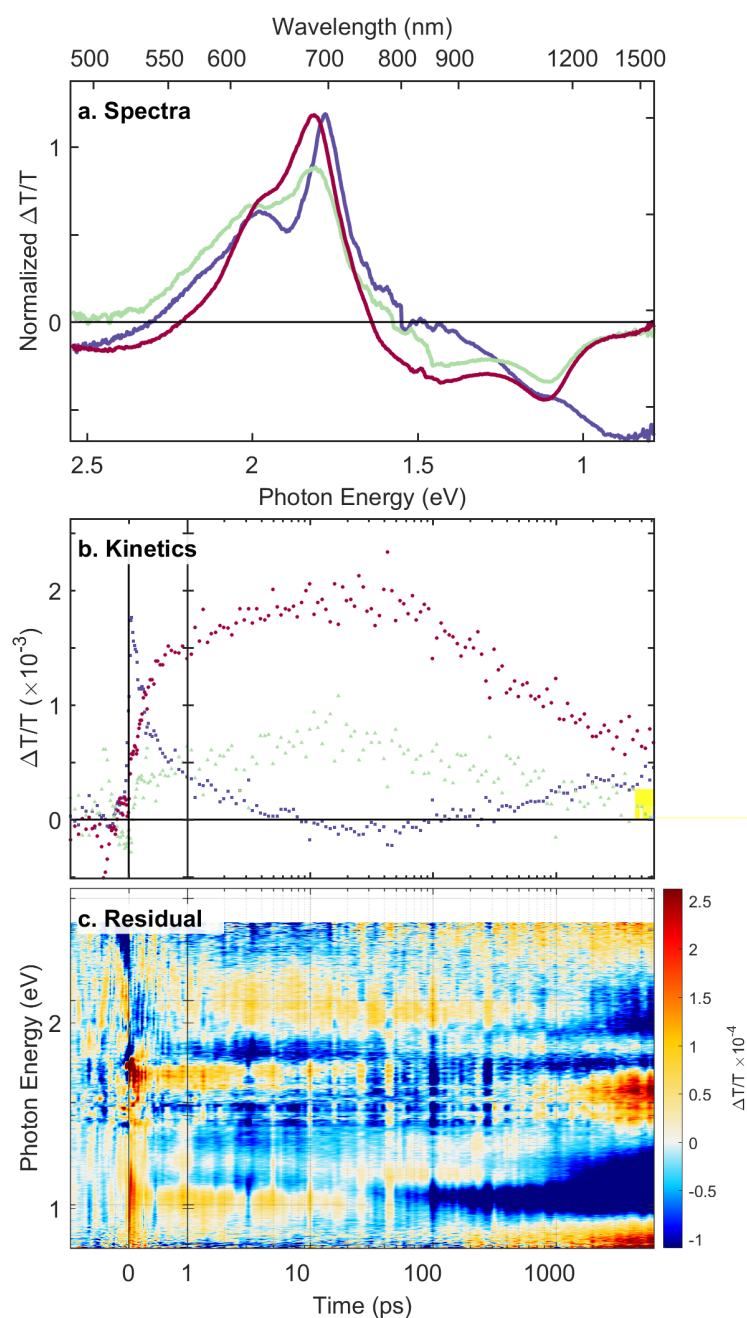


Figure 4.6: Results of bilinear decomposition of PTB7:P(NDI2OD-T2) after excitation at 700 nm $1.4 \mu\text{J cm}^{-2}$. In panel a. are the three spectra features, b. are the time-dependent behaviour of the populations associated with the spectra in a. c. are the residues after using spectra and kinetics in a. and b. to represent the TA surface

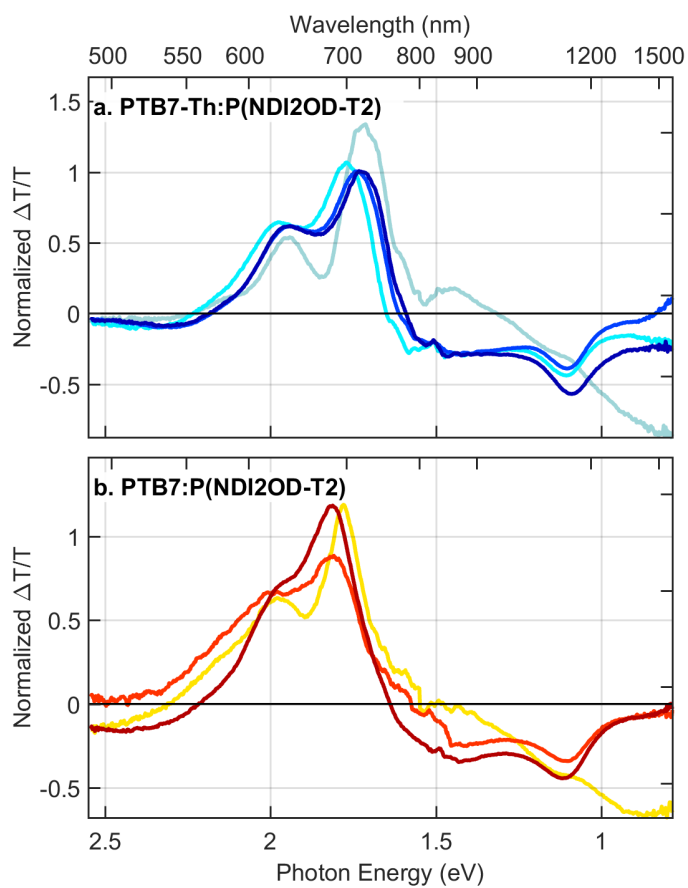


Figure 4.7: The spectra used for PTB7-Th:P(NDI2OD-T2) (a) PTB7:P(NDI2OD-T2) (b) in the bilinear decomposition at the various excitation wavelengths (400 nm, 600 nm, and 700 nm).

The remainder of the spectra are attributed to charge species, specifically hole polarons in the donor polymer as the optical signatures of the acceptor are too weak to observe. All of these polaron spectra retain the ground state bleach and do not have stimulated emission signal as seen in the neat donor polymer spectra. The need for multiple spectral components accounts for the dynamically red-shifting photo-induced absorption peak near 1280 nm (0.97 eV). A similar spectral shift has been attributed to charges migrating to lower-energy sites,⁹² and in some cases to triplet formation.^{139,140} The possibility of a triplet is excluded by comparison to triplet spectrum obtained by sensitising films of the donor polymer with platinum porphyrin chromophore. Figure 4.8 shows the polaron PIA migration at various times (coloured) compared with the triplet spectrum, for both donor polymers, the variations are significant enough to rule out triplets.

The dynamics of donor polymer excitons and charges are shown in Figure 4.9, in this plot the spectra have been normalised by considering the GSB regions, 560-750 nm (2.2-1.7 eV) for the PTB7 blend and around 620-750 nm (2.0-1.7 eV) for the PTB7-Th blend, to internally reference the intensities of all components. Once the signal has been normalised across the species present, the summation has been scaled to unity, warranted by the high PL quenching efficiencies. For the presentation of the polaron population (c) the kinetics of all charge components have been added, in this way the spectral shifts are ignored and just the population can be considered. With a comparative population for each blend resolved, the dynamics will be discussed in two parts below; charge generation, and charge recombination.

The charge generation can be broken down into three parts. First, we will discuss the prompt generation (<200 fs inside our instrument response function). Figure 4.9a shows the exciton decay dynamics are essentially identical decay between PTB7:P(NDI2OD-T2) and PTB7-Th:P(NDI2OD-T2) supporting the morphology conclusions that domain sizes are similar in both blends. The prompt charge generation cannot be compared using exciton signal as the rapid decay (<1 ps)

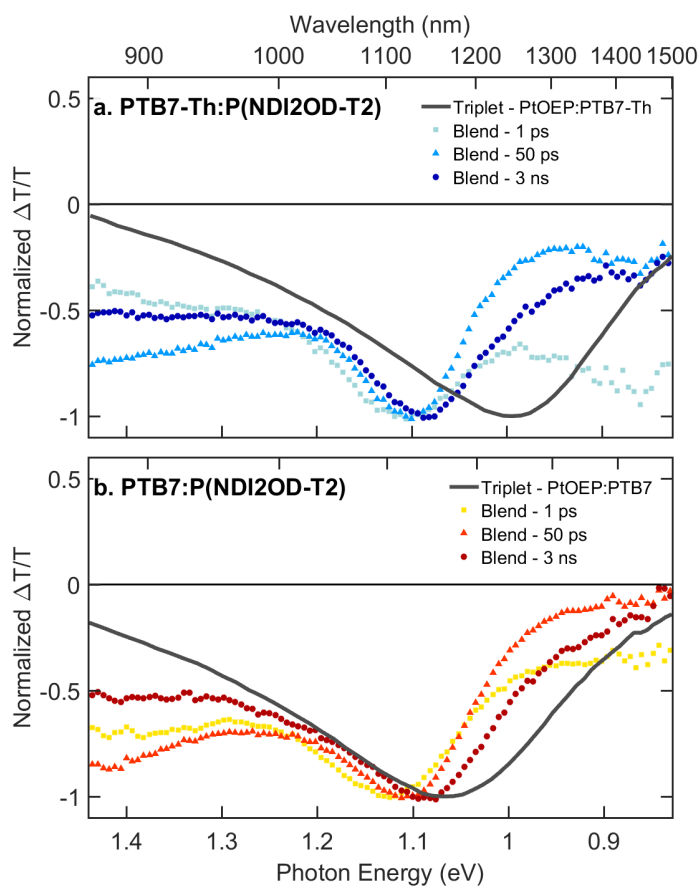


Figure 4.8: A comparison between sensitised triplet (grey) and the TA spectra observed when blend P(NDI2OD-T2) at various time delays. (a) a film of PTB7-Th:P(NDI2OD-T2) after excitation at 700 nm $0.6 \mu J cm^{-2}$ (b) a film of PTB7:P(NDI2OD-T2) after excitation at 700 nm $1.4 \mu J cm^{-2}$.

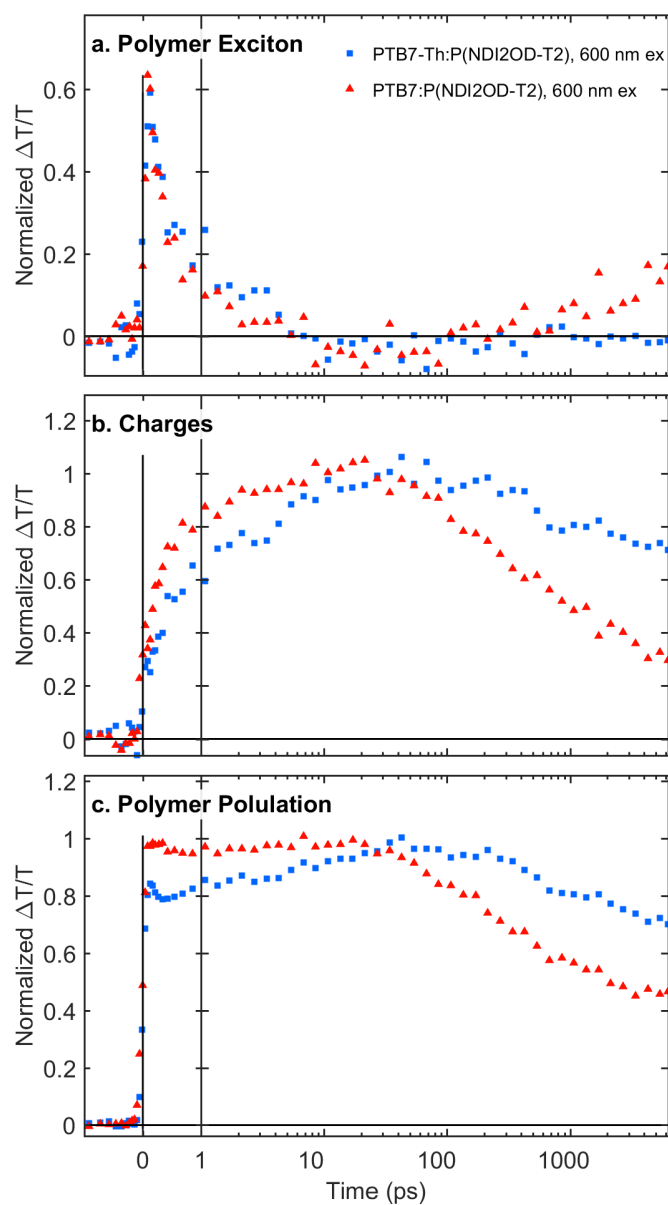


Figure 4.9: Population dynamics for the various species extracted via the above described method. PTB7-Th:P(NDI2OD-T2) is shown in red following 600 nm excitation $0.6 \mu\text{J cm}^{-2}$, while in blue PTB7:P(NDI2OD-T2) also after 600 nm excitation $1.5 \mu\text{J cm}^{-2}$. (a) shows the exciton decay, (b) are the charge generation and decay dynamics (c) is the overall excited state population on each polymer.

leads to large uncertainty in the initial amplitude as it is convoluted with the instrument response function (IRF) (Section 2.3).

Instead, the charge population (b) can be used, showing a distinct difference with PTB7–Th having ~50 % of charges generated within 200 fs lower than the ~70 % seen in PTB7. The ratio of prompt and delayed charge generation reflects the balance of intermixed and pure polymer phases, with the PTB7–Th blend having a lower fraction of intermixed regions.

Although the weaker optical signatures of the P(NDI2OD–T2) acceptor component mean that the measurement only resolves excitations in the PTB7–Th donor polymer, insight into the P(NDI2OD–T2) phase can still be gained by considering the total donor polymer population (Figure 4.9c, excitons + charges). From this we can conclude that the early picosecond (<10 ps) kinetics are dominated by excitons in PTB7–Th donor phase. It is also possible to measure the timescale of hole injection from the increase in polymer population; P(NDI2OD–T2) hole injection is slower than electron transfer from the donor polymer occurring on the order of 10s picoseconds. This contrasts significantly with PTB7 whereby the only observed charges are either promptly generated, could be from either P(NDI2OD–T2) or PTB7 phase, or from exciton migration in the PTB7 phase, this suggests that P(NDI2OD–T2) is more intermittently mixed in PTB7, an effect unseen in the morphological data. However, fast charge photogeneration does not necessarily translate to efficient charge extraction; finely intermixed blends (both polymer:polymer and polymer:fullerene) frequently suffer from severe geminate recombination losses when their morphology or interfacial electronic structures restrict charges from escaping the domains in which they were generated.^{92,95,130,144–149}

While the charge generation points to PTB7–Th having less intermixed domains that could be beneficial for charge extraction and separation, this is also supported by the charge recombination dynamics. We can consider the charge recombination dynamics by looking at delay times greater than 50 ps, Figure 4.9b.

In the PTB7:P(NDI2OD-T2) blend, recombination is faster at comparable fluences; half of the charges recombine within approximately 1 ns, compared to PTB7-Th:P(NDI2OD-T2) blend where there is still more than half of the charges present after 6 ns. The decreased J_{sc} can be accounted for by the faster geminate recombination, whereby due to the shorter lifetimes, the charges are less likely to be extracted.

To investigate the variation in excess energy, and how the photophysical behaviour in the donor or acceptor phase excitation TA with at 400 nm, 600 nm and 700 nm excitation was measured. The excitation ratio for donor and acceptor are summarised in Table 4.3, with 400 nm primarily absorbed into the P(NDI2OD-T2) phase (1:3, polymer:P(NDI2OD-T2)) and 600 nm having the inverse ratio favouring the donor polymer. When exciting at 700 nm the ratio differs between the two donor polymers, PTB7-Th:P(NDI2OD-T2) is 2.6:1 while PTB7:P(NDI2OD-T2) is 1.6:1, in both cases they favour the donor polymer, which will increase in P(NDI2OD-T2) absorption when compared to 600 nm excitation.

Material	400 nm	600 nm	700 nm
PTB7-Th:P(NDI2OD-T2)	1:3.2 (24 %)	3.1:1 (76 %)	2.6:1 (72 %)
PTB7:P(NDI2OD-T2)	1:3.1 (24 %)	3.2:1 (76 %)	1.6:1 (62 %)

Table 4.3: Calculated absorption fraction into each material phase for P(NDI2OD-T2) blended with PTB7-Th or PTB7. The number in brackets represents the percentage of absorbed photons that make it into the donor phase.

Figure 4.10 presents a comparison of the extracted dynamics for donor excitons (top), charges (middle) and the total donor polymer population (bottom), with the two different blends shown on either side; PTB7-Th:P(NDI2OD-T2) on the left, and PTB7:P(NDI2OD-T2) on the right. Comparing the singlet exciton contribution (a,b) after 400 nm excitation results in a significantly smaller signal when compared to excitation at either 600 nm or 700 nm. This is seen for both blends and is not unexpected as at 400 nm the donor polymer phase only absorbs ~25 % of the light with a significant portion of that undergo prompt charge generation.

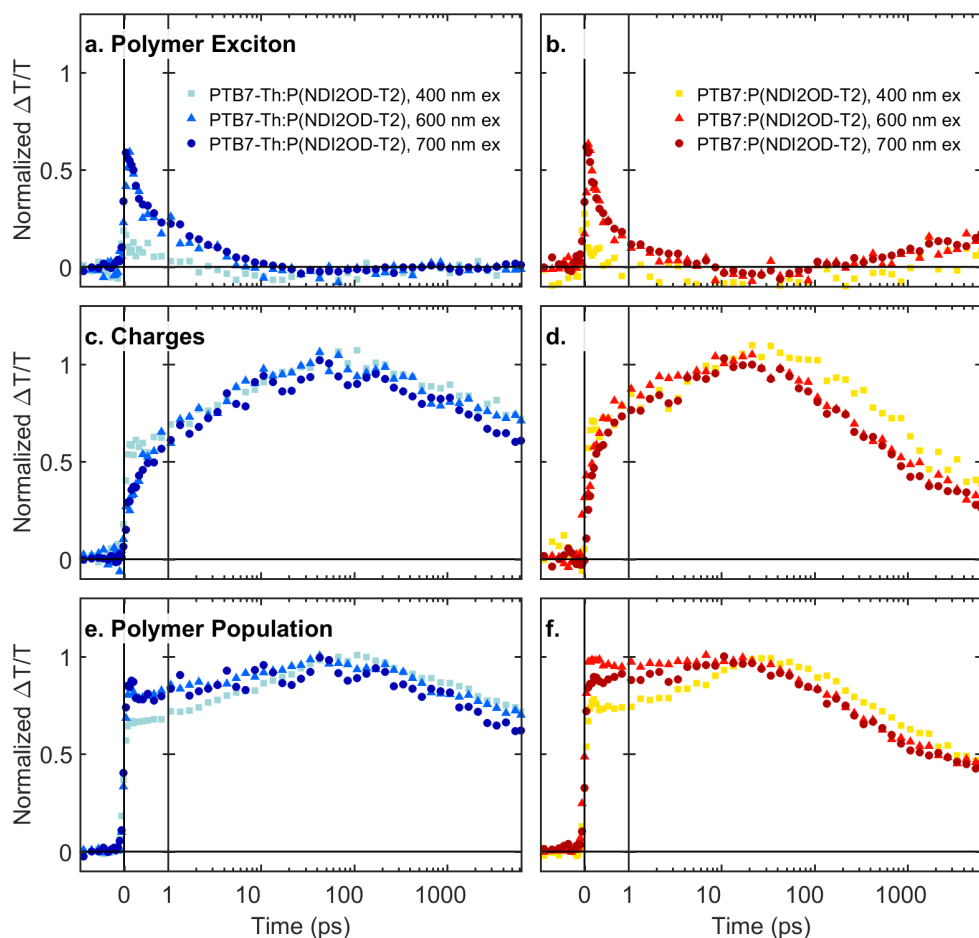


Figure 4.10: Population of the various species observed; a. and b. donor exciton, c. and d. charges, e. and f. overall excited state population. Each panel contains a single donor:acceptor blend excited at various wavelengths.

There is no difference in donor exciton signal between 600 nm and 700 nm excitation, consistent with only a small percentage decrease in light absorbed by the donor phase (4–14 %).

The charge generation profiles are similar across all the excitation wavelengths measured (Figure 4.10 c. and d.). The fact that the prompt charge generation is ~50 % and independent of excitation wavelength suggests that there is no preferential between the two phases for prompt charge generation. The decay dynam-

ics shows that charges from both the donor and acceptor undergo similar decay dynamics suggesting that both pathways are of equal value to the overall PCE.

The hole injection from the P(NDI2OD-T2) phase is measured via the proxy of donor polymer population; this is because the P(NDI2OD-T2) hole injection will increase the polymer population as a new charge excited state is formed. For both polymers, the hole injection timescale remains unchanged with the population peaking at ~30 ps. In the PTB7:P(NDI2OD-T2) blend there higher fraction of holes injected when compared with 600 nm or 700 nm excitation, while PTB7-Th:P(NDI2OD-T2) shows the expected decrease to no hole injection at 600 nm with the lowest fraction of light absorbed and the most substantial value following 400 nm excitation. The variation of excitation wavelength shows that both the donor and acceptor phase produce charges of equal value to the final PCE, with a decrease in excess energy not affecting the charge decay dynamics. This adds supports that the variation is due to the difference in the geminate lifetime of charges, as discussed previously.

4.2.4 Summary

The transient absorption studies reveal the cause for the significant difference in PCE. Lower prompt charge generation in PTB7-Th:P(NDI2OD-T2) suggests that PTB7-Th has purer domains with less mixing between the two-phase, something that unfortunately could not be collaborated with the morphological studies. This balance of pure and mixed is likely an important factor for driving long-range charge separation and suppressing charge recombination.^{92,95,130,144–149} Charges generated in intermixed phases may be driven apart into pure regions, provided that the intermixed phase is not so large that charges remain trapped there. This observation is corroborated by the longer recombination lifetimes of PTB7-Th:P(NDI2OD-T2) as the now separated charges have a higher energy cost in order to undergo recombination. Even if the lifetimes do not reflect a difference between separated and bound charges, the longer charge lifetime will

benefit charge extraction, giving more time for the charges to reach the electrodes and add to the photocurrent.

4.3 Impact of acceptor fluorination on the performance of all-polymer solar cells

This section aims to understand how fluorination of the acceptor polymer influences device performance and if the underlying photophysics are changed. To achieve this, we investigate the effect of fluorinating an NDI-based acceptor polymer comparing the substitution of two, and four, hydrogen atoms with fluorine, and also looking at the behaviour of the un-fluorinated base polymer. Each of these acceptor polymers is then blended with PTB7-Th to produce the active layer of a bulk-heterojunction (BHJ) solar cell.

Structural modification of the P(NDI2OD-T2) polymers has been studied with various degree of success by several research groups.^{98,132,301,305,336–339} An unmodified P(NDI2OD-T2) has achieved an efficiency of 5.7 %²⁶⁸ while polymers based on the core structure can achieve an efficiency of 7.7 %.³⁰⁵ Fluorination of the acceptor polymer P(NDI2OD-T2) to improve OPV performance has been investigated previously.^{301,338,340} With the addition of fluorine to the thiophene groups of P(NDI2OD-T2) results in gains in short circuit current, open-circuit voltage, and fill factor when blended with PTB7-Th. The increased bandgap, balanced hole and electron mobility and better exciton dissociation was presented as the leading cause for higher efficiency.³⁰¹ In another report, PNDI2OD-T2F, the same acceptor polymer mentioned above, was blended with PBDTTPD, leading to a marked improvement in mixing. Transient absorption results indicate longer-lived polarons and faster hole transfer being the drivers of the observed three-fold increase in PCE upon fluorination.³³⁸ If considering acceptor polymers not using an NDI moiety, a fluorinated thieno-pyrrole-dione (TPD) based acceptor gave greater than 4 % efficiency with balanced charge mobility due to improved morphology.³⁰² And a B-N bridged bipyridine based acceptor give ef-

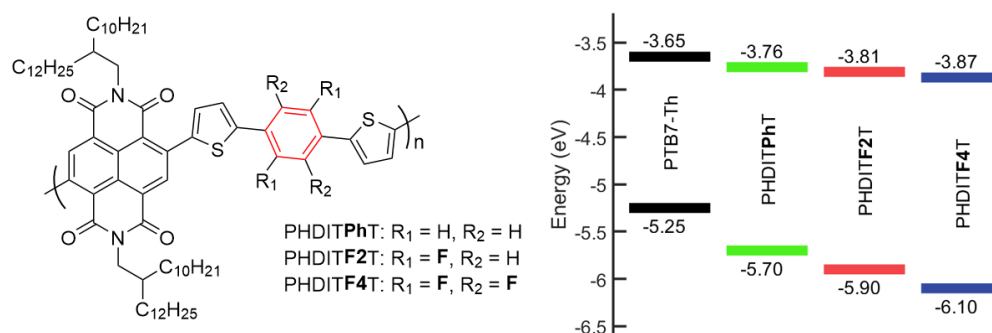


Figure 4.11: Structures of the acceptor polymer used in this section, the main moiety, is based on P(NDI2OD-T2), with the inserted phenyl ring highlighted in red. The energy levels of the donor and the acceptors are presented on the right-hand side. The value in brackets refers to the band-gap calculated from the difference in HOMO and LUMO levels.

efficiency of 6.2 % with a high open-circuit voltage (V_{oc}) due to the charge transfer (CT) state energy.³⁰³ From these studies, we can see that improvements in morphology are commonly observed, with bimolecular and longer-lived polarons and matched electron and hole mobilities being reasons behind the improved performance.

The polymers studied are shown in Figure 4.11. The acceptor polymers are all derivatives of P(NDI2OD-T2) with a phenyl ring inserted between the thiophene rings. To create the series of fluorination polymer acceptors studied the hydrogen atoms on the phenyl ring are substituted to varying degrees: none (NoF), bi- (PNDITF2T), and -tetra (PNDITF4T). The effect of this fluorination is both structural and electronic, Figure 4.11, with the HOMO energy shifting from -5.7 eV to -6.1 eV as fluorination increases, while the LUMO energy sees a much smaller change of ~0.1 eV. To this effect, we have both a structural change and electronic change to consider, with the lowering of the HOMO increasing the driving force while also shifting the absorption spectra (discussed in Section 4.3.2).

The focus of this section is understanding role of photophysics (after accounting for morphology and device physics) as the fluorination of the acceptor polymer

is increased. By characterising the material using many techniques, a systematic picture can be derived of how fluorination leads to an increase in solar cell efficiency. The main contributions made by this author is in understanding the photophysics, which requires the measurement of transient absorption, steady-state absorption and photoluminescence. Other characterisation methods are not the main focus of this work and have been shown in Section 4.3.1, with the discussion focusing on aspects that can be corroborated or that influence the photophysics. A summary of the other important effects in understanding the fluorination of these polymer acceptors is also presented. The transient absorption results show there is little difference in charge decay dynamics with excitation to both the donor and acceptor phase displaying similar behaviour. The decay is almost identical, providing strong evidence that the charge lifetimes are not the cause of the variation. The charge mobility at <6 ns is seen to be consistent across the materials, ruling out the idea that photophysics has a considerable influence on performance in this material system.

4.3.1 Morphology and device characterisation

In order to understand the device as a whole, the morphology and device characteristics are presented. The measurements and analysis presented here were completed by collaborators but need to be considered when discussing the photophysics and its impact on device performance. For this APSC, the device characterisation provides insight into the underlying reason for the variation in performance as the photophysics are largely unchanged.

Table 4.4 presents device characterisation measurements when varying the acceptor polymer from PNDITPhT to PNDITF4T. There is a trend of PCE increasing with fluorination, 3.1 % PNDITPhT, 3.8 % PNDITF2T, and 4.6 % for PNDITF4T. The increase in efficiency is due to higher J_{sc} with increased fluorination (7.7 to $11.7 \text{ (mAcm}^{-2}\text{)})$ which is more than enough to compensate for a decrease in V_{oc} from 0.86 V (PNDITPhT) to 0.78 V (PNDITF4T). The decrease in V_{oc} of 0.8 V is similar to the 0.11 eV change in LUMO levels. When looking at EQE, it is clear

that increased absorption is not the only cause of higher J_{sc} and improved charge generation, charge separation, or charge collection must also be a contributor.

Blend	V_{oc}	J_{sc}	J_{sc} EQE	FF	PCE
PTB7-Th:	(V)	($mAcm^{-2}$)	($mAcm^{-2}$)		(%)
PNDITPhT	0.86	7.7	7.3	0.45	3.1
PNDITF2T	0.80	9.8	9.2	0.50	3.8
PNDITF4T	0.78	11.7	11.3	0.52	4.6

Table 4.4: Electrical characterisation of PTB7-Th blended with P(NDI2OD-T2) and derivatives with varying degrees of fluorination, collected under the illumination of AM 1.5.

In addition to the above measurements space-charge limited current show that hole mobility is constant, while electron mobility increases five-fold when moving from PNDITPhT to PNDITF4T.³⁴¹ Transient photovoltage points to a possible loss mechanism of PNDITPhT with there being a decrease in photocurrent on the terms to hundreds of nanoseconds point to intensity-dependent recombination.^{342,343}

The morphology was studied using several techniques that reveal differences in the domain size and purity of the blended films. AFM and transmission electron microscopy are used to probe the surface of the films, in the neat film they show that the series of acceptor polymers are fibrillar, with the addition of PTB7-Th slightly decreasing the fibrillar nature. transmission electron microscopy measurements show a distinct difference in phase separation with PNDITF4T having dark features on the 50–100 nm range indicating phase separation that is not observed in the other blends. The surface composition was probed using x-ray absorption near edge structure (NEXAFS) this showed that a favourable PTB7-Th rich interfaces are formed at the top electrode in PNDITF4T. The polymer packing and orientation was measured via grazing-incidence wide-angle x-ray scattering (GIWAXS), and it was not very easy to distinguish the two polymer phases due to similar lamella and π - π stacking features. In general, there was little variation in the packing between the neat films and those blended with PTB7-Th;

all have lamella stacking ~ 2.3 nm. PNDITF4T was seen to have a face-on orientation in bulk (similar to PNDITF2T and PNDITPhT) but the surface had an edge-on orientation. Resonant soft x-ray scattering (R-SoXS) measurements of domain purity again proved difficult to separate the polymer components but indicates that increasing domain size and purity with increased fluorination is consistent with the domains being seen in transmission electron microscopy with PNDITF4T.

The PCE measurements show that increasing fluorination leads to higher PCE going from 3.1 % to 4.6 % this is driven by higher J_{sc} not caused by increased absorption of incident photons. The morphological changes are hard to measure due to overlapping donor and acceptor signals, but indicate increasing domain size and purity with increase fluorination and little change in crystallinity. The most noticeable change is from transmission electron microscopy, which shows PTB7-Th:PNDITF4T has distinct features on the 50–100 nm scale. These results indicate that charge generation, separation or extraction are possible causes for the change in PCE. Steady-state absorption and PL measurements will be able to look into changes in average blend environment when compared to neat along with an indication of the charge separation process. The photophysics of charge generation and decay, and an indication of open-circuit mobility will be investigated using transient absorption spectroscopy.

4.3.2 Steady-state absorption and photoluminescence

Absorption spectra of the neat polymers used in the devices are presented in Figure 4.12a normalised by the peak intensity. For the three acceptor polymers, there is a $\pi \leftarrow \pi^*$ absorption band at ~ 370 nm and a broad charge-transfer absorption band located in the visible to near-infrared region. As expected, from the change in frontier energy levels, the lower energy absorption blue-shift with increasing fluorination, shifting from ~ 680 nm in PNDITPhT to 630 nm in PNDITF2T and then out to 590 nm in the highest fluorinated acceptor polymer, PNDITF4T. The low-bandgap polymer, PTB7-Th, has a characteristic broad absorption span-

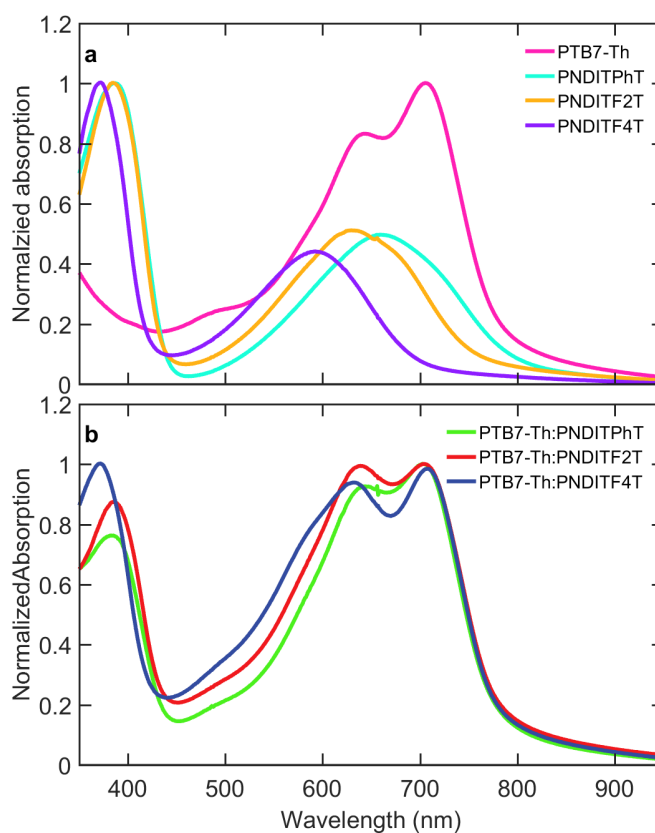


Figure 4.12: Normalised absorption spectra of the various neat polymers (a) and the blends (b).

ning from 550 nm to 790 nm, with the lowest energy vibronic peak located at 715 nm.²⁶⁴

The absorption spectra of PTB7-Th blended with the various acceptor polymers shown in Figure 4.12b. Differences in the absorption profile can be seen in the 450-700 nm (2.8-1.8 eV) range; the absorbance at the near-infrared end of the spectrum decreases, with an increase in absorption intensity in the visible observed. To further understand the origins of this change, whether it is solely due to the blue-shift or because of morphological changes, the absorption spectra of the blends are decomposed into contributions from the neat constituents. Figure 4.13 presents a linear least-squares fit of the neat spectra, each panel con-

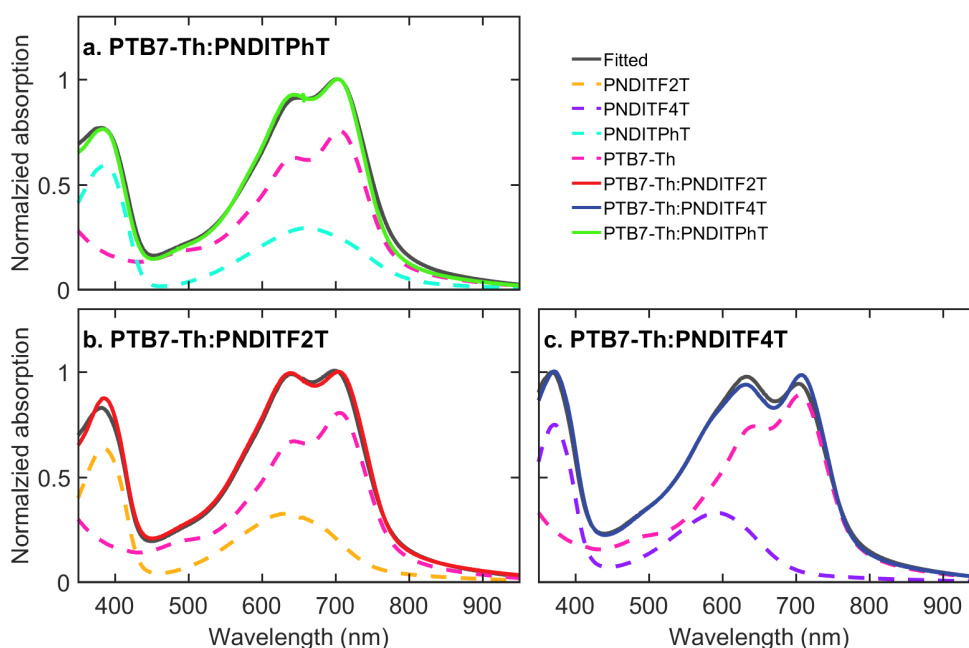


Figure 4.13: Normalised absorption spectra of the various blends are shown in solid coloured lines, and weighted constituent neat absorption are shown in dashed lines. Each panel a–c contains one of the fluorinated acceptor polymers blended with PTB7–Th absorption spectra (various colours). The black line shows the best–fit of the constituent components and is the sum of the dashed lines shown (pink and the other colour).

tains blended spectra and the weighted neat contributions which are summed to give the fit (shown in black). In all cases; the blend is well fit by the constituent neat spectra meaning that the enhanced absorption can be solely attributed to the blue–shift in the acceptor polymer with fluorination. As PNDITF4T has the largest blue–shift, it is the most complementary to PTB7–Th, allowing the two polymers to complement each other enhancing absorption across the solar spectrum.

To gain information about domain size and purity photoluminescence measurements at with excitation wavelengths of 532 nm, 625 nm and 715 nm were carried out. By considering the blend absorption film as a linear combination of donor and acceptor spectra 532 nm and 625 nm, (Figure 4.13) are absorbed by

both phases. In contrast, 715 nm excitation primarily excites the donor phase. The specific ratio and percentages absorbed by the donor phase are summarised in Table 4.5. This contrast is further enhanced for PNDITF4T where 715 nm only interacts with the donor. In this way, the PL quenching from the various excitation wavelengths provides an indication of the behaviours and hence domain size and purity of the donor and acceptor phases.

Material	532 nm	625 nm	715 nm
PTB7–Th:PNDITPhT	2.8:1 (74 %)	2.3:1 (70 %)	3.2:1 (76 %)
PTB7–Th:PNDITF2T	1.8:1 (64 %)	1.9:1 (66 %)	4.9:1 (83 %)
PTB7–Th:PNDITF4T	1.2:1 (55 %)	2.5:1 (71 %)	20:1 (95 %)

Table 4.5: The excitation wavelengths used for photoluminescence and the corresponding ratio of photons absorbed into the donor (PTB7–Th) or acceptor (various) phase; the percentage absorbed by the donor is shown in brackets.

Before we can move onto the PL quenching the normalised neat PL spectra are presented in Figure 4.14 following 625 nm excitation. The donor polymers all show a similar PL shape, a distinct higher energy peak at 700 nm PNDITF4T, 750 nm PNDITF2T, and 810 nm and then a shoulder that continues into the near-infrared regions. The only variation is the energy of the features with a blue-shift (i.e. same as absorption spectra) observed with increasing fluorination. Due to the blue shift, the shoulder of PNDITPhT is not observed as it is outside of the detector window. PTB7–Th (pink) has an onset at ~700 nm and then continues into the near-infrared region.

Figure 4.14 presents the relative intensity ratio of the polymer materials. The PNDITF4T has a nine-fold highest PL intensity when compared to its unfluorinated counterpart. The PL intensity decreases with fluorination putting the intensity of PTB7–Th between PNDITF4T and PNDITF2T. When calculating the PL quenching efficiency we need to account for the variation of PL intensity in donor and acceptor, and the wavelength dependence of the photons absorbed into each phase. This is done by using the decomposition of the absorption spec-

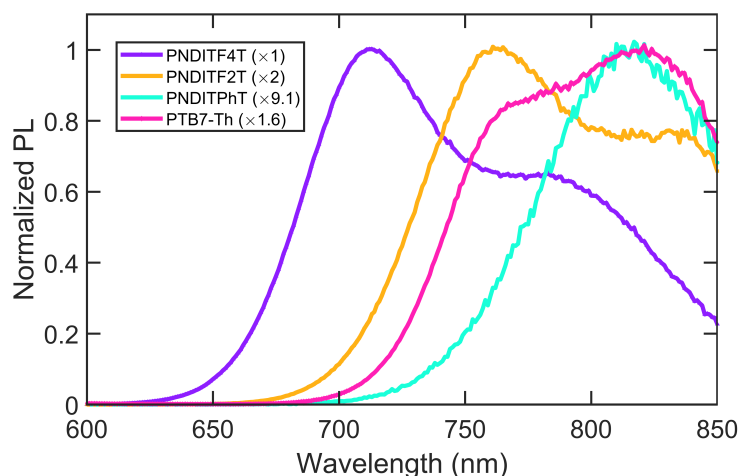


Figure 4.14: Steady-state photoluminescence spectra of neat PTB7-Th and the various acceptor polymers films collected after 625 nm excitation. The spectra are presented normalised, with the details showing the relative scale factor used after correcting for absorbed photons.

tra to calculate the fraction absorbed into each phase and then using these fractions to calculate the expected PL intensity, with the final quenching value being the percentage of this expected PL observed in the blended films.

Figure 4.15 presents the calculated PL quenching values, the observed values are all >90 % indicating generally efficient exciton dissociation at the donor acceptor interface. The PNDITPhT blend exhibits the most consistently high quenching values of ~94 % across the excitation wavelengths while PNDITF2T is slightly lower at 93 % but still independent of excitation wavelength. Looking at PNDITF4T blend the decrease in PL quenching observed is consistent with the morphological data that should PNDITF4T had larger acceptor domains, as the excitation wavelength moves from mostly the acceptor phase (532 nm) to exclusivity the donor (715 nm) we see a drop in quenching from 95 % to 90 %. The decrease in PL quenching shows that the donor phase has a higher purity than the acceptor in PNDITF4T blends. For the other two donor polymers, it is hard to rule out a similar change in purity as an excitation at 715 nm overlaps with the acceptor polymer absorption band, which could hide the variation.

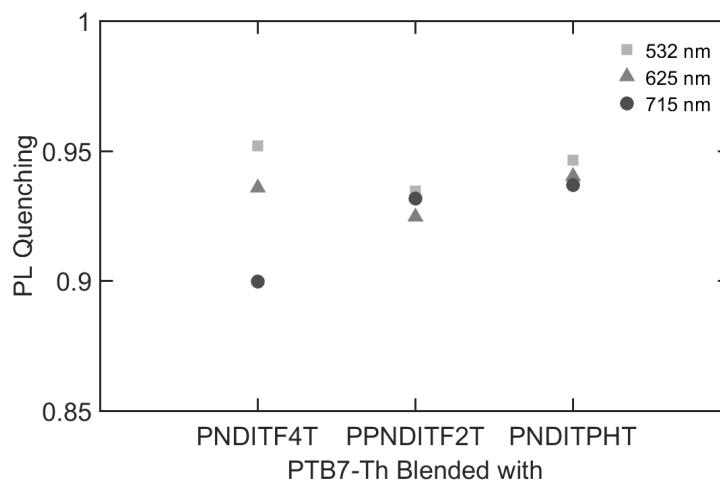


Figure 4.15: PL quenching as a function of fluorination more fluorination on the left, tightly grouped points represents low dependence on excitation wavelength (i.e. the phase of the blend which is excited).

The steady-state measurements confirm that there is little change in the polymer packing between the neat and blended films with blends having an absorption spectra that is a linear combination of its neat components. PL quenching shows >93 % quenching across all blends and excitation wavelengths, except PNDITF4T in the donor phase suggesting that for this blend the donor phase is purer than the acceptor phase. Nothing above suggests an explanation for the difference in observed PCE, as such, we move onto the analysis of transient absorption spectroscopy. With transient absorption spectroscopy, we will track the timescales of charge generation and decay, with an indication of the phase purity or size given by the fraction of charges generated in <100 fs and the timescale of subsequent charge generation respectively.

4.3.3 Ultrafast photophysics

As in the above section, we begin our interpretation of the TA data by identifying and assign features present in the neat film. Figure 4.16 presents the early time TA spectra associated with singlet exciton, following from 532 nm excita-

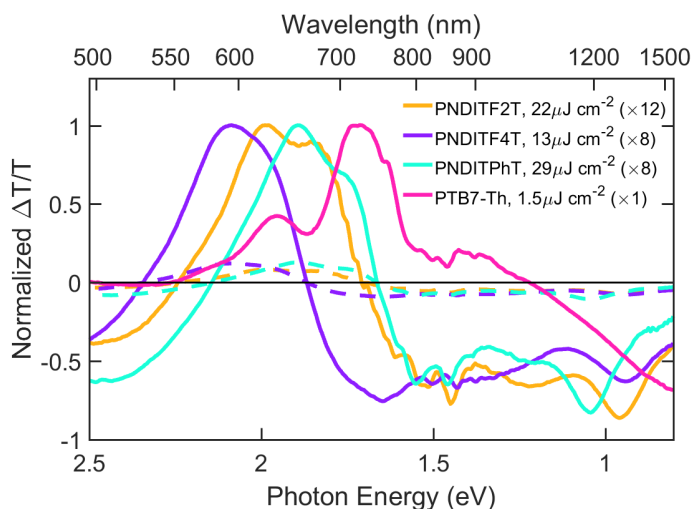


Figure 4.16: TA spectra attributed to singlet exciton for PTB7-Th ($532 \text{ nm } 1.5 \mu\text{J cm}^{-2}$) and various fluorinated acceptors (532 nm fluence shown in plot), collected in a neat blend. The spectra are normalised to show the spectral features, with the PC₇₁BM having 8–12 times stronger signal than the acceptor polymers, this emphasises the by the dashed signals which represent the acceptor scaled for the difference in signal strength.

tion. The PTB7-Th spectra is the same as mentioned with the notable features being a ground state bleach (GSB, $\Delta T/T > 0$) in the $580\text{--}780 \text{ nm}$ ($2.1\text{--}1.6 \text{ eV}$), and a broad photo-induced absorption (PIA, $\Delta T/T < 0$) in the near-infrared region $>940 \text{ nm}$ ($<1.32 \text{ eV}$). Moving onto the acceptor polymers, the first thing to note is the relatively weak signal strength after correcting for absorbed photons (dotted lines) with the signals being 8–10 times weaker than PTB7-Th. Due to the relative signal strengths of the donor and acceptor, the acceptor polymers will not contribute significantly to the observed TA signals observed in the blends. Nevertheless; they can be described as having a GSB that overlaps with the steady-state absorption, $530\text{--}710 \text{ nm}$ ($2.3\text{--}1.7 \text{ eV}$), which blue-shifts with increasing fluorination. There is also a distinctive PIA peak seen at $\sim 1240 \text{ nm}$ (1.00 eV) that undergoes a shift to lower energy as fluorination increases. Finally, a broad PIA is seen across the whole spectrum.

Figure 4.17 shows a series of TA spectra for the PTB7–Th blended with various polymer acceptors following 532 nm (2.33 eV) excitation. Panel (a) contains the PTB7–Th:PNDITPhT, where the TA spectra are dominated by the signature of the donor polymer as expected by the much weaker signals seen for the neat acceptor films. The spectra are described by a combination of excitons and charges. The excitons have a photo-induced absorption peak around 1550 nm (0.80 eV) and the charges have a photo-induced absorption peak around 1300 nm (0.95 eV). Both types of excitation also lead to ground-state bleaching in 540–775 nm (2.3–1.6 eV) region, also there is a broad sub-gap PIA starting at around 830 nm (1.49 eV) that is likely due to electroabsorption. The loss of exciton PIA peak without a change in the ground-state bleach reveals the process of excitons being converted into charges. The spectral series for the other two blends are presented in panel b (PTB7–Th:PNDITF2T) and c (PNDITF4T) and contain almost identical features as those described above for PNDITPhT. There is a slight difference in vibronic ratio with PTB7–Th:PNDITF4T having a relatively stronger 0–0 intensity, this change in the vibronic ratio can give some insight into the donor polymer structure. Stronger 0–0 comparative to 0–1 vibronic peak is indicative of more extended chains consistent with higher inter-chain order, the extended order is consistent with purer domains.

Due to the overlapping nature of the exciton and charge species to gain further insight into the charge generation and recombination dynamics, the TA surfaces are bilinearly decomposing into pairs of spectra and kinetics. While an infinite set of solutions does exist the exciton spectra from the neat material and charge species from later time measurements are used to constrain the spectra, with the results being used to discuss all further species decay. A single set of spectra are used for each excitation wavelength and blend. Figure 4.18 is one example of the bi-linear decomposition it presents the low-fluence measurement of a PTB7–Th:PNDITF4T blend following excitation at 532 nm, 100 fs pulse. Panel (a) has spectral components used, this includes an exciton species, showing the clear PIA peak at 1550 nm (0.80 eV), there are then two charge spectra one of which is higher weighted following 700 ps pulse excitation. These two charge species are

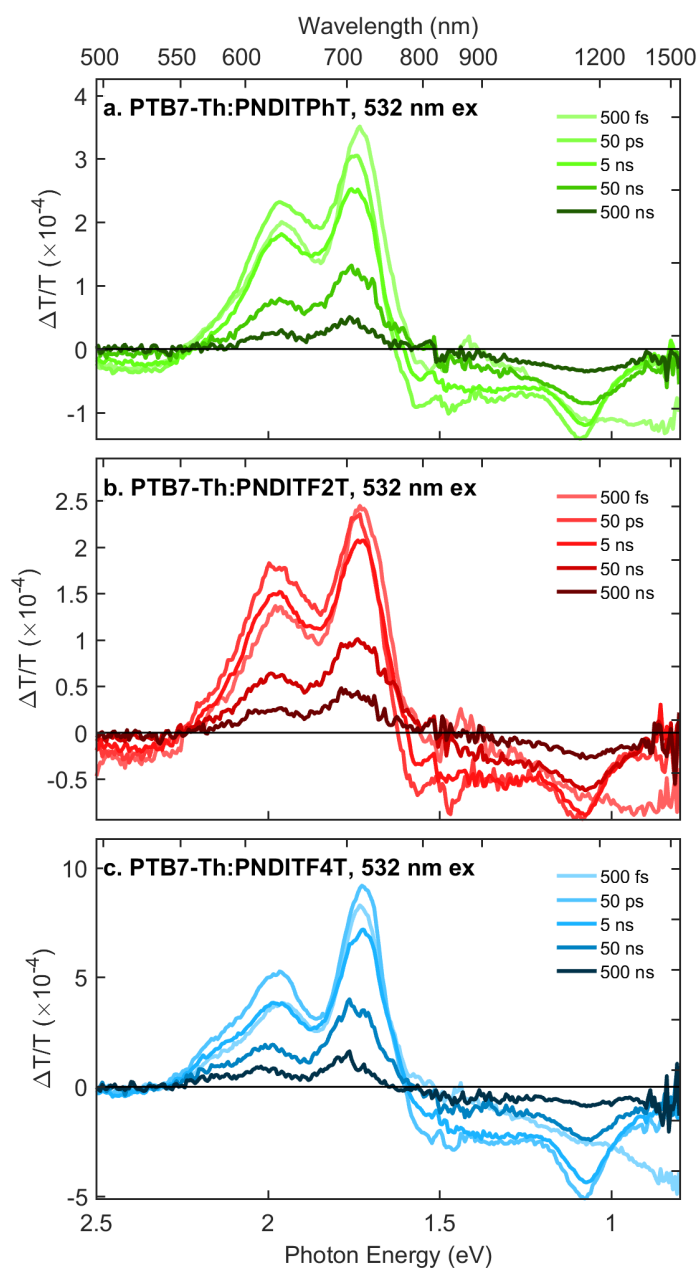


Figure 4.17: Series of TA spectra taken at various time slices to shown the interconversion of excitons to charges, the 532 nm excitation is resonant with both the donor and acceptor phases and has a pulse width of 100 fs for times <3 ns and 500 ps at longer times. (a) PTB7-Th:PNDITPhT ($0.37 \mu\text{J cm}^{-2}$). (b) PTB7-Th:PNDITF2T ($0.35 \mu\text{J cm}^{-2}$). (c) PTB7-Th:PNDITF4T ($0.66 \mu\text{J cm}^{-2}$).

then combined after normalising the GSB region of the spectra to give the decay of the total charge population.

Figure 4.19 shows the charge dynamics for each of the three blends, from the sub-picosecond to microsecond timescale following 532 nm excitation. The figure is broken down into three panels showing the exciton (a), charge (b), and PTB7–Th excited state populations (c). The exciton dynamics are indistinguishable between blends suggesting that in all cases the PTB7–Th exciton to charge generation process happens on a similar timescale. Moving onto the charge dynamics (b), approximately half of the charge population appears promptly after photoexcitation, with the remaining charges formed following exciton diffusion on the picosecond timescale before recombination sets in from around 100 ps. The yield of prompt charge generation is slightly lower with higher fluorine content in the acceptor polymer, which is consistent with the improved phase separation. A small difference between these kinetics profiles is seen when looking at the PTB7–Th population (Figure 4.19c), in this case, we monitor the number of charges created via hole injection from the acceptor polymer. As charges are formed from dissociation of donor excitons a hole is injected into PTB7–Th leading to an increase in ground state bleach. The observed trend follows that of the fraction of photons absorption into the donor phase following 532 nm excitation, with the blue-shifted PNDITF4T having ~20 % of charges injected while PNDITPhT has almost no charges injected.

To try and get a better understanding about the charge generation pathways the blends are excited with 715 nm excitation this leads to significant variation in the fraction of PTB7–Th absorbed in the case of PTB7–Th:PNDITF2T (2.5 times) and PTB7–Th:PNDITF4T (20 times), but the ratio remains almost unchanged for PNDITPhT (1.1 times). Figure 4.20 presents the comparison between total PTB7–Th population and the charge dynamics after 532 nm and 715 nm excitation. For PTB7–Th:PNDITPhT (a) where the ratio remains constant there is no difference between either excitation wavelength, with approximately 50 % of the charges being formed promptly and no evidence of hole transfer form

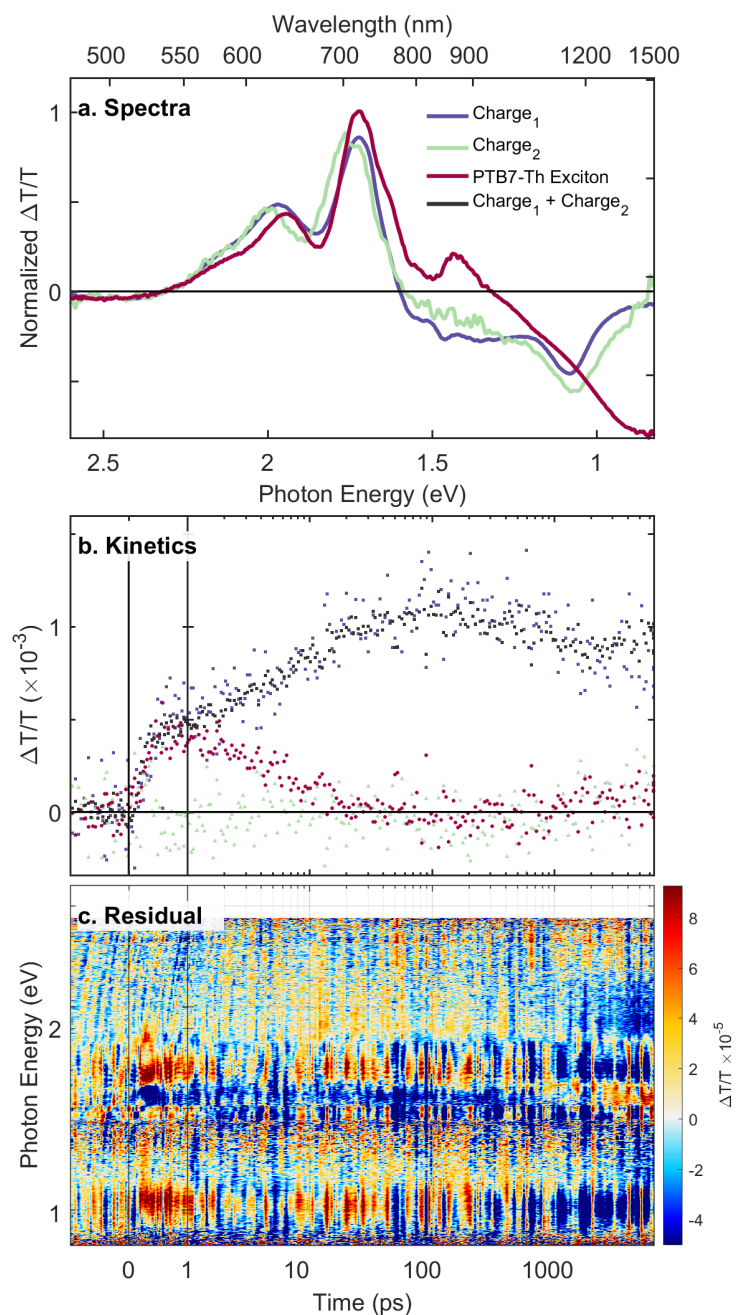


Figure 4.18: Example of mathematical decomposition of a TA surface for PTB7-Th:PNDITF4T following excitation at 532 nm ($\mu\text{J cm}^{-2} 0.66$). (a) Associated spectra of exciton and charge species. (b) Kinetics of exciton and charge species, where spectral shift changes on longer timescales are captured via two charge species spectra. Two distinct charge species are not included in the subsequent analysis; instead, the black dots represent the sum of all charge species. (c) Residuals from mathematical decomposition (note the different orders of magnitudes for each surface, 10^{-3} and residuals, 10^{-5}).

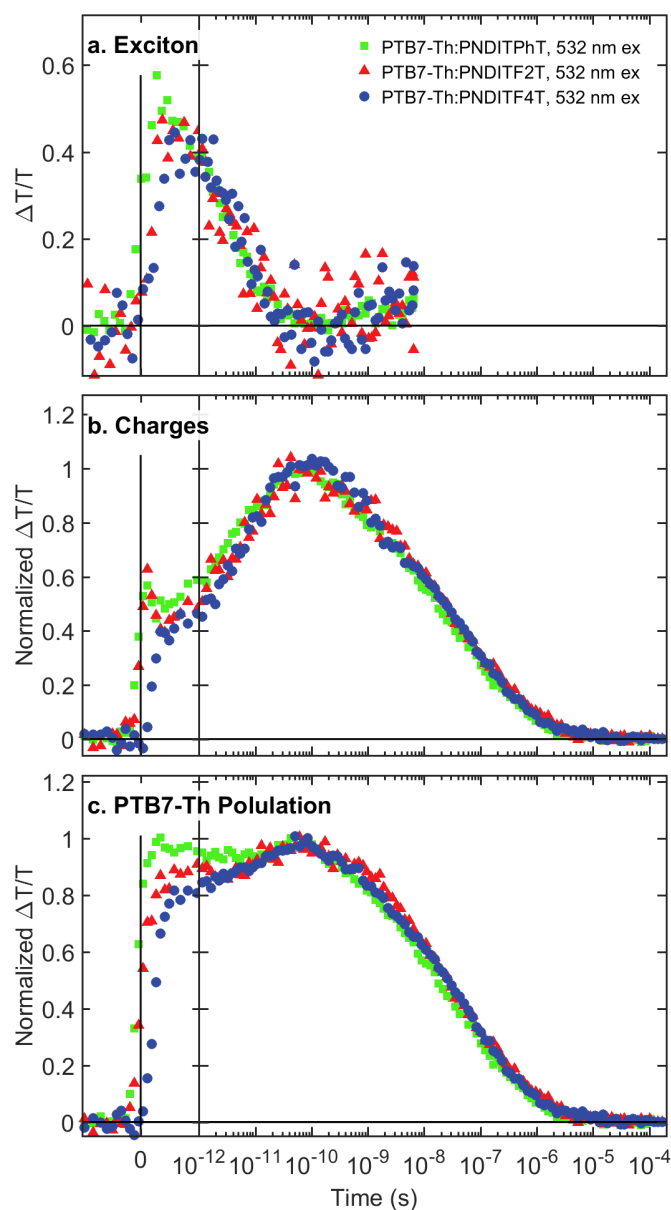


Figure 4.19: The dynamics of the exciton (a), charge (b), and PTB7–Th excited state populations (c) following 532 nm excitation at various excitation densities (PTB7–Th:PNDITPhT $0.37 \mu\text{J cm}^{-2}$, PTB7–Th:PNDITF2T $0.35 \mu\text{J cm}^{-2}$, PTB7–Th:PNDITF4T $0.66 \mu\text{J cm}^{-2}$) are shown in the respective panels. The dynamics are extracted following the mathematical decomposition of the data shown in Figure 4.18.

PNDITPhT to PTB7–Th. With PTB7–Th:PNDITF2T the charge dynamics are unchanged, but there is a reduction of hole injection with PTB7–Th absorbing ~80 % of incident light the donor phase has no delayed charge generation. For PTB7–Th:PNDITF4T whereby 95 % of the light is absorbed by PTB7–Th (vs 55 % at 532 nm) the most significant deviations are seen. Like the other acceptors, the prompt charge fraction is the same irrespective of the excitation wavelength, but the charge generated at later times varies. Due to PTB7–Th absorbing the majority of the light species in the PNDITF4T can be excluded from playing a role, from this we can see that PTB7–Th exciton to charge conversion yields are lower, with yield being 20 % less than with 532 nm excitation. A lower yield of charges is consistent with decreased steady–state PL quenching in the PTB7–Th:PNDITF4T the PTB7–Th. The lower charges yield indicates; purer domains as there is a lower likelihood of the exciton reaching an interface and thus undergoing charge separation. The lower excitation energy, 715 nm (1.73 eV), could add to the lower yield as the excess energy of excitation as this has a direct effect on how far excitons will travel.^{27,61,61,73}

With the differences between charge generation and decay dynamics revealing little difference between the three acceptor polymers, we move onto intensity–dependent measurements to see if the mobility of charges or other intensity–dependent effects can provide some insight. Figure 4.21 presents normalised extracted kinetics for excitons (left) and charges (right) for the various blends; follow 715 nm, 100 fs excitation. The excitation fluence is varied to adjust the population of charges or excitons present to see if there is a change in the observed dynamics, which would reveal information about the bimolecular process that are correlated with charge mobility, and exciton diffusion. The exciton decay (Figure 4.21, Panels, a, c, and e) shows no variation in decay for any of the donor polymers showing that the exciton diffusion is low enough not to be a loss pathway. Commenting about variation in exciton diffusion between the different blends is not possible as we are not at high enough density to see bimolecular processes on such short timescales. Moving onto the charge decay kinetics (panels b,d,f) a variation dynamics is seen at >50 ps for all blends; this allows

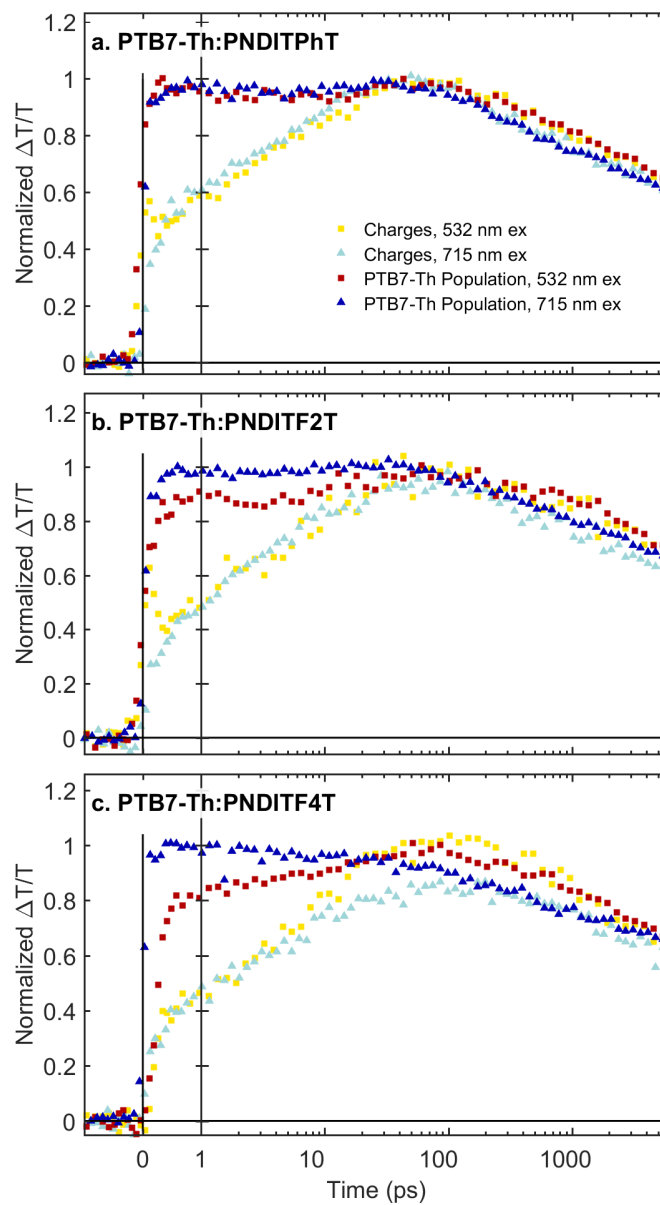


Figure 4.20: The dynamics of charges and excited states in PTB7-Th after excitation at 532 nm, and 715 nm are presented. Each panel (a, b, c) contains a different acceptor polymer blended with PTB7-Th. Excitation fluence is kept below $1 \mu\text{J cm}^{-2}$ in all cases.

the comparison of charge mobility under open-circuit conditions. A qualitative comparison suggests that there is little difference with all blends decreasing from ~80 % at 6 ns down to 50 % as the fluence is increased by approximately 16 times.

A more quantitative comparison of the bimolecular decay is presented in Figure 4.22. The charge signal integrated before any intensity-dependent deviation (3.7–6.2 ps), is plotted against the signal remaining at the end of the measurement window. The black line represents the expected signal intensity following a linear extrapolation, i.e. no intensity-dependent deviation. The resulting decrease from this line is due to bimolecular processes (electron-hole interactions) which lead to decay to the ground state. The sub-linear deviation is of similar magnitude across all the blends suggesting that the intensity-dependent decay pathways are similar under open-circuit conditions.

4.3.4 Conclusion

Transient absorption spectroscopy has resolved the exciton to charge generation process for both donor and acceptor polymer phases. The generation dynamics are similar across all three donor materials, with the most substantial difference being the fraction of promptly generated charges. The decay dynamics are similar across all blends and experimental conditions; variation of the fluence and excitation wavelength. Thus, we can confidently conclude that the charge generation and recombination dynamics do not account for the observed differences in device efficiencies. If the lack of variation in photophysics is considered with the morphological changes noted, the increased PCE is attributed to improved charge collection due to coarser domains.

4.4 Experimental

All active layers studied were prepared and provided by Professor Chris McNeill's team. They were stored in the dark in a parafilm sealed plastic container while shipping, and upon receipt and when not under study, they were stored in

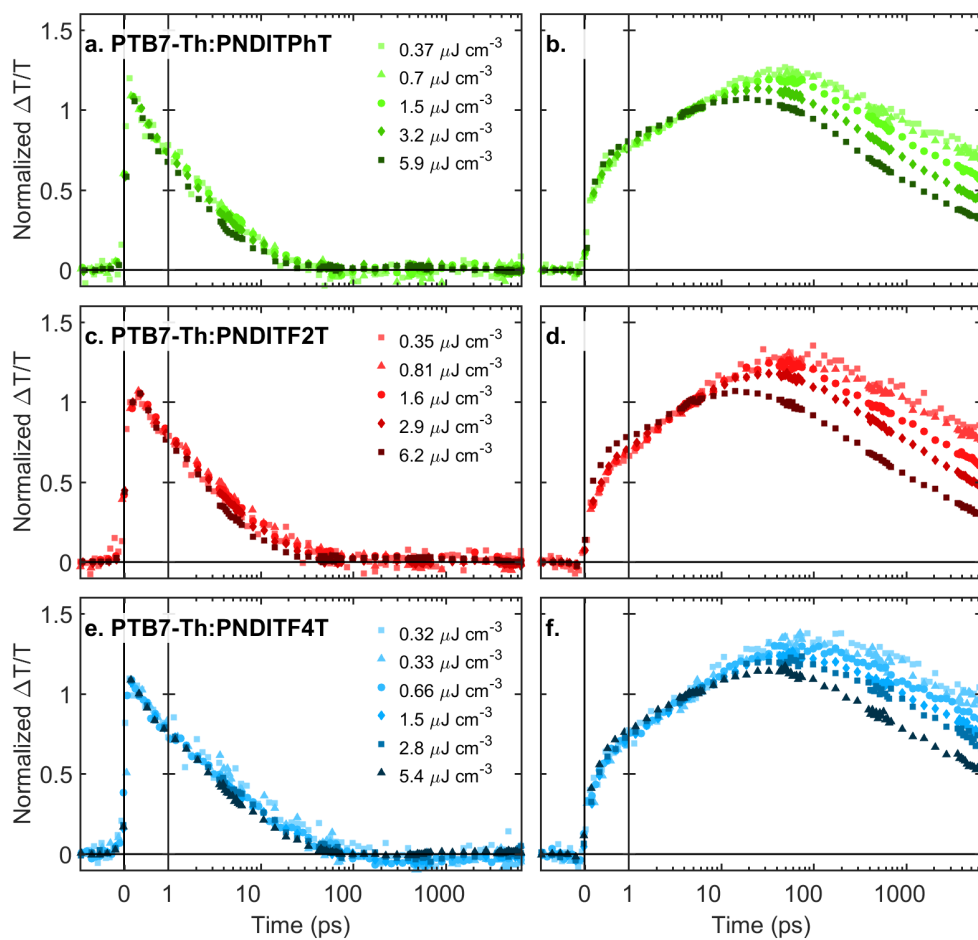


Figure 4.21: Fluence dependent exciton (Column 1) and charge dynamics (Column 2) extracted from TA surfaces following 100 fs 715 nm excitation pulse of varying fluence. (a,b) PTB7-Th:PNDDITPhT, (c,d) PTB7-Th:PNDDITF2T, (e,f) PTB7-Th:PNDDITF4T.

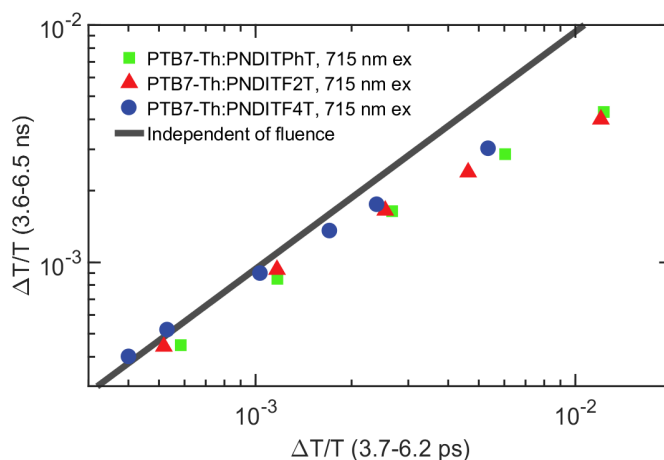


Figure 4.22: Comparison of early time (3.7–6.2 ps) charge population with that remaining at the end of the measurement (3.9–6.5 ns), the population is measured via the extracted charge signal at various fluences discussed above. The black line is the predicted linear-power dependent response using the lowest fluence.

a nitrogen atmosphere in the dark. With the active layer being blended in a 1:1.5 (donor:P(NDI2OD-T2)) ratio for PTB7-Th and 1:1 for PTB7. The blend provided for study are optimisation to give the best PCE, and the difference is justified as each system needs to be studied in an optimum state to understand the cause decrease in PCE for PTB7. The transient absorption set-up is the final optimised layout as noted in Chapter 2. The transient absorption measurements were carried out under a dynamic vacuum. No sample degradation was detected during TA measurements, as the signal intensity and dynamics did not change between measurement repetitions. Steady-state absorption spectra were collected using a Varian Cary 50 Bio spectrophotometer. The sample was loaded into the vacuum chamber and oriented to have the incident probe light the same as the TA measurements. Steady-state photoluminescence spectra (PL) were collected using a Horiba Fluorolog-3 spectrofluorometer. The same films used in TA were loaded into the spectrometer, and PL was collected using a front-facing geometry. For each series of films studied, the incident angle of excitation was consistent between all films in the series.

Chapter 5

The photophysics of a fused ring electron acceptor used in a BHJ-OPV with efficiencies of over 12 %

This chapter investigates organic photovoltaic (OPV) devices fabricated with a small molecule IC-C6IDT-IC (IDIC) as the electron acceptor achieving a power conversion efficiency (PCE) above 12 %. We report that the charge dynamics in a IDIC blend are similar to those generally observed in efficient polymer:fullerene blends when the photovoltaic (PV) performance is maximised by picking an appropriate donor polymer. Then, the photophysics of an efficient IDIC:polymer (where the polymer is FTAZ) blend were measured; specifically the effects of morphology, and the change in photophysics when fullerene is exchanged for IDIC. It was found that the majority of the performance gains are accounted for by the increased absorption, and the photophysics are similar compared to those observed when using a fullerene acceptor. Furthermore, triplets are ruled out as a loss mechanism in this low-bandgap bulk-heterojunction (BHJ) solar cell.

Professor Xiaowei Zhan provided the active layers of each device. The electrical, morphological and steady-state data presented in this chapter were collected and analysed by Professor Xiaowei Zhan's team.

The data presented in this chapter has been published in:

- Lin, Y.; et al. Mapping Polymer Donors toward High-Efficiency Fullerene Free Organic Solar Cells. *Adv. Mater.* **2017**, 29 (3).
- Lin, Y.; et al. Balanced Partnership between Donor and Acceptor Components in Nonfullerene Organic Solar Cells with > 12 % Efficiency. *Adv. Mater.* **2018**, 30 (16), 1–8.

5.1 Introduction

Small molecule (electron) acceptors (SMAs), are a rapidly developing area in the organic photovoltaic (OPV) field with many reviews published recently (c.a. 2018),^{107–109,128,299,344} The rise of SMAs began in 2015 with the publication of ITIC and the efficiency has improved each year since.^{107,112} Moreover, there have been more than four hundred publications published between 2014 and 2018¹⁰⁹, documenting an improvement in the power conversion efficiency (PCE) from 6 % to >13 %.¹⁰⁷ Small-molecule acceptors (SMA) have become a popular acceptor molecule in bulk-heterojunction organic photovoltaics (BHJ-OPV) replacing the more common fullerene which has been the dominant acceptor for the past decade.^{29,99,109,299,344} The distinction between fullerenes and SMAs as classes of acceptors arises purely from the dominance of fullerenes as an acceptor in OPVs. Fullerenes are technically SMAs, and therefore SMAs are also referred to as non-fullerene acceptors (NFAs). To clarify, in this work, SMA refers to non-fullerene small molecule electron acceptors.

The power conversion efficiency (PCE) of a polymer:SMA OPV (14.2 %)^{107,244} surpasses the PCE reported in polymer:fullerene OPVs (11.7 %).^{31,111,288} This improvement in PCE epitomises the dramatic rise in the use of SMAs in BHJ OPVs.

SMA will play a vital role in the future of OPVs because they can achieve PCEs higher than the theorised limit of fullerene-based OPVs (i.e. 11 %).^{102,244}

Along with PCE gains, the stability of the material in the long-term is a necessary consideration if the end goal is to use the material in commercial applications.^{28,108} SMA has shown promise in overcoming the stability³⁴⁵ and burn-in³⁴⁶ (burn-in refers to the initial drop in OPV performance once exposed to sunlight⁶⁷) issues, which are significant challenges still faced by fullerene acceptors.^{64,316,347,348}

When used as electron acceptors, SMA has some distinct advantages when compared with fullerenes. These include improved synthetic tunability, complementary absorption and lower voltage loss. Each of these advantages will be discussed in further detail below.

Improved synthetic tunability should be considered as a limitation of fullerenes rather than a benefit of SMA. Fullerenes possess a limited number of chemically active sites if the core structure is to remain intact (conjugated C₆₀, C₇₀), i.e. they are not as flexible with the ability to add different functional groups in order to improve various properties (e.g. energy levels).¹⁰⁸

The broad spectrum of solar irradiation gives rise to two properties need to be optimised in a single junction solar cell; the band edge of the lowest absorber (ideal at 1.3 eV (946 nm)) and the bandwidth, i.e. the amount of the solar spectrum absorbed. The absorption cross-section of an SMA is higher than that of a fullerene allowing SMA to play a dual role as an absorber and charge separation partner. The absorption of most fullerenes is negligible and therefore they are unable to aid in light collection, making fullerenes primary role in BHJ OPVs to aid in charge separation.^{108,349} The pathway for fullerene-based OPVs is generally through ternary and tandem configurations.^{350–354} While tandem or ternary configurations might still play a role in optimised SMA devices^{247,355}, the greater absorption band of SMA are a benefit over fullerenes in simple two material systems.

Empirically, blends containing fullerenes have a substantial voltage loss. The voltage loss seems to be an intrinsic property, attributed to the broad tail of states at the absorption edge, or the presence of an emissive low energy state formed between the donor and acceptor (usually referred to as a charge transfer state).^{57,119,127,356,357} While a voltage loss is necessary, achieving a minimal voltage loss will maximise the efficiency of the OPV device. A loss of 0.3–0.5 V is typical in silicon or perovskite cells^{57,108} whereas in fullerene OPV devices a loss of 0.7 V is typically observed.^{127,358} This voltage loss in SMA based OPV devices are already lower than the practical limit observed in fullerenes, with losses of less than 0.5 V reported.^{359–361} The lower voltage loss of SMA compared to fullerene could be due to the much sharper absorption edge (i.e. no tail of charge–transfer states)^{119,358,362} or a decrease in the driving force required for charge separation.^{137,362} The observation of voltage loss lower than that of fullerene–based devices is a step in the right direction; even if the mechanism is not well understood.

Many distinct structural moieties fall under the term SMA, each has a different synthetic strategy to tune the various properties important to OPV efficiency, e.g. energy levels. Two classes dominate the SMA literature, fused–ring electron acceptor (FREA) and rylene–diimides; perylene diimide (PDI) or naphthalenediimide (NDI). This chapter focuses on the photophysics of the FREA IDIC, also known as IC–C6IDT–IC, and shown in Figure 5.1. FREA are sometimes called A–D–A type acceptors due to the acceptor–donor–acceptor structure. The efficiency of reported FREA 14.2 % is significantly higher than the other classes, with the next highest SMA outside this being PDI with 8.47 % reported.^{107,109} FREA contain a central fused–ring structure at its core (i.e. IDT) with electron withdrawing substitutions at either end (i.e. INCN). This core can have aryl or alkyl side–chains which end up spatially above the plane of the fused conjugated A–D–A core.²⁹⁹ For a comprehensive discussion of the various structural modifications possible the reader is referred to the excellent review by He Yan and co–workers.¹⁰⁹ Presented here is a summary of the structural modifications possible to FREA comparing the benefits with other SMA.

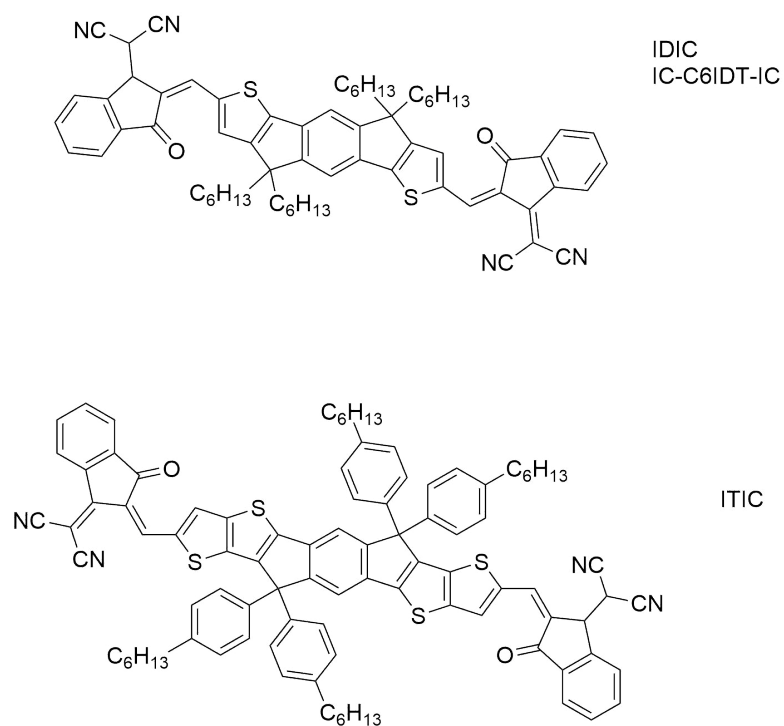


Figure 5.1: FREA, IDIC is shown on top, and the prototypical FREA from which it is derived is shown below. The photophysics of IDIC is the focus of this chapter.

The various pathway of structural modification available in A–D–A acceptors is an asset in the quest for a high PCE OPV device. FREA have moieties that can be modified independently; side chain, electron donation, and electron accepting groups.^{109,245} These are ideal for improving the performance of OPVs as various parameters need to be tuned, i.e. morphology, light absorption, charge separation, in order to achieve a high PCE. The independence of modification arises from the convergent synthetic strategy used for FREA, as each moiety is prepared before being combined in the final step or steps.¹²⁹ Modification of the core A–D–A structure will affect the electronics, and the side-chains can give morphological control.^{129,299} Intramolecular push–pull modifies the absorption band via the energy levels, leading to a broader absorption and tunability of the highest occupied molecular orbital (HOMO) and lowest unoccupied molecular orbital (LUMO) levels.^{129,245,299} Incorporation of electron–rich groups onto the ends of the acceptors increases the energy of the LUMO, while fluorination, in a similar position, decreases LUMO energy.^{245,288,363}

In comparison to other SMA, FREAs have overcome the aggregation problem and have an absorption that is complementary to the extensive library of existing polymer donors.^{108,109}

The fine–tuning of morphology possible by FREA is distinct from many other classes of SMA; this is because they possess side–chains attached to the core unit (A–D–A) that are very similar to donor polymers. The combination of planar conjugated core and side–chains allow fine–tuning of miscibility and crystallisation tendencies.^{109,299,364} Because of the side–chains, FREA can be modified to form pure crystalline domains with nanoscale structures; one of the most important factors for efficient charge separation.^{95,130,144–149,344} This morphology control while maintaining high extinction coefficients and adequate charge mobility set FREA apart from other SMA (e.g. PDI and NDI) where the right balance has not yet been achieved.^{109,299}

The broadband absorption, i.e. from red–NIR wavelengths (700–900 nm), of FREA allows them to be matched with the vast library of existing low to medium band-gap polymers.^{108,109,365} The development trajectory of polymer donors has fortuitously led to an extensive library of donor polymers whereby many complement the absorption of SMA (i.e. those that absorb in the near-infrared). Moreover, a large selection of donor HOMO levels that can be matched with FREA to facilitate charge separation.¹⁰⁹ In comparison, PDI and NDI have significantly higher bandgap putting their absorption further to the blue end of the solar spectrum, 620 nm (2.00 eV), making HOMO– LUMO matching to current polymer donors more difficult.¹⁰⁹

In order to achieve optimum efficiency under typical solar irradiation, it is necessary to shift the band-edge into the near-infrared, 1130 nm (1.10 eV). If using a fullerene acceptor, this shift in absorption must be achieved by the polymer donor. Moving absorption into the near-infrared is an area where the A–D–A structure of FREA is beneficial; the A–D–A structure allows for delocalisation of the electron, in a push–pull nature to allow for the shifting of absorption into the near-infrared.²⁴⁵ Recently an absorption edge nearing 1000 nm (1.24 eV) has been achieved^{288,365,366} (with a PCE of 10–13 %) showing it is possible to lower the bandgap below the ideal single junction value of 928 nm (1.34 eV) band-gap in FREA.¹⁰³

Achieving high enough electron mobility to function as an OPV is an area where FREA of the ITIC type has excelled. The improved mobility is attributed to the rigid core structure that reduces reorganisation energy required for electron hopping.³⁴⁴ For optimum packing, the electron deficient end capping groups are exposed to each other, allowing them to make sufficient contact with adjacent molecules resulting in enhanced electron mobility (i.e. the A–D–A π conjugated system is extended between molecules).²⁵⁷

One area where PDIs show an advantage over FREA is in the electron mobility, PDIs have mobility typically an order of magnitude higher than FREA (10^{-5}

vs $10^{-4} \text{ cm}^2 \text{ V}^{-1} \text{ S}^{-1}$).¹⁰⁹ The electron mobility serves to limit device thickness, therefore leading a narrow range of optimal thickness. The limit on thickness can be a problem for the number of photons absorbed or manufacturing process.^{367–369}

The molecule used in this work is IDIC, shown in Figure 5.1, which differs from ITIC (the prototypical A–D–A acceptor) by the shortening of the conjugation in the donor part of the A–D–A structure, whereby the number of thiophene moieties in the core is reduced from four to two.³⁷⁰ The decreased conjugation has little effect on the absorption spectrum,^{113,370} but allows the synthesis to be simplified into a single step that is high yielding, using only commercially available starting materials.³⁷⁰ At the time of publication, IDIC had the highest reported PCE for a non–fullerene acceptor, at 8.71 %, more importantly, it was achieved without optimisation of the donor polymer or device morphology.³⁷⁰

This work begins to address the need for a better understanding of the photophysics of SMA and how it compares to that of fullerene–based devices.^{128,344} We address the open question of how the charge generation and decay dynamics are affected by replacing fullerene with SMA, specifically IDIC. We first notice that if the polymer donor is optimised to match IDIC, charge generation from both donor and acceptor phase is similar to that observed for efficient fullerene OPVs. To further investigate these observations a series of devices are prepared whereby IDIC is substituted with PC₆₁BM and morphology is optimised using 1,8–diiodooctane (DIO). In addition, the effect of an advanced light capture coating, which gives the device a record–setting efficiency, on the underlying photophysics is investigated. The exciton pathway from initial excitation placed in either polymer, IDIC, and PC₆₁BM phases is tracked from charge generation (~ 100 fs) to geminate recombination (~ 1 μ s); and the biomolecular dynamics are probed. The majority of improvements in PCE is due to the complementary absorption of IDIC and FTAZ; this effect is enhanced by the advanced light capturing pattern further boosting absorption. Because the absorption of the acceptor (IDIC) is measurable using transient absorption (TA) spectroscopy, we can rule

out triplet formation as a loss pathway. We find that once the device morphology is optimised with DIO there is little observable difference in the charge decay lifetimes between IDIC and Fullerene.

5.2 Finding a donor for IDIC acceptor

To understand how the energy level alignment and chemical structure of donor polymer affects the efficiency of BHJ solar cell containing IDIC; five different polymer donors are characterised. The PCE of these devices varies from 5.24 % to 9.2 % illustrating the need to select a well-matched donor polymer. The efficiency is further increased to 11.03 % by optimising morphology. In order to understand the properties that lead to high PCE each polymer was characterised using a multitude of techniques to explore the steady-state optical properties, morphology, and device parameters. We studied only the most efficient polymer in depth, as such the photophysics of the PTFBDT-BZS:IDIC without DIO has been characterised via TA spectroscopy and compared with other efficient polymer:fullerene blends. The observation of similar photophysics provides a prelude to the importance of matching absorption spectra and indicates that the photophysics of optimised IDIC blend is similar to fullerenes.

The five polymer donors; PTB7-Th,¹²⁵ J51,³⁷¹ PDCBT,³⁷² PDBTT1,³⁷³ and PTFBDT-BZS³⁷⁴, were chosen because they have varying energy levels, absorption, and chemical structures. The donor polymers are shown in Figure 5.2, they include thiophene, benzodithiophene, and dithienobenzodithiophene on the main chains. Each polymer is blended with IDIC (5.2), FREA, to give the active layer of the OPV device. The final OPV is fabricated with an indium tin oxide (ITO)/ZnO/active layer/MoOx/Ag structure.

While the overall aim of the research was to find an optimised donor material for IDIC, our main contribution is understanding the photophysics, i.e. charge generation and recombination, in the most efficient polymer:IDIC Blend (PTFBDT-BZS). As such, determining the optimal polymer donor is summarised in Section 5.2.1;

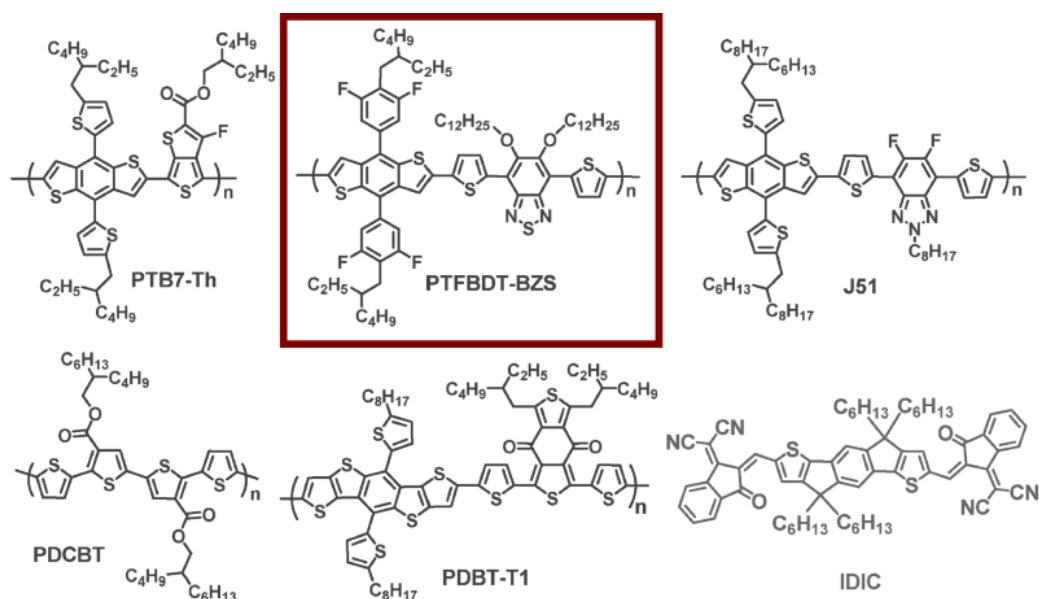


Figure 5.2: Chemical structures of the five polymer donors PTB7-Th, J51, PDCBT, PDBT-T1, and PTFBDT-BZS and the small-molecule acceptor IDIC used to make bulk heterojunction organic solar cells. The red box surrounds the structure that was studied with TA.

including a summary of the morphological and device characteristics that support PTFBDT-BZS as being the most efficient donor polymer. Then the ultra-fast charge generation and recombination in the PTFBDT-BZS blend are probed by TA, and a detailed analysis of signal assignment is presented. From this, a comparison between charges in the donor and acceptor phase is made. Overall excitation of either the donor or acceptor phase leads to similar charge dynamics, with the only a minor change in timescales. Furthermore, it is noted that the charge dynamics observed are not out of place when compared with efficient polymer:fullerene BHJ solar cells.

5.2.1 Electrical and morphology measurements to understand the most efficient polymer

This section presents an overview of how the electrical and steady-state absorption of all five measured polymers indicating PTFBDT-BZS and PDBT-T1 as the

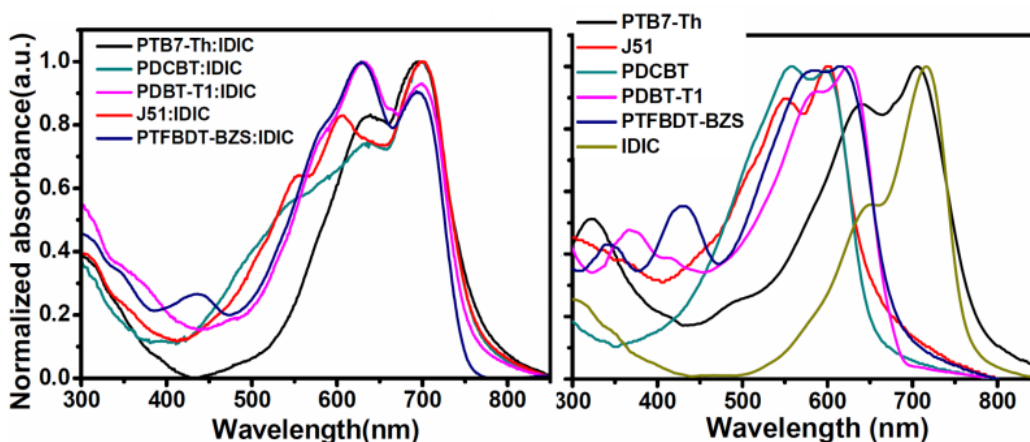


Figure 5.3: Normalized absorption spectra for the five polymers and IDIC (right) and the polymer:IDIC blend (left)

top candidates for morphological optimisation. Following the optimisation of morphology, with DIO, it is seen that increased mobility and the complementary light absorption is the key reason for explaining why PTFBDT-BZS is a better donor for IDIC.

Figure 5.3 (a) shows the normalised absorption spectra of the blends while (b) show the neat polymer donors and IDIC. PTB7-Th (black) absorption has a substantial overlap with IDIC while the remaining have the absorption offset shifted ~ 100 nm when compared with IDIC. The effect of this on device absorption (a) is seen with all polymers showing an enhanced absorption across the 400–630 nm region.

Table 5.1 summaries the current vs. voltage (J–V) measurement results. The open-circuit voltage (V_{oc}) is closely related to the HOMO of the donor with J51 having the lowest V_{oc} (0.80 V) and PTFBDT-BZS having the highest (0.92 V). The variation J_{sc} is explained by changes in absorption, as the external quantum efficiency (EQE), also known as incident photon efficiency) in the 500 to 600 nm range is significantly lower in the PTB7-Th blend. The EQE is mirroring the absorption as the complementary absorbing PTFBDT-BZS and PDBT-T1 having

significantly higher J_{sc} than the almost overlapping PTB7–Th. The atomic force microscopy (AFM) showed similar roughness for all films and grazing-incidence wide-angle x-ray scattering (GIWAXS) showed ordered π – π stacking present, indicating that in all cases the IDIC has good miscibility in all polymer donor used.

Material	V_{OC}	$J_{SC}(mAcm^{-2})$	FF	PCE (%)
J51	0.796	12.24	0.660	6.94
PTB7–Th	0.806	10.90	0.561	5.24
PDCBT	0.814	11.31	0.641	6.28
PDBT–T1	0.850	15.85	0.680	9.20
PTFBDT–BZS	0.921	14.52	0.602	8.06

Table 5.1: Electrical characterisation under the illumination of AM 1.5, 100 $mWcm^{-2}$ for devices,.

The best performing systems (PDBT–T1, and PTFBDT–BZS) were optimised further by adding DIO during spin coating. This lead to improvements in PCE to 11.03 %, with a noticeable improvement in fill factor (FF) and J_{sc} , table 5.2. The morphology underwent a noticeable change for both donors, with coherence length improving from ~ 2.6 to 4.9 nm consistent with the higher hole and electron mobility measured. The measured hole mobilities increased from 1.9×10^{-5} to 6.2×10^{-5} for PTFBDT–BZS and from 4.0×10^{-5} to 6.3×10^{-5} for PDBT–T1. The resonant soft x-ray scattering (R–SoXS) shows domain sizes moved towards a more optimal 50 nm, with purity increasing; this is beneficial for charge transport and dissociation respectively.^{101,145}

The addition of DIO leads to increased charge mobility, optimal domain size, and increased domain purity. The increased mobility should result in a faster bimolecular decay, which is unfortunately not measured here, while the higher domain purity would prolong the observed singlet and also decrease the geminate recombination. As such, compared to the measured photophysics discussed below (without DIO), the lifetime of exciton and charges are shorter.

Material	V_{OC}	$J_{SC}(mAcm^{-2})$	FF	PCE (%)
PDBT-T1	0.850	15.85	0.680	9.20
PDBT-T1 (0.25 % DIO)	0.834	16.98	0.732	10.37
PDBT-T1 (0.5 % DIO)	0.826	14.81	0.662	8.62
PTFBDT-BZ	0.921	14.52	0.602	8.06
PTFBDT-BZS (0.25 % DIO)	0.905	17.30	0.708	11.03
PTFBDT-BZS (0.5 % DIO)	0.891	14.51	0.622	8.04

Table 5.2: Electrical characterisation data collected under the illumination of AM 1.5, 100 $mWcm^{-2}$ for two most efficient OPV

Our collaborators show that a BHJ solar cell with PTFBDT-BZS as the acceptor and IDIC as a small-molecular acceptor produced an efficient device, the photophysics studied via transition absorption (TA) spectroscopy are discussed in the context of fullerene-based OPV.

5.2.2 Ultrafast charge generation and recombination

Transient absorption spectroscopy (TA) was used to understand the charge generation and recombination in the most efficient system, PTFBDT-BZS:IDIC. The photophysics of the IDIC and PTFBDT-BZS phases are separated by using two excitation wavelengths. These excitation wavelengths are chosen by comparing the neat absorption spectra of both IDIC and PTFBDT-BZS. With 712 nm excitation only the IDIC phase is excited, while excitation at 475 nm primarily probes the PTFBDT-BZS phase.

To understand the TA spectra and dynamics in the of both the donor and acceptor in the blended film TA measurements of neat PTFBDT-BZS and IDIC films are first assigned. Figure 5.4a shows the spectra for the neat donor and acceptor 600 fs and 100 ps after excitation. The TA spectra of PTFBDT-BZS (green) and IDIC (purple) exhibit characteristic ground-state bleach signals (GSB, $\Delta T/T > 0$) overlapping with their visible absorption, along with photo-induced absorption peaks (PIA, $\Delta T/T < 0$) in the near infrared. IDIC exhibits stimulated emission

($\Delta T/T > 0$) 700 nm (1.77 eV). For both IDIC and PTFBDT-BZS there is no change in the spectra between 600 fs and 100 ps indicating a single excited state species being present before decay to the ground state. These TA spectra are attributed to the singlet excited state as they are formed initially after excitation, and in the case of IDIC a stimulated emission peak is present. Importantly the following details about the PIA and GSB should be noted for discussion of the blend film. PIA feature indicative of an exciton is, for IDIC, a sharp peak centred on 900 nm (1.38 eV) and for PTFBDT-BZS, a broad peak at 1240 nm (1.00 eV). While signals from the donor and acceptor overlap throughout the spectra a positive signal at approximately 520 nm (2.38 eV) can only be from PTFBDT-BZS being in an excited state. This because the IDIC component does not contribute to the GSB at that wavelength.

To make a comparison of the singlet exciton decay between the neat material and blend two things must be done. The first as shown in Figure 5.4b for both materials, is demonstrating that increasing the fluence does not lead to any noticeable change in the decay. The lack of fluence dependent response shows that lifetimes are population independent and indicative of inherent lifetimes. The second is to compare the lifetimes between neat and blend material and an amplitude weighted lifetime is calculated for each polymer. The amplitude weighting method is necessary due to the dispersive decay profile requiring three exponentials to fit the decay adequately.^{375–377} This gives an average lifetime ($\langle \tau \rangle$) of 68 ps and 93 ps for PTFBDT-BZS and IDIC respectively, which can be compared to the blend to give a qualitative idea about exciton quenching efficiency and charge yield.

Figure 5.5a shows TA spectra after exciting the blend at 712 nm (1.74 eV), where only IDIC absorbs. IDIC exciton features are evident in the 300 fs spectra, along with additional ground-state bleaching in the blue PTFBDT-BZS region. A photo-induced absorption shoulder near 950 nm (1.31 eV) is seen from 300 fs in the blend, this feature was not present in either neat IDIC or PTFBDT-BZS, and grows into a prominent peak by 2 ps. This shoulder can be attributed to the

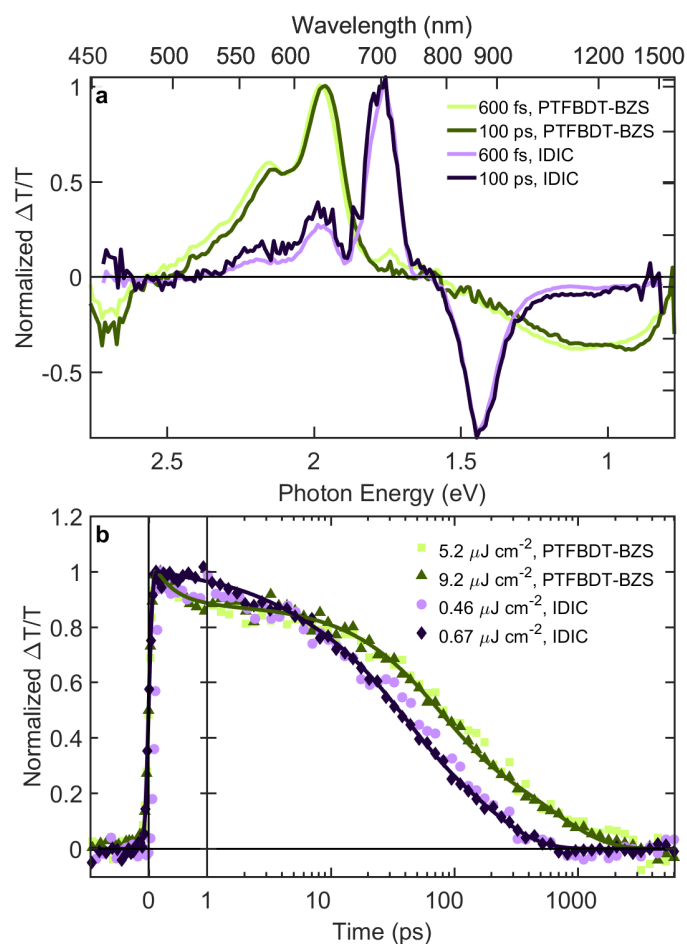


Figure 5.4: (a) Spectra slices taken at 600 fs and 100 ps of neat films of PTFBDT-BZS excited at 475 nm, $6.4 \mu\text{J cm}^{-2}$, and IDIC excited at 712 nm, $1.3 \mu\text{J cm}^{-2}$. (b) Representative decay profiles of the spectra shown in (a) collected at two different fluence to show fluence independent decay dynamic, solid lines are exponential fits to give amplitude weighted lifetimes.

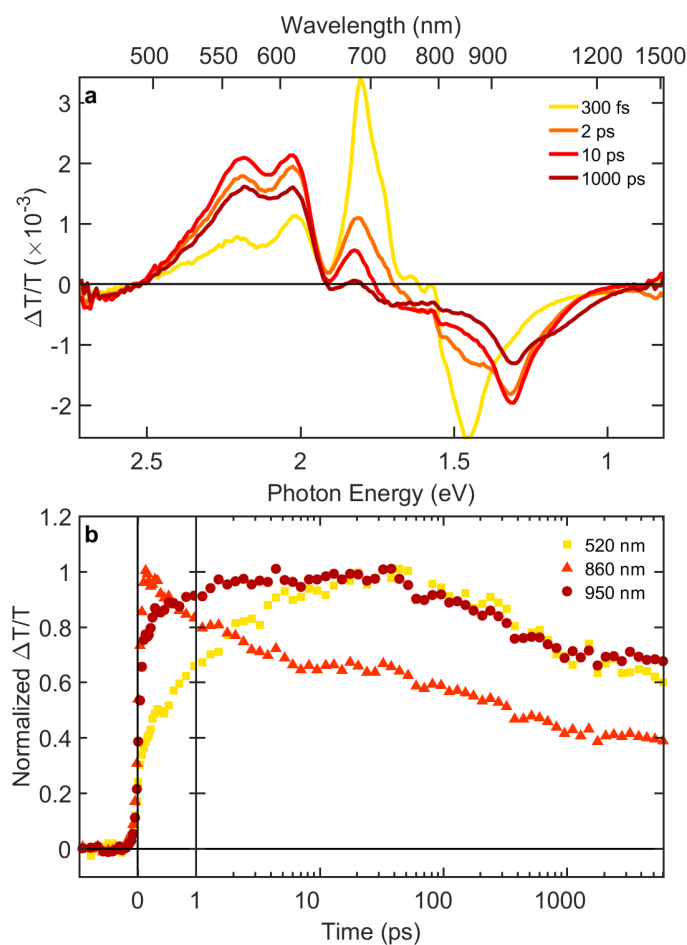


Figure 5.5: (a) Series of TA spectra for a blended film of PTFBBDT-BZS:IDIC (without DIO), after 100 fs excitation resonant with the IDIC acceptor at 712 nm ($5.2 \mu\text{J cm}^{-2}$). b) Kinetics from the same measurements as part (a) at selected wavelengths.

prompt (in <300 fs) formation of charge pairs, supported by the ground-state bleaching in the visible region from both the donor and acceptor components. As GSB for PTFBBDT-BZS is only possible if it is perturbed from its ground state, where energy transfer from IDIC to PTFBBDT-BZS is excluded on thermodynamic grounds, as well by the absence of PTFBBDT-BZS exciton absorption at wavelengths > 1200 nm (1.03 eV). Hence the signal near 950 nm (1.31 eV) is assigned to the formation of charge pairs.

To monitor the exciton-to-charge conversion process several wavelengths regions are integrated, these are shown in Figure 5.5b, these are normalised to emphasise the decay dynamics. The IDIC exciton photo-induced absorption peak at 860 nm (1.44 eV) initially decays dispersively with an average lifetime of 1.0 ps, leaving a residual signal from the overlapping charge peak. By comparison with the 93 ps exciton lifetime of IDIC, we conclude near unit charge transfer efficiency. This decay being attributed to charge generation is further supported by comparison to the growth of the 520 nm (2.38 eV) PTFBDT-BZS GSB which grows on the same timescale, this correlation is due to charge pairs occupy both PTFBDT-BZS (holes) and IDIC (electrons).

Prompt and delayed charge generation components are evident from the 520 nm (2.38 eV) signal where the bleaching signal comes exclusively from charges occupying PTFBDT-BZS without any contribution of exciton signals. Approximately half of the charge pairs are formed within 200 fs, with a slower phase of charge commensurate with the 1.0 ps timescale of exciton quenching and complete by ~30 ps. From the magnitude of the signal, we can conclude that ~50 % of the final charge population is formed promptly when considering IDIC phase. The charge decay can be followed at 950 nm (1.31 eV) although its dynamics are also affected by the overlapping IDIC exciton peak. The overlap is only present at times <30 ps as seen by the similar dynamics between the 520 nm (2.38 eV) (PTFBDT-BZS GSB) meaning the timescale >30 ps represent the evolution of the charge population. Within 1 ns ~30 % of charges recombine. The fluence independence charge decay dynamics (Figure 5.6) points towards geminate recombination via charge transfer (CT) states as a possible explanation for the lower J_{sc} of the blend prepared without DIO as compared to with DIO.

Figure 5.7a compares the TA spectra probing only the IDIC phase by using 712 nm excitation (red-yellow, discussed above) and probing primarily the PTFBDT-BZS phase (blue-teal) using 475 nm excitation. The spectra from 300 fs show a broad PIA peak at 1240 nm (1.00 eV) showing evidence of an exciton on PTFBDT-BZS, and this difference is not unexpected as 475 nm excitation will directly excite the

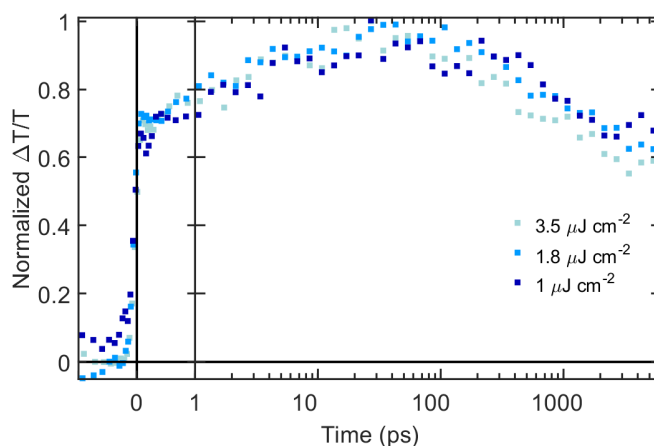


Figure 5.6: TA kinetics traces taken at 520 nm for a film of PTFBTD-BZS:IDIC (without DIO), after 100 fs excitation resonant with the PTFBTD-BZS phase at 475 nm. The excitation is noted in the legend, and the dynamics show a fluence independent response suggesting the decay dynamics are not bimolecular.

polymer phase. Furthermore, the charge shoulder seen at 950 nm (1.31 eV) after 712 nm excitation is now a distinct peak due to the ratio of IDIC exciton to charges moving in favour of charge pairs. The change in spectra shape could be due to more prompt charge generation or relatively less absorption in the IDIC phase as at 475 nm PTFBTD-BZS also absorbed some of the incident photons. Looking at the 1000 ps spectra there is no significant difference; this shows that the charges formed from exciting the donor or acceptor regions are equivalent, and the excess energy of 475 nm excitation does not affect the fate of charge pairs.

Moving on to the charge generation and decay, Figure 5.7b shows a very short-lived polymer exciton signal is initially seen at > 1200 nm (1.03 eV) with an average lifetime of 700 fs. The absence of a longer-lived polymer exciton phase may reflect the smaller polymer domains, as well as an intermediate energy transfer step to IDIC. The charge decay 520 nm (2.38 eV) is the same for both excitation wavelengths further supporting the similar species seen in the spectra. When looking at the prompt charge generation following 475 nm excitation the picture is not as clear as previously, now the PTFBTD-BZS exciton contributes to the GSB

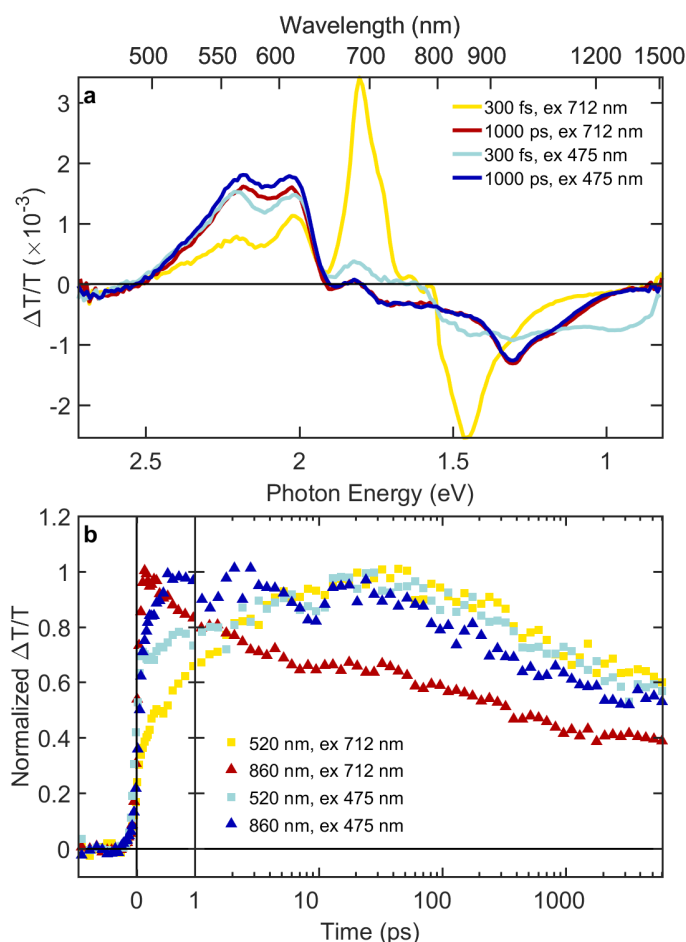


Figure 5.7: (a) TA spectra slices taken at 300 fs and 1000 ps for a film of PTFBTD-BZS:IDIC (without DIO), after 100 fs excitation resonant with the IDIC acceptor at 712 nm ($5.2 \mu\text{J cm}^{-2}$) and mostly PTFBTD-BZS phase at 475 nm ($0.7 \mu\text{J cm}^{-2}$). b) Kinetics from the same measurements as part (a) at selected wavelengths to show the difference between charge and exciton dynamics.

signal at 520 nm (2.38 eV) mixing together the exciton decay and charge generation profiles hiding the prompt fraction. Looking at the ratio of PTFBTD-BZS GSB to exciton PIA it appears similar to the neat PTFBTD-BZS suggesting that the fraction of promptly generated charges is small.

The observed charge generation has a comparatively higher fraction of delayed charge generation when compared to efficient polymer:fullerene blends,^{166,378} The

prompt component arises from excitons formed at the interface of PTFBDT-BZS and IDIC including intermixed regions^{92,378} along with delocalised exciton.¹⁵⁷ The delayed component is from those excitons formed in a pure phase and therefore must diffuse before they can reach an interface, i.e. exciton in pure IDIC domains.

By probing both the donor and acceptor channels, we have shown that both channels are high-efficiency charge generation pathways, cementing their complementarity nature. With 30 % of charges recombining within a 1 ns timescale (Figure 5.5) the large J_{sc} gains seen by adding DIO are explained. Increasing domain purity decreases the likelihood of charge recombination; as the electron and hole both reside on different molecules. Therefore by increasing domain purity and thus decreases charge recombination a more substantial fraction of generated charges percolate to the electrodes, hence a higher J_{sc} is observed.

5.3 Balanced donor and acceptor absorption profile push efficiency above 12 %

By taking the lessons learned from optimising the donor polymer, i.e. balancing absorption, a BHJ-OPV with efficiencies higher than 12 % when incorporating advanced light capturing patterning was fabricated. The active layer of which is the focus of this section. Comparisons between the donor polymer, FTAZ, blended with PC₆₁BM and IDIC are shown with the PCE improving from 5.34 % to 11.6 % when IDIC is used instead of PC₆₁BM. The morphology (controlled via DIO), advanced light capture and the effect of using IDIC are probed via many advanced characterisation techniques. While the morphology changes, the majority of the benefits are attributed to the balanced absorption of the donor and acceptor pair as the photophysics show little variation across the studied devices.

Figure 5.8a shows the normalised absorption spectra of FTAZ (black) and IDIC (blue). There is almost no (<0.2) absorption from IDIC across the 400–600 nm re-

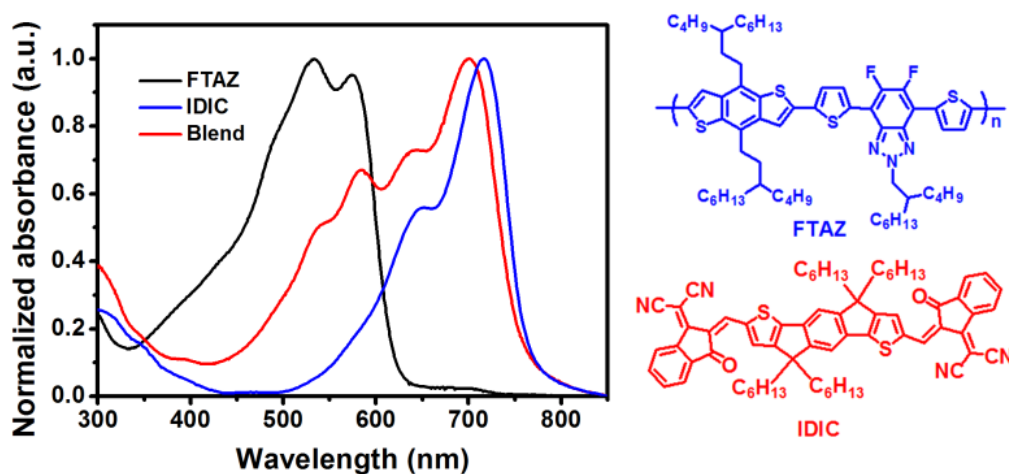


Figure 5.8: Normalised absorption spectra of neat IDIC, FTAZ and a blend 1:1.5 ratio films. Chemical structures of the FTAZ medium band-gap donor polymer and IDIC small-molecule acceptor.

gion where FTAZ absorbs, and where IDIC absorbs, 600–800, FTAZ has similar low absorption. This donor and acceptor pair is exemplary of using both materials in the BHJ to optimise absorption. The chemical structures are also shown for completeness; the IDIC is the same donor used in Section 5.2, while the donor polymer FTAZ has been chosen to balance the absorption profiles further.

The active layers are fabricated with FTAZ and either IDIC or 6,6-phenyl C₆₁ butyric acid methyl ester (PC₆₁BM) as the electron acceptor. Morphological effects are also investigated with active layers produced with and without the addition of DIO. The working devices are fabricated with a device structure of; tin oxide (ITO)/ZnO/FTAZ:IDIC, or PC₆₁BM/MoO_x/Ag. The ZnO layer has a light enhancement pattern applied where noted. Ultrafast transient absorption spectroscopy used to investigate the photophysics of the active layers (IDIC with and without DIO, PC₆₁BM with DIO) of the various devices deposited onto a quartz substrate. In addition, the most efficient blend, FTAZ:IDIC with DIO, the quartz is replaced with ZnO substrate with and without the light capturing pattern.

The focus of this research is to understand the photophysical changes that result from a shift in PCE from 5.34 % to 12.5 %. We also take the opportunity to explore the differences between FREA and PC₆₁BM acceptors. The main contribution made by this author is the TA measurements and analysis that reveals the charge generation and recombination dynamics across the series of devices studied. As such, the other measurements are summarised in Section 5.2.1, this includes electrical and morphological characterisation. We highlight the crucial parameters of devices (i.e. domain purity, domain size and crystallinity) and discuss these with reference to the TA results. It is found that excitation of either the donor or acceptor phase leads to similar behaviour of the charge pairs. This trend continues when changing the IDIC for PC₆₁BM and also when patterning the ZnO surface. The triplet decay mechanism can be excluded by taking advantage of the IDIC having much stronger absorption than PC₆₁BM providing a clear distinction between charges and triplets.

5.3.1 Characterisation of the device morphology, electrical, and steady-state properties

In this section the analysis from our collaborators on steady-state absorption, electrical, and morphological measurements are summarised. GIWAXS and R-SoXS are used to probe crystal orientation, domain size, and domain purity. Electrical and steady-state absorption measurements show the primary cause of the increased PCE is due to higher J_{sc} attributed to better absorption across the 600–800 nm from IDIC.

IDIC replaces PC₆₁BM the J_{sc} almost doubles from 9.5 to 18.5 $mAcm^{-2}$, the primary cause of this is increased absorption as PC₆₁BM has almost no absorption in the 400–600 nm region where FTAZ absorbs. The increase in the PCE is attributed to the additional absorption band and is supported by the enhanced EQE over this region.

Material	V_{OC} (V)	J_{SC} ($mAcm^{-2}$)	FF	PCE (%)	Thickness (nm)
FTAZ:PC ₆₁ BM (DIO, Flat)	0.80	9.51	0.67	5.34	135
FTAZ:IDIC (DIO, Flat)	0.85	18.5	0.73	11.6	110
FTAZ:IDIC (DIO, Pattern)	0.84	20.1	0.72	12.5	110
FTAZ:IDIC (Flat)	0.86	16.4	0.69	9.70	85

Table 5.3: Electrical characterisation data collected under the illumination of AM 1.5, 100 $mWcm^{-2}$ for all devices studied, and film thickness measurements.

AFM, GIWAXS, R-SoXS measurements were carried out to compare the morphology of the various blends and substrates. The AFM shows that the patterned ZnO surface effects the top surface topology (measured by roughness) increases from 1.2 nm (both IDIC and PC₆₁BM) to 3.67 nm on the patterned surface. The GIWAXS data shows the IDIC improved molecular packing of FTAZ when compared with PC₆₁BM, while the addition of DIO enhances the packing of both phases. GIWAXS measurements indicate a strong coherence of the IDIC phase that is beneficial for charge transport. The coherence length is slightly reduced on a patterned ZnO from 3.5 to 3.3 nm. The domain size and purity (calculated from R-SoXS) show an interesting variation between PC₆₁BM and IDIC with IDIC having larger (52 nm vs 22 nm) and purer (1 vs 0.3) domains. Unfortunately, the domain size without DIO was difficult to resolve (potentially around <5 nm), but purity was reduced to 0.81. The patterning of ZnO reduced the IDIC domain size to 20 nm and decreased the purity to 0.89. This decrease in purity is ordinarily detrimental to PV performance; however, in this case, the photophysical characterisation suggests it has little effect on the photophysics. The absolute PCE is challenging to distinguish via TA spectroscopy as relative charge populations are hard to monitor due to morphological induced changes in the observed spectra.⁹² The morphological changes that are important to the interpretation of the charge dynamics have been summarised in Table 5.4. The domain purity will impact the prompt vs delayed charge generation; the prompt generation is related to mixed-phase, while the delayed charge generation is from excitons

in isolated phases migrating to the interface. The size of the pure phase will increase the time taken for excitons to reach the interface and undergo charge separation, and this will be seen in the growth lifetime of charge generation.

Material	Domain purity	Domain size (nm)
FTAZ:PC ₆₁ BM (DIO, Flat)	0.3	22
FTAZ:IDIC (DIO, Flat)	1	52
FTAZ:IDIC (DIO, Pattern)	0.89	22
FTAZ:IDIC (Flat)	0.89	<5

Table 5.4: Summary of R-SoXS domain purity and domain size results.

Transient absorption spectroscopy will be used to compare the charge generation, and recombination pathways and rates across the materials looking at the effect of adding DIO and patterning the ZnO substrate. The results reveal that patterning the ZnO substrate increases efficiency solely through increased light harvesting and that the photophysics of FTAZ:IDIC blends is relatively insensitive to morphological changes.

5.3.2 Ultrafast charge generation and recombination

To understand the differences between PC₆₁BM, IDIC, and patterning the substrate a series of TA experiments was carried out, this included using different excitation wavelengths in order to probe the charge generation and decay dynamics in both the donor and acceptor phases. We find that there are minimal differences in the charge decay dynamics and diffusion dynamics across the materials studied here. The charge growth dynamics are effected by domain size differences between donor and acceptor phase and the addition of DIO. Finally, the formation of triplets is ruled out based on the observation of a GSB signal arising from IDIC. This is normally seen in fullerene-based devices because of the much lower extinction coefficients in the spectrally resolved region.

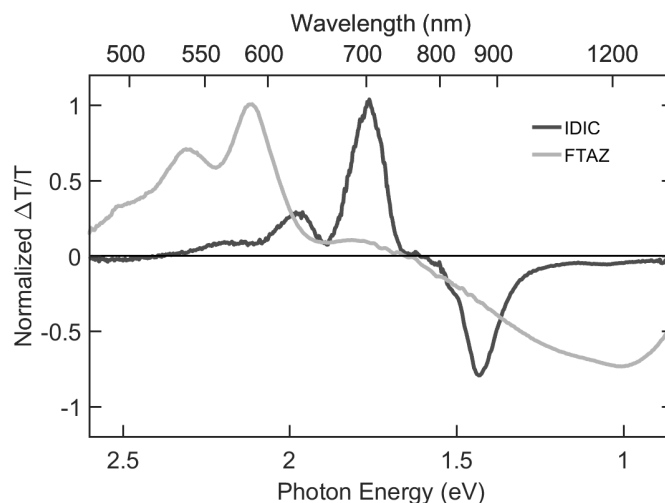


Figure 5.9: TA spectra collect from neat films of IDIC (712 nm $0.46 \mu\text{J cm}^{-2}$) and FTAZ (475 nm $5.2 \mu\text{J cm}^{-2}$). Representative of singlet excitons species.

TA signal assignments

The neat TA spectra and dynamics of FTAZ and IDIC are discussed; this will aid in understanding the more complex blend spectra. Figure 5.9 shows time-integrated spectra that are assigned to a singlet excited state as there is no noticeable change in the spectral features before decay. Both IDIC (described in Sections 5.2.2) and the FTAZ spectra exhibit characteristic ground-state bleach signals (GSB, $\Delta T/T > 0$) coinciding with their visible absorption, photo-induced absorption peaks (PIA, $\Delta T/T < 0$) in the near infrared, and stimulated emission ($\Delta T/T > 0$) ~ 700 nm (1.77 eV). The PIA features are distinct for both FTAZ and IDIC and are diagnostic of a singlet excited state. For IDIC a sharp peak centred on 900 nm (1.38 eV) and FTAZ has a broad peak at 1240 nm (1.00 eV). Non-overlapping regions of the GSB can be seen for FTAZ < 540 nm (2.30 eV) allowing the unambiguous separation of excited state populations remaining on FTAZ or IDIC.

When using 712 nm (1.74 eV) to excite the blend, IDIC is primary excited (Figure 5.10a). The initial TA spectrum (200 fs) is similar to the neat IDIC spectrum pre-

sented above, ground-state bleach peaks are present at approximately 650 nm (1.91 eV) and 730 nm (1.70 eV), and a photo-induced absorption peak at 890 nm (1.39 eV). In the subsequent time slices (2 ps to 5 ns) the IDIC exciton spectrum is replaced by a spectrum attributed to charge pairs. Hole transfer from IDIC to FTAZ means the GSB of the IDIC is complemented with bleaching of the FTAZ polymer, i.e. a positive signal above 620 nm (2.00 eV). In addition, the IDIC photo-induced absorption peak at 885 nm (1.40 eV) is replaced by a new PIA peak at 950 nm (1.31 eV). The new PIA peak at 950 nm (1.31 eV) is indicative of electrons in IDIC, and is present in the TA signals observed for IDIC blended with a different donor polymer (Section 5.2.2 and is absent when IDIC is replaced with fullerene (below).

To compare excitation of the donor and acceptor channels, the donor component of the FTAZ:IDIC blend is excited with 532 nm (2.33 eV) Figure 5.10b. The variation is that signatures of an exciton in both FTAZ and IDIC are present, i.e. a PIA peak at both 890 nm (1.39 eV) and 1240 nm (1.00 eV). The FTAZ exciton is identified by the initial peak at 1240 nm (1.00 eV) which decays by 2 ps, with neat TA spectra of FTAZ support this assignment see Figure 5.9. The FTAZ exciton then undergoes electron transfer to generate charges before 5 ns.

The TA spectra of FTAZ:PC₆₁BM blend is presented in Figure 5.10c. In this blend, only excitation of the donor, 532 nm (2.33 eV), was possible due to PC₆₁BM having very low visible absorption. At early times (200 fs) the FTAZ exciton is present with PIA at 1200 nm (1.03 eV), this decays to give charges following electron transfer to PC₆₁BM. In this system, GSB from PC₆₁BM is not expected due to the low extinction coefficient. Holes in FTAZ have a broad near infrared absorption spanning between 650-950 nm (1.9-1.3 eV), the assignment as holes is made based on the consistency with the above charge spectra and the electro-absorption arising from charge pairs in the material.^{275,276,379}

To understand the effects seen in the TA surfaces a mathematically decomposition was performed. In order to extract the decay dynamics for IDIC, FTAZ and

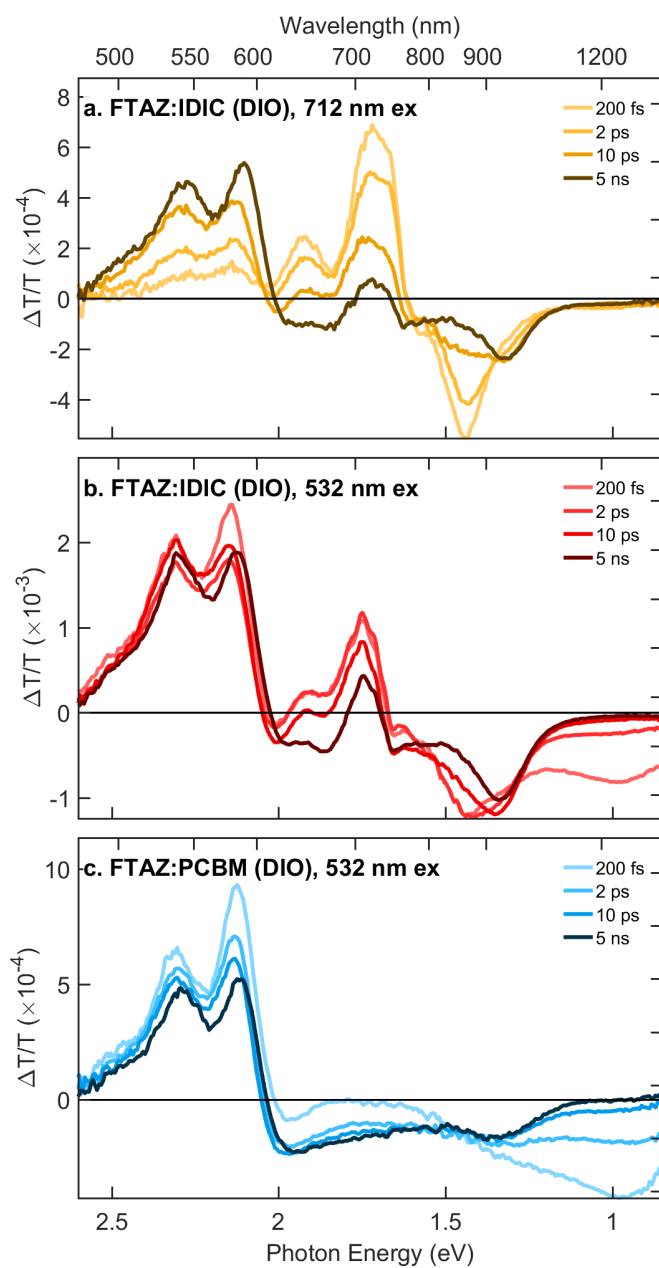


Figure 5.10: Series of TA spectra showing interconversion of excitons to charges for: (a) blended film of FTAA:IDIC (DIO), after 100 fs excitation resonant with the IDIC acceptor at 712 nm. (b) same film as (a) after 100 fs, 532 nm excitation resonant with the FTAA donor. (c) FTAA:PC₆₁BM film after 100 fs 532 nm excitation.

charges the neat IDIC, neat FTAZ, and the second charge component are used. Then an iterative process is performed as described in Section 2.4.2. After decomposition, it is possible to compare charge dynamics for each of the blends, and electron- vs. hole-transfer channels. Figure 5.11 is an example of the mathematical decomposition, (a) shows species associated spectra that when combined with the kinetics in (b) and added to the residuals (c) adequately represent the TA surface.

The two charge species used are not evidence of two distinct charge populations but could be required due to spectral shifts. A change in the electro-absorption, or changes in spectra could be related to the mixed and ordered phases.⁹² The idea that the change is related to different phases is supported when taking into consideration the steady-state absorption spectra, where the more ordered neat IDIC is redshifted when compared with the FTAZ:IDIC blend. In any case, the two species are used to produce a good representation of the TA surface. Here the charge species are used to compare kinetics between excitation wavelength and blend mixture. To that effect, the FTAZ bleaching is normalised between all datasets; in this manner the kinetics are comparable between samples and excitation wavelengths. The final charge population is taken to be the sum of the two charge species.

5.3.3 Charge generation

Figure 5.12 shows the charge dynamics. About 40 % of exciton undergo charge generation in less than 200 fs (i.e. prompt charge generation) in the FTAZ:PC₆₁BM blend, this is significantly less than the typically 70–90 % observed in other high-performance polymer:fullerene blends. This rapid charge generation has even been proposed to be vital to achieving high PCE. The remainder of excitons need to diffuse to the interface before charge generation that proceeds in picoseconds. The lower fraction of prompt charge generation suggests that FTAZ polymer domains are purer or larger than typical fullerene blends. When PC₆₁BM is replaced with IDIC a similar charge generation profile is seen upon the excitation of the

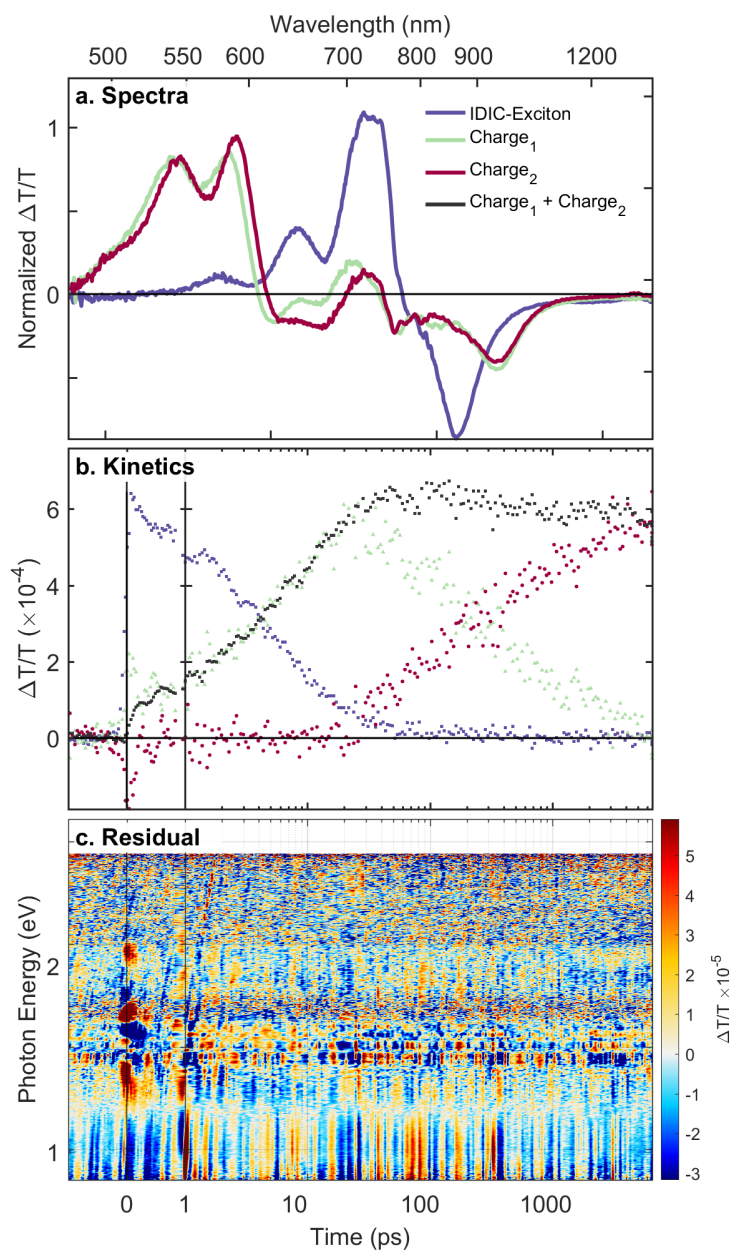


Figure 5.11: Illustrative example of mathematical decomposition of a TA surface for FTAZ:IDIC (1:1.5, w/w, 0.25 % DIO) following excitation at 712 nm ($0.26 \mu\text{J cm}^{-2}$). (a) Associated spectra of exciton and charge species. (b) Kinetics of exciton and charge species, where spectral shifts on longer timescales are captured via two charge species spectra. We do not presume two distinct charge species, but rather sum their populations in subsequent analysis. (c) Residuals from mathematical decomposition fit (note the lack of structure in this surface, and the smaller scale).

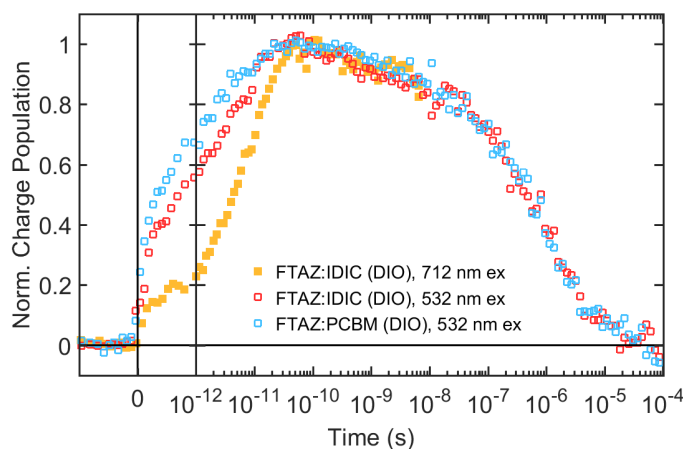


Figure 5.12: Extracted charge dynamics extracted from a decomposition of the TA surfaces for the range of blends and excitation wavelengths indicated ($0.6 - 2 \mu J cm^{-2}$), with charge populations normalised assuming unit efficiency of exciton-to-charge conversion in the low fluence limit.

acceptor ($PC_{61}BM$ or IDIC). Therefore we conclude that the FTAZ phase remains relatively unchanged with similar domain size and purity.

When examining the hole-transfer channel in the FTAZ:IDIC blend, i.e. excitation of IDIC at 712 nm (1.74 eV), a different charge profile is seen (Figure 5.12). Approximately 10 % of charges are generated promptly while the remainder are generated on the picosecond timescale. In the system a with balanced absorption the hole-transfer channel (i.e. from the electron acceptor) plays an essential role in the overall photocurrent. The high phase purity found in the morphological studies is consistent with the slow charge generation.

5.3.4 Charge recombination

Both the hole and electron transfer channel gives rise to a slow, but efficient, charge generation mechanism in FTAZ:IDIC blends, here we move onto investigating the charge recombination. Figure 5.12 reveals similar recombination profiles observed for all blends and generation channels, with recombination occurring from 100 ps into the microsecond regime. Rapid recombination typically in-

icates geminate recombination as a significant loss channel, but in these blends, we find that EQE > 80 % suggesting recombination on these timescales is not a significant problem.

To evaluate the charge mobility for different blends and excitation channels, we fit fluence-dependent charge dynamics with bimolecular recombination incorporating a moving window. Figure 5.13 shows an example of the fitted results following 532 nm excitation. The grey markers indicate the decay of charge population, and this is scaled to match in the population at time equals zero (± 200 fs), while the rainbow series of lines indicates the various fits. These use a bimolecular rate constant and a monomolecular decay, with a moving window of 30 times points (approximately an order of magnitude) and using the same rate constants across all fluence values.

Figure 5.14 shows that the bimolecular recombination constant is above $10^{-14} \text{ cm}^3 \text{ s}^{-1}$ on the hundreds of picosecond timescale for all blends treated with DIO. The bimolecular rate constant decay is a result of mobility dispersion.³⁸⁰ The magnitude and dynamics of bimolecular recombination constants are similar irrespective of the initial formation pathways and whether IDIC or PC₆₁BM is used as the electron acceptor. To understand if the bimolecular rate constant is too high the lifetimes need to be estimated under solar illumination. Steady-state solar illumination corresponds to excitation fluence of $10^{16} \text{ cm}^3 \text{ s}^{-1}$ would result in charge lifetimes exceeding microseconds. At these long bimolecular lifetimes, there is sufficient time for charge extraction to prevail. Instead, these high bimolecular rates indicate both donor and acceptor channels produce highly mobile charges that are able to diffuse away from interfaces swiftly.

5.3.5 Effect of DIO

To study the changes in photophysics due to morphology, a similar set of measurements as described above are carried out on a blend of FTAZ:IDIC without the DIO. They show that the increase in IDIC domain size, from <5 nm to 22 nm, caused by the addition of DIO results in a decreased fraction of prompt charge

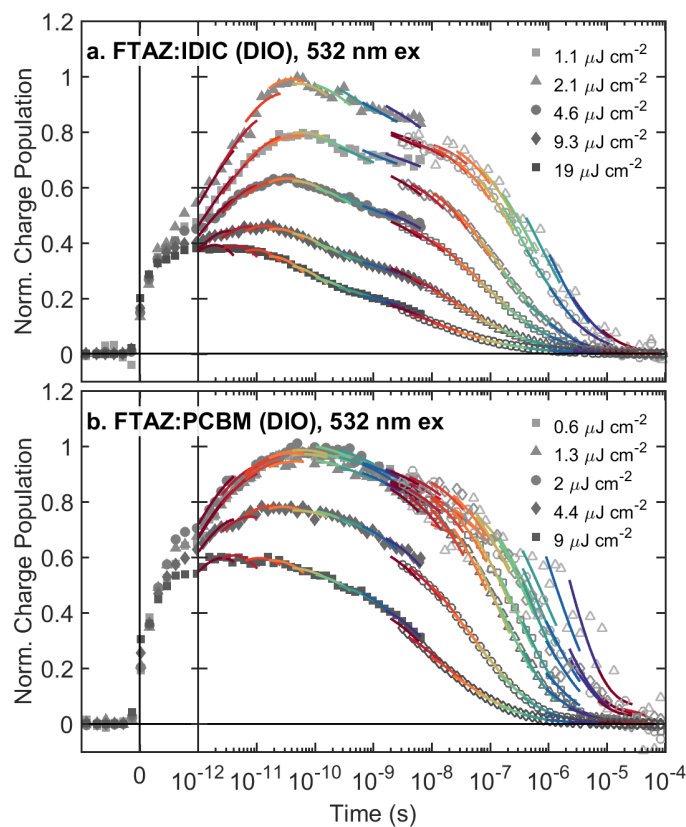


Figure 5.13: Fluence dependent charge dynamics following excitation at 532 nm for (a) FTAZ:IDIC (1:1.5, w/w, 0.25% DIO) on a fused silica substrate, and (b) FTAZ:PCBM (1:1.5, w/w, 0.25% DIO) on a fused silica substrate. Kinetics out to 5 ns were collected following 100 fs excitation pulses, whereas the later data (beginning from 2 ns) was recorded following 700 ps excitation. Also shown in coloured lines are windowed fits of bimolecular recombination constants, β , that globally account for kinetics at each intensity within small moving time window.

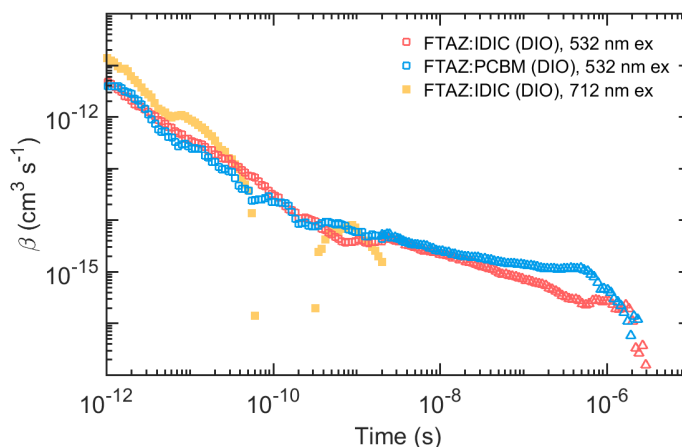


Figure 5.14: Bimolecular recombination constant, β , extracted from a moving window global fit. All films deposited on a quartz substrate in 1:1.5 w/w ratio cast with 0.25 % DIO.

generation. We also observe an increase in the charge lifetime. With no substantial difference seen in the bimolecular (non-geminate) recombination rates.

The spectra resulting from decomposing the TA surface as described are presented in Figure 5.15. The IDIC exciton (a) from directly exciting the IDIC phase it is broadly similar. The removal of DIO enhances the polaron PIA peak, a similar effect can be seen for the FTAZ exciton (b). When considering the charge species (c), a slight shift in the FTAZ GSB (also seen in FTAZ exciton) and the IDIC GSB is observed. These slight changes in the spectra are not significant enough to change the species assigned to each spectrum but suggest a change in the packing of each phase or environment of the charge pairs.

Figure 5.16 presents the charge dynamics for FTAZ:IDIC blends with and without DIO. Considering direct excitation of IDIC (712 nm, orange and green) charge generation is completed in ~ 60 ps suggesting that the variation in domain size does not significantly affect the charge generation time. The offset between growth dynamics caused by the removal of DIO can be explained by the reducing phase-purity as there is a lower fraction on promptly generated charges when DIO is used. The charge generation from the FTAZ phase is probed with 532 nm

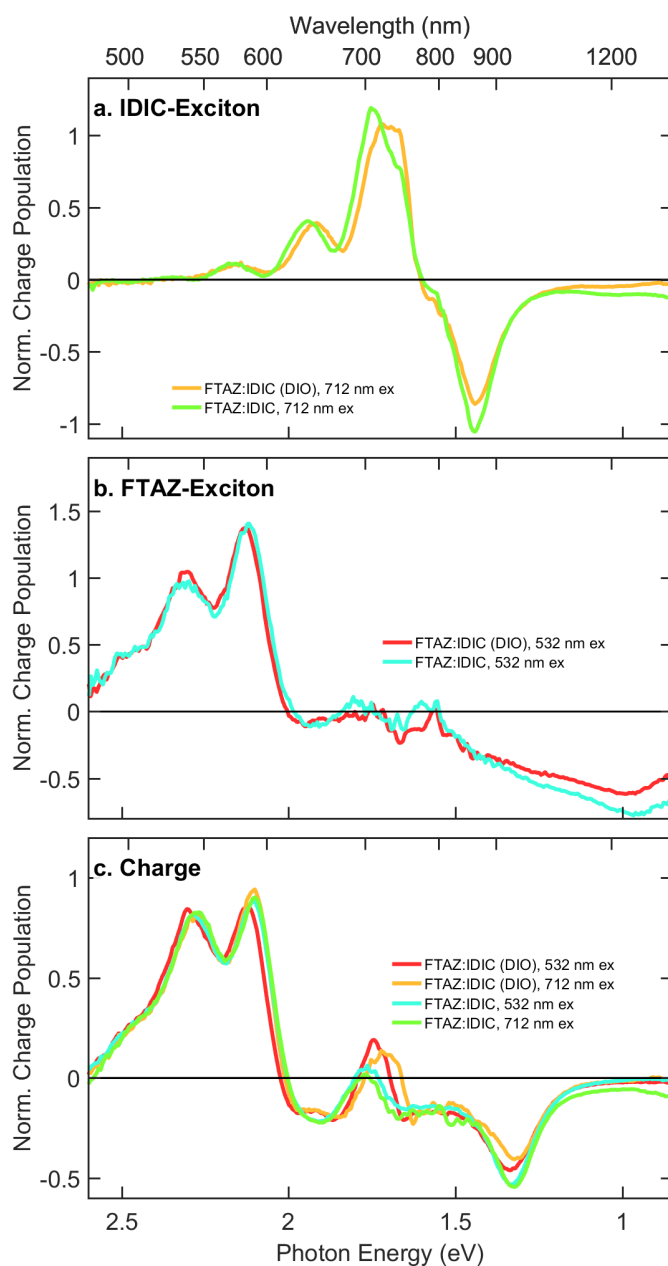


Figure 5.15: Indicative species spectra decomposition from the TA surfaces for the range of blends, normalised assuming unit efficiency of exciton-to-charge conversion in the low fluence limit. (a) IDIC exciton spectra following 712 nm excitation. (b) FTAZ exciton spectra after 532 nm excitation. (c) Charge spectra after exciton decay following excitation as noted.

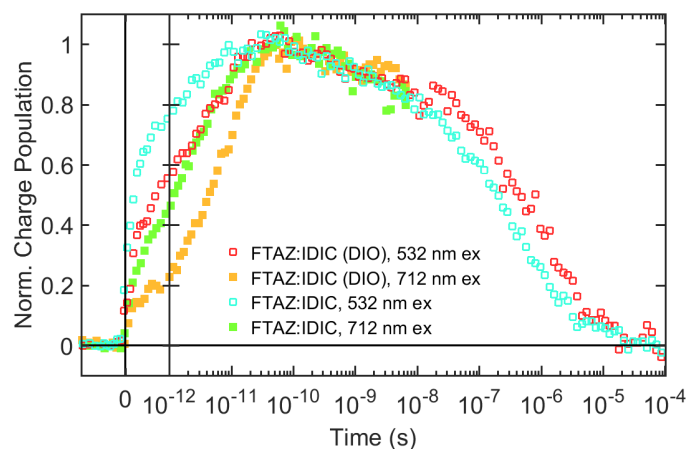


Figure 5.16: Charge dynamics extracted from a decomposition of the TA surfaces for the range of blends and excitation wavelengths indicated, with charge populations normalised assuming unit efficiency of exciton-to-charge conversion in the low fluence limit.

excitation (red, teal –unfilled); the changes are similar to those observed in the IDIC phase. Therefore generation timescales are similar and adding DIO reduces the prompt fraction (intensity ~ 200 fs) consistent with the decreased domain purity. The decay profiles show an increase in lifetimes with DIO with the half-life increasing by a factor of 2, giving extended time for percolation and therefore allowing an increase in optimal device thickness, as observed; 85 nm without DIO to 110 nm with DIO.

The results of the windowed bimolecular fit are presented in Figure 5.17. The increased noise in the 1–30 ps region is due to the lower number of initial excitation data being collected when using a femtosecond excitation source. The extracted bimolecular recombination constant (β) without DIO due to the noise it is hard to comment, but it looks to have a similar trend as with DIO. Therefore we can conclude that there is still mobility relaxation due to dispersion, but it is hard to comment on if the mobility has increased with DIO or the only effect is better percolation pathways.

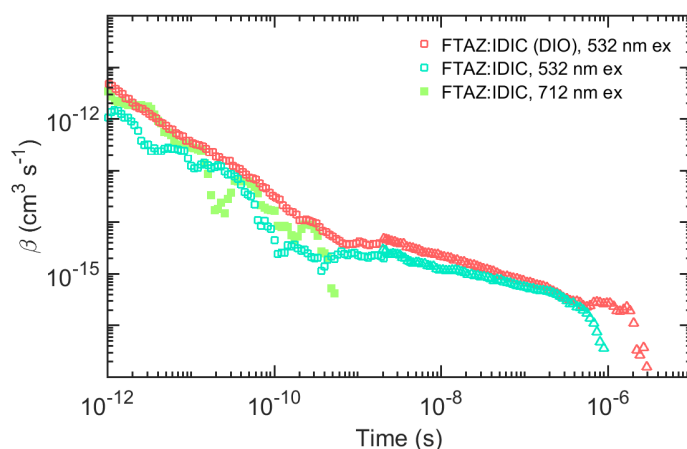


Figure 5.17: Bimolecular recombination constant, β , extracted from a moving window global fit. All films deposited on a quartz substrate in 1:1.5 w/w ratio. The film was cast with 0.25 % DIO.

The removal of DIO has little effect on the photophysics observed via TA; there is a slight decrease in geminate charge lifetime while the bimolecular recombination is unaffected. There is a change in prompt charge generation, but this does not have a strong correlation to with the decay, extraction, or mobility dynamics of charges. It is safe to conclude that the DIO treatment allows for a purer domain, perhaps helping charge separation, and allowing for a thicker device to be produced.

5.3.6 Effect of ZnO

The substitution of IDIC for PCBM, and the addition of DIO has shown little difference in photophysics. Here we assess the impact of patterning the ZnO surface. This is done by studying two materials; the first is a control material whereby the active layers is deposited onto flat ZnO. ZnO is a charge extraction layer and does have an effect on the observed spectra shapes. Following this, the patterned ZnO can be studied to see if the changes are from the addition or the patterning of the ZnO layer. As with the previous modification, it is found that the photophysics are not sensitive to ZnO and does not change when the ZnO

is patterned. A shift in the IDIC exciton spectra is revealed, and the timescale of electron extraction from IDIC is resolved.

The large changes in IDIC exciton spectra when adding a ZnO layer are shown in 5.18 (a). There is a significant shift in the PIA peak from 890 nm (1.39 eV) to 960 nm (1.29 eV) meaning that there is an overlap with the charge PIA at 930 nm (1.33 eV). Assigning this spectral feature to the IDIC exciton is in part due to the lack of features observed in the 500-600 nm (2.5-2.1 eV) where the hole would be expected to bleach the FTAZ. In contrast to IDIC, the FTAZ exciton is unchanged by the addition of ZnO layer. There is a noticeable difference in the charge spectra (c), with the FTAZ GSB vibration ratio becoming more prominent due to narrowing of each peak along with an increase in the 0-0 vibronic peak. The charge PIA peak is no longer a distinct peak, this could be due to a new PIA in the 620-830 nm (2.0-1.5 eV) region. However, a change in IDIC contribution could also be the cause, as the IDIC exciton spectra have also been affected. Notwithstanding these changes, the assignment to a charge is still valid due to GSB of both the IDIC and FTAZ species being present. This indicates that an electron and hole are present in the IDIC and FTAZ phase respectively. When adding the advanced light capturing pattern to the ZnO substrate, i.e. green in Figure 5.18, there are no significant changes to the resolved spectra showing that the spectral assignment from the ZnO substrate are valid with and without patterning.

Figure 5.19 presents the charge generation and decay dynamics of FTAZ:IDIC on quartz (red), ZnO (purple) and patterned ZnO (green) substrates, following excitation of FTAZ (a, 532 nm excitation) and IDIC (b, 712 nm excitation) phases. There is little to compare because there are no noticeable differences present, even analysis of the bimolecular recombination rate shows no change in magnitude or trend. The lack of variation strongly supports the pattern adding only to the light capture without affecting the photophysics.

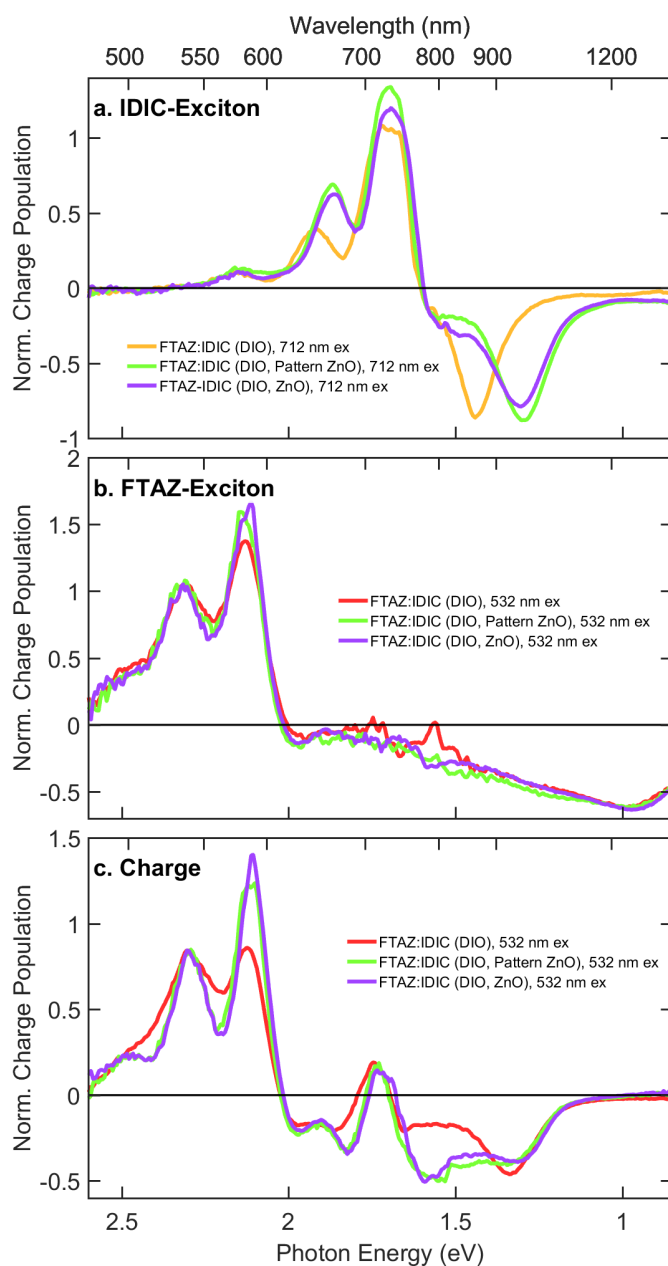


Figure 5.18: Indicative species spectra decomposition from the TA surfaces for the range of blends, normalised assuming unit efficiency of exciton-to-charge conversion in the low fluence limit. (a) IDIC exciton spectra following 712 nm excitation. (b) FTAZ exciton spectra after 532 nm excitation. (c) Charge spectra after exciton decay following 532 nm excitation.

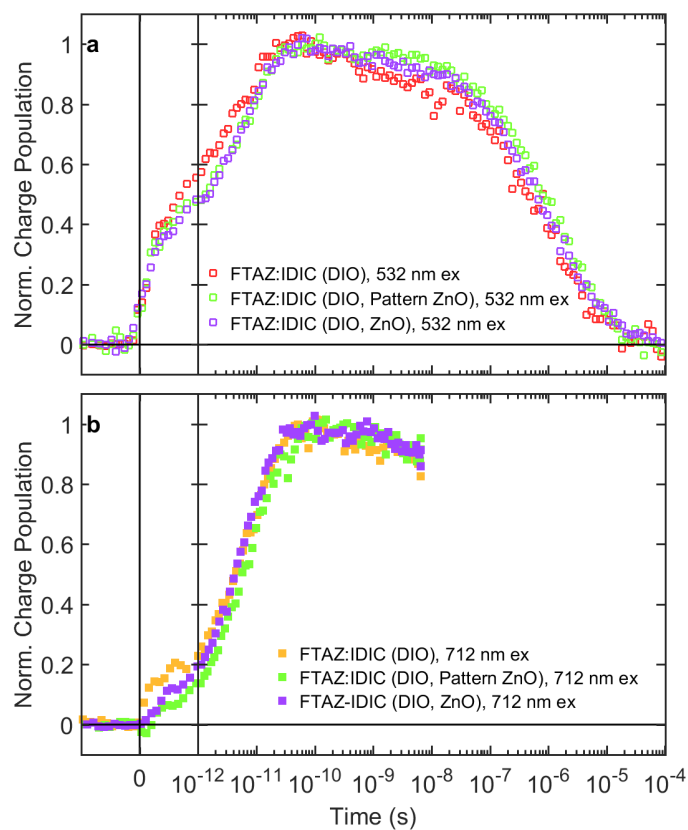


Figure 5.19: Charge dynamics extracted from a decomposition of the TA surfaces for the range of blends, with charge populations normalised assuming unit efficiency of exciton-to-charge conversion in the low fluence limit. (a) shows population following 532 nm excitation and (b) following 712 nm excitation. The film represented in (a) and (b) are the same.

Depositing the IDIC:FTAZ blend on ZnO substrate (flat or patterned) does not affect these charge generation dynamics, suggesting that the local environment experienced by exciton is not strongly affected by the morphological differences as a result of patterning resolved via R-SoXS. This supports the conclusion that enhanced light absorption is the main benefit of substrate patterning, rather than enhancing internal quantum efficiency.

5.3.7 Triplets

Recently, it has been proposed by Manke et al. (2016) that low band-gap polymers might have a fundamental limit imposed on them by the lower lying triplet state.¹⁴¹ This comes about due to rapid bimolecular recombination to triplet states that lie below the charge-transfer states.^{139–141} Distinguishing between charge pairs and triplets is simplified for FTAZ:IDIC, because IDIC has a spectrum of comparable intensity unlike the much weaker spectra in fullerene. Hence, triplets are identifiable because both IDIC and FTAZ GSB contribute to the spectrum when a charge pair is present, while only one component would contribute to a spectrum of triplet excitons.

The effects that triplet energy levels plays is illustrated in Figure 5.20. When trying to lower the band-gap of either the donor (a) or acceptor (b) a definitive shift in the corresponding triplet level is observed, this triplet might not have always been present, but it is known to be an issue in low band-gap polymer donors.^{139–141} If the triplet energy is lowered below the charge transfer state then a new loss pathway is opened up via the triplet state. If the acceptor is lowered in energy relative to the shrinking charge transfer prevents this pathway from occurring. The thermalisation loss in the electron donor can be used to maintain any triplet energy (in the hole transport material) above the CT energy.

Figure 5.21 shows spectra for FTAZ:IDIC blends during the charge recombination time frame. An excited state in FTAZ is identified bleach above 620 nm (2.00 eV) while IDIC species contribute bleaching around 1.7 eV, which while it is negative in some regions due to the FTAZ hole PIA, it is clearly distinguished as it is much

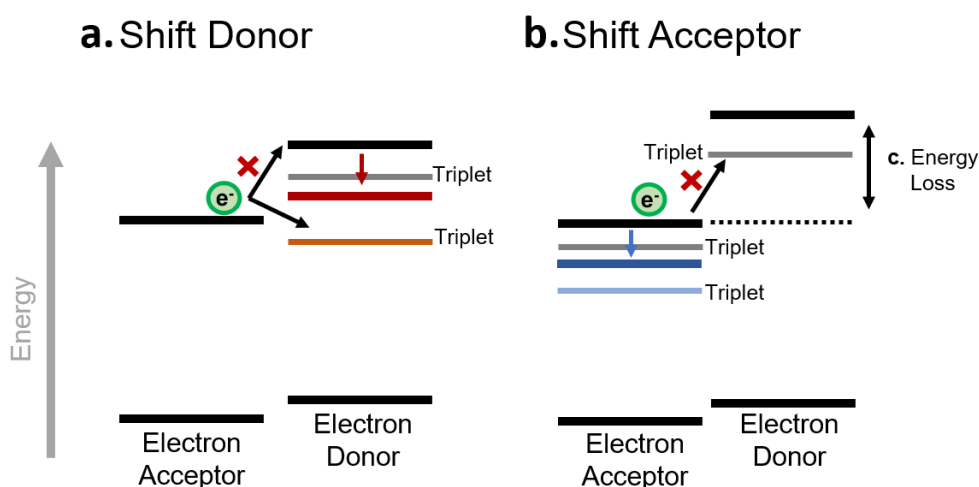


Figure 5.20: Illustration of the effect of role triplet energy levels plays when trying to lower the band-gap of either the donor (a) or acceptor (b). If the triplet energy is lowered below the charge transfer state, then a new loss pathway is opened up via the triplet state. If the acceptor is lower this also electron energy relative to the shrinking charge transfer preventing this pathway.

sharper than the holes. Spectral evolution occurs in the subgap region of FTAZ as discussed in Section 5.3.3. It is likely due to electron migration in IDIC phase or changes in electro-absorption signals associated with interfacial electric fields. Therefore due to the unchanging magnitude of FTAZ and IDIC bleaching signals triplets are ruled out as a decay pathway.

The role triplet energy levels in BHJ OPVs is illustrated in Figure 5.20. An illustrative shift in the corresponding triplet level is shown, a triplet level below LUMO may not always be present but it is an issue in low band-gap polymer donors.^{139–141} When trying to lower the band-gap of either the donor (a) or acceptor (b) the effect on triplet energy relative to the electron acceptor must be considered. If the triplet energy is lowered below the charge transfer state, then a new loss pathway is opened up via the triplet state. If the electron acceptor is lowered (b) then both LUMO and triplet energy shift together such that the triplet is always higher energy than the CT state preventing loss via triplet state. Figure

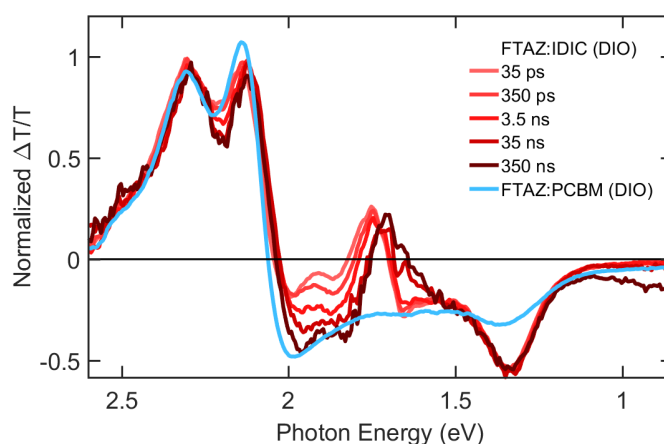


Figure 5.21: Normalised series of TA spectra for the FTAZ:IDIC blend (1:1.5, w/w, 0.25 % DIO) following 532 nm with either 100 fs ($2.1 \mu\text{J cm}^{-2}$) or ~ 700 ps ($0.6 \mu\text{J cm}^{-2}$) pulses, for delays less than or greater than 5 ns, respectively.

5.20 shows how the thermalisation loss incorporated into a medium band-gap electron donor can be used to maintain the triplet energy above the CT energy.

5.4 Conclusion

In Section 5.2 it is shown that the fused-ring electron acceptor, IDIC, blend with the medium-bandgap polymers show better device performance than the narrow-bandgap PTB7-Th device, revealing balanced absorption of donor and acceptors is needed for high efficiency. Further to this DIO is used to improve the morphology and push efficiency up to 11.0 %. TA confirms that excitation of both PTFBDT-BZS and IDIC leads to efficient charge generation, with the dynamics being quantitatively similar to other efficient polymer:fullerene blends, except for the low prompt charge generation. Building on the importance of a complementary donor and acceptor absorption shown Section 5.2 we fabricate an OPV with 12.5 % PCE the highest reported to date for a BHJ organic solar cell. Using a medium-bandgap polymer donor FTAZ and a narrow-bandgap acceptor IDIC;

the performance is significantly higher than the same polymer with the acceptor, IDIC, replaced by PC₆₁BM ()

The FTAZ:IDIC blend shows domain purity and phase separation benefit both charge separation and transport. Excitation of either the donor or acceptor components results in surprisingly slow charge generation dynamics. Domains remain small enough for excitons to reach the interface for efficient charge generation. Fluence dependent measurements reveal photo-generated charges to be highly mobile, without being so mobile that solar illumination would lead to rapid bimolecular recombination. Adding an advanced light harvesting pattern to the ZnO substrate does not result in a change of photophysics but instead drives higher PCE by increasing the absorption cross section. Unlike fullerene blends that require low-bandgap polymers to absorb across the visible spectrum, using IDIC as a low band-gap component the polymer triplet state is prevented from acting as a loss mechanism, intelligently using the excess photon-energy. We report on non-fullerene acceptors that can have suitable morphologies and energy levels to unlock the next series of efficiency gains in BHJ OPVs. The substantial contribution of the acceptor to photocurrent relieves undesirable constraints on donor energy levels and should permit further tuning of energy levels to boost cell voltage and efficiency.

5.5 Experimental

All active layers studied were prepared and provided by Professor Professor Xiaowei Zhan's team. They were encapsulated throughout the measurement. During shipping, they were stored in the dark in a parafilm sealed plastic, and upon receipt and when not under study, they were stored in a nitrogen atmosphere in the dark. The transient absorption set-up is the final optimised layout as noted in Chapter 2. The transient absorption measurements were carried out under a dynamic vacuum. No sample degradation was detected during TA measurements,

as the signal intensity and dynamics did not change between measurement repetitions.

Chapter 6

Conclusion & The Future

In this work, we characterise the photophysics in a multitude of different BHJ-OPV systems looking for correlations and understanding how changes to the material system affect the photophysics and how they relate to performance (PCE), morphology, and electrical parameters (J_{sc} , V_{oc}). We have identified the bottlenecks related to photophysics and if they are particular to the materials under study or form a more general trend. Moreover, we have characterised the bottlenecks and driving forces responsible for charge generation in OPVs. We have identified that the typical behaviour seen in fullerenes is needed for high PCE devices, and in some cases, the underlying photophysics are not related to the overall PCE.

The focus of this work is the characterisation of photophysics in a multitude of different BHJ-OPV systems looking for correlations and understanding how changes to the material system affect the photophysics and if any general conclusions can be drawn across the various systems studied. To this end, investigating the interplay between morphology and photophysics, revealing if this relationship is important for the device performance, i.e. what are the underlying photophysics and are specific conditions needed for charge generation influenced

by morphology. The characterisation of photophysics is the focus of this thesis, with the various changes discussed in reference to the electrical and morphology characterisation completed by collaborators.

Various techniques are employed to optimise and create more efficient OPV devices. By characterising the underlying photophysics for each of these techniques, we can improve our understanding of the pathways involved and how these may drive, or decrease, efficiency in the materials used. As we try to optimise the efficiency of OPV devices, we can see there is a clear trade-off between each of the steps required to develop a functional OPV device. By considering these steps individually and characterising their photophysics, we can identify driving forces and mitigate issues impacting the performance of each of the materials. Understanding the relationship between structure, morphology, photophysics and performance produces a greater understanding of how charge carriers are generated within these devices and identifies areas to improve to produce more efficient BHJ-OPV devices.

In this work, we have identified the requirements and implemented a transient absorption experiment designed to investigate BHJ-OPVs. The transient absorption experiment was implemented with high sensitivity, a broad spectral range 450-1550 nm (2.8-0.8 eV) and covers the lifetimes of species from initial excitation to charge carrier recombination (100 fs – 150 μ s). It was also necessary to extend the delay stage from 3 ns to 6 ns to overlap a nano-second laser to extend the time range to the microsecond range to monitor charge recombination. Once these improvements were implemented, it was possible to collect time-resolved spectroscopic data with a sensitivity of $10^{-4}\Delta$ OD in as little as 30 minutes. The rapid acquisition time allowed for various materials, excitation wavelengths, and excitation powers to be used to get a complete picture of the photophysics for the various systems studied. These capabilities were then used to study the three typical BHJ-OPV acceptors present in the literature: fullerenes, polymers, and small molecule acceptors.

We investigated two different methods of optimising fullerene devices in three different systems (Chapter 3). In the first, we investigate the performance of one system and vary the fullerene concentration (PC_{71}BM). We found that in varying the concentration of the fullerene (PC_{71}BM), the changes observed in photophysics are consistent with the changes in domain size and purity, indicating that it is crucial to understand both the morphology and photophysics of the material in order to optimise the efficiency of a BHJ-OPV. In the second, we observe how changing the functionality of the fullerene contributes to performance by comparing three different systems (PC_{61}BM , PC_{71}BM , and ICBA). The differences in each are subtle, but we observed that while ICBA and PC_{61}BM blends generate charges promptly, a combination of poor quenching in the ICBA blend and shorter lifetimes in the PC_{61}BM blend explain the higher power conversion efficiency of the PC_{71}BM system.

Two different methods of optimising polymer systems were investigated in Chapter 4. Two different donor polymers (PTB7-Th + PTB7) were blended with a polymer acceptor (P(NDI2OD-T2)). We observed longer-lived and more mobile charges in the polymer donor blend with the polymer acceptor, which can be considered a result of a doubling in PCE (from 2.1 % to 4.4 %). Next, we investigate how increasing fluorination in the polymer acceptor (PNDITPhT) impacts photophysics and power conversion efficiency (PCE). No change was observed in photophysics as fluorination was increased. However, the PCE increased by more than 30 % (from 3.1 % to 4.3 %). For this system, the photophysics of a polymer electron acceptor/donor system has little to no correlation to the overall PCE.

Finally, we investigate the impact on performance by changing the small polymer acceptor in the system (see Chapter 5). Upon comparison of several polymer acceptors, we have observed that the photophysics of an efficient IDIC SMA blend are similar to those observed when using a fullerene acceptor. Additionally, we have observed that when the SMA is energetically matched with a low-bandgap

polymer, the materials do not suffer from the triplet loss mechanism present in low-bandgap BHJ-OPVs.

The Future

The transient absorption experiment developed during this work has a few key characteristics; it covers the nanosecond gap with a broad spectral range. Covering the nanosecond range and resolving non-emissive species, i.e. triplets, makes it applicable for many areas that involve photophysics, particularly molecular singlet fission and triplet-triplet annihilation, which have many processes that occur in the nanoseconds to 100's of nanosecond timescale and involve (mostly) dark triplet states. Reduced measurement time and high sensitivity enable multi-variate studies, e.g., two-dimensional electronic spectroscopy, temperature dependence, or pressure dependence.

During this work, the need for additional measurements to generate data to constrain the inherent ambiguities observed in any 2-D dataset has raised the prospect of combining absorption with other techniques that can measure the lifetimes or spectral signatures of species present. Combining time-resolved broadband photoluminescence (as the sample gives off photons during a TA measurement) would aid in constraining the spectra and lifetimes of emissive species. Additionally, further work could be done to reveal the phase information of the probe, giving information of the refractive index changes allowing for further differentiation of overlapping species.

The role of morphology and how to control different aspects provides valuable tools that could be expanded to other fields; the energetic landscape used to control charge-generation, charge separation, and percolation to electrodes could be mimicked in other systems where trade-offs need to be made between separation and recombination (e.g. singlet fission).

The outlook for solar power technology is bright, but unfortunately for BHJ-OPV, the progress made in reducing the cost of silicon PV panels makes BHJ-

OPVs unlikely to allow it to break into traditional PV applications. There is still plenty of hope for BHJ-OPVs with the development of three (or more phases) to control morphology and a grasp a growing understanding of how morphology affects performance a further expansion and incorporation of other photonic processes (i.e. singlet fission and triplet-triplet annihilation) could lead to next-generation BHJ-OPVs pushing 40 % PCE. The tunable nature of organic molecules used in BHJ-OPVs makes them ideal candidates for transparent or tunable PVs. This class of PV is niche, and the design of these can incorporate benefits from both power production and reduced costs of heating (e.g. in office buildings) while being incorporated seamlessly into our everyday environment to replace many transparent surfaces.

Bibliography

- [1] BP, *Statistical Review of World Energy globally consistent data on world energy markets . and authoritative publications in the field of energy The Statistical Review world of World Energy and data on world energy markets from is The Review has been providing*; 2020; p 66.
- [2] EIA, Annual Energy Outlook. 2020; <https://www.eia.gov/outlooks/aeo/>.
- [3] Tiwari, S.; Tiwari, T.; Carter, S. A.; Scott, J. C.; Yakhmi, J. V. *Handbook of Ecomaterials*; Springer International Publishing: Cham, 2018; pp 1–48.
- [4] Yu, J.; Zheng, Y.; Huang, J. *Polymers* **2014**, 6, 2473–2509.
- [5] NOAA, Carbon Dioxide. 2021; <https://climate.nasa.gov/vital-signs/carbon-dioxide/>.
- [6] Etheridge, D. M.; Steele, L. P.; Langenfelds, R. L.; Francey, R. J.; Barnola, J.-M.; Morgan, V. I. *Journal of Geophysical Research: Atmospheres* **1996**, 101, 4115–4128.
- [7] Ades, M. et al. *Bulletin of the American Meteorological Society* **2020**, 101, S9–S128.
- [8] Inganäs, O. *Advanced Materials* **2018**, 30, 1–26.
- [9] Angstrom, A. *Quarterly Journal of the Royal Meteorological Society* **1924**, 50, 121–126.

- [10] Ulgen, K.; Hepbasli, A. *Energy Sources* **2004**, *26*, 507–520.
- [11] Pazikadin, A. R.; Rifai, D.; Ali, K.; Malik, M. Z.; Abdalla, A. N.; Faraj, M. A. *Science of the Total Environment* **2020**, *715*, 136848.
- [12] Fritts, C. E. *American Journal of Science* **1883**, *s3-26*, 465–472.
- [13] Chapin, D. M.; Fuller, C. S.; Pearson, G. L. *Journal of Applied Physics* **1954**, *25*, 676–677.
- [14] Green, M. A. *Physica E: Low-dimensional Systems and Nanostructures* **2002**, *14*, 11–17.
- [15] Markvart, T.; Castañer, L. *Solar Cells*; Elsevier, 2013; pp 3–25.
- [16] NREL, Best Research Cell Efficiencies. 2020; <https://www.nrel.gov/pv/cell-efficiency.html>http://www.nrel.gov/ncpv/images/efficiency_chart.jpg.
- [17] Green, M.; Dunlop, E.; Hohl-Ebinger, J.; Yoshita, M.; Kopidakis, N.; Hao, X. *Progress in Photovoltaics: Research and Applications* **2021**, *29*, 3–15.
- [18] Tayebjee, M. J. Y.; Gray-Weale, A. A.; Schmidt, T. W. *Journal of Physical Chemistry Letters* **2012**, *3*, 2749–2754.
- [19] Kurtz, S.; Myers, D.; McMahon, W. E.; Geisz, J.; Steiner, M. *Progress in Photovoltaics: Research and Applications* **2008**, *16*, 537–546.
- [20] Meillaud, F.; Shah, A.; Droz, C.; Vallat-Sauvain, E.; Miazza, C. *Solar Energy Materials and Solar Cells* **2006**, *90*, 2952–2959.
- [21] Hirst, L. C.; Ekins-Daukes, N. J. *Progress in Photovoltaics: Research and Applications* **2011**, *19*, 286–293.
- [22] NREL, Best Research-Cell Efficiency Chart. <https://www.nrel.gov/pv/cell-efficiency.html>.

- [23] Haegel, N. M. et al. *Science* **2017**, 356, 141–143.
- [24] Woodhouse, M.; Smith, B.; Ramdas, A.; Robert Margolis, *National Renewable Energy Laboratory* **2019**, 1–46.
- [25] Tiwari, S.; Tiwari, S. *Solar Energy Materials and Solar Cells* **2006**, 90, 1621–1628.
- [26] Carlé, J. E.; Helgesen, M.; Hagemann, O.; Hösel, M.; Heckler, I. M.; Bundgaard, E.; Gevorgyan, S. A.; Søndergaard, R. R.; Jørgensen, M.; García-Valverde, R.; Chaouki-Almagro, S.; Villarejo, J. A.; Krebs, F. C. *Joule* **2017**, 1, 274–289.
- [27] Ostroverkhova, O. *Chemical Reviews* **2016**, 116, 13279–13412.
- [28] Kang, H.; Kim, G.; Kim, J.; Kwon, S.; Kim, H.; Lee, K. *Advanced Materials* **2016**, 28, 7821–7861.
- [29] Heeger, A. J. *Advanced Materials* **2014**, 26, 10–28.
- [30] Mazzio, K. A.; Luscombe, C. K. *Chemical Society Reviews* **2015**, 44, 78–90.
- [31] Gaspar, H.; Figueira, F.; Pereira, L.; Mendes, A.; Viana, J.; Bernardo, G. *Materials* **2018**, 11, 2560.
- [32] Bhandari, K. P.; Collier, J. M.; Ellingson, R. J.; Apul, D. S. *Renewable and Sustainable Energy Reviews* **2015**, 47, 133–141.
- [33] Espinosa, N.; Hösel, M.; Angmo, D.; Krebs, F. C. *Energy and Environmental Science* **2012**, 5, 5117–5132.
- [34] Anctil, A.; Lee, E.; Lunt, R. R. *Applied Energy* **2020**, 261, 114429.
- [35] Luo, W.; Khoo, Y. S.; Kumar, A.; Low, J. S. C.; Li, Y.; Tan, Y. S.; Wang, Y.; Aberle, A. G.; Ramakrishna, S. *Solar Energy Materials and Solar Cells* **2018**, 174, 157–162.

- [36] Tran, T. T.; Smith, A. D. *Renewable and Sustainable Energy Reviews* **2017**, *80*, 1372–1388.
- [37] Krebs, F. C.; Gevorgyan, S. A.; Alstrup, J. *Journal of Materials Chemistry* **2009**, *19*, 5442–5451.
- [38] Kaur, N.; Singh, M.; Pathak, D.; Wagner, T.; Nunzi, J. M. *Synthetic Metals* **2014**, *190*, 20–26.
- [39] Andersen, T. R.; Cooling, N. A.; Almyahi, F.; Hart, A. S.; Nicolaidis, N. C.; Feron, K.; Noori, M.; Vaughan, B.; Griffith, M. J.; Belcher, W. J.; Das-toor, P. C. *Solar Energy Materials and Solar Cells* **2016**, *149*, 103–109.
- [40] Huang, Y. C.; Cha, H. C.; Chen, C. Y.; Tsao, C. S. *Progress in Photovoltaics: Research and Applications* **2017**, *25*, 928–935.
- [41] Dou, L.; You, J.; Hong, Z.; Xu, Z.; Li, G.; Street, R. A.; Yang, Y. *Advanced Materials* **2013**, *25*, 6642–6671.
- [42] Darling, S. B.; You, F. *RSC Advances* **2013**, *3*, 17633–17648.
- [43] Brütting, W. *Physics of Organic Semiconductors* **2006**, 1–14.
- [44] Chiang, C. K.; Fincher, C. R.; Park, Y. W.; Heeger, A. J.; Shirakawa, H.; Louis, E. J.; Gau, S. C.; MacDiarmid, A. G. *Physical Review Letters* **1977**, *39*, 1098–1101.
- [45] Tang, C. W. *Applied Physics Letters* **1986**, *48*, 183–185.
- [46] Koezuka, H.; Tsumura, A.; Ando, T. *Synthetic Metals* **1987**, *18*, 699–704.
- [47] Burroughes, J. H.; Jones, C. A.; Friend, R. H. *Nature* **1988**, *335*, 137–141.
- [48] Horowitz, G.; Fichou, D.; Peng, X.; Xu, Z.; Garnier, F. *Solid State Communications* **1989**, *72*, 381–384.
- [49] Tang, C. W.; VanSlyke, S. A. *Applied Physics Letters* **1987**, *51*, 913–915.

- [50] Burroughes, J. H.; Bradley, D. D. C.; Brown, A. R.; Marks, R. N.; Mackay, K.; Friend, R. H.; Burns, P. L.; Holmes, A. B. *Nature* **1990**, 347, 539–541.
- [51] Braun, D.; Heeger, A. J. *Applied Physics Letters* **1991**, 58, 1982–1984.
- [52] Bredas, J. L.; Street, G. B. *Accounts of Chemical Research* **1985**, 18, 309–315.
- [53] Parida, B.; Iniyar, S.; Goic, R. *Renewable and Sustainable Energy Reviews* **2011**, 15, 1625–1636.
- [54] Kim, T.; Kim, J. H.; Kang, T. E.; Lee, C.; Kang, H.; Shin, M.; Wang, C.; Ma, B.; Jeong, U.; Kim, T. S.; Kim, B. J. *Nature Communications* **2015**, 6, 1–7.
- [55] Baran, D.; McCulloch, I.; Wadsworth, A.; Marks, A.; Gasparini, N.; Moser, M.; Little, M. S.; Brabec, C. J. *Chemical Society Reviews* **2018**, 1596–1625.
- [56] de Gier, H. D.; Rietberg, B. J.; Broer, R.; Havenith, R. W. A. *Computational and Theoretical Chemistry* **2014**, 1040–1041, 202–211.
- [57] Polman, A.; Knight, M.; Garnett, E. C.; Ehrler, B.; Sinke, W. C. *Science* **2016**, 352.
- [58] Vogelbaum, H. S.; Sauvé, G. *Synthetic Metals* **2017**, 223, 107–121.
- [59] Li, G.; Chang, W. H.; Yang, Y. *Nature Reviews Materials* **2017**, 2, 1–13.
- [60] Malliaras, G.; Friend, R. *Physics Today* **2005**, 58, 53–58.
- [61] Pelzer, K. M.; Darling, S. B. *Mol. Syst. Des. Eng.* **2016**, 1, 10–24.
- [62] Zhang, Y.; Samuel, I. D.; Wang, T.; Lidzey, D. G. *Advanced Science* **2018**, 5.
- [63] Park, S.; Kim, T.; Yoon, S.; Koh, C. W.; Woo, H. Y.; Son, H. J. *Advanced Materials* **2020**, 32, 1–29.
- [64] Mateker, W. R.; McGehee, M. D. *Advanced Materials* **2017**, 29.

- [65] Hoke, E. T.; Sachs-Quintana, I. T.; Lloyd, M. T.; Kauvar, I.; Mateker, W. R.; Nardes, A. M.; Peters, C. H.; Kopidakis, N.; McGehee, M. D. *Advanced Energy Materials* **2012**, 2, 1351–1357.
- [66] Speller, E. M. et al. *ACS Energy Letters* **2019**, 4, 846–852.
- [67] Roesch, R.; Faber, T.; Von Hauff, E.; Brown, T. M.; Lira-Cantu, M.; Hoppe, H. *Advanced Energy Materials* **2015**, 5, 1–24.
- [68] Haynes, W. H., Ed. *CRC Handbook of Chemistry and Physics*, 97th ed.; CRC Press, 2016; Vol. 268.
- [69] Zhokhavets, U.; Goldhahn, R.; Gobsch, G.; Al-Ibrahim, M.; Roth, H. K.; Sensfuss, S.; Klemm, E.; Egbe, D. A. *Thin Solid Films* **2003**, 444, 215–220.
- [70] Flatz, K.; Grobosch, M.; Knupfer, M. *Applied Physics A: Materials Science and Processing* **2008**, 90, 243–246.
- [71] Pevzner, B.; Hebard, A. *Physical Review B - Condensed Matter and Materials Physics* **1997**, 55, 16439–16449.
- [72] Fu, Z.; Zhang, X.; Zhang, H.; Li, Y.; Zhou, H.; Zhang, Y. *Chinese Journal of Chemistry* **2021**, 39, 381–390.
- [73] Clarke, T. M.; Durrant, J. R. *Chemical Reviews* **2010**, 110, 6736–6767.
- [74] Pivrikas, A.; Sariciftci, N. S.; Juška, G.; Österbacka, R. *Progress in Photo-voltaics: Research and Applications* **2007**, 15, 677–696.
- [75] Brédas, J.-L.; Norton, J. E.; Cornil, J.; Coropceanu, V. *Accounts of Chemical Research* **2009**, 42, 1691–1699.
- [76] Yu, G.; Heeger, A. J. *Journal of Applied Physics* **1995**, 78, 4510–4515.
- [77] Shaw, P. E.; Ruseckas, A.; Samuel, I. D. W. *Advanced Materials* **2008**, 20, 3516–3520.

- [78] Cook, S.; Liyuan, H.; Furube, A.; Katoh, R. *Journal of Physical Chemistry C* **2010**, *114*, 10962–10968.
- [79] Lewis, A.; Ruseckas, A.; Gaudin, O.; Webster, G.; Burn, P.; Samuel, I. *Organic Electronics* **2006**, *7*, 452–456.
- [80] Kozub, D. R.; Vakhshouri, K.; Kesava, S. V.; Wang, C.; Hexemer, A.; Gomez, E. D. *Chemical Communications* **2012**, *48*, 5859–5861.
- [81] Guo, X.; Zhou, N.; Lou, S. J.; Smith, J.; Tice, D. B.; Hennek, J. W.; Ortiz, R. P.; Navarrete, J. T.; Li, S.; Strzalka, J.; Chen, L. X.; Chang, R. P.; Facchetti, A.; Marks, T. J. *Nature Photonics* **2013**, *7*, 825–833.
- [82] Luhman, W. A.; Holmes, R. J. *Advanced Functional Materials* **2011**, *21*, 764–771.
- [83] Halls, J. J.; Walsh, C. A.; Greenham, N. C.; Marseglia, E. A.; Friend, R. H.; Moratti, S. C.; Holmes, A. B. *Nature* **1995**, *376*, 498–500.
- [84] Yu, G.; Gao, J.; Hummelen, J. C.; Wudl, F.; Heeger, A. J. *Science* **1995**, *270*, 1789–1791.
- [85] Jain, N.; Chandrasekaran, N.; Sadhanala, A.; Friend, R. H.; McNeill, C. R.; Kabra, D. *Journal of Materials Chemistry A* **2017**, *5*, 24749–24757.
- [86] Scharber, M. C.; Mühlbacher, D.; Koppe, M.; Denk, P.; Waldauf, C.; Heeger, A. J.; Brabec, C. J. *Advanced Materials* **2006**, *18*, 789–794.
- [87] Gurney, R. S.; Lidzey, D. G.; Wang, T. *Reports on Progress in Physics* **2019**, *82*, 036601.
- [88] Padinger, F.; Rittberger, R.; Sariciftci, N. *Advanced Functional Materials* **2003**, *13*, 85–88.
- [89] Reyes-Reyes, M.; Kim, K.; Carroll, D. L. *Applied Physics Letters* **2005**, *87*, 083506.

- [90] Salleo, A.; Kline, R. J.; DeLongchamp, D. M.; Chabinyc, M. L. *Advanced Materials* **2010**, *22*, 3812–3838.
- [91] Cowan, S. R.; Banerji, N.; Leong, W. L.; Heeger, A. J. *Advanced Functional Materials* **2012**, *22*, 1116–1128.
- [92] Gallaher, J. K. J.; Prasad, S. S. K. K.; Uddin, M. A. M.; Kim, T.; Kim, J. Y. J.; Woo, H. Y. H.; Hodgkiss, J. M. J. *Energy and Environmental Science* **2015**, *8*, 2713–2724.
- [93] Ohkita, H.; Cook, S.; Astuti, Y.; Duffy, W.; Tierney, S.; Zhang, W.; Heeney, M.; McCulloch, I.; Nelson, J.; Bradley, D. D.; Durrant, J. R. *Journal of the American Chemical Society* **2008**, *130*, 3030–3042.
- [94] Collins, B. A.; Tumbleston, J. R.; Ade, H. *Journal of Physical Chemistry Letters* **2011**, *2*, 3135–3145.
- [95] Ruderer, M. A.; Meier, R.; Porcar, L.; Cubitt, R.; Müller-Buschbaum, P. *Journal of Physical Chemistry Letters* **2012**, *3*, 683–688.
- [96] Scarongella, M.; Paraecattil, A. A.; Buchaca-Domingo, E.; Douglas, J. D.; Beaupré, S.; McCarthy-Ward, T.; Heeney, M.; Moser, J.-E. E.; Leclerc, M.; Fréchet, J. M. J.; Stingelin, N.; Banerji, N. *Journal of Materials Chemistry A* **2014**, *2*, 6218–6230.
- [97] Tang, H.; Lu, G.; Li, L.; Li, J.; Wang, Y.; Yang, X. *Journal of Materials Chemistry* **2010**, *20*, 683–688.
- [98] Li, Z.; Xu, X.; Zhang, W.; Meng, X.; Ma, W.; Yartsev, A.; Inganäs, O.; Andersson, M. R.; Janssen, R. A.; Wang, E. *Journal of the American Chemical Society* **2016**, *138*, 10935–10944.
- [99] Lu, L.; Zheng, T.; Wu, Q.; Schneider, A. M.; Zhao, D.; Yu, L. *Chemical Reviews* **2015**, *115*, 12666–12731.
- [100] Yin, W.; Dadmun, M. *ACS Nano* **2011**, *5*, 4756–4768.

- [101] Ade, H.; Wang, M.; Tumbleston, J. R.; Huang, F.; Gann, E.; Ma, W. *Advanced Energy Materials* **2013**, 3, 864–872.
- [102] Koster, L. J.; Mihailetschi, V. D.; Blom, P. W. *Applied Physics Letters* **2006**, 88, 86–89.
- [103] Rühle, S. *Solar Energy* **2016**, 130, 139–147.
- [104] Zhang, Z. G.; Yang, Y.; Yao, J.; Xue, L.; Chen, S.; Li, X.; Morrison, W.; Yang, C.; Li, Y. *Angewandte Chemie - International Edition* **2017**, 56, 13503–13507.
- [105] He, Y.; Shao, M.; Xiao, K.; Smith, S. C.; Hong, K. *Solar Energy Materials and Solar Cells* **2013**, 118, 171–178.
- [106] Eftaiha, A. F.; Sun, J. P.; Hill, I. G.; Welch, G. C. *Journal of Materials Chemistry A* **2014**, 2, 1201–1213.
- [107] Li, H.; Wang, J.; Wang, Y.; Bu, F.; Shen, W.; Liu, J.; Huang, L.; Wang, W.; Belfiore, L. A.; Tang, J. *Solar Energy Materials and Solar Cells* **2019**, 190, 83–97.
- [108] Cheng, P.; Li, G.; Zhan, X.; Yang, Y. *Nature Photonics* **2018**, 12, 131–142.
- [109] Zhang, G.; Zhao, J.; Chow, P. C.; Jiang, K.; Zhang, J. J. J.; Zhu, Z.; Zhang, J. J.; Huang, F.; Yan, H. *Chemical Reviews* **2018**, 118, 3447–3507.
- [110] Lin, Y.; Zhao, F.; Prasad, S. K. K.; Chen, J.; Cai, W.; Zhang, Q.; Chen, K.; Wu, Y.; Ma, W.; Gao, F.; Tang, J.; Wang, C.; You, W.; Hodgkiss, J. M.; Zhan, X. *Advanced Materials* **2018**, 30, 1706363.
- [111] Zhao, J.; Li, Y.; Yang, G.; Jiang, K.; Lin, H.; Ade, H.; Ma, W.; Yan, H. *Nature Energy* **2016**, 1, 15027.
- [112] Lin, Y.; Zhang, Z. G.; Bai, H.; Wang, J.; Yao, Y.; Li, Y.; Zhu, D.; Zhan, X. *Energy and Environmental Science* **2015**, 8, 610–616.

- [113] Lin, Y.; Wang, J.; Zhang, Z.-G.; Bai, H.; Li, Y.; Zhu, D.; Zhan, X. *Advanced Materials* **2015**, *27*, 1170–1174.
- [114] Sutti, S.; Williams, G.; Aziz, H. *Journal of Photonics for Energy* **2014**, *4*, 040999.
- [115] Qarony, W.; Hossain, M. I.; Jovanov, V.; Knipp, D.; Tsang, Y. H. *Applied Nanoscience (Switzerland)* **2018**, *8*, 339–346.
- [116] Elumalai, N. K.; Uddin, A. *Energy and Environmental Science* **2016**, *9*, 391–410.
- [117] Lu, N.; Li, L.; Sun, P.; Liu, M. *Chemical Physics Letters* **2014**, *614*, 27–30.
- [118] Banerjee, S.; Iyer, S. S. K. *Organic Electronics* **2010**, *11*, 2032–2036.
- [119] Vandewal, K.; Tvingstedt, K.; Gadisa, A.; Inganäs, O.; Manca, J. V. *Nature Materials* **2009**, *8*, 904–909.
- [120] Kim, M. S.; Kim, B. G.; Kim, J. *ACS Applied Materials and Interfaces* **2009**, *1*, 1264–1269.
- [121] Jao, M. H.; Liao, H. C.; Su, W. F. *Journal of Materials Chemistry A* **2016**, *4*, 5784–5801.
- [122] Brabec, C. J.; Cravino, A.; Meissner, D.; Serdar Sariciftci, N.; Fromherz, T.; Rispen, M. T.; Sanchez, L.; Hummelen, J. C. *Advanced Functional Materials* **2001**, *11*, 374–380.
- [123] Ramirez, I.; Causa', M.; Zhong, Y.; Banerji, N.; Riede, M. *Advanced Energy Materials* **2018**, *8*, 1703551.
- [124] Tan, J. K.; Png, R. Q.; Zhao, C.; Ho, P. K. *Nature Communications* **2018**, *9*, 1–8.
- [125] Liao, S. H.; Jhuo, H. J.; Cheng, Y. S.; Chen, S. A. *Advanced Materials* **2013**, *25*, 4766–4771.

- [126] Scharber, M. C.; Sariciftci, N. S. *Progress in Polymer Science* **2013**, *38*, 1929–1940.
- [127] Scharber, M. C. *Advanced Materials* **2016**, *28*, 1994–2001.
- [128] Huang, C.; Liao, X.; Gao, K.; Zuo, L.; Lin, F.; Shi, X.; Li, C. Z.; Liu, H.; Li, X.; Liu, F.; Chen, Y.; Chen, H.; Jen, A. K. *Chemistry of Materials* **2018**, *30*, 5429–5434.
- [129] Nielsen, C. B.; Holliday, S.; Chen, H.-Y.; Cryer, S. J.; McCulloch, I. *Accounts of Chemical Research* **2015**, *48*, 2803–2812.
- [130] McNeill, C. R. *Energy and Environmental Science* **2012**, *5*, 5653–5667.
- [131] Zhao, F.; Wang, C.; Zhan, X. *Advanced Energy Materials* **2018**, *8*, 1–34.
- [132] Lee, C.; Kang, H.; Lee, W.; Kim, T.; Kim, K. H.; Woo, H. Y.; Wang, C.; Kim, B. J. *Advanced Materials* **2015**, *27*, 2466–2471.
- [133] Holcombe, T. W.; Norton, J. E.; Rivnay, J.; Woo, C. H.; Goris, L.; Piliego, C.; Grifffini, G.; Sellinger, A.; Brédas, J. L.; Salleo, A.; Fréchet, J. M. *Journal of the American Chemical Society* **2011**, *133*, 12106–12114.
- [134] Ye, L.; Jiao, X.; Zhao, W.; Zhang, S.; Yao, H.; Li, S.; Ade, H.; Hou, J. *Chemistry of Materials* **2016**, *28*, 6178–6185.
- [135] Vohra, V.; Anzai, T. *Journal of Nanomaterials* **2017**, *2017*, 1–18.
- [136] Vandewal, K. et al. *Nature Materials* **2014**, *13*, 63–8.
- [137] Zhu, L.; Yi, Y.; Wei, Z. *Journal of Physical Chemistry C* **2018**, *122*, 22309–22316.
- [138] Verlaak, S.; Beljonne, D.; Cheyns, D.; Rolin, C.; Linares, M.; Castet, F.; Cornil, J.; Heremans, P. *Advanced Functional Materials* **2009**, *19*, 3809–3814.

- [139] Rao, A.; Chow, P. C. Y.; Gélinas, S.; Schlenker, C. W.; Li, C. Z.; Yip, H. L.; Jen, A. K. Y.; Ginger, D. S.; Friend, R. H. *Nature* **2013**, *500*, 435–439.
- [140] Etzold, F.; Howard, I. A.; Forler, N.; Melnyk, A.; Andrienko, D.; Hansen, M. R.; Laquai, F. *Energy and Environmental Science* **2015**, *8*, 1511–1522.
- [141] Menke, S. M.; Sadhanala, A.; Nikolka, M.; Ran, N. A.; Ravva, M. K.; Abdel-Azeim, S.; Stern, H. L.; Wang, M.; Sirringhaus, H.; Nguyen, T. Q.; Brédas, J. L.; Bazan, G. C.; Friend, R. H. *ACS Nano* **2016**, *10*, 10736–10744.
- [142] Song, J.; Zhang, M.; Yuan, M.; Qian, Y.; Sun, Y.; Liu, F. *Small Methods* **2018**, *2*, 1700229.
- [143] Hedley, G. J.; Ward, A. J.; Alekseev, A.; Howells, C. T.; Martins, E. R.; Serrano, L. A.; Cooke, G.; Ruseckas, A.; Samuel, I. D. *Nature Communications* **2013**, *4*, 1–10.
- [144] Treat, N. D.; Varotto, A.; Takacs, C. J.; Batara, N.; Al-Hashimi, M.; Heeney, M. J.; Heeger, A. J.; Wudl, F.; Hawker, C. J.; Chabinyc, M. L. *Journal of the American Chemical Society* **2012**, *134*, 15869–15879.
- [145] Collins, B. A.; Li, Z.; Tumbleston, J. R.; Gann, E.; McNeill, C. R.; Ade, H. *Advanced Energy Materials* **2013**, *3*, 65–74.
- [146] Bartelt, J. A.; Beiley, Z. M.; Hoke, E. T.; Mateker, W. R.; Douglas, J. D.; Collins, B. A.; Tumbleston, J. R.; Graham, K. R.; Amassian, A.; Ade, H.; Fréchet, J. M.; Toney, M. F.; McGehee, M. D. *Advanced Energy Materials* **2013**, *3*, 364–374.
- [147] Bloking, J. T.; Giovenzana, T.; Higgs, A. T.; Ponec, A. J.; Hoke, E. T.; Vandewal, K.; Ko, S.; Bao, Z.; Sellinger, A.; McGehee, M. D. *Advanced Energy Materials* **2014**, *4*, 1–12.
- [148] Kesava, S. V.; Fei, Z.; Rimshaw, A. D.; Wang, C.; Hexemer, A.; Asbury, J. B.; Heeney, M.; Gomez, E. D. *Advanced Energy Materials* **2014**, *4*, 1–10.

- [149] Paraecattil, A. A.; Banerji, N. *Journal of the American Chemical Society* **2014**, *136*, 1472–1482.
- [150] Barford, W. *Journal of Physical Chemistry A* **2013**, *117*, 2665–2671.
- [151] Hwang, I.; Scholes, G. D. *Chemistry of Materials* **2011**, *23*, 610–620.
- [152] Masters, B. *The European Physical Journal H* **2014**, *39*, 87–139.
- [153] Tamai, Y.; Ohkita, H.; Bente, H.; Ito, S. *Journal of Physical Chemistry Letters* **2015**, *6*, 3417–3428.
- [154] Mikhnenko, O. V.; Blom, P. W.; Nguyen, T. Q. *Energy and Environmental Science* **2015**, *8*, 1867–1888.
- [155] Menke, S. M.; Holmes, R. J. *Energy and Environmental Science* **2014**, *7*, 499–512.
- [156] Mikhnenko, O. V.; Cordella, F.; Sieval, A. B.; Hummelen, J. C.; Blom, P. W. M.; Loi, M. A. *The Journal of Physical Chemistry B* **2008**, *112*, 11601–11604.
- [157] Chen, K.; Barker, A. J.; Reish, M. E.; Gordon, K. C.; Hodgkiss, J. M. *Journal of the American Chemical Society* **2013**, *135*, 18502–18512.
- [158] Arkhipov, V. I.; Bäessler, H. *Physica Status Solidi (A) Applied Research* **2004**, *201*, 1152–1187.
- [159] Bittner, E. R.; Ramon, J. G. S.; Karabunarliev, S. *The Journal of Chemical Physics* **2005**, *122*, 214719.
- [160] Scheblykin, I. G.; Yartsev, A.; Pullerits, T.; Gulbinas, V.; Sundström, V. *The Journal of Physical Chemistry B* **2007**, *111*, 6303–6321.
- [161] Hood, S. N.; Kassal, I. *The Journal of Physical Chemistry Letters* **2016**, *7*, 4495–4500.

- [162] Ma, W.; Gopinathan, A.; Heeger, A. J. *Advanced Materials* **2007**, *19*, 3656–3659.
- [163] Groves, C. *Energy and Environmental Science* **2013**, *6*, 3202–3217.
- [164] Vakhshouri, K.; Kozub, D. R.; Wang, C.; Salleo, A.; Gomez, E. D. *Physical Review Letters* **2012**, *108*, 1–5.
- [165] Nalwa, K. S.; Kodali, H. K.; Ganapathysubramanian, B.; Chaudhary, S. *Applied Physics Letters* **2011**, *99*, 263301.
- [166] Barker, A. J.; Chen, K.; Hodgkiss, J. M. *Journal of the American Chemical Society* **2014**, *136*, 12018–12026.
- [167] Ochsmann, J. R.; Chandran, D.; Gehrig, D. W.; Anwar, H.; Madathil, P. K.; Lee, K.-s.; Laquai, F. *Macromolecular Rapid Communications* **2015**, *36*, 1122–1128.
- [168] Andersson, L. M.; Melianas, A.; Infahasaeng, Y.; Tang, Z.; Yartsev, A.; Inganäs, O.; Sundström, V. *Journal of Physical Chemistry Letters* **2013**, *4*, 2069–2072.
- [169] Guo, J.; Ohkita, H.; Bente, H.; Ito, S. *Journal of the American Chemical Society* **2009**, *131*, 16869–16880.
- [170] Clarke, T. M.; Jamieson, F. C.; Durrant, J. R. *Journal of Physical Chemistry C* **2009**, *113*, 20934–20941.
- [171] Lakhwani, G.; Rao, A.; Friend, R. H. *Annual Review of Physical Chemistry* **2014**, *65*, 557–581.
- [172] Turbiez, M.; Koster, L. J. A.; Neher, D.; Pérez, I. d. C.; Kniepert, J.; Bartesaghi, D.; Roland, S. *Nature Communications* **2015**, *6*, 2–11.
- [173] Langevin, P. *Annales de chimie et de physique* **1903**, 433.

- [174] Proctor, C. M.; Kuik, M.; Nguyen, T. Q. *Progress in Polymer Science* **2013**, *38*, 1941–1960.
- [175] Koster, L. J.; Mihailetschi, V. D.; Blom, P. W. *Applied Physics Letters* **2006**, *88*, 1–3.
- [176] Hamilton, R.; Shuttle, C. G.; O'Regan, B.; Hammant, T. C.; Nelson, J.; Durrant, J. R. *Journal of Physical Chemistry Letters* **2010**, *1*, 1432–1436.
- [177] Albrecht, S.; Schindler, W.; Kurpiers, J.; Kniepert, J.; Blakesley, J. C.; Dumsch, I.; Allard, S.; Fostiropoulos, K.; Scherf, U.; Neher, D. *The Journal of Physical Chemistry Letters* **2012**, *3*, 640–645.
- [178] Burke, T. M.; Sweetnam, S.; Vandewal, K.; McGehee, M. D. *Advanced Energy Materials* **2015**, *5*, 1500123.
- [179] Kim, Y. J.; Jang, W.; Wang, D. H.; Park, C. E. *Journal of Physical Chemistry C* **2015**, *119*, 26311–26318.
- [180] Bittner, E. R.; Lankevich, V.; Gélinas, S.; Rao, A.; Ginger, D. A.; Friend, R. H. *Physical Chemistry Chemical Physics* **2014**, *16*, 20321–20328.
- [181] Gehrig, D. W.; Howard, I. a.; Laquai, F. *Journal of Physical Chemistry C* **2015**, *119*, 13509–13515.
- [182] Clark, J.; Silva, C.; Friend, R. H.; Spano, F. C. *Physical Review Letters* **2007**, *98*, 1–4.
- [183] Nguyen, T. Q.; Schwartz, B. J. *Journal of Chemical Physics* **2002**, *116*, 8198–8208.
- [184] Manas, E. S.; Spano, F. C. *Journal of Chemical Physics* **1998**, *109*, 8087–8101.
- [185] Gao, Y.; Martin, T. P.; Niles, E. T.; Wise, A. J.; Thomas, A. K.; Grey, J. K. *Journal of Physical Chemistry C* **2010**, *114*, 15121–15128.

- [186] Cook, S.; Katoh, R.; Furube, A. *The Journal of Physical Chemistry C* **2009**, *113*, 2547–2552.
- [187] Bakulin, a. a.; Rao, A.; Pavelyev, V. G.; van Loosdrecht, P. H. M.; Pshenichnikov, M. S.; Niedzialek, D.; Cornil, J.; Beljonne, D.; Friend, R. H. *Science* **2012**, *335*, 1340–1344.
- [188] Grancini, G.; Maiuri, M.; Fazzi, D.; Petrozza, A.; Egelhaaf, H.-J. J.; Brida, D.; Cerullo, G.; Lanzani, G. *Nature Materials* **2013**, *12*, 29–33.
- [189] Etzold, F.; Howard, I. A.; Mauer, R.; Meister, M.; Kim, T.-D. D.; Lee, K.-S. S.; Baek, N. S.; Laquai, F. F. *Journal of the American Chemical Society* **2011**, *133*, 9469–9479.
- [190] Brabec, C. J.; Zerza, G.; Cerullo, G.; De Silvestri, S.; Luzzati, S.; Hummel, J. C.; Sariciftci, S. *Chemical Physics Letters* **2001**, *340*, 232–236.
- [191] Hwang, I.-W.; Soci, C.; Moses, D.; Zhu, Z.; Waller, D.; Gaudiana, R.; Brabec, C. J.; Heeger, A. J. *Advanced Materials* **2007**, *19*, 2307–2312.
- [192] Engel, E.; Leo, K.; Hoffmann, M. *Chemical Physics* **2006**, *325*, 170–177.
- [193] Cook, S.; Furube, A.; Katoh, R.; Han, L. *Chemical Physics Letters* **2009**, *478*, 33–36.
- [194] Gelinas, S.; Rao, A.; Kumar, A.; Smith, S. L.; Chin, a. W.; Clark, J.; van der Poll, T. S.; Bazan, G. C.; Friend, R. H. *Science* **2014**, *343*, 512–516.
- [195] Savoie, B. M.; Rao, A.; Bakulin, A. a.; Gelinas, S.; Movaghar, B.; Friend, R. H.; Marks, T. J.; Ratner, M. a. *Journal of the American Chemical Society* **2014**, *136*, 2876–2884.
- [196] Foggi, P.; Bussotti, L.; Neuwahl, F. V. R. *International Journal of Photoenergy* **2001**, *3*, 103–109.
- [197] Megerle, U.; Pugliesi, I.; Schrieffer, C.; Sailer, C. F.; Riedle, E. *Applied Physics B: Lasers and Optics* **2009**, *96*, 215–231.

- [198] Dietzek, B.; Pascher, T.; Sundström, V.; Yartsev, a. *Laser Physics Letters* **2007**, 4, 38–43.
- [199] Riedle, E.; Bradler, M.; Wenninger, M.; Sailer, C. F.; Pugliesi, I. *Faraday Discussions* **2013**, 163, 139.
- [200] Ruckebusch, C.; Sliwa, M.; Pernot, P.; de Juan, A.; Tauler, R. *Journal of Photochemistry and Photobiology C: Photochemistry Reviews* **2012**, 13, 1–27.
- [201] Berera, R.; van Grondelle, R.; Kennis, J. T. M. *Photosynthesis research* **2009**, 101, 105–18.
- [202] van Stokkum, I. H. M.; Larsen, D. S.; van Grondelle, R. *Biochimica et biophysica acta* **2004**, 1657, 82–104.
- [203] Jalali-Heravi, M.; Parastar, H.; Kamalzadeh, M.; Tauler, R.; Jaumot, J. *Chemometrics and Intelligent Laboratory Systems* **2010**, 104, 155–171.
- [204] Ruckebusch, C.; Sliwa, M.; Réhault, J.; Naumov, P.; Huvenne, J. P.; Buntinx, G. *Analytica chimica acta* **2009**, 642, 228–34.
- [205] Müller, J. G.; Lupton, J. M.; Feldmann, J.; Lemmer, U.; Scharber, M. C.; Sariciftci, N. S.; Brabec, C. J.; Scherf, U. *Physical Review B* **2005**, 72, 195208.
- [206] Howard, I. A.; Etzold, F.; Laquai, F.; Kemerink, M. *Advanced Energy Materials* **2014**, 4, 1–9.
- [207] Krylov, V.; Gallus, J.; Wild, U.; Kalintsev, A.; Rebane, A. *Applied Physics B: Lasers and Optics* **2000**, 70, 163–168.
- [208] Boyd, R. *Nonlinear optics*; Academic Press, 2002.
- [209] Petrov, V.; Ghotbi, M.; Kokabee, O.; Esteban-Martin, a.; Noack, F.; Gaydardzhiev, a.; Nikolov, I.; Tzankov, P.; Buchvarov, I.; Miyata, K.; Majchrowski, a.; Kityk, I.; Rotermund, F.; Michalski, E.; Ebrahim-Zadeh, M. *Laser & Photonics Reviews* **2010**, 4, 53–98.

- [210] Couairon, A.; Mysyrowicz, A. *Physics Reports* **2007**, *441*, 47–189.
- [211] Kandidov, V.; Kosareva, O.; Golubtsov, I.; Liu, W.; Becker, A.; Akozbek, N.; Bowden, C.; Chin, S. *Applied Physics B: Lasers and Optics* **2003**, *77*, 149–165.
- [212] Nagura, C.; Suda, A.; Kawano, H.; Obara, M.; Midorikawa, K. *Applied optics* **2002**, *41*, 3735–42.
- [213] Bradler, M.; Baum, P.; Riedle, E. *Applied Physics B* **2009**, *97*, 561–574.
- [214] Dudley, J. M.; Coen, S. *Reviews of Modern Physics* **2006**, *78*, 1135–1184.
- [215] Dubietis, A.; Tamošauskas, G.; Šuminas, R.; Jukna, V.; Couairon, A. *Lithuanian Journal of Physics* **2017**, *57*, 113–157.
- [216] Zheltikov, A. M. *Physics-Uspekhi* **2006**, *49*, 605.
- [217] Lorenc, M.; Ziolk, M.; Naskrecki, R.; Karolczak, J.; Kubicki, J.; Maciejewski, A. *Applied Physics B: Lasers and Optics* **2002**, *74*, 19–27.
- [218] Kovalenko, S.; Dobryakov, a.; Ruthmann, J.; Ernsting, N. *Physical Review A* **1999**, *59*, 2369–2384.
- [219] Ekvall, K.; der Meulen, P. V. *Journal of Applied Physics* **2000**,
- [220] Yan, L.; Si, J.; Chen, F.; Jia, S.; Zhang, Y.; Hou, X. *Optics Express* **2009**, *17*, 21509.
- [221] Kim, I.-S.; Sohn, B.-u.; Hwang, S. I.; Lee, C.-L.; Ko, D.-K. *Laser Physics* **2014**, *24*, 045701.
- [222] Mouton, N.; de Juan, A.; Sliwa, M.; Ruckebusch, C. *Chemometrics and Intelligent Laboratory Systems* **2011**, *105*, 74–82.
- [223] Xie, Y.; Li, Y.; Xiao, L.; Qiao, Q.; Dhakal, R.; Zhang, Z.; Gong, Q.; Galipeau, D.; Yan, X. *Journal of Physical Chemistry* **2010**, *114*, 14590–14600.

- [224] Bakulin, A. A.; Akshay Rao.; Vlad G. Pavelyev.; Paul H.M. van Loosdrecht.; Maxim S. Pshenichnikov.; Dorota Niedzialek.; Jérôme Cornil.; David Beljonne.; Friend, R. H. *Science* **2012**, 335, 1340–1344.
- [225] Kogelnik, H.; Li, T. *Proc IEEE* **1966**, 54, 1312–&.
- [226] Bélanger, P. A. *Optics Letters* **1991**, 16, 196.
- [227] Koster, L. J. A.; Mihailetschi, V. D.; Blom, P. W. M. *SPIE Newsroom* **2007**, 9–10.
- [228] Minnaert, B.; Veelaert, P. *Materials* **2012**, 5, 1933–1953.
- [229] Zeitouny, J.; Katz, E. A.; Dollet, A.; Vossier, A. *Scientific Reports* **2017**, 7, 1–9.
- [230] Johns, J. E.; Muller, E. A.; Frechet, J. M.; Harris, C. B. *Journal of the American Chemical Society* **2010**, 132, 15720–15725.
- [231] Lin, Y.; Li, Y.; Zhan, X. *Chemical Society Reviews* **2012**, 41, 4245–4272.
- [232] Ruckebusch, C.; Blanchet, L. *Analytica Chimica Acta* **2013**, 765, 28–36.
- [233] Howard, I. A.; Mangold, H.; Etzold, F.; Gehrig, D.; Laquai, F. *Ultrafast Dynamics in Molecules, Nanostructures and Interfaces* **2013**, 53–78.
- [234] Strang, G. *Linear Algebra and Its Applications*; 2005; p 496.
- [235] Ginsburg, J. *The American Mathematical Monthly* **1928**, 35, 347–349.
- [236] Dobryakov, A. L.; Kovalenko, S. A.; Weigel, A.; Pérez-Lustres, J. L.; Lange, J.; Müller, A.; Ernsting, N. P. *The Review of Scientific Instruments* **2010**, 81, 113106.
- [237] Blanchet, L.; Ruckebusch, C.; Huvenne, J. P.; de Juan, A. *Chemometrics and Intelligent Laboratory Systems* **2007**, 89, 26–35.

- [238] De Juan, A.; Maeder, M.; Martínez, M.; Tauler, R. *Chemometrics and Intelligent Laboratory Systems* **2000**, *54*, 123–141.
- [239] de Juan, A.; Casassas, E.; Tauler, R. *Encyclopedia of Analytical Chemistry*; 2000; pp 1–38.
- [240] Renk, K. F. *Basics of Laser Physics, Graduate Texts in Physics*; Springer, Cham, 2012; p 666.
- [241] Locharoenrat, K. *Optical Properties of Solids*; Jenny Stanford Publishing, 2016.
- [242] Eichhorn, M. *Laser Physics: From Principles to Practical Work in the Lab*; Springer International Publishing, 2014; pp 1–21.
- [243] Jaumot, J.; de Juan, A.; Tauler, R. *Chemometrics and Intelligent Laboratory Systems* **2015**, *140*, 1–12.
- [244] Li, S.; Ye, L.; Zhao, W.; Yan, H.; Yang, B.; Liu, D.; Li, W.; Ade, H.; Hou, J. *Journal of the American Chemical Society* **2018**, *140*, 7159–7167.
- [245] Bureš, F. *RSC Advances* **2014**, *4*, 58826–58851.
- [246] Benten, H.; Mori, D.; Ohkita, H.; Ito, S. *Journal of Materials Chemistry A* **2016**, *4*, 5340–5365.
- [247] Lu, L.; Kelly, M. A.; You, W.; Yu, L. *Nature Photonics* **2015**, *9*, 491–500.
- [248] Pan, M. A.; Lau, T. K.; Tang, Y.; Wu, Y. C.; Liu, T.; Li, K.; Chen, M. C.; Lu, X.; Ma, W.; Zhan, C. *Journal of Materials Chemistry A* **2019**, *7*, 20713–20722.
- [249] Graham, K. R.; Cabanetos, C.; Jahnke, J. P.; Idso, M. N.; El Labban, A.; Ngongang Ndjawa, G. O.; Heumueller, T.; Vandewal, K.; Salleo, A.; Chmelka, B. F.; Amassian, A.; Beaujuge, P. M.; McGehee, M. D. *Journal of the American Chemical Society* **2014**, *136*, 9608–9618.

- [250] Huang, W.; Gann, E.; Thomsen, L.; Dong, C.; Cheng, Y. B.; McNeill, C. R. *Advanced Energy Materials* **2015**, *5*, 1–11.
- [251] Wan, Q.; Guo, X.; Wang, Z.; Li, W.; Guo, B.; Ma, W.; Zhang, M.; Li, Y. *Advanced Functional Materials* **2016**, *26*, 6635–6640.
- [252] Fan, R.; Huai, Z.; Sun, Y.; Li, X.; Fu, G.; Huang, S.; Wang, L.; Yang, S. *Journal of Materials Chemistry C* **2017**, *5*, 10985–10990.
- [253] Jagadamma, L. K.; Sajjad, M. T.; Savikhin, V.; Toney, M. F.; Samuel, I. D. *Journal of Materials Chemistry A* **2017**, *5*, 14646–14657.
- [254] Kobori, T.; Fukuda, T. *Organic Electronics* **2017**, *51*, 76–85.
- [255] Collins, B. A.; Gann, E.; Guignard, L.; He, X.; McNeill, C. R.; Ade, H. *Journal of Physical Chemistry Letters* **2010**, *1*, 3160–3166.
- [256] Moulé, A. J.; Meerholz, K. *Advanced Materials* **2008**, *20*, 240–245.
- [257] Yao, H.; Ye, L.; Hou, J.; Jang, B.; Han, G.; Cui, Y.; Su, G. M.; Wang, C.; Gao, B.; Yu, R.; Zhang, H.; Yi, Y.; Woo, H. Y.; Ade, H.; Hou, J. *Advanced Materials* **2017**, *29*.
- [258] Zhang, S.; Ye, L.; Zhao, W.; Liu, D.; Yao, H.; Hou, J. *Macromolecules* **2014**, *47*, 4653–4659.
- [259] Huang, W.; Chandrasekaran, N.; Prasad, S. K.; Gann, E.; Thomsen, L.; Kabra, D.; Hodgkiss, J. M.; Cheng, Y. B.; McNeill, C. R. *ACS Applied Materials and Interfaces* **2016**, *8*, 29608–29618.
- [260] He, Z.; Xiao, B.; Liu, F.; Wu, H.; Yang, Y.; Xiao, S.; Wang, C.; Russell, T. P.; Cao, Y. *Nature Photonics* **2015**, *9*, 174–179.
- [261] Huang, W.; Gann, E.; Cheng, Y. B.; McNeill, C. R. *ACS Applied Materials and Interfaces* **2015**, *7*, 14026–14034.

- [262] Huo, L.; Zhang, S.; Guo, X.; Xu, F.; Li, Y.; Hou, J. *Angewandte Chemie - International Edition* **2011**, *50*, 9697–9702.
- [263] Chen, H. Y.; Hou, J.; Zhang, S.; Liang, Y.; Yang, G.; Yang, Y.; Yu, L.; Wu, Y.; Li, G. *Nature Photonics* **2009**, *3*, 649–653.
- [264] Cui, C.; Wong, W. Y.; Li, Y. *Energy and Environmental Science* **2014**, *7*, 2276–2284.
- [265] Chen, J. D.; Cui, C.; Li, Y. Q.; Zhou, L.; Ou, Q. D.; Li, C.; Li, Y.; Tang, J. X. *Advanced Materials* **2015**, *27*, 1035–1041.
- [266] Kong, J.; Hwang, I. W.; Lee, K. *Advanced Materials* **2014**, *26*, 6275–6283.
- [267] Liu, S.; You, P.; Li, J.; Li, J.; Lee, C. S.; Ong, B. S.; Surya, C.; Yan, F. *Energy and Environmental Science* **2015**, *8*, 1463–1470.
- [268] Mori, D.; Bente, H.; Okada, I.; Ohkita, H.; Ito, S. *Energy and Environmental Science* **2014**, *7*, 2939–2943.
- [269] Zhao, W.; Ye, L.; Zhang, S.; Fan, B.; Sun, M.; Hou, J. *Scientific Reports* **2014**, *3*, 1–7.
- [270] Huang, W.; Gann, E.; Xu, Z. Q.; Thomsen, L.; Cheng, Y. B.; McNeill, C. R. *Journal of Materials Chemistry A* **2015**, *3*, 16313–16319.
- [271] Li, Z.; Gao, F.; Greenham, N. C.; McNeill, C. R. *Advanced Functional Materials* **2011**, *21*, 1419–1431.
- [272] McNeill, C. R.; Hwang, I.; Greenham, N. C. *Journal of Applied Physics* **2009**, *106*.
- [273] Wood, S.; Blakesley, J. C.; Castro, F. A. *Physical Review Applied* **2018**, *10*, 1.
- [274] O'Regan, B. C.; Bakker, K.; Kroeze, J.; Smit, H.; Sommeling, P.; Durrant, J. R. *Journal of Physical Chemistry B* **2006**, *110*, 17155–17160.

- [275] Devižis, A.; De Jonghe-Risse, J.; Hany, R.; Nüesch, F.; Jenatsch, S.; Gulbinas, V.; Moser, J. E. *Journal of the American Chemical Society* **2015**, *137*, 8192–8198.
- [276] Gulbinas, V.; Kananavičius, R.; Valkunas, L.; Bässler, H. *Physical Review B - Condensed Matter and Materials Physics* **2002**, *66*, 1–4.
- [277] Scarongella, M.; De Jonghe-Risse, J.; Buchaca-Domingo, E.; Causa, M.; Fei, Z.; Heeney, M.; Moser, J. E.; Stingelin, N.; Banerji, N. *Journal of the American Chemical Society* **2015**, *137*, 2908–2918.
- [278] He, Y.; Chen, H.-y. Y.; Hou, J.; Li, Y. *Journal of the American Chemical Society* **2010**, *132*, 1377–1382.
- [279] Cheng, P.; Li, Y.; Zhan, X. *Energy and Environmental Science* **2014**, *7*, 2005–2011.
- [280] Hoke, E. T.; Vandewal, K.; Bartelt, J. A.; Mateker, W. R.; Douglas, J. D.; Noriega, R.; Graham, K. R.; Fréchet, J. M.; Salleo, A.; McGehee, M. D. *Advanced Energy Materials* **2013**, *3*, 220–230.
- [281] Seon, H.; Kim, B.; Kang, J. *IEEE Transactions on Nuclear Science* **2017**, *64*, 1739–1743.
- [282] He, Y.; Li, Y. *Physical Chemistry Chemical Physics* **2011**, *13*, 1970–1983.
- [283] Shuttle, C. G.; O'Regan, B.; Ballantyne, A. M.; Nelson, J.; Bradley, D. D.; De Mello, J.; Durrant, J. R. *Applied Physics Letters* **2008**, *92*, 1–4.
- [284] Shuttle, C. G.; Hamilton, R.; Nelson, J.; O'Regan, B. C.; Durrant, J. R. *Advanced Functional Materials* **2010**, *20*, 698–702.
- [285] Wang, G.; Melkonyan, F. S.; Facchetti, A.; Marks, T. J. *Angewandte Chemie - International Edition* **2019**, *58*, 4129–4142.
- [286] Facchetti, A. *Materials Today* **2013**, *16*, 123–132.

- [287] Kang, H.; Lee, W.; Oh, J.; Kim, T.; Lee, C.; Kim, B. J. *Accounts of Chemical Research* **2016**, *49*, 2424–2434.
- [288] Zhao, W.; Li, S.; Yao, H.; Zhang, S.; Zhang, Y.; Yang, B.; Hou, J. *Journal of the American Chemical Society* **2017**, *139*, 7148–7151.
- [289] Krebs, F. C.; Espinosa, N.; Hösel, M.; Søndergaard, R. R.; Jørgensen, M. *Advanced Materials* **2014**, *26*, 29–39.
- [290] Mulligan, C. J.; Wilson, M.; Bryant, G.; Vaughan, B.; Zhou, X.; Belcher, W. J.; Dastoor, P. C. *Solar Energy Materials and Solar Cells* **2014**, *120*, 9–17.
- [291] Savagatrup, S.; Printz, A. D.; O'Connor, T. F.; Zaretski, A. V.; Rodriguez, D.; Sawyer, E. J.; Rajan, K. M.; Acosta, R. I.; Root, S. E.; Lipomi, D. J. *Energy and Environmental Science* **2015**, *8*, 55–80.
- [292] Kim, T.; Choi, J.; Kim, H. J.; Lee, W.; Kim, B. J. *Macromolecules* **2017**, *50*, 6861–6871.
- [293] Genene, Z.; Mammo, W.; Wang, E.; Andersson, M. R. *Advanced Materials* **2019**, *31*, 1807275.
- [294] Zhou, N.; Facchetti, A. *Materials Today* **2018**, *21*, 377–390.
- [295] Venkateswararao, A.; Liu, S. W.; Wong, K. T. *Materials Science and Engineering R: Reports* **2018**, *124*, 1–57.
- [296] Guo, X.; Tu, D.; Liu, X. *Journal of Energy Chemistry* **2015**, *24*, 675–685.
- [297] Chang, R. P. H.; Guo, P.; Zhou, N.; Hartnett, P.; Manley, E. F.; Huang, H.; Facchetti, A.; Chen, L. X.; Loser, S.; Marks, T. J.; Lin, H.; Yu, X.; Wasielewski, M. R.; Lou, S. J. *Advanced Energy Materials* **2013**, *4*, 1300785.
- [298] Sun, H.; Tang, Y.; Koh, C. W.; Ling, S.; Wang, R.; Yang, K.; Yu, J.; Shi, Y.; Wang, Y.; Woo, H. Y.; Guo, X. *Advanced Materials* **2019**, *31*, 1–8.

- [299] Yan, C.; Barlow, S.; Wang, Z.; Yan, H.; Jen, A. K.; Marder, S. R.; Zhan, X. *Nature Reviews Materials* **2018**, *3*, 1–19.
- [300] Yang, J.; Xiao, B.; Tajima, K.; Nakano, M.; Takimiya, K.; Tang, A.; Zhou, E. *Macromolecules* **2017**, *50*, 3179–3185.
- [301] Jung, J. W.; Jo, J. W.; Chueh, C. C.; Liu, F.; Jo, W. H.; Russell, T. P.; Jen, A. K. *Advanced Materials* **2015**, *27*, 3310–3317.
- [302] Liu, S.; Kan, Z.; Thomas, S.; Cruciani, F.; Brédas, J. L.; Beaujuge, P. M. *Angewandte Chemie - International Edition* **2016**, *55*, 12996–13000.
- [303] Long, X.; Ding, Z.; Dou, C.; Zhang, J.; Liu, J.; Wang, L. *Advanced Materials* **2016**, 6504–6508.
- [304] Guo, Y.; Li, Y.; Awartani, O.; Han, H.; Zhao, J.; Ade, H.; Yan, H.; Zhao, D. *Advanced Materials* **2017**, *29*, 1–6.
- [305] Hwang, Y. J.; Courtright, B. A.; Ferreira, A. S.; Tolbert, S. H.; Jenekhe, S. A. *Advanced Materials* **2015**, *27*, 4578–4584.
- [306] Li, S.; Zhang, H.; Zhao, W.; Ye, L.; Yao, H.; Yang, B.; Zhang, S.; Hou, J. *Advanced Energy Materials* **2016**, *6*, 1–9.
- [307] Jung, J.; Lee, W.; Lee, C.; Ahn, H.; Kim, B. J. *Advanced Energy Materials* **2016**, *6*, 1–10.
- [308] Xu, X.; Li, Z.; Wang, J.; Lin, B.; Ma, W.; Xia, Y.; Andersson, M. R.; Janssen, R. A.; Wang, E. *Nano Energy* **2018**, *45*, 368–379.
- [309] Kim, W.; Choi, J.; Kim, J. H.; Kim, T. S. T.; Lee, C.; Lee, S.; Kim, M.; Kim, B. J.; Kim, T. S. T. *Chemistry of Materials* **2018**, *30*, 2102–2111.
- [310] Root, S. E.; Savagatrup, S.; Printz, A. D.; Rodriguez, D.; Lipomi, D. J. *Chemical Reviews* **2017**, *117*, 6467–6499.

- [311] Bhosale, S. V.; Bhosale, S. V.; Bhargava, S. K. *Organic and Biomolecular Chemistry* **2012**, *10*, 6455–6468.
- [312] Kim, S. W.; Choi, J.; Bui, T. T. T.; Lee, C.; Cho, C.; Na, K.; Jung, J.; Song, C. E.; Ma, B.; Lee, J. Y.; Shin, W. S.; Kim, B. J. *Advanced Functional Materials* **2017**, *27*, 2–9.
- [313] Xu, X.; Li, Z.; Zhang, W.; Meng, X.; Zou, X.; Di Carlo Rasi, D.; Ma, W.; Yartsev, A.; Andersson, M. R.; Janssen, R. A.; Wang, E. *Advanced Energy Materials* **2018**, *8*, 1–11.
- [314] Li, Z.; Zhang, W.; Xu, X.; Genene, Z.; Di Carlo Rasi, D.; Mammo, W.; Yartsev, A.; Andersson, M. R.; Janssen, R. A.; Wang, E. *Advanced Energy Materials* **2017**, *7*, 1–11.
- [315] Kong, J.; Song, S.; Yoo, M.; Lee, G. Y.; Kwon, O.; Park, J. K.; Back, H.; Kim, G.; Lee, S. H.; Suh, H.; Lee, K. *Nature Communications* **2014**, *5*, 1–8.
- [316] Jørgensen, M.; Norrman, K.; Gevorgyan, S. A.; Tromholt, T.; Andreasen, B.; Krebs, F. C. *Advanced Materials* **2012**, *24*, 580–612.
- [317] Kim, T.; Younts, R.; Lee, W.; Lee, S.; Gundogdu, K.; Kim, B. J. *Journal of Materials Chemistry A* **2017**, *5*, 22170–22179.
- [318] Zhang, Y.; Xu, Y.; Ford, M. J.; Li, F.; Sun, J.; Ling, X.; Wang, Y.; Gu, J.; Yuan, J.; Ma, W. *Advanced Energy Materials* **2018**, *8*, 1–10.
- [319] Wang, J.; Enevold, J.; Edman, L. *Advanced Functional Materials* **2013**, *23*, 3220–3225.
- [320] Piersimoni, F.; Degutis, G.; Bertho, S.; Vandewal, K.; Spoltore, D.; Vangerven, T.; Drijkoningen, J.; Van Bael, M. K.; Hardy, A.; D’Haen, J.; Maes, W.; Vanderzande, D.; Nesladek, M.; Manca, J. *Journal of Polymer Science, Part B: Polymer Physics* **2013**, *51*, 1209–1214.

- [321] Lee, C.; Li, Y.; Lee, W.; Lee, Y.; Choi, J.; Kim, T.; Wang, C.; Gomez, E. D.; Woo, H. Y.; Kim, B. J. *Macromolecules* **2016**, *49*, 5051–5058.
- [322] Lee, C.; Giridhar, T.; Choi, J.; Kim, S.; Kim, Y.; Kim, T.; Lee, W.; Cho, H. H.; Wang, C.; Ade, H.; Kim, B. J. *Chemistry of Materials* **2017**, *29*, 9407–9415.
- [323] Schubert, M. et al. *Advanced Functional Materials* **2014**, *24*, 4068–4081.
- [324] Yan, H.; Chen, Z.; Zheng, Y.; Newman, C.; Quinn, J. R.; Dötz, F.; Kastler, M.; Facchetti, A. *Nature* **2009**, *457*, 679–686.
- [325] Moore, J. R.; Albert-Seifried, S.; Rao, A.; Massip, S.; Watts, B.; Morgan, D. J.; Friend, R. H.; McNeill, C. R.; Sirringhaus, H. *Advanced Energy Materials* **2011**, *1*, 230–240.
- [326] Fabiano, S.; Chen, Z.; Vahedi, S.; Facchetti, A.; Pignataro, B.; Loi, M. A. *Journal of Materials Chemistry* **2011**, *21*, 5891–5896.
- [327] Bao, X.; Zhang, Y.; Wang, J.; Zhu, D.; Yang, C.; Li, Y.; Yang, C.; Xu, J.; Yang, R. *Chemistry of Materials* **2017**, *29*, 6766–6771.
- [328] Fan, B.; Ying, L.; Wang, Z.; He, B.; Jiang, X. F.; Huang, F.; Cao, Y. *Energy and Environmental Science* **2017**, *10*, 1243–1251.
- [329] Yi, Y.; Zhao, J.; Yang, S.; Facchetti, A.; Liu, P.; Jiang, K.; Chen, Z.; Mu, C.; Wei, Z.; Ade, H.; Ma, W.; Yan, H.; Huang, F.; Zhang, K.; Wang, J. *Advanced Materials* **2014**, *26*, 7224–7230.
- [330] Mori, D.; Bente, H.; Okada, I.; Ohkita, H.; Ito, S. *Advanced Energy Materials* **2014**, *4*, 1–6.
- [331] Wu, H.; He, Z.; Cao, Y.; Xu, M.; Zhong, C.; Su, S. *Nature Photonics* **2012**, *6*, 591–595.
- [332] Liang, Y.; Xu, Z.; Xia, J.; Tsai, S. T.; Wu, Y.; Li, G.; Ray, C.; Yu, L. *Advanced Materials* **2010**, *22*, 135–138.

- [333] Kakara, T.; Kawashima, K.; Takimiya, K.; Osaka, I.; Koganezawa, T.; Murata, H.; Vohra, V. *Nature Photonics* **2015**, *9*, 403–408.
- [334] Kline, R. J.; McGehee, M. D. *Polymer Reviews* **2006**, *46*, 27–45.
- [335] Steyrlleuthner, R.; Schubert, M.; Howard, I.; Klaumünzer, B.; Schilling, K.; Chen, Z.; Saalfrank, P.; Laquai, F.; Facchetti, A.; Neher, D. *Journal of the American Chemical Society* **2012**, *134*, 18303–18317.
- [336] Earmme, T.; Hwang, Y. J.; Murari, N. M.; Subramaniyan, S.; Jenekhe, S. A. *Journal of the American Chemical Society* **2013**, *135*, 14960–14963.
- [337] Hwang, Y. J.; Earmme, T.; Courtright, B. A.; Eberle, F. N.; Jenekhe, S. A. *Journal of the American Chemical Society* **2015**, *137*, 4424–4434.
- [338] Uddin, M. A.; Kim, Y.; Younts, R.; Lee, W.; Gautam, B.; Choi, J.; Wang, C.; Gundogdu, K.; Kim, B. J.; Woo, H. Y. *Macromolecules* **2016**, *49*, 6374–6383.
- [339] Jung, I. H.; Zhao, D.; Jang, J.; Chen, W.; Landry, E. S.; Lu, L.; Talapin, D. V.; Yu, L. *Chemistry of Materials* **2015**, *27*, 5941–5948.
- [340] Deng, P.; Ho, C. H. Y.; Lu, Y.; Li, H. W.; Tsang, S. W.; So, S. K.; Ong, B. S. *Chemical Communications* **2017**, *53*, 3249–3252.
- [341] Murgatroyd, P. N. *Journal of Physics D: Applied Physics* **1970**, *3*, 151–156.
- [342] Hwang, I.; McNeill, C. R.; Greenham, N. C. *Journal of Applied Physics* **2009**, *106*.
- [343] Li, Z.; Lakhwani, G.; Greenham, N. C.; McNeill, C. R. *Journal of Applied Physics* **2013**, *114*, 034502.
- [344] Gasparini, N.; Wadsworth, A.; Moser, M.; Baran, D.; McCulloch, I.; Brabec, C. J. *Advanced Energy Materials* **2018**, *8*, 1–15.
- [345] Zhao, W.; Qian, D.; Zhang, S.; Li, S.; Inganäs, O.; Gao, F.; Hou, J. *Advanced Materials* **2016**, *28*, 4734–4739.

- [346] Gasparini, N.; Salvador, M.; Strohm, S.; Heumueller, T.; Levchuk, I.; Wadsworth, A.; Bannock, J. H.; de Mello, J. C.; Egelhaaf, H. J.; Baran, D.; McCulloch, I.; Brabec, C. J. *Advanced Energy Materials* **2017**, 7, 1700770.
- [347] Li, Z.; Wu, F.; Lv, H.; Yang, D.; Chen, Z.; Zhao, X.; Yang, X. *Advanced Materials* **2015**, 27, 6999–7003.
- [348] Wang, S.; Qu, Y.; Li, S.; Ye, F.; Chen, Z.; Yang, X. *Advanced Functional Materials* **2015**, 25, 748–757.
- [349] Van Krevelen, D.; Te Nijenhuis, K. *Properties of Polymers* **2009**, 287–318.
- [350] Gasparini, N.; Lucera, L.; Salvador, M.; Prosa, M.; Spyropoulos, G. D.; Kubis, P.; Egelhaaf, H. J.; Brabec, C. J.; Ameri, T. *Energy and Environmental Science* **2017**, 10, 885–892.
- [351] Ameri, T.; Khoram, P.; Min, J.; Brabec, C. J. *Advanced Materials* **2013**, 25, 4245–4266.
- [352] Ameri, T.; Li, N.; Brabec, C. J. *Energy and Environmental Science* **2013**, 6, 2390–2413.
- [353] Bob, B.; Duan, H.-S.; Li, G.; Chen, W.; Chang, W.-H.; Dou, L.; Yang, Y. *Nature Photonics* **2015**, 9, 190–198.
- [354] Qin, Y.; Wei, Z.; Yu, R.; Hou, J.; Zhang, J.; Li, W.; Zheng, Z.; Zhang, S. *Advanced Materials* **2016**, 28, 5133–5138.
- [355] Hanifi, D. A. et al. *Nature Materials* **2016**, 16, 363–369.
- [356] Deibe, C.; Strobe, T.; Dyakonov, V. *Advanced Materials* **2010**, 22, 4097–4111.
- [357] Rau, U. **2007**, 76, 085303–085311.
- [358] Tuladhar, S. M.; Azzouzi, M.; Delval, F.; Yao, J.; Guilbert, A. A.; Kirchartz, T.; Montcada, N. F.; Dominguez, R.; Langa, F.; Palomares, E.; Nelson, J. *ACS Energy Letters* **2016**, 1, 302–308.

- [359] Chen, S.; Liu, Y.; Zhang, L.; Chow, P. C.; Wang, Z.; Zhang, G.; Ma, W.; Yan, H. *Journal of the American Chemical Society* **2017**, *139*, 6298–6301.
- [360] Ade, H.; Hou, J.; Baran, D.; Ye, L.; Song, X.; Yao, H.; Gasparini, N. *ACS Energy Letters* **2018**, *3*, 669–676.
- [361] Cui, Y.; Yao, H.; Gao, B.; Qin, Y.; Zhang, S.; Yang, B.; He, C.; Xu, B.; Hou, J. *Journal of the American Chemical Society* **2017**, *139*, 7302–7309.
- [362] Huang, W.; Wang, R.; Zhang, Z.; Yuan, J.; Meng, D.; Yang, Y.; Cheng, P.; Huang, T.; Gao, F.; Zhang, H.; Yang, J. L.; Zou, Y.; Chang, S.-Y. *Nature Communications* **2019**, *10*, 1–8.
- [363] Li, S.; Ye, L.; Zhao, W.; Zhang, S.; Mukherjee, S.; Ade, H.; Hou, J. *Advanced Materials* **2016**, *28*, 9423–9429.
- [364] Zhang, J.; Tan, H. S.; Guo, X.; Facchetti, A.; Yan, H. *Nature Energy* **2018**, *3*, 720–731.
- [365] Yao, H.; Cui, Y.; Yu, R.; Gao, B.; Zhang, H.; Hou, J. *Angewandte Chemie - International Edition* **2017**, *56*, 3045–3049.
- [366] Li, Y.; Lin, J. D.; Che, X.; Qu, Y.; Liu, F.; Liao, L. S.; Forrest, S. R. *Journal of the American Chemical Society* **2017**, *139*, 17114–17119.
- [367] ning Huang, H. J.; Nan, H. R.; Yang, Y. G.; Gao, X. Y.; Chen, F.; Chen, Z. K. *Advanced Materials Interfaces* **2018**, *5*, 1–10.
- [368] Oosterhout, S. D.; Braunecker, W. A.; Owczarczyk, Z. R.; Ayzner, A. L.; Toney, M. F.; Olson, D. C.; Kopidakis, N. *Organic Electronics* **2017**, *47*, 57–65.
- [369] Yin, H.; Cheung, S. H.; Ngai, J. H.; Ho, C. H. Y.; Chiu, K. L.; Hao, X.; Li, H. W.; Cheng, Y.; Tsang, S. W.; So, S. K. *Advanced Electronic Materials* **2017**, *3*, 1700007.

- [370] Lin, Y.; He, Q.; Zhao, F.; Huo, L.; Mai, J.; Lu, X.; Su, C. J.; Li, T.; Wang, J.; Zhu, J.; Sun, Y.; Wang, C.; Zhan, X. *Journal of the American Chemical Society* **2016**, *138*, 2973–2976.
- [371] Min, J.; Zhang, Z. G.; Zhang, S.; Li, Y. *Chemistry of Materials* **2012**, *24*, 3247–3254.
- [372] Zhang, M.; Guo, X.; Ma, W.; Ade, H.; Hou, J. *Advanced Materials* **2014**, *26*, 5880–5885.
- [373] Huo, L.; Liu, T.; Sun, X.; Cai, Y.; Heeger, A. J.; Sun, Y. *Advanced Materials* **2015**, *27*, 2938–2944.
- [374] Li, G.; Gong, X.; Zhang, J.; Liu, Y.; Feng, S.; Li, C.; Bo, Z. *ACS Applied Materials and Interfaces* **2016**, *8*, 3686–3692.
- [375] Lakowicz, J. R. *Springer, New York, USA*; 2006; p 362.
- [376] Plonka, A. *Dispersive Kinetics*; Springer Netherlands: Dordrecht, 2001; Vol. 97; pp 91–147.
- [377] James, D. R.; Ware, W. R. *Chemical Physics Letters* **1985**, *120*, 455–459.
- [378] Alex Marsh, R.; Hodgkiss, J. M.; Albert-Seifried, S.; Friend, R. H. *Nano Letters* **2010**, *10*, 923–930.
- [379] Teuscher, J.; Brauer, J. C.; Stepanov, A.; Solano, A.; Boziki, A.; Chergui, M.; Wolf, J. P.; Rothlisberger, U.; Banerji, N.; Moser, J. E. *Structural Dynamics* **2017**, *4*, 1–27.
- [380] Melianas, A.; Etzold, F.; Savenije, T. J.; Laquai, F.; Inganäs, O.; Kemerink, M. *Nature Communications* **2015**, *6*, 8778.